Simulation of Richtmyer–Meshkov flows for elastic–plastic solids in planar and converging geometries using an Eulerian framework

Thesis by

Alejandro López Ortega

In Partial Fulfillment of the Requirements
for the Degree of
Doctor of Philosophy

1891

California Institute of Technology
Pasadena, California

2013
(Defended February 15, 2013)

A mi familia, especialmente mis padres y mis abuelos,
que hicieron posible que pudiera llegar hasta aquí.

Acknowledgements

I would like to start by expressing my deepest gratitude to Professors Dale Pullin and Daniel Meiron for giving me the opportunity of working on this project and for their guidance, insightful advice, and complete support in these three and a half years. You were always there to propose ideas to try (that usually worked!) when things were not looking good and I will remember our group and individual meetings as one of the most educative and fulfilling parts of my Caltech experience. I extend this recognition to my committee members, Professors Michael Ortiz, Guruswami Ravichandran, and Oscar Bruno, for their expert academic and professional advice. My deepest appreciation goes to Dr. Manuel Lombardini, Dr. David Hill, Dr. Philip Barton, and Dr. Julian Cummings for their encouragement and all the in-depth discussions that led this dissertation to its completion.

My arrival at Caltech would not have been possible without the involvement of Professor Pilar Ariza from the University of Seville and Professor Michael Ortiz as my first-year academic advisor. I acknowledge the extensive assistance of the Andalusian Regional Government in its initial financial support through the Agency of Innovation and Development of Andalusia. I cannot forget to thank the Caltech PSAAP Center—directed by Professor Michael Ortiz and Dr. Mark Saltzer, and supported by the Department of Energy National Nuclear Security Administration under Award Number DE-FC52-08NA28613—for the economic support. Thanks to the PSAAP and GALCIT staff for making my life easier, arranging my trips to conferences, and solving quickly those little problems that distract you from work.

I would like to extend my warmest gratitude to Professor Guglielmo Scovazzi of Duke University (former senior staff member at Sandia National Laboratories) for his support in the course of two 10-week internships in Albuquerque, and for the many scientific and personal discussions we've had since then.

My life at Caltech would not have been complete without my labmates (Daniel, Yu, Geoff, Michio, Jack, Namiko, Dustin, Marcello), the Spaniards at Caltech (Celia, Paco, Molainer, Fran, Pelayo, Nacho, Juan Pedro, Adrián, Carlos, Dani, Ricardo, Pablo), my friends in the Caltech Flying Club and the board of directors, my classmates from the master year, and all others that I met through these years (Esperanza, Ana, Monica,...) and who have helped in brightening my life.

Finally, I would not be the person I am and I would not have completed this step of my life

without the love of my family: my parents who always showed me the importance of pursuing my dreams and fully supported me in my decision of coming to the United States even when that meant having a son 10.000 kilometers away from home, my sister who is always there listening to my stories and dilemmas, my aunt Carmen for treating me as her own son, and my grandparents who gave everything they had for a brighter future for their sons and grandsons. My last words go to the love of my life, Romelia: meeting you simply justifies having come to Caltech and you have always been there when I needed it most. Gracias a todos.

Abstract

This thesis presents a numerical and analytical study of two problems of interest involving shock waves propagating through elastic–plastic media: the motion of converging (imploding) shocks and the Richtmyer–Meshkov (RM) instability. Since the stress conditions encountered in these cases normally produce large deformations in the materials, an Eulerian description, in which the spatial coordinates are fixed, is employed. This formulation enables a direct comparison of similarities and differences between the present study of phenomena driven by shock-loading in elastic-plastic solids, and in fluids, where they have been studied extensively.

An approximate description of the motion of an elastic–plastic material processed by a cylindrically/spherically converging shock was obtained through the use of Whitham's shock dynamics (WSD) theory. Originally applied with success to various gas dynamics problems, this theory is presented for solid media, in both elastic and plastic regimes. Comparison of the theoretical predictions with numerical simulations utilizing several isothermal and non-isothermal constitutive laws reveal that WSD is an accurate tool for characterizing the evolution of converging shocks at all stages, even when shear deformations and plasticity are considered. While the hydrostatic part of the energy essentially determines the strong-shock behavior, the shear modulus and yield stress modify the compression ratio and velocity of the shock far from the axis/origin. A description of the evolution of an initially elastic shock into the plastic regime as it is strengthened by the converging geometry is also given: an elastic shock is initially followed by a plastic compression region that exhibits a nonuniform radial profile and that becomes progressively narrower and steepens to become a quasi-discontinuous profile as it approaches the axis/origin, finally overtaking the elastic precursor.

An impulsive Richtmyer–Meshkov model was developed to describe the effect of the immediate acceleration of a perturbed interface separating different elastic materials. The resulting initial boundary value problem was solved using Laplace transform techniques. Analysis of the singularities in the complex transform domain suggests the existence of two kinds of stable interface behavior: ringing and oscillatory decay, depending on the material parameters and boundary conditions employed. A detailed study of the vorticity distribution shows that the propagation of shear waves are responsible for the stabilization of the interface.

The study of the Richtmyer–Meshkov flow for elastic–plastic materials requires extensive use of numerical simulations. An updated version of a previously developed multi-material, level-set-based, Eulerian framework for solid mechanics is used to this effect. The revised code includes the use of a new multi-material HLLD Riemann problem for imposing material boundary conditions, and a new formulation of the equations of motion that makes use of the stretch tensor while avoiding the degeneracy of the stress tensor under rotation. The case of a solid–vacuum interface in planar geometry is first examined. Ejecta formation is appreciated under certain initial conditions while in other conditions, after an initial period of growth, the interface displays a quasi-stationary long-term behavior. A linear relation between the material strength and the maximum amplitude of the interface perturbations is recovered, in agreement with previous results in the literature.

Finally, a parametric study of the behavior of a solid–gas interface in a converging geometry and in the presence of a cylindrically converging shock is performed. The initial growth rate of the interface is scaled by the interface geometry, initial density ratio, and shock strength. A second phase reversal of the interface that does not occur in the planar case appears as a result of the converging geometry and the high density ratio between the solid and the gas. After the re-shock event, a turbulent mixing zone, similar to what is observed in gas–gas interfaces, is created, especially when materials with low strength driven by moderate to strong shocks are considered.

Contents

Acknowledgements **iv**

Abstract **vi**

Contents **ix**

List of Figures **xiii**

List of Tables **xxiii**

1 Introduction **1**

1.1 Motivation 2

1.2 Previous related work 4

1.2.1 Eulerian solid mechanics 4

1.2.2 Multi-material simulations 5

1.2.3 Converging shock waves 6

1.2.4 Richtmyer–Meshkov instability (RMI) 7

1.3 Outline of present work 8

2 Description of the Eulerian framework for solid mechanics **10**

2.1 Introduction 10

2.2 Equations of motion for elastic solid media 11

2.2.1 Lagrangian–Eulerian mapping 12

2.2.2 Equations of motion for the deformation and inverse deformation tensors . . 12

2.2.2.1 Inverse deformation tensor 13

2.2.2.2 Deformation tensor 14

2.2.3 Stretch and strain tensors 15

2.2.4 Closure relations and constitutive laws 16

2.3 Plasticity 17

2.4 Characteristic speeds 23

2.5 Summary 23

3 Numerical implementation 25

3.1 Introduction 25
3.2 Single-material implementation 26
3.2.1 $\mathbf{F}^e$ formulation 27
3.2.2 Inverse deformation tensor–plastic deformation tensor formulation 28
3.2.3 Elastic inverse deformation tensor formulation 29
3.2.4 Use of the stretch tensor 30
3.2.5 Time and spatial discretization 33
3.2.6 Inelastic update 36
3.3 Multi-material implementation 38
3.3.1 Level-set advection and reinitialization 39
3.3.2 Boundary conditions at material interfaces and free surfaces 40
3.3.3 HLLD Multi-material Riemann solver 42
3.3.3.1 Wave speed estimation 45
3.3.3.2 Numerical examples 46
3.3.4 Effect of the Cartesian grid on the level-set method 49
3.3.5 Mass conservation in the level-set method 53
3.3.5.1 IVP 1 53
3.3.5.2 IVP 2 54
3.3.5.3 Test results 54
3.4 Summary 57

4 Converging shocks in elastic–plastic solids 60

4.1 Introduction 60
4.2 Elastic motion 62
4.2.1 Governing equations for radially symmetric motion 62
4.2.2 Numerical method and computational geometry 62
4.2.3 Whitham's shock dynamics and Rankine–Hugoniot jump conditions 63
4.2.4 Neo-Hookean isothermal constitutive law 64
4.2.4.1 Polynomial dependence for $p(\rho)$ 66
4.2.4.2 Arctanh form for $p(\rho)$ 68
4.2.5 Neo-Hookean non-isothermal constitutive law 70
4.3 Plastic motion 71
4.3.1 Perfectly plastic model 74
4.3.1.1 Shock dynamics for elastic–perfectly plastic solids 74

4.3.2 Numerical simulation of elastic–plastic shocks 75

4.3.2.1 Elastic–plastic transition 76

4.3.3 Influence of the shear modulus and plasticity on the shock velocity 79

4.4 Summary 80

5 Analytical model for linearized impulsive-driven Richtmyer–Meshkov flow in elastic solids 82

5.1 Introduction 82

5.2 Problem description 83

5.3 Equations of motion and boundary conditions 84

5.3.1 Boundary conditions 85

5.4 Base flow and linearization 86

5.4.1 Linearization 86

5.5 Solution of the problem 87

5.6 Analysis of the interface behavior 90

5.6.1 Short-time interface behavior 91

5.6.2 Long-time interface behavior 92

5.6.2.1 The contributions of the branch cuts 93

5.6.2.2 The contributions of the poles 94

5.6.3 Conclusions of the analysis 96

5.7 Results 97

5.7.1 Interface behavior 97

5.7.2 Oscillation period 98

5.7.3 Vorticity 101

5.7.4 Comparison with numerical results 105

5.8 Summary 106

6 Numerical simulations of Richtmyer–Meshkov instability in multiple material interfaces 109

6.1 Introduction 109

6.2 Constitutive laws 110

6.3 Planar Richtmyer–Meshkov instability in solid–vacuum interfaces 111

6.4 Cylindrical Richtmyer–Meshkov instability in solid–gas interfaces 116

6.4.1 Computational domain. Boundary and initial conditions 117

6.4.2 Baseline problem description 118

6.4.3 Convergence studies 123

6.4.3.1 Fluid mass conservation 123

6.4.3.2 Preservation of cylindrical geometry in a multi-material level-set algorithm . . . 128

6.4.3.3 Summary of convergence studies . . . 129

6.4.4 Interface parametric analysis . . . 129

6.4.4.1 Influence of the initial geometry of the interface . . . 131

6.4.4.2 Influence of the density ratio . . . 133

6.4.4.3 Influence of the initial shock Mach number . . . 137

6.4.4.4 Influence of yield stress . . . 144

6.4.4.5 Summary of parametric analysis . . . 147

6.5 Summary . . . 149

7 Conclusion 151

7.1 Summary . . . 151

7.2 Future work . . . 153

A Method of characteristics and Whitham's shock dynamics 155

A.1 Isothermal constitutive law . . . 156

A.1.1 Elastic motion . . . 156

A.1.2 Perfectly plastic motion . . . 157

A.2 Non-isothermal constitutive law for elastic motion . . . 158

B Approximation for the growth rate using linearization around branch cuts 160

C Additional mass conservation examples 164

C.1 Planar solid–gas with no perturbation in a two-dimensional grid . . . 164

C.2 Planar solid–solid Richtmyer–Meshkov . . . 167

D Density contour plots from parametric studies 171

D.1 Influence of the initial interface parameters . . . 172

D.2 Influence of the density ratio . . . 180

D.3 Influence of the initial shock Mach number . . . 188

D.4 Influence of the yield stress . . . 196

Bibliography 202

List of Figures

2.1 Stress–strain curves for tensile one-dimensional experiments. Experimental data in (a) is represented by symbols and obtained from [47], data in (b) has been obtained from experiments conducted in Prof. Ravichandran's lab and is represented by dashed lines. Theoretical results after calibration of parameters in Eq. (2.46) are represented by continuous lines. Figures were produced by Philip Barton [9]. 22

3.1 Initial condition for a one-dimensional problem in which two pieces of the same unstressed elastic material are rotated $\frac{\pi}{2}$ with respect to each other 33

3.2 Density, components of the inverse deformation tensor, and velocity after 3 and 8 time-steps for the initial problem described in Fig. 3.1 using the $\mathbf{g}$ formulation with and without density penalty terms. Each tick in the x-axis represents a cell boundary. . . 34

3.3 Diagram of ghost cells around a two-material interface. Orange-flagged cells represent ghost cells for material 1, with solid color and diagonal lines marking the inner band, populated by the solution of a Riemann problem, and the outer region, populated by extrapolation from inner band, respectively. The same pattern is used for the ghost cells of material 2, colored in blue. 41

3.4 Waves and states in the approximate HLLD multi-material Riemann problem 42

3.5 L_2-error computed using Eq. (6.7) for the inner and outer material boundary as a function of time for the examined grid resolutions. The convergence rate is also shown. 51

3.6 Position of the interface as a function of the azimuthal position for $t = t_f = 3\,\mu$s. Different colors are used to describe the results produced by the examined grid resolutions. For the color legend, see Fig. 3.5(a). 52

3.7 Errors in 2D simulations for different grid resolutions taking as reference the analytical result in [56] at $t = t_f = 3\,\mu$s. The error in the mean position of the interface is represented in (a). Azimuthally averaged deviations from radial symmetry are shown in (b). 52

3.8 Mass percentage with respect to the initial mass as a function of time for IVP 2 in a single-material simulation (no level set). Uni-grid and two-level simulations with and without fix-up algorithm are also shown. Uni-grid produces exact conservation of mass. The addition of an extra level of refinement degrades the solution, an effect that can be partially fixed by the use of the fix-up algorithm. 55

3.9 Mass percentage with respect to initial mass as a function of time for IVP 1. Results are depicted for the mass contained in each of the two level-sets and the total mass. The last figure represents the mass errors evolution in the L_2-norm with the number of cells in each direction of the base grid. 57

3.10 Mass percentage with respect to initial mass as a function of time for IVP 2. Results are depicted for the mass contained in each of the two level-sets and the total mass. The last figure represents the mass errors evolution in the L_2-norm with the number of cells in each direction of the base grid. 58

4.1 Spherically symmetric ($s = 3$) converging shock initially started at $R = R_i$ with $J_i = 0.9$ (i.e., $M_i \approx 1.14$) and propagating from left to right into a purely elastic solid medium described by the isothermal constitutive law (4.8) with polynomial pressure form (4.13): (a) Density radial profiles obtained from the numerical simulation at equally spaced times (dashed lines) and density ratio immediately behind the shock ($r = R(t)^+$) given by WSD (solid line); (b) $u + a$-characteristics obtained from numerical simulation (dashed lines) and shock trajectory $r = R(t)$ vs t obtained from WSD (solid line); (c) Shock Mach number M as a function of the shock position $R(t)$ plotted in a log–log scale, from the simulation (dashed line) and WSD (solid line). 67

4.2 Spherically symmetric ($s = 3$) converging shock initially started at $R = R_i$ with $J_i = 0.9$ (i.e., $M_i \approx 1.02$) and propagating from left to right into a purely elastic solid medium described by the isothermal constitutive law (4.8), using the Arctanh pressure form (4.16) with the choice $J_\infty = 1/6$, $p_0 = 10\,\mathrm{GPa}$ and $\beta = 5$. See Fig. 4.1 for keys. . 69

4.3 Spherically symmetric ($s = 3$) converging shock initially started at $R = R_i$ with $J_i = 0.9$ (i.e., $M_i \approx 1.07$) and propagating from left to right into a purely elastic solid medium described by the non-isothermal constitutive law (4.19) with $\gamma = 1.4$ (i.e., $J_\infty = 1/6$). See Fig. 4.1 for keys. 72

4.4 Spherically symmetric ($s = 3$) converging shock initially started at $R = R_i$ with $J_i = 0.9$ (i.e., $M_i \approx 1.01$) and propagating from left to right into an elastic–plastic solid medium following the isothermal constitutive law (4.26) with the polynomial pressure form (4.13), and given the von Mises constraint (4.28) with $\sigma_Y = 0.29$ GPa (aluminum). See Fig. 4.1 for keys. 77

4.5 Density radial profiles obtained from the numerical simulation for (a) spherically symmetric converging and (b) planar motion. Elastic–plastic deformations follow the isothermal constitutive law (4.26), using the polynomial pressure form (4.13) with $c_1 = c_2 = c_3 = 1$GPa, and given the von Mises constraint (4.28) with $\sigma_Y = 7$GPa. Note that for the planar case an initial shock Mach number cannot be defined since the shock is started beyond the elastic–plastic transition. The elastic precursor Mach number is $M^e \approx 1.02$ for both simulations 78

4.6 $|\sigma_{rr} - \sigma_{\theta\theta}|/\sigma_Y$ vs $J(= \rho_0/\rho)$ immediately behind the shock for an elastic–plastic material. The Hugoniot curve (i.e., the locus of the possible post-shock states of the material for a given initial condition) is completed by some Rayleigh lines (i.e., the thermodynamic path connecting the initial state with a post-shock state). Isothermal polynomial pressure form is considered, but the shape of the Hugoniot curve and the different regions can be reproduced for other constitutive laws. 79

4.7 (a) Shock trajectory and (b) J immediately behind the shock vs R for a spherically symmetric ($s = 3$) converging shock initially stated at $r = R_i$ with $J_i = 0.9$. Comparisons between the purely elastic, elastic–plastic and zero-shear solid simulations using the isothermal constitutive law (4.8) or (4.26), with the polynomial pressure form (4.13). $\sigma_Y = 0.29$ GPa was used for the elastic–plastic case. 80

5.1 Description of the problem. The interface is $x_1 = \eta(x_2, t)$. Left and right states are denoted "−" and "+", respectively. 83

5.2 Set of branch cuts used for the analysis and deformation of the Bromwich integral. Two poles are shown in the imaginary axis, which is not a general case. For any pole found, the contour is deformed to surround it. 92

5.3 Regions of existence / non-existence of pure imaginary poles. A parametric set that lies in the first / second region produces an oscillatory / decaying behavior of the interface, respectively. 95

5.4 Position of the closest pole with respect to the imaginary axis and relative to the branch cuts (horizontal dashed lines). Another conjugate pole lies in $Im(s) < 0$. Arrows show the direction the poles follow when incrementing c_- leaving c_+ and r unchanged. When both velocities are similar, the poles lie on the imaginary axis and the interface oscillates. After reaching the branch cut, the pole reappears and tends to the imaginary axis as $c_- \to \infty$. 96

5.5 Interface amplitude varying c_-/c_+ from 1 to 3 and r 99

5.6 Interface amplitude varying c_-/c_+ from 0.2 to 1 and fixed r 100

5.7 Oscillation period for fixed density ratio 6.182 and varying shear modulus. The complete model result is calculated performing numerically the inverse Laplace transform of the interface amplitude and counting the time between oscillations. The long-term estimate uses Eq. (5.63). The estimate of Piriz et al. uses Eq. (5.64). The pole frequency is calculated by locating the pole in the complex plane. 101

5.8 Oscillation period for varying density ratio and fixed ratio of shear modulus μ_+/μ_-. The complete model result is calculated performing numerically the inverse Laplace transform of the interface amplitude and counting the time between oscillations. The long-term estimate uses Eq. (5.63). The estimate of Piriz et al. uses Eq. (5.64). The pole frequency is calculated by locating the pole in the complex plane. 102

5.9 Amplitude of vorticity at different times for $c_-/c_+ = 1$, $r = 2$. Equal shear wave velocities produce a symmetric distribution of vorticity at each time. 103

5.10 Amplitude of vorticity at different times for $c_-/c_+ = 3$, $r = 2$. Vorticity is carried off the interface faster in the material with higher wave velocity 104

5.11 Evolution of the tangential velocity jump across the interface for two different sets of parameters. The first set (continuous line) corresponds to an oscillatory long-term behavior while the second one (dashed line) corresponds to a decaying behavior. . . . 105

5.12 Comparison of interface growth rate, defined as $U(0, t)$ between the analytical model prediction and numerical simulation results. 107

6.1 Time evolution of density contours for a solid–vacuum Richtmyer-Meshkov problem with parameters for copper, $\sigma_Y = 0.5\,\text{GPa}$, $\eta_0 k = 0.4$, and $M_s = 1.67$. (a,b) show initial conditions and propagation of the shock, (c) depicts the state after shock–interface interaction with interface phase reversal, (d,e,f) show unbounded spike growth and break-up. 113

6.2 Comparison between spike and bubble amplitudes with time obtained from AMROC simulations (continuous lines) and Dimonte et al. (PAGOSA) results [27] (dashed lines) for four different values of the initial amplitude of the interface $k\eta_0 = 0.125$ (blue), 0.18 (red), 0.22 (brown), and 0.4 (black). Material used is copper with initial shock strength $M_s = 1.67$ and $\sigma_Y = 0.5\,\text{GPa}$. 115

6.3 Maximum non-dimensional spike amplitude ($k\eta_{sp}^{max}$) vs. maximum non-dimensional spike growth rate squared ($\rho_0|V^{sp}|^2/\sigma_Y$) for different initial conditions and yield stresses. Circles represent AMROC spike results with $\sigma_Y = 0.25$ (green), 0.5 (magenta), 0.75 (red) and 1 (orange) GPa. Dimonte et al. results [27] for spikes are denoted by crosses. The blue and black continuous lines are the linear fits obtained from the data points for AMROC and PAGOSA simulations, respectively. Finally, maximum bubble amplitudes are also shown using black squares and blue diamonds for AMROC and Dimonte et al.'s results, respectively. Material used is copper with equation of state (6.1). . . . 116

6.4 Schematic representation of boundary conditions, initial fluid and solid regions, material interfaces, and position of the incoming shock for the converging Richtmyer–Meshkov flow in a solid–gas interface with $n = 16$. 118

6.5 $r - t$ wave diagram for radially converging solid–gas flow constructed using density (grey) and pressure (black) gradients. The initial Riemann problem in the solid produces a shock towards the solid–gas interface, a contact discontinuity and an expansion. The shock–interface interaction produces a transmitted shock in the fluid and a reflected expansion in the solid. The interface starts moving towards the axis. As the transmitted shock reaches the axis, it is reflected as a stronger shock which produces a secondary interaction with the interface. As a result, shocks appear in both fluid and solid. This process is repeated with weaker shocks at each time, until the solid–gas interface reaches an stationary position. The series of transmitted shocks in the solid finally merge in a single outwards shock. 120

6.6 Time evolution of density contours for the baseline solid–gas Richtmyer–Meshkov problem with parameters for copper, $\sigma_Y = 0.12\,\text{GPa}$, $\eta_0 n/R_0 = 0.05$, and $M_s = 1.65$. Individual frames show: (a,b) initial conditions and propagation of the shock, (c) state after shock–interface interaction, (d) reflected shock at the axis and growth of instability before first re-shock, (e,f) state after re-shocks and outbound shock. 121

6.7 Time evolution of density contours for the baseline solid–gas Richtmyer-Meshkov problem with parameters for copper, $\sigma_Y = 0.12\,\text{GPa}$, $\eta_0 n/R_0 = 0.05$, and $M_s = 1.65$ with emphasis on the region close to the axis. Individual frames show: (a) Kelvin-Helmholtz instability and outbound shock after imploding shock reaches the axis, (c,d) structure of various shocks and interface instability growth, (e,f) state after re-shocks with growing of mixing zone. Roughness in the density contours of the first frames are due to use of rectangular grid, limitations of the approximate Riemann problem and numerical errors when computing normals at the interface once Kelvin-Helmholtz instability appears. 122

6.8 Mass of fluid evolution with respect to initial mass for simulations with 5 levels of refinement and variable base-grid size. The legend values represent the equivalent number of cells (cells in one direction that an uni-grid simulation needs in order to match the resolution of the finest level) 125

6.9 Density color-contour plots highlighting the mixing zone for five different resolutions at $t = 1.5$ 125

6.10 Mass conservation errors given by Eq. (6.6) for multiple final times $t_f = \{0.5, 0.75, 1, 1.25, 1.5\}$. Different number of total levels (with 1 level corresponding to uni-grid) and base-grid resolutions are considered, with results unified using the equivalent number of cells (number of cells needed in an uni-grid simulation to match the resolution of the finest AMR level) in each direction. First-order convergence is obtained for early times as the problem is well posed. For later times, as multiple source of instability are present, the problem is ill-posed and an increment in resolution does not monotonically decrease conservation errors. 127

6.11 L_2-error and convergence rate for the preservation of radial symmetry in a solid–gas cylindrical interface processed by a shock wave. Continuous and dashed lines represent uni-grid and AMR computations respectively. The number of cells in the legend represent the effective resolution. 130

6.12 Interface evolution as a function of time for $n = \{4, 8, 12, 16\}$ and $C \equiv \frac{\eta_0 n}{R_0} = \{0.05, 0.1\}$ (see legend in (a)). Figures (a) and (b) show the whole simulation time, including events after re-shocks. Figures (c) and (d) focus on the short-term behavior after the first shock–interface interaction. 132

6.13 Density contour plots close to the axis for the case with initial parameters $n = 16$ and $C = 0.1$. New spikes form in the cusp of the bubbles in the period between $t = 0.8$ and $t = 0.883$ (Figures (a) and (b)). These new spikes grow producing a second phase reversal, with previous spikes becoming bubbles. The interface is re-shocked in (c) and a mixing zone typical of gas–gas Richtmyer–Meshkov instability is formed. 134

6.14 Evolution of the interface position, normal velocity $\dot{R}$, normal stress σ_{rr}, and Atwood ratio A_t at the interface as a function of time for $r_i = \{10, 100, 500\}$ with $\eta_0 = 0$. A lower initial density ratio reduces the initial velocity of the interface and its acceleration before the first re-shock. 136

6.15 Interface evolution as a function of time for $r_i = \{10, 100, 500\}$, $n = \{4, 16\}$, and $C \equiv \frac{\eta_0 n}{R_0} = 0.05$ (see legend in (a)). Figures (a) and (b) show the whole simulation time, including events after re-shocks. Figures (c) and (d) focus on the short-term behavior after the first shock–interface interaction. 138

6.16 Volume fraction $\overline{X}_f(r,t)$ of fluid computed by sweeping azimuthally for each r: $\overline{X}_f(r,t) = \int_0^{\frac{\pi}{2}} X_f(r,\theta,t)\, d\theta$. Results are shown for $r_i = \{100,\ 500\}$, $n = \{4,\ 16\}$ and $t = \{1.2,\ 1.4\}$. 139

6.17 Density contour plots close to the axis at $t = 1.2$ for $r_i = 500$ and $n = \{4, 16\}$. Comparison with equivalent figures for $r_i = 100$ (Figs. 6.7(e) and 6.13(f)) shows that the volume of fluid is reduced due to its lower initial density. However, the fluid pockets are more sparsely distributed, leading to a higher value of the interface amplitude (computed as the size of the mixing zone). 139

6.18 Density contour plots in the region close to the axis for the case with initial parameters $r_i = 10$, $n = 16$, and $C = 0.05$. The fluid is more compressible than the solid, which produces a positive A_t after the transmitted shock in the fluid is reflected at the axis (between figures (a) and (b)). The re-shock is then a heavy-light Richtmyer–Meshkov case, which produces an interface inversion ((d) et seq.). 140

6.19 Evolution of the interface position, normal velocity $\dot{R}$, normal stress σ_{rr}, and Atwood ratio A_t at the interface as a function of time for $M_s = \{1.16,\ 1.31,\ 1.48,\ 1.65,\ 1.83\}$ and $\eta_0 = 0$. A lower initial density ratio reduces the initial velocity of the interface and its acceleration before the first re-shock. 141

6.20 Evolution of the interface position and non-dimensional normal velocity $\dot{R}$, normal stress σ_{rr}, and Atwood ratio A_t at the interface as a function of time scaled with V_0 for $M_s = \{1.16,\ 1.31,\ 1.48,\ 1.65,\ 1.83\}$ and $\eta_0 = 0$. 142

6.21 Interface evolution as a function of time for $M_s = \{1.16,\ 1.31,\ 1.48,\ 1.65,\ 1.83\}$, $n = \{4,\ 16\}$, and $C \equiv \frac{\eta_0 n}{R_0} = 0.05$ (see legend in (a,c)). Figures (a,b,c,d) show the whole simulation time, including events after re-shocks. Figures (e) and (f) focus on the short-term behavior after the first shock–interface interaction. 143

6.22 Density contours for $M_s = \{1.16,\ 1.31,\ 1.48,\ 1.65,\ 1.83\}$ and $n = 16$ at the end of the simulation time. The mixing zone expands and becomes more fluid-like when increasing the Mach number of the incoming shock. 145

6.23 Evolution of normal velocity $\dot{R}$ as a function of time for $\sigma_Y = \{0,\ 0.12,\ 0.5,\ 1\}$ GPa and $\eta_0 = 0$. Differences in the evolution are indistinguishable. 146

6.24 Interface evolution as a function of time for $\sigma_Y = \{0,\ 0.12,\ 0.5,\ 1\}$ GPa and $\eta_0 = 0$, $n = \{4, 16\}$, and $C \equiv \frac{\eta_0 n}{R_0} = 0.05$ (see legend in (a)). Figures (a,b) show the whole simulation time, including events after re-shocks. Figures (c) and (d) focus on the short-term behavior after the first shock–interface interaction. 146

6.25 Density contour plots close to the axis at $t = 1.5$ for $\sigma_Y = \{0,\ 0.12,\ 0.5,\ 1\}$ GPa and $n = 4$ 147

6.26 Density contour plots close to the axis at $t = 1.5$ for $\sigma_Y = \{0,\ 0.12,\ 0.5,\ 1\}$ GPa and $n = 16$ 148

B.1 Contribution of the integral over the branch cuts to the growth rate using a numerical quadrature method to integrate the growth rate function and using the first term of the approximation around the branch points 163

C.1 Initial configuration for solid–gas one-dimensional shock–interface problem 164
C.2 Fluid mass conservation time evolution with respect to the initial value 165
C.3 Fluid mass conservation errors computed using Eq. (C.1) with $t_f = 2$ (final simulation time) 166
C.4 Close up near the left boundary for the final simulation time ($t_f = 2$) in a simulation with effective resolution 4096 × 512 (base grid 2048 × 256 and one level of refinement). The fluid region spans over a very small number of computational cells. 166
C.5 Time evolution of density contour plots for the free-slip case. (a) Initial configuration, (b) shock directed towards interface, (c) interface reversal typical of heavy–light configurations, (d) re-shock, (e,f) vortex development 168
C.6 Mass conservation evolution with respect to the initial value with time. Continuous and dashed lines represent free-slip and no-slip simulations respectively. All simulations are run with four total levels (3 levels of refinement) with base-grid resolutions: 48×16 (blue), 96×32 (red), 192×64 (green), 384×128 (magenta), and 768×256 (black). . 168
C.7 Mass conservation errors computed using Eq. (C.1) with $t_f = 6$ (final simulation time) 169
C.8 Density color-contour plots for final simulation time and different resolutions in the free-slip case 170
C.9 Density color-contour plots for final simulation time and different resolutions in the no-slip case 170

D.1 $C \equiv \frac{\eta_0 n}{R_0} = 0.05$, $n = 4$, $r_i = 100$, $M_s = 1.65$, $\sigma_Y = 0.12\,\text{GPa}$. 172
D.2 $C \equiv \frac{\eta_0 n}{R_0} = 0.05$, $n = 8$, $r_i = 100$, $M_s = 1.65$, $\sigma_Y = 0.12\,\text{GPa}$. 173
D.3 $C \equiv \frac{\eta_0 n}{R_0} = 0.05$, $n = 12$, $r_i = 100$, $M_s = 1.65$, $\sigma_Y = 0.12\,\text{GPa}$. 174
D.4 $C \equiv \frac{\eta_0 n}{R_0} = 0.05$, $n = 16$, $r_i = 100$, $M_s = 1.65$, $\sigma_Y = 0.12\,\text{GPa}$. 175
D.5 $C \equiv \frac{\eta_0 n}{R_0} = 0.1$, $n = 4$, $r_i = 100$, $M_s = 1.65$, $\sigma_Y = 0.12\,\text{GPa}$. 176
D.6 $C \equiv \frac{\eta_0 n}{R_0} = 0.1$, $n = 8$, $r_i = 100$, $M_s = 1.65$, $\sigma_Y = 0.12\,\text{GPa}$. 177
D.7 $C \equiv \frac{\eta_0 n}{R_0} = 0.1$, $n = 12$, $r_i = 100$, $M_s = 1.65$, $\sigma_Y = 0.12\,\text{GPa}$. 178
D.8 $C \equiv \frac{\eta_0 n}{R_0} = 0.1$, $n = 16$, $r_i = 100$, $M_s = 1.65$, $\sigma_Y = 0.12\,\text{GPa}$. 179
D.9 $C \equiv \frac{\eta_0 n}{R_0} = 0.05$, $n = 4$, $r_i = 10$, $M_s = 1.65$, $\sigma_Y = 0.12\,\text{GPa}$. 180
D.10 $C \equiv \frac{\eta_0 n}{R_0} = 0.05$, $n = 16$, $r_i = 10$, $M_s = 1.65$, $\sigma_Y = 0.12\,\text{GPa}$. 181
D.11 $C \equiv \frac{\eta_0 n}{R_0} = 0.1$, $n = 4$, $r_i = 10$, $M_s = 1.65$, $\sigma_Y = 0.12\,\text{GPa}$. 182
D.12 $C \equiv \frac{\eta_0 n}{R_0} = 0.1$, $n = 16$, $r_i = 10$, $M_s = 1.65$, $\sigma_Y = 0.12\,\text{GPa}$. 183
D.13 $C \equiv \frac{\eta_0 n}{R_0} = 0.05$, $n = 4$, $r_i = 500$, $M_s = 1.65$, $\sigma_Y = 0.12\,\text{GPa}$. 184

D.14 $C \equiv \frac{\eta_0 n}{R_0} = 0.05$, $n = 16$, $r_i = 500$, $M_s = 1.65$, $\sigma_Y = 0.12\,\mathrm{GPa}$. 185

D.15 $C \equiv \frac{\eta_0 n}{R_0} = 0.1$, $n = 4$, $r_i = 500$, $M_s = 1.65$, $\sigma_Y = 0.12\,\mathrm{GPa}$. 186

D.16 $C \equiv \frac{\eta_0 n}{R_0} = 0.1$, $n = 16$, $r_i = 500$, $M_s = 1.65$, $\sigma_Y = 0.12\,\mathrm{GPa}$. 187

D.17 $C \equiv \frac{\eta_0 n}{R_0} = 0.05$, $n = 4$, $r_i = 100$, $M_s = 1.16$, $\sigma_Y = 0.12\,\mathrm{GPa}$. 188

D.18 $C \equiv \frac{\eta_0 n}{R_0} = 0.05$, $n = 16$, $r_i = 100$, $M_s = 1.16$, $\sigma_Y = 0.12\,\mathrm{GPa}$. 189

D.19 $C \equiv \frac{\eta_0 n}{R_0} = 0.05$, $n = 4$, $r_i = 100$, $M_s = 1.31$, $\sigma_Y = 0.12\,\mathrm{GPa}$. 190

D.20 $C \equiv \frac{\eta_0 n}{R_0} = 0.05$, $n = 16$, $r_i = 100$, $M_s = 1.31$, $\sigma_Y = 0.12\,\mathrm{GPa}$. 191

D.21 $C \equiv \frac{\eta_0 n}{R_0} = 0.05$, $n = 4$, $r_i = 100$, $M_s = 1.48$, $\sigma_Y = 0.12\,\mathrm{GPa}$. 192

D.22 $C \equiv \frac{\eta_0 n}{R_0} = 0.05$, $n = 16$, $r_i = 100$, $M_s = 1.48$, $\sigma_Y = 0.12\,\mathrm{GPa}$. 193

D.23 $C \equiv \frac{\eta_0 n}{R_0} = 0.05$, $n = 4$, $r_i = 100$, $M_s = 1.83$, $\sigma_Y = 0.12\,\mathrm{GPa}$. 194

D.24 $C \equiv \frac{\eta_0 n}{R_0} = 0.05$, $n = 16$, $r_i = 100$, $M_s = 1.83$, $\sigma_Y = 0.12\,\mathrm{GPa}$. 195

D.25 $C \equiv \frac{\eta_0 n}{R_0} = 0.05$, $n = 4$, $r_i = 100$, $M_s = 1.65$, $\sigma_Y = 0\,\mathrm{GPa}$. 196

D.26 $C \equiv \frac{\eta_0 n}{R_0} = 0.05$, $n = 16$, $r_i = 100$, $M_s = 1.65$, $\sigma_Y = 0\,\mathrm{GPa}$. 197

D.27 $C \equiv \frac{\eta_0 n}{R_0} = 0.05$, $n = 4$, $r_i = 100$, $M_s = 1.65$, $\sigma_Y = 0.5\,\mathrm{GPa}$. 198

D.28 $C \equiv \frac{\eta_0 n}{R_0} = 0.05$, $n = 16$, $r_i = 100$, $M_s = 1.65$, $\sigma_Y = 0.5\,\mathrm{GPa}$. 199

D.29 $C \equiv \frac{\eta_0 n}{R_0} = 0.05$, $n = 4$, $r_i = 100$, $M_s = 1.65$, $\sigma_Y = 1\,\mathrm{GPa}$. 200

D.30 $C \equiv \frac{\eta_0 n}{R_0} = 0.05$, $n = 16$, $r_i = 100$, $M_s = 1.65$, $\sigma_Y = 1\,\mathrm{GPa}$. 201

List of Tables

3.1 Coefficients of third-order WENO finite-difference method 36
3.2 Coefficients of third-order TVD Runge-Kutta method 36
3.3 Comparison between results of approximate Riemann solvers and exact solution for a one-dimensional solid–gas interface Riemann problem involving an expansion wave in the solid and a compression shock in the gas. The solid follows the constitutive law (3.58) and the gas is considered perfectly caloric. The approximate methods considered are: a) HLLD single-pass, b) HLLD with multiple passes, c) characteristic-based single-pass, d) characteristic-based with multiple passes. 47
3.4 Comparison between results of approximate Riemann solvers and exact solution for a solid–gas interface Riemann problem involving an expansion wave and a shear shock in the solid and a compression shock in the gas. The solid follows the constitutive law (3.58) and the gas is considered perfectly caloric. The approximate methods considered are: a) HLLD single-pass, b) HLLD with multiple passes, c) characteristic-based single-pass, d) characteristic-based with multiple passes. 48
3.5 L_2-errors and convergence rate for IVP 1 56
3.6 L_2-errors and convergence rate for IVP 2 58

6.1 Parametric study of the Ritchmyer–Meshkov flow for solid–gas interfaces in cylindrical geometry 117
6.2 L_2-errors and convergence rate for $t = \{0.5, 0.75, 1.0\}$. Cases with the same equivalent resolution but run with different levels of refinement have been averaged. 126
6.3 L_2-errors and convergence rate averaged for $t = \{1.25, 1.5\}$. Cases with the same equivalent resolution but run with different levels of refinement have been averaged. . 126
6.4 Interface parameters in shock–interface problem with different initial density ratios . . 135
6.5 Interface parameters in shock–interface problem with different initial shock Mach numbers 138

C.1 L_2-errors and convergence rate for different levels of refinement 165
C.2 L_2-errors and convergence rate for free-slip and no-slip boundary conditions 169

Chapter 1

Introduction

Significant interest has arisen in the modeling and simulation of dynamic events that involve high-load conditions and large deformations in solids (i.e., shock-driven motion, impacts, and implosions). The numerical analysis of this set of problems demands the implementation of very specific capabilities that enable the simulation of multiple materials and their interaction through sharp interfaces along with accurate descriptions of boundary conditions and high-resolution shock and wave capturing. Significant challenges arise for traditional computational solid mechanics when employed in this context.

In the classical Lagrangian approach [16], the equations for mass, momentum, and energy conservation, in conjunction with constitutive models for the strength of the material, are solved using a computational mesh that conforms to the material boundaries and moves with particles. The benefits of such methods stem from the fact that typical boundary conditions (i.e., prescribed displacements and stresses) are directly imposed along boundary surfaces in a simple way as well as from material states needed to formulate the constitutive model of materials being stored in each element. On the other hand, large relative displacements of particles with respect to each other generally lead to a computational mesh that can get heavily distorted or twisted, resulting in a restriction of the size of the time-steps or failure of the method due to element inversion.

Purely Eulerian formulations, in which the computational grid remains fixed, do not suffer from grid entanglement and have been widely used in simulating the response of hyperbolic systems of equations, especially for gases under extreme loading conditions, with very satisfactory results. These methods are readily applicable to solid mechanics when the special set of hyper-elastic constitutive laws, wherein stresses are derived from internal energy in a thermodynamically consistent way, are used. It can be shown that under these conditions the system of equations becomes hyperbolic in nature [71]. Contrary to Lagrangian approaches, this implementation comes at the expense of having to include equations of motion for describing the deformation history of solid particles as they are allowed to flow in the computational grid and designing an algorithm for tracking the position of material boundaries. In addition, the computational grid must be initially allocated in a way such that the materials are contained in it throughout the total simulation time. All these particularities increase computation time and are the main reason that the field of Eulerian solid mechanics has not seen significant development until massive computational capacity has become widely available. At the same time, the description of the motion of elastic–plastic solids in fixed grids offers several important advantages, such as the capability of capturing shocks, triple-points, and waves naturally and providing a smooth transition between solid and fluids in the case of phase changes.

With both Eulerian and Lagrangian approaches having potentially important drawbacks, arbitrary Lagrangian-Eulerian (ALE) [29, 51], methods constitute an attempt to include in one implementation the best qualities of each. In the most common approach, a Lagrangian time-step is followed by an Eulerian remapping algorithm in pseudo-time in which the mesh is regularized and the variables at the new nodes computed [69]. However, an optimal approach to the way this step is performed and tailored to the needs of different problems remains an open subject of research. Finally, other approaches attempt to reduce the mesh constraints in large deformation problems while remaining Lagrangian in nature. Examples of these are the mesh-free [64] and free-Lagrange methods [56]. With these latter approaches still being perfected, it makes sense to explore in depth the capabilities of Eulerian approaches to solid mechanics for offering solutions to several problems of interest involving large deformations.

1.1 Motivation

The aim of this research is to investigate the way in which multiple approaches that have been the focus of attention in recent years in the field of compressible fluid dynamics can be extrapolated to solid mechanics. In particular, this dissertation focuses on:

1. the motion of converging (imploding) shocks in cylindrical and spherical geometries,
2. the Richtmyer–Meshkov (RM) flow for elastic and elastic–plastic solids in multiple geometries with distinct material interfaces.

The decision to use the Eulerian description of the equations of motion for solid mechanics becomes natural in exploring these problems given its benefits in handling large deformations. In addition, a direct comparison can often be established with the fluid counterparts of the analyzed problems, since the vast majority of them are also commonly examined from the point of view of Eulerian frameworks.

The problem of imploding shocks in converging geometries is of interest in the production of high temperatures and pressures in condensed matter, with direct applications, for example, in inertial confinement fusion [62, 11, 5]. However, experimental studies reveal complications related to measurement techniques and the difficulty of maintaining a quasi-radially symmetric flow at all times [118]. Previous numerical and analytical studies for elastic–plastic solids rely on the volumetric stress modeled using Mie–Grüneisen equations of state and neglecting shear stresses (see paragraph 1.2.3). While it is true that hydrostatic stresses become dominant in imploding situations as the shock strength increases, the presence of shear stresses can modify the evolution of the shock wave in weak and moderate converging shocks. These stresses are also essential for explaining the transition from the elastic to the plastic regime as the converging geometry strengthens an initially weak shock.

The unstable effect of the passage of a shock wave on a perturbed interface separating two fluids of different properties was named after and first described by Richtmyer [96], who constructed an analytical solution for the growth rate of a slightly perturbed contact discontinuity using an impulsive model that replicates the passage of a shock parallel to the main position of the interface, and Meshkov [74], who qualitatively confirmed the predicted results using shock-tube experiments. Baroclinic vorticity, generated by the misalignment of the density gradient (normal to the interface) and the pressure gradient (normal to the shock) causes the interface perturbations to grow unless there exists a mechanism that could dissipate or advect the initially deposited vorticity. This problem was originally regarded as the impulsive limit of the Rayleigh–Taylor instability (RTI), in which a perturbed density interface evolves under the effect of a continuous or sustained acceleration [103]. However, in recent years, the Richtmyer–Meshkov instability (RMI) has gained in relevance and independence from RTI studies, as indicated by several annual reviews in the subject (e.g., Zabusky [128] and Brouillete [20]) and its relevance in a myriad of fields, including compressible turbulent mixing [75, 126, 114, 130, 66], combustion [59], magnetohydrodynamics [120], plasma physics [63], inertial confinement fusion [63], astrophysical phenomena [6, 36, 70, 102], and solid mechanics [95, 90]. In this last field, multiple features of interest naturally appear. In the first place, shear waves are able to carry vorticity away from the interface, reducing and even canceling the growth of the perturbations. The effect of inelasticity is also relevant as it establishes a duality between the aforementioned stable behavior in which the interface does not grow in the long-term and the unstable fluid-like behavior characteristic of the plastic regime. Dynamic transitions between these two regimes at a material interface can potentially dramatically change the stability characteristics of the flow.

Analytical models were constructed, and numerical simulations were conducted using the multi-material adaptive mesh refinement AMROC [25] framework as part of the Virtual Test Facility (VTF) [26] to achieve the objectives of the project. In addition to the tangible physical relevance of the problems studied, there exists an overarching interest in identifying the limits, weaknesses and strengths of the newly implemented multi-material solid mechanics capabilities in AMROC [8] as part of its validation and verification, as well as identifying and developing improvements over the previous versions of the code. This numerical framework constitutes the central piece of the work developed by the computational fluid dynamics (CFD) group, led by Professors Dale Pullin and Daniel Meiron and staffed by researchers Dr. Philip Barton, Dr. David Hill, Dr. Julian

Cummings and Dr. Manuel Lombardini, and myself as a graduate student, in the framework of the Predictive Science Academic Alliance Program (PSAAP) at Caltech, directed by Prof. Michael Ortiz and funded by the National Nuclear Security Administration (NNSA). The goal of Caltech PSAAP center is to produce a "validated, large-scale, multidisciplinary, simulation-based predictive science as a major academic and applied research program for hypervelocity normal and oblique impact of metallic projectiles and targets, at velocities up to 10 km/s", for which the Eulerian multi-material solid mechanics code plays a central role in the simulation program.

1.2 Previous related work

1.2.1 Eulerian solid mechanics

The study of solid mechanics in an Eulerian framework is intimately connected to problems in which solid media are subjected to large deformations. This analysis requires an extended system of Euler equations for which two formulations have been historically used. The first form stems from the work of Godunov and Romenski [43, 42] where, in addition to the five equations required to describe mass, linear momentum, and energy conservation, the inclusion of the nine evolution equations for the deformation tensor (i.e., the gradient of the actual configuration of the material with respect to its initial configuration) in conservative form was proposed. For modeling inelastic effects, the former nine equations are modified by plastic source terms and an additional equation is needed to keep track of work hardening. The second approach proposes the employment of the inverse deformation tensor (i.e., gradient of initial configuration with respect of the actual configuration of the material). The equations governing this system were first discussed by Plohr and Sharp [92] for the elastic case and subsequently expanded to include rate-dependent and rate-independent plasticity [93], increasing the number of equations to be solved to 21: mass (1), linear momentum (3) and energy (1) conservation, inverse deformation tensor evolution (9), plastic strain (6) and work hardening (1).

The general framework for computational modeling of finite deformation in solids was introduced by Trangenstein and Colella [110], who described many of the complications involved in these computations, such as the loss of hyperbolicity when using particular constitutive laws. Miller and Collela [78], expanded the previous work clearly establishing conditions for the stability of high-order Godunov methods for elastic–plastic materials when kinematic constraints of the inverse deformation tensor are included. The proposed model involves a total of 24 equations as the plastic deformation tensor is employed, replacing the symmetric plastic strain tensor. Barton et al. [10] later developed a WENO finite-volume [99] algorithm based on the equations of motion in [43, 42]. The computational methods described above require the solution of approximate or exact Riemann problems at the cell boundaries. This procedure is often challenging for elastic–plastic materials given the large variety of constitutive laws available and the effect of inelastic behavior in the solution of such Riemann problems. Hill et al. [49] proposed a hybrid WENO centered-difference finite-difference method based on the system of equations in [78] and fractional steps separating the elastic and plastic parts of the problem that circumvents these difficulties by means of the evaluation of wall fluxes using a third-order WENO finite-difference scheme [57] and Lax–Friedrichs flux splitting. This method does not require the solution of a Riemann problem nor the evaluation of the eigenvectors of the hyperbolic system. In addition to these traditional implementations, it is worth mentioning the combined Eulerian–interface front tracking approaches developed by Walter at al. [115, 116].

Perhaps the greatest difficulty in the development of numerical methods for large deformations is the absence of a universal constitutive law. The only a priori requirement for the closure relations in order to preserve a hyperbolic system of equations is that they be formulated in the hyper-elastic form. In this formulation, stresses are directly derived by differentiation of the internal energy, written as $e = e(\mathbf{F}, \varsigma)$, where $\mathbf{F}$ is the deformation tensor and ς the entropy, with respect to the components of the deformation tensor in a way such that the equation of motion for the internal energy is satisfied and the eigenvalues of the resulting system of partial differential equations are real. Upon this prescription, a myriad of variants have been proposed, based on different materials but also adapted to different stress conditions. Thus, the development of universal Riemann solvers able to handle this variety of constitutive relations becomes a challenging task. Examples of isentropic closure relations (i.e., $e = e(\mathbf{F})$) are the Mooney-Rivlin-Ogden model [82] for rubber materials and the isentropic Miller and Collela [78] model for the flyer-plate problem. Other models, normally used for high-pressure and temperature problems include a dependency on entropy. Some examples are the Miller and Collela model [77] where the internal energy is divided in shear, hydrostatic, and thermal parts, the model by Gavrilyuk et al. [37], in which the hydrostatic part that imitates a stiffened gas, and the semi-empirical Mie–Grüneisen model with shear terms presented in [107, 10, 8].

In order to model inelasticity of materials, multiple procedures have been developed. The approaches of LeFloch and Olsson [34] and Titarev et al.[107] include inelastic effects in the solution of the Riemann problem at the cell boundaries. The majority of approaches, however, make use of fractional steps (i.e., [8, 78, 49]), first evaluating the homogeneous part of the problem and finally including plastic corrections in the shape of source terms. These corrections follow closely the radial return algorithms developed in computational plasticity [101], in which the stress state is relaxed towards the hydrostat until the yield surface is encountered.

1.2.2 Multi-material simulations

In the last years, multiple research efforts have been directed towards the simulation of complex problems containing interactions between different media (i.e., fluid–structure interactions [12], multiphase flows [112]). Contrary to Lagrangian formulations, in which the problem can be naturally addressed by collocating nodal points at the initial position of the interface, Eulerian formulations need an algorithm for tracking material interfaces and a way to resolve mixed cells where multiple materials coexist. In this context, different methods for interface tracking and solving have been proposed. The volume-of-fluid (VOF) [52, 77] method is conservative and allows diffusion, which makes it appropriate for mixing or combustion problems. The level-set approach [86, 85] preserves sharp interfaces between materials, making it appropriate for the modeling of solid materials despite the fact that some formulations are not intrinsically conservative. Some attempts to address conservation problems in particular situations have been proposed [83]. In between the two approaches lies the phase-field method [33], which acts as a level set except for the region close to the interface, where boundary conditions are enforced via a partial differential equation that governs the phase field, a function that takes two distinct values (for instance $+1$ and -1) in each of the respective phases, with a smooth transition between both values in the zone around the interface, which is then diffused with a finite width. More complex methods are also under development, such as interface reconstruction in VOF methods [3] or moment-of-fluid (MOF) methods [31].

1.2.3 Converging shock waves

The theoretical study of converging shock waves in fluid mechanics can be tracked back to Guderley's work [46] on similarity solutions in cylindrical and spherical configurations, which showed that, as the shock approaches the strong-shock limit, its radial location $R(t)$ is proportional to a geometry-dependent power of the time measured from the instant when the shock has imploded to $r = 0$. This result was later closely matched by Whitham's shock dynamics (WSD) theory [122]. In WSD, the characteristic equations and Rankine–Hugoniot conditions across the shock are combined to obtain an ordinary differential equation that approximates the shock evolution and strength in time. This approach also offers reasonable approximations far from the strong-shock limit (even for infinitesimally weak shocks [54]) and in diverse geometries (e.g., wedges) [14]. In addition, WSD has been applied to converging shocks in solid media. Yadav & Singh [125] analyzed spherical shocks in metals employing a hydrostatic Mie–Grüneisen equation of state that does not reflect the effects of shear. The study differentiates between the behavior of light metals like aluminum, which behave like gases in the strong-shock limit, and heavier materials like copper, which exhibit a slight variation of this behavior.

Several examples of studies based on numerical simulations of imploding shocks in fluids and solids exist. Payne [87] employed a finite-difference scheme to replicate the evolution of a cylindrical shock, which was produced from an initial Riemann problem caused by the rupture of a cylindrical diaphragm separating regions of fluid at rest with different densities and pressures, showing agreement with Guderley's solutions as the shock approaches the axis. Hiroe, Matsuo & Fujiwara [50] simulated a cylindrically imploding shock (and its subsequent reflection off the axis) propagating in solid media modeled using a Mie–Grüneisen equation of state and employing a random choice numerical method. They observed that the self-similar regime commonly observed with gases is only achieved in extreme proximity of the axis. The same type of equation of state was used by Nagayama and Murakami [81] in a finite-difference Lax–Wendroff method to study converging shocks propagating through layers of different solid materials. In particular, the authors considered systems composed of inner iron rods and outer shells made of copper or boron nitride, observing that the pressure profile behind the shock only deviates from a planar pattern when the shock is very close to the origin. They also identified conditions under which the inner iron rod can enter a tension stress state and subsequently break after the shock is reflected at the axis and interacts with the material interface for a second time.

Experimental studies of implosive shock waves are constrained by the inherent complications of producing an initial shock with minimal excursions from radial symmetry. In particular, potentially unstable polygonal shock waves are commonly developed as the shock moves inwards [118, 98]. Different methods have been proposed to improve the symmetry of the shock using annular shock tubes [55] or shock lensing techniques [28]. Several authors have achieved converging shocks in solids. Coleburn and Forbes [24] used the high pressure produced by a shock to transform hexagonal boron nitride into wurtzite and its cubic form, Belov et al. [11] investigated the formation of solid deuterium using an explosion-driven shock generator that produced a spherical shock wave in an aluminum sheet that was later transmitted into the inner core of deuterium, and Brown et al. [21] presented an experimental method for measuring the high-pressure Hugoniot relation of solid materials that employed a concentrical cylindrical setup consisting of an outer shell of a well-characterized material and an inner rod made of the material of interest. In some cases, excursions from the radial symmetry are desirable for the study of instabilities that can result in the collapse of materials. For instance, adiabatic shear bands [106] are self-organized narrow regions of localized shear deformations caused by a nonuniform temperature distribution in materials with plastic deformations and they are usually responsible for catastrophic failure of materials. Due to the existence of large plastic deformations, heat is produced that cannot be dissipated in adiabatic processes. The resulting increment in temperature allows for additional plastic deformations as the strength of the material is decreased by thermal softening. Xue et al. [124] conducted experiments for analyzing the nucleation and distribution of adiabatic shear bands in thick cylindrical titanium specimens under high strain rates ($10^4\,\mathrm{s}^{-1}$). In order to achieve such strain rates, the motion was induced by an implosion in a concentrical-shell driver made of copper.

1.2.4 Richtmyer–Meshkov instability (RMI)

Most of the efforts to describe the Richtmyer–Meshkov instability by means of analytical models, numerical simulations, or experiments have occurred in the field of fluid dynamics. A significant part of these studies is devoted to modeling the small-perturbation linear regime in plane geometries, with the aim of describing the start-up process and identifying the initial growth rate of interface perturbations [68, 45, 113, 123]. When these models are compared to numerical [68] and experimental results [58, 53], discrepancies often arise in the case of strong shocks or large density ratios across the interface. The evolution of the interface in the nonlinear regime was studied by Samtaney and Zabusky [97], who thoroughly analyzed the circulation evolution of the interface and described how the heavy fluid penetrates in the light fluid in the form of "spikes" while "bubbles" of light fluid are formed as a result of mass conservation. Studies in curved or converging geometries are more scarce. Mikelian [76] developed a model for the start-up process that applies to both RMI and RTI. Zhang et al. [129] performed numerical simulations to qualitatively explain the differences between the four possible problem configurations: heavy–light or light–heavy density ratio across the material interface and imploding or exploding direction of the shock. Finally, Lombardini [67] proposed an incompressible, impulse-driven, and linearized model for the problem that retains first and second-order effects of the converging geometry.

In the field of solid mechanics, Plohr and Plohr [95] performed a semi-numerical analysis of the Richtmyer–Meshkov flow for linearized compressible elasticity. These results included a limited range of initial conditions and material parameters for which the interface separating two solids was oscillatory and stable after the shock wave–interface interaction. Piriz et al., [90] developed an oscillatory model of the interface and conducted simulations to derive an approximate result for the long-term behavior of the perturbations. Later, Piriz et al. [91] expanded their analytical model to elastic–plastic solids, predicting an initial fluid–like linear growth rate of the amplitude driven by the solid exhibiting plastic behavior that eventually turns into stable behavior as stresses are relaxed below the yield stress. However, this model needs input from numerical simulations in order to realistically define the interface behavior. Nonetheless, results suggest the existence of a relation between the maximum amplitude achieved by the interface before it enters the elastic regime and the strength of the material. Dimonte et al. [27] later performed a series of simulations using continuum mechanics and molecular dynamics codes contrasted with experiments that drew the same conclusions with respect to the yield stress–maximum amplitude relation.

1.3 Outline of present work

Chapter 2 is mainly descriptive as it introduces the equations of motion in an Eulerian framework. Chapter 3 introduces the different formulations available for tracking the deformations of materials in an Eulerian framework. A new set of equations with some advantages with respect to the approaches of Godunov and Romenski [42] and Plohr and Sharp [92] is presented. Special emphasis is given to the fact that all these formulations can be solved by a polar decomposition of the deformation or inverse deformation gradients, with benefits for the handling of certain classes of plastic flow, for example when material interfaces come into mutual contact. This chapter also includes a description of the elements involved in the multi-material implementation accompanied by test results concerning mass conservation and the accuracy of the multi-material Riemann solver employed. The remainder of chapters are devoted to applications. In Chapter 4 the effects of shear deformations and plasticity are considered in the analytical and numerical study of converging imploding shocks in solids. The last two chapters are devoted to the study of the Richtmyer–Meshkov flow in solid media. Chapter 5 describes an analytical model for the impulsive Richtmyer–Meshkov flow in incompressible elastic solids. Finally, in Chapter 6, numerical simulations are used for studying the Richtmyer–Meshkov flow of interfaces separating different compressible media. In particular, the cases of a perturbed interface separating an elastic–plastic solid from a vacuum or gas are examined in planar and cylindrical geometries, respectively. A parametric study of the latter is performed in order to characterize the dependency of the problem on initial conditions (i.e., amplitude and shape of the perturbations and shock Mach number) and material parameters (i.e., initial density ratio and yield stress).

Chapter 2

Description of the Eulerian framework for solid mechanics

2.1 Introduction

The equations of motion for elastic–plastic solid materials in an Eulerian framework are described in this chapter. In contrast to inviscid fluid dynamics, where the equations for mass, linear momentum, and energy conservation are sufficient to define a closed system of equations when an appropriate equation of state is used, the solid mechanics description requires additional expressions in order to track the relative displacements of particles with respect to their neighbors. It can be shown that, at least for isotropic materials, only the three invariants of the strain tensor are needed to define a consistent elastic–plastic constitutive law. Unfortunately, since an expression for the evolution of these invariants cannot be formulated in conservative form, the system of equations must be extended to include the evolution of the nine components of the deformation gradient, from which the strain tensor and its invariants can be derived. Two directions have been historically followed for including the deformation gradient in the Euler equations. The first approach [43, 42, 8, 7, 10] makes use of the Lagrangian deformation tensor $\mathbf{F}$, which is the gradient of the mapping that relates the actual configuration of the material with respect to its initial position. The second approach [92, 78, 110, 49] includes in the equations of motion the inverse of the deformation tensor (appropriately called inverse deformation tensor) $\mathbf{g}$, defined as the gradient of the initial position of the material particles with respect to the actual location. Both formulations are described in the first part of the chapter, devoted to introducing the equations of motion and constitutive laws for elastic media.

The form of the equations when inelasticity is considered comprises the second part of the chapter. A multiplicative decomposition of the deformation gradient into elastic and plastic parts is employed. A phenomenological approach consistent with the postulates of isochoric plasticity is used to model the plastic component, which is capable of replicating visco-elastic behavior, perfect plasticity, strain rate hardening and thermal softening.

The last part of the chapter summarizes the hyperbolic nature of the system of equations and offers a general recipe for computing the different families of characteristics.

2.2 Equations of motion for elastic solid media

In a fixed Cartesian frame of reference (x_1, x_2, x_3), the equations of motion in differential form for any material considered as a continuum are prescribed by conservation of mass, linear momentum and energy:

$$\frac{\partial \rho}{\partial t} + \frac{\partial \rho u_i}{\partial x_i} = 0, \tag{2.1a}$$

$$\frac{\partial \rho u_i}{\partial t} + \frac{\partial \left(\rho u_i u_j - \sigma_{ij}\right)}{\partial x_j} = 0, \tag{2.1b}$$

$$\frac{\partial \rho E}{\partial t} + \frac{\partial \left(\rho E u_j - \sigma_{ij} u_i\right)}{\partial x_j} = 0, \tag{2.1c}$$

where ρ is the density, u_i is the material velocity in the x_i direction, E is the total energy and σ_{ij} is the Cauchy stress. Einstein index notation is employed throughout this dissertation. At this point, the system of equations is not complete since the physical behavior of the material has not been included. For instance, a closure is provided by the equation of state, namely $\sigma_{ij} = -p(\rho, e)\delta_{ij}$, where $e = E - \frac{1}{2}u_i^2$ is the specific internal energy, in inviscid fluid dynamics. In the case of viscous fluids, the closure relation also includes the dependency on the strain rate tensor $\partial u_i / \partial x_j$:

$$\sigma_{ij} = -p(\rho, e)\delta_{ij} + \mu(\rho, e)\left(\frac{\partial u_i}{\partial x_j} + \frac{\partial u_j}{\partial x_i} - \frac{2}{3}\delta_{ij}\frac{\partial u_k}{\partial x_k}\right), \tag{2.2}$$

where μ is the dynamic viscosity.

The main difference between solids and fluids hinges on their response to deformations. While fluids respond to the rate at which these deformations occur, solids respond directly to the deformations themselves. For example, when twisting a small section of a large piece of rubber, the neighboring material will attempt to restore the initial configuration. If the same experiment is replicated in a fluid, the neighboring particles may slow down the rate at which the twisting occurs but the initial configuration cannot be restored. In consequence, the equations of state for solids cannot be formulated solely in terms of the density, energy, and velocity fields and additional equations need to be included to identify the displacements of particles which respect to each other in time.

2.2.1 Lagrangian–Eulerian mapping

The notion of the deformed and undeformed configuration of a material must be introduced in order to measure relative displacements between particles. To this effect, a fixed Eulerian Cartesian frame (x_1, x_2, x_3) and a second Lagrangian Cartesian frame (X_1, X_2, X_3) that follows particle paths are introduced. A bijective mapping $x_i = x_i(X_I, t)$ defines the position in the deformed configuration, at a particular time-step t, of the particle whose position in the undeformed configuration was X_I. In practice, it is convenient to set $X_I = x_i(X_I, 0)$. The inverse mapping $X_I = X_I(x_i, t)$ conversely determines the initial position of a particle given its position at a particular time. Since X_I is attached to the motion of particles, this field satisfies an advection equation,

$$\frac{DX_I}{Dt} = \frac{\partial X_I}{\partial t} + u_j \frac{\partial X_I}{\partial x_j} = 0, \tag{2.3}$$

in the Eulerian frame of reference.

As was stated above, the closure of the equations of motion for a solid must depend on the relative displacement with respect to neighboring particles. The relative change in separation between a particle labeled X_I and some neighbor $X_I + \epsilon e_J$, where e_J is any unitary vector in the Lagrangian frame is given by:

$$\frac{x_i\left(X_I + \epsilon e_J, t\right) - x_i\left(X_I, t\right)}{\epsilon}, \tag{2.4}$$

and taking the limit for small ϵ, the definition of the deformation tensor F_{iJ} appears:

$$F_{iJ} = \lim_{\epsilon \to 0} \frac{x_i\left(X_I + \epsilon e_J, t\right) - x_i\left(X_I, t\right)}{\epsilon} = \frac{\partial x_i}{\partial X_J}. \tag{2.5}$$

Alternatively, we can define the inverse deformation tensor

$$g_{Ij} = \frac{\partial X_I}{\partial x_j}, \tag{2.6}$$

such that $\mathbf{g} = \mathbf{F}^{-1}$. This tensor is considered more appropriate for Eulerian formulations since in its definition, derivatives with respect to the fixed frame of reference $\mathbf{x}$ are used.

2.2.2 Equations of motion for the deformation and inverse deformation tensors

As was observed empirically for solids, stresses are intimately related to deformations in the material. It is necessary then to track the evolution in time of the tensors $\mathbf{F}$ and $\mathbf{g}$ defined in the previous paragraph in order to complement the system of equations in Eq. (2.1) and provide a closure to the problem through the appropriate modeling of a constitutive law. By the use of kinematic arguments, the equations of motion for the components of the deformation and inverse deformation tensors are subsequently derived in this paragraph. Special relevance is given to the fact that both formulations are theoretically equivalent and to the kinematic constraints that naturally arise.

2.2.2.1 Inverse deformation tensor

Given the evolution equation for the Lagrangian field X_I in the fixed frame of reference (Eq. (2.3)) and differentiating with respect to x_k, the conservative form of the inverse deformation tensor is obtained:

$$\frac{\partial X_I}{\partial t \partial x_k} + \frac{\partial}{\partial x_k}\left(u_j \frac{\partial X_I}{\partial x_j}\right) = \frac{\partial g_{Ik}}{\partial t} + \frac{\partial \left(g_{Ij} u_j\right)}{\partial x_k} = 0. \tag{2.7}$$

The components of $\mathbf{g}$ are subject to kinematic constraints (i.e., they are not purely independent from each other). The first of these conditions is given by the invariance with respect to the order of the derivatives and it is directly related to the Saint-Venant compatibility principle between displacements and deformations,

$$\frac{\partial g_{Ij}}{\partial x_k} = \frac{\partial X_I}{\partial x_j \partial x_k} = \frac{\partial X_I}{\partial x_k \partial x_j} = \frac{\partial g_{Ik}}{\partial x_j}, \tag{2.8}$$

or, in other words, if the initial condition is curl free, this property is maintained at all times,

$$G_{Ii} \equiv \epsilon_{ijk} \frac{\partial g_{Ik}}{\partial x_j} = 0. \tag{2.9}$$

The second constraint comes from the intrinsic relation between the determinant of the inverse deformation tensor and the density.

$$\frac{\rho}{\rho_0} = \det\left(\mathbf{g}\right). \tag{2.10}$$

If Eq. (2.1a) is compared to the determinant of (2.7), one may appreciate that they are not equivalent unless the curl constraint (2.9) is actively enforced. This detail may seem to be irrelevant given that the curl free condition of the inverse deformation tensor should be always satisfied. In numerical implementations this is not always the case due to numerical errors. Hence, it is preferred to rewrite Eq. (2.7) in a way such that the mass conservation equation is recovered automatically when taking its determinant, regardless of the value of the curl,

$$\frac{\partial g_{Ik}}{\partial t} + \frac{\partial \left(g_{Ij} u_j\right)}{\partial x_k} = \epsilon_{kmn} u_m G_{In}. \tag{2.11}$$

2.2.2.2 Deformation tensor

The equations of motion for the deformation tensor can be derived from Eq. (2.11), which can be rearranged in a material derivative form,

$$\frac{Dg_{Ij}}{Dt} = -g_{Ik}\frac{\partial u_k}{\partial x_j}. \tag{2.12}$$

Using the inverse matrix differentiation properties, the previous expression is written as:

$$(F^{-1})_{Im}\frac{DF_{mN}}{Dt}(F^{-1})_{Nj} = (F^{-1})_{Ik}\frac{\partial u_k}{\partial x_j}. \tag{2.13}$$

Finally, multiplying by $\mathbf{F}$ from the left and right of the expression, one obtains

$$\frac{\partial F_{iJ}}{\partial t} + u_k\frac{\partial F_{Ij}}{\partial x_k} - F_{Kj}\frac{\partial u_i}{\partial x_k} = 0. \tag{2.14}$$

Combining the expression above with mass conservation (Eq. 2.1a), a set of equations for each of the components of the deformation tensor in conservative form is derived,

$$\frac{\partial \rho F_{iJ}}{\partial t} + \frac{\partial\left(\rho F_{iJ}u_k - \rho F_{kJ}u_i\right)}{\partial x^k} = -u_i\frac{\partial \rho F_{kJ}}{\partial x_k}. \tag{2.15}$$

It can be shown that the right-hand side term, $u_i\frac{\partial \rho F_{kJ}}{\partial x_k}$, is identically zero in an analogy to the curl free constraint of the inverse deformation tensor. Using the differentiation formulae for an inverse matrix and the determinant of a matrix together with Eq. (2.10), one can obtain

$$\frac{\partial F_{kJ}}{\partial x_k} = -F_{kM}F_{nJ}\frac{\partial g_{Mn}}{\partial x_k}, \tag{2.16a}$$

$$\frac{\partial \rho}{\partial x_k} = \rho F_{nN}F_{kJ}\frac{\partial g_{Nm}}{\partial x_k}. \tag{2.16b}$$

Finally,

$$\frac{\partial \rho F_{kJ}}{\partial x_k} = \rho\frac{\partial F_{kJ}}{\partial x_k} + F_{kJ}\frac{\partial \rho}{\partial x_k} = \rho F_{iJ}F_{mN}\left(\frac{\partial g_{Nm}}{\partial x_i} - \frac{\partial g_{Ni}}{\partial x_m}\right) = 0. \tag{2.17}$$

In addition, the density constraint can be reformulated in terms of the deformation tensor

$$\frac{\rho_0}{\rho} = \det\left(\mathbf{F}\right), \tag{2.18}$$

since $\mathbf{F} = \mathbf{g}^{-1}$. Similarly to the inverse deformation tensor case, the continuity equation is not directly recovered by taking the determinant of Eq. (2.15) unless the right-hand side is included.

2.2.3 Stretch and strain tensors

Any matrix $\mathbf{A}$ admits a polar decomposition $\mathbf{A} = \mathbf{VR} = \mathbf{RU}$, in which $\mathbf{V}$ and $\mathbf{U}$ are symmetric, definite positive matrices and $\mathbf{R}$ is an orthogonal rotation matrix. In the particular case of $\mathbf{A}$ being the deformation tensor $\mathbf{F}$, $\mathbf{V}$ and $\mathbf{U}$ are called the left and right stretch matrices, respectively. This decomposition is useful as it separates the contributions due to the change in distance among neighboring particles from the contribution of rigid-body rotations, contained in the stretch and rotation matrices, respectively [71]. In consequence, the constitutive law in an elastic solid must exhibit dependency on $\mathbf{V}$ or $\mathbf{U}$ only. These constitutive relations often appear formulated as functions of the left and right Cauchy–Green strain tensors,

$$\mathbf{b} = \mathbf{F}\mathbf{F}^T = \mathbf{V}^2, \tag{2.19a}$$

$$\mathbf{C} = \mathbf{F}^T\mathbf{F} = \mathbf{U}^2. \tag{2.19b}$$

An equation of motion independent of $\mathbf{F}$ can be derived for the components of the left Cauchy–Green tensor $\mathbf{b}$:

$$\frac{Db_{ij}}{Dt} = \frac{DF_{iK}}{Dt}F_{jK} + F_{iK}\frac{DF_{jK}}{Dt} = F_{jK}F_{mK}\frac{\partial u_i}{\partial x_m} + F_{iK}F_{mK}\frac{\partial u_j}{\partial x_m} = b_{kj}\frac{\partial u_i}{\partial x_k} + b_{ik}\frac{\partial u_j}{\partial x_k}, \tag{2.20}$$

or, including the mass conservation equation (2.1a),

$$\frac{\partial \rho b_{ij}}{\partial t} + \frac{\partial \rho b_{ij} u_k}{\partial x_k} = \rho b_{kj}\frac{\partial u_i}{\partial x_k} + \rho b_{ik}\frac{\partial u_j}{\partial x_k}. \tag{2.21}$$

However, that is not the case for the right Cauchy-Green tensor $\mathbf{C}$:

$$\frac{DC_{IJ}}{Dt} = \frac{DF_{kI}}{Dt}F_{kJ} + F_{kI}\frac{DF_{kJ}}{Dt} = F_{kJ}F_{lI}\frac{\partial u_k}{\partial x_l} + F_{kI}F_{lJ}\frac{\partial u_j}{\partial x_l} \tag{2.22}$$

The above relations for the Cauchy–Green tensors cannot be expressed in conservative form and weak solutions across a discontinuity cannot be directly determined for them. Thus, it is not possible to substitute the nine equations of motion for the components of the deformation or inverse deformation tensor by the six relations needed to track the evolution of the symmetric strain tensors in a numerical implementation of the system of equations describing the motion of elastic materials. A total of 14 equations (5 from (2.1) and 9 from (2.11) or (2.15)) must be solved concurrently. The resultant system of equations is redundant, since the knowledge of $\mathbf{F}$ or $\mathbf{g}$ allows the computation of the density without having to use the continuity equation. Diverse methods have been proposed, discussed in Chapter 3, for solving this ambiguity in numerical implementations.

2.2.4 Closure relations and constitutive laws

As discussed in the previous section, the constitutive law needed to model an elastic solid is expressed as a function of the left or right Cauchy-Green tensors and some other thermodynamic variable. A typical form for the internal energy is,

$$e = e(\mathbf{b}, \varsigma) \text{ or } e = e(\mathbf{C}, \varsigma), \tag{2.23}$$

where ς is the entropy. Cauchy stresses σ_{ij} remain to be determined. Early production codes for large deformations in solid media used to rely extensively on a set of constitutive laws known as hypo-elastic [111]. The stresses for these materials were derived phenomenologically and were generally not consistent with thermodynamic principles. In this approach, hyper-elastic constitutive laws are used. A hyper-elastic material is defined by the acquisition of the stress state via direct differentiation of the constitutive law for the internal energy in consistency with the energy conservation equation. Given a general expression for $e = e(g_{Ij}, \varsigma)$, the equation of motion for the internal energy is:

$$\frac{De}{Dt} = \frac{\partial e}{\partial g_{Ij}} \frac{Dg_{Ij}}{Dt} + \frac{\partial e}{\partial \varsigma} \frac{D\varsigma}{Dt} = \frac{1}{\rho} \sigma_{ij} \frac{\partial u_i}{\partial x_j}, \tag{2.24}$$

One can consider an elastic particle path of constant entropy and Eq. 2.12 to obtain,

$$\frac{\partial e}{\partial g_{Ij}} \frac{Dg_{Ij}}{Dt} = -\frac{\partial e}{\partial g_{Ij}} g_{Ik} \frac{\partial u_k}{\partial x_j} = \frac{1}{\rho} \sigma_{ij} \frac{\partial u_i}{\partial x_j}, \tag{2.25}$$

and by simple identification of terms,

$$\sigma_{ij} = -\rho g_{Ki} \frac{\partial e}{\partial g_{Kj}}, \tag{2.26}$$

or equivalently, making use of the deformation tensor,

$$\sigma_{ij} = \rho F_{iK} \frac{\partial e}{\partial F_{jK}}. \tag{2.27}$$

In the particular case of an isotropic material, expressions (2.23, 2.26, 2.27) can be simplified since the internal energy and stresses are formally independent of axis orientation. In other words, only three invariants (or eigenvalues) of the strain tensors are needed to fully determine e,

$$e = e\left(I_1^{\mathbf{M}}, I_2^{\mathbf{M}}, I_3^{\mathbf{M}}, \varsigma\right), \tag{2.28}$$

where $I_i^{\mathbf{M}}$ are the canonical invariants of the left (or right) Cauchy-Green tensor:

$$\begin{aligned}
I_1^{\mathbf{M}} &= \operatorname{tr}(\mathbf{M}), && (2.29a)\\
I_2^{\mathbf{M}} &= \frac{1}{2}\left(\operatorname{tr}(\mathbf{M}^2) - (\operatorname{tr}(\mathbf{M}))^2\right), && (2.29b)\\
I_3^{\mathbf{M}} &= \det(\mathbf{M}), && (2.29c)
\end{aligned}$$

with $\mathbf{M} = \{\mathbf{b}, \mathbf{C}\}$. Equations (2.26–2.27) can also be written as functions of the matrix invariants,

$$\sigma_{ij} = -\rho g_{Ki} \frac{\partial e}{\partial I_m^{\mathbf{M}}} \frac{\partial I_m^{\mathbf{M}}}{\partial g_{Kj}}, \tag{2.30a}$$

$$\sigma_{ij} = \rho F_{iK} \frac{\partial e}{\partial I_m^{\mathbf{M}}} \frac{\partial I_m^{\mathbf{M}}}{\partial F_{jK}}. \tag{2.30b}$$

The derivatives of the invariants of the strain tensor with respect to the components of the deformation (or inverse deformation) tensor can be obtained from differentiation of Eqs. (2.19) and (2.29) (see [49] and [7] for a detailed description of these expressions).

A general structure of the constitutive laws normally adopted for isotropic hyper-elastic materials assumes an additive decomposition $e = e_s + e_h$. The first term e_s represents the contribution of shear to the internal energy and is normally considered a function of the three invariants of the Cauchy-Green tensors (i.e., $e_s = e_s(I_1^{\mathbf{M}}, I_2^{\mathbf{M}}, I_3^{\mathbf{M}})$, with $\mathbf{M} = \{\mathbf{b}, \mathbf{C}\}$). The second term is related to isotropic effects and hence only a function of the third invariant (i.e., the density) and entropy, $e_h = e_h(I_3^{\mathbf{M}}, \varsigma)$. In following chapters, a more detailed description of the constitutive laws used for each application will be given.

Hence, the description of the motion of elastic solids in an Eulerian frame of reference is completely defined by the Euler equations (2.1), with the addition of the deformation evolution equations written in terms of $\mathbf{g}$ (2.11) or $\mathbf{F}$ (2.15). These relations have to be applied consistently with the appropriate kinematic constraints (2.9, 2.10) or (2.17, 2.18). Finally, the system is closed by a constitutive relation of the form (2.23), such that Cauchy stresses can be computed using Eqs. (2.26) or (2.27). The next section will expand this system of equations to account for the inelastic effects generally observed when solids are submitted to high stresses in particular configurations.

2.3 Plasticity

Most materials submitted to sufficiently high stress conditions undergo large strains when small stress increments are additionally applied, and residual deformations remain even when the stresses are removed. This defines the plastic regime [100]. Plasticity is intimately ligated to the microstructure of the material, more specifically to the number density of dislocations in the crystalline structure. Dislocation theory has its roots in the work of Taylor [104], Orowan [84], Gilman [41, 40], and Gillis

[38, 39]. In most materials, as the number density of dislocations increase, additional shear stress is required to produce more dislocations, resulting in what is known as strain hardening of the material. Conversely, thermal softening refers to the reduced shear stress needed to create new dislocations as the temperature of the material is increased. The limit of thermal softening is melting, in which the material transitions to a fluid state with stresses strictly dependent on the rate at which deformations occur.

Macroscopically, when uniaxial-stress conditions are applied to a deformable medium, the transition between the elastic state and the plastic state can be defined by a limit stress, normally called yield stress. For stress states below yielding, deformations in the material are due to stretching of the crystalline structure and they disappear when the loading is removed. Above the yield stress, dislocations are created and result in permanent deformations. The formation of dislocations is a nonreversible and dissipative process that, in consequence, increases entropy. For other stress conditions involving more than one component of the stress tensor, more complex yield criteria determine whether a material point is in plastic or elastic state. Yield criteria are usually based on the deviatoric part of the stress tensor since plasticity appears to be (at least for metals) an incompressible process (i.e., dislocations do not change the volume of the material) and is therefore intimately related to shear deformations. To account for strain hardening and thermal softening at a macroscopic level, the yield stress can be made dependent on the history of deformations and entropy in the case of strain hardening and on the temperature and pressure in the case of thermal softening.

The study of finite viscoplasticity utilizes a multiplicative decomposition of the deformation tensor $\mathbf{F}$

$$\mathbf{F} = \mathbf{F}^e \mathbf{F}^p, \tag{2.31}$$

where $\mathbf{F}^e$ and $\mathbf{F}^p$ are considered to be the elastic and inelastic part, respectively, of the total kinematic deformation. As is shown further in this section, this hypothesis allows the treatment of elastic–plastic solids in a way similar to purely elastic solids and still consistent with experimental evidence. As suggested by experiments, plasticity is independent of the compression/tension state of the material, hence $\det(\mathbf{F}^p) = 1$. Conversely, for the inverse deformation tensor, a similar decomposition can be defined,

$$\mathbf{g} = \mathbf{g}^p \mathbf{g}^e, \tag{2.32}$$

where $\mathbf{g}^e = \mathbf{F}^{e-1}$ and $\mathbf{g}^p = \mathbf{F}^{p-1}$. The specific internal energy is, under the multiplicative decomposition of $\mathbf{F}$, a function of the elastic and plastic parts of the deformation tensor $e = e(\mathbf{F}\mathbf{g}^p, \mathbf{F}^p, \varsigma)$ and stresses can be computed using Eqs. (2.26) or (2.27). However, an application of the chain rule shows that stresses can be obtained by simple differentiation with respect to the elastic deformations,

$$\sigma_{ij} = -\rho g^e_{Ki} \frac{\partial e}{\partial g^e_{Kj}}, \tag{2.33a}$$

$$\sigma_{ij} = \rho F^e_{iK} \frac{\partial e}{\partial F^e_{jK}}. \tag{2.33b}$$

As a final simplification, the energy contribution given by $\mathbf{F}^p$ is likely to be small in metal plasticity compared to the elastic strain and thermal contributions of $\mathbf{F}^e$ and ς. Under this consideration, constitutive laws are often formulated as independent of the plastic part of the deformation tensor (i.e., $e = e(\mathbf{F}^e, \varsigma)$).

The evolution of the plastic deformation tensor satisfies the general expression,

$$\frac{D\mathbf{F}^p}{Dt} = \mathbf{L}^p \mathbf{F}^p, \tag{2.34}$$

which can be written in conservative form as,

$$\frac{\partial \rho F^p_{IJ}}{\partial t} + \frac{\partial \rho F^p_{IJ} u_k}{\partial x_k} = \rho L^p_{IK} F^p_{KJ}. \tag{2.35}$$

The problem of plasticity then reduces to modeling $\mathbf{L}^p$, which is called the plastic deformation rate tensor and is normally written in terms of local variables (i.e., the plastic state at any given particle of the material only depends on its stress state). The set of equations proposed in [78, 49] contemplates the evolution in time of the total inverse deformation tensor and the plastic deformation tensor (Eqs. (2.7,2.35)) for a total of 23 equations defining the motion of an elastic–plastic solid. In contrast, the formulation of Godunov and Romenski [42] proposes to keep track of $\mathbf{F}^e$ alone in the equations of motion. A differential expression for the motion of the elastic deformations $\mathbf{F}^e$ is obtained from the algebraic manipulation of Eqs. (2.15), (2.31) and (2.34):

$$\frac{\partial \rho F^e_{iJ}}{\partial t} + \frac{\partial \left(\rho F^e_{iJ} u_k - \rho F^e_{kJ} u_i\right)}{\partial x_k} = -u_i \frac{\partial \rho F^e_{kJ}}{\partial x_k} - \rho F^e_{iK} L^p_{KJ}. \tag{2.36}$$

Alternatively, a formulation based on the elastic inverse deformation tensor results from inverting Eq. (2.36) to obtain

$$\frac{\partial g^e_{Ij}}{\partial t} + \frac{\partial \left(g^e_{Ik} u_k\right)}{\partial x_j} = \epsilon_{jmn} u_m G^e_{In} + L^p_{IK} g^e_{Kj}, \tag{2.37}$$

where $G^e_{Ij} \equiv \epsilon_{jmn} \frac{\partial g^e_{In}}{\partial x_m}$ is the curl of the elastic inverse deformation tensor. It is important to note that $\mathbf{F}^e$ and $\mathbf{g}^e$ are not, respectively, divergence and curl free in general. If $\mathbf{L}^p$ is zero, then these tensors are equivalent to $\mathbf{F}$ and $\mathbf{g}$ and comply with (2.17) and (2.9), respectively. However, when plastic deformations exist and considering the local nature of the plastic deformation rate tensor, the kinematic constraints for $\mathbf{F}$ and $\mathbf{g}$ are not applicable to $\mathbf{F}^e$ and $\mathbf{g}^e$. The kinematic source terms $-u_i \frac{\partial \rho F^e_{kJ}}{\partial x_k}$ and $\epsilon_{kmn} u_m G^e_{In}$ must always be included in Eqs. (2.36) and (2.37) so when their determinant is taken the continuity equation is recovered.

The structure of $\mathbf{L}^p$ remains to be determined. Under the assumption of isochoric plasticity (i.e., $\det(\mathbf{F^p}) = 1$), the material derivative of the determinant of $\mathbf{F}^p$ is identically zero. If Jacobi's rule,

$$\frac{D}{Dt}\det(\mathbf{M}) = \det(\mathbf{M})\operatorname{tr}\left(\frac{D\mathbf{M}}{Dt}\mathbf{M}^{-1}\right), \tag{2.38}$$

is applied to Eq. 2.34, it is found that,

$$\operatorname{tr}(\mathbf{L}^p) = 0. \tag{2.39}$$

The second argument that models the form of the plastic deformation rate tensor is related to the second law of thermodynamics. Consider an specific internal energy function e, such that $e = e(\mathbf{F}^e, \varsigma)$. Applying the chain rule to the Eq. (2.24), one obtains

$$\frac{\partial e}{\partial F^e_{iJ}}\left(\frac{\partial F^e_{iJ}}{\partial F_{aB}}\frac{DF_{aB}}{Dt} + \frac{\partial F^e_{iJ}}{\partial F^p_{AB}}\frac{DF^p_{AB}}{Dt}\right) + \frac{\partial e}{\partial \varsigma}\frac{D\varsigma}{Dt} = \frac{1}{\rho}\sigma_{ij}\frac{\partial u_i}{\partial x_j}. \tag{2.40}$$

Taking into account Eqs. (2.33b), (2.14) and (2.34), and the identities,

$$\frac{\partial F^e_{iJ}}{\partial F_{aB}} = \delta_{ia}\delta_{MB}F^p_{MJ}, \tag{2.41a}$$

$$\frac{\partial F^e_{iJ}}{\partial F^p_{AB}} = -F_{iK}(F^{p-1})_{KA}(F^{p-1})_{BJ}. \tag{2.41b}$$

The material derivative of the entropy can be expressed as:

$$\rho_0\frac{D\varsigma}{Dt} = -\frac{1}{T}\Sigma_{IJ}L^p_{IJ} > 0, \tag{2.42}$$

where,

$$\Sigma = -\frac{\rho_0}{\rho}\mathbf{F}^{eT}\sigma\mathbf{g}^{eT}, \tag{2.43}$$

is the so-called Mandel stress and $T = \frac{\partial e}{\partial \varsigma}|_\rho$ is the temperature. It must be emphasized that the entropy evolution equation (2.42) is only valid in smooth flows. In non-smooth flows, an additional increment in entropy appears across shocks satisfying the Rankine-Hugoniot conditions for the equations of motion. In [10], it is proposed to keep track of an additional variable ς_p, which follows Eq. (2.42) and satisfies $\varsigma \geq \varsigma^p$. This variable only registers entropy increments due to plastic work and can be used to parametrize strain hardening.

It can be easily shown that a plastic deformation rate tensor of the form,

$$\mathbf{L}^p = \chi\mathbf{g}^e\frac{\sigma'}{||\sigma'||}\mathbf{F}^e, \tag{2.44}$$

where χ is a scalar plastic-rate parameter, $\mathbf{M}'$ is the deviatoric part of a given matrix $\mathbf{M}$ (i.e., $\mathbf{M}' = \mathbf{M} - \frac{1}{3}\mathrm{tr}\left(\mathbf{M}\right)\mathbf{I})$ and $||\mathbf{M}|| = \sqrt{M_{ij}M_{ij}}$, satisfies the conditions given by Eqs. (2.39) and (2.42). Godunov and Romenski in [42] proposed a general form for χ:

$$\chi = \frac{1}{2\mu\tau}||\sigma'||, \tag{2.45}$$

where μ is the shear modulus and τ is the relaxation time, such that the material deforms in a way phenomenologically consistent to the Maxwell solid model. A general form for the relaxation time that allows hardening and thermal softening modeling is presented, following the work in [9],

$$\tau = \tau_0 \left(\frac{\sigma_0 f_H(\sigma_m, \varsigma^p) f_T(\rho, \varsigma)}{\sigma_m} \right)^{n_1}, \quad \sigma_m = \sqrt{\frac{3}{2}}||\sigma'||, \tag{2.46}$$

where τ_0 is a reference relaxation time, σ_0 is a characteristic yield stress, n_1 is an exponent which controls rate dependence, and the functions f_H and f_T represent the response to strain hardening and thermal softening, respectively. The latter take the form:

$$f_H(\sigma_m, \varsigma^p) = 1 + f_{H,0}\left(C_H \frac{\varsigma^P}{c_v \sigma_m} \right)^{n_2}, \quad f_T(\rho, \varsigma) = 1 - \langle \frac{T(\rho,\varsigma) - T_r}{T_M(\rho) - T_r} \rangle^{n_3}, \tag{2.47}$$

with $\langle \phi \rangle = \left(\phi + |\phi|\right)/2$ and where $f_{H,0}$ and C_H are material parameters, T_M is the melting temperature considered as a function of the local density, and T_r is a threshold temperature below which the temperature dependence is nonexistent. This expression for the relaxation time can be simplified to perfect plasticity by setting $f_H = f_T = 1$, $\sigma_0 = \sigma_Y$ (i.e., the yield stress), and n_1 high enough so the equivalent stress σ_m conforms to the yield surface defined by σ_Y almost immediately. Perfect plasticity is in many cases a convenient oversimplified model that reduces the study of inelasticity to a single parameter. However, such model is useful for obtaining a first approximation of the effects of plasticity. For instance, in Chapter 4, perfect plasticity is employed along with Whitham's shock dynamics theory in order to find a closed expression for the evolution of plastic shocks in converging geometries. In Chapter 6, perfect plasticity is also considered as it simplifies the parametric study of the Richmyer–Meshkov instability for elastic–plastic solids. Modeling of the strain hardening and thermal softening terms in Eq. (2.46) allows for more realistic simulations. As Fig. 2.1 shows, the strain hardening parameters in Eq. (2.47) for multiple materials were calibrated in a way such that the plastic evolution deviates minimally from results of tensile tests at different strain rates reported in [47] for OFHC copper and performed by Prof. Ravichandran's group for aluminum and steel.

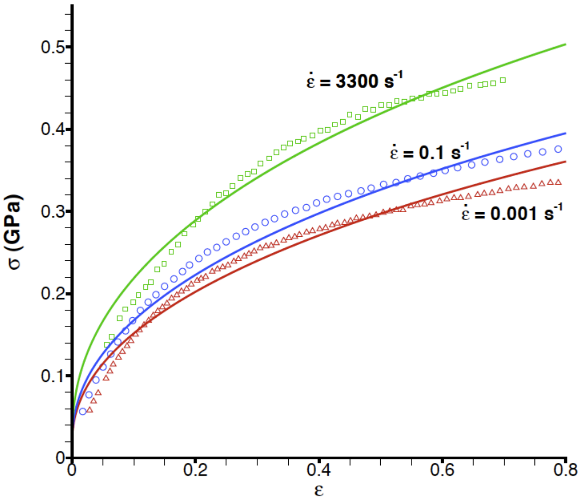

(a) OHFC copper

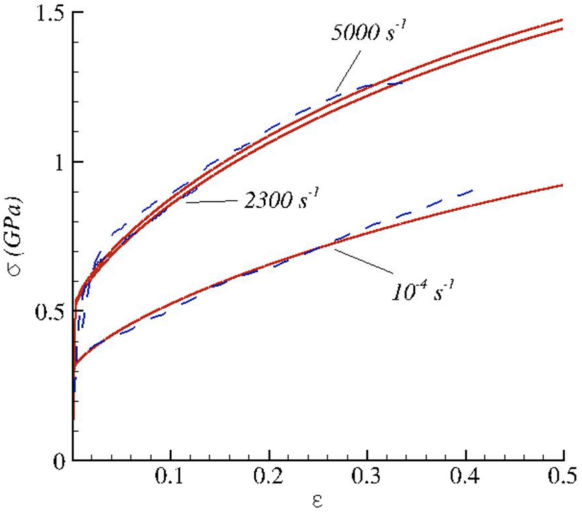

(b) 304 steel

Figure 2.1: Stress–strain curves for tensile one-dimensional experiments. Experimental data in (a) is represented by symbols and obtained from [47], data in (b) has been obtained from experiments conducted in Prof. Ravichandran's lab and is represented by dashed lines. Theoretical results after calibration of parameters in Eq. (2.46) are represented by continuous lines. Figures were produced by Philip Barton [9].

2.4 Characteristic speeds

The system of equations formed by Eqs. (2.1) and, depending on the formulation used, Eqs. (2.11)-(2.35), Eq. (2.37) or Eq. (2.36) is hyperbolic in nature when a hyper-elastic constitutive law is used [71, 42]. The characteristic polynomial in the spatial directions $k = 1, 2, 3$ takes the form

$$(u_k - \lambda)^n \det\big(\boldsymbol{\Omega}(\mathbf{e}_k) - (u_k - \lambda)^2 \mathbf{I}\big) = 0. \tag{2.48}$$

where λ is the characteristic speed, $\mathbf{e}_k$ are the standard basis vectors and $\boldsymbol{\Omega}(\mathbf{v})$ is the acoustic tensor, defined as,

$$\boldsymbol{\Omega}(\mathbf{v}) = \frac{1}{\rho} \sum_{k=1}^{3} \left(\mathbf{v}^T \mathbf{F}^{\mathbf{e}}\right)_k \mathbf{A}(\mathbf{e}_k, \mathbf{v}), \quad \mathbf{A}(\mathbf{w}, \mathbf{v}) = \frac{\partial \sigma \mathbf{v}}{\partial \mathbf{F}^e \mathbf{w}}. \tag{2.49}$$

The derivatives of stresses with respect to deformations that appear in Eq. (2.49) can be evaluated analytically (see [7]). The solution of the characteristic polynomial gives, in each direction, seven distinct waves with velocities:

$$u_k - \sqrt{\omega_1}, u_k - \sqrt{\omega_2}, u_k - \sqrt{\omega_3}, u_k, u_k + \sqrt{\omega_3}, u_k + \sqrt{\omega_2}, u_k + \sqrt{\omega_1}, \tag{2.50}$$

where ω_i are the eigenvalues of $\boldsymbol{\Omega}$. Starting in both directions from the central entropy wave u_k, they represent two shear waves and a longitudinal wave. While the eigenvalues $\lambda = u_k \pm \sqrt{\omega_i}$ only have one associated eigenvector, $\lambda = u_k$ is degenerate and its algebraic multiplicity depends on the number of equations considered in the system. As will be stated in Chapter 3, the numerical scheme employed does not require the computation of eigenvectors (see [10] for a complete description of them).

2.5 Summary

In this chapter, the equations of motion defining the behavior of elastic–plastic solids were introduced. In addition to the classical mass, linear momentum, and energy conservation, the response of solid materials to relative displacements between particles requires the formulation of constitutive laws that are functions of the strain tensors (or their invariants for isotropic materials). Since a conservative form of the equations of motion for the symmetric strain tensors cannot be obtained, it is necessary to evolve in time the nine different components of the deformation tensors, for which diverse formulations can be used based on the Eulerian or Lagrangian mappings. Inelastic behavior was modeled in accordance to a series of postulates empirically observed and in a way such that perfect plasticity, strain hardening, and material melting can be captured. Finally, the hyperbolic nature of the problem enables the application of the wide range of numerical techniques (for instance, see [108]) that have been developed for this type of system of partial differential equations, especially in the field of fluid mechanics, over the last years. The particular numerical implementation of the equations employed here is presented in the next chapter.

Chapter 3

Numerical implementation

3.1 Introduction

Conservative Eulerian formulations have been successfully employed for solving hyperbolic systems of equations. In particular, the numerical simulation of the response of gases to extreme conditions through shock capturing algorithms [44] have experienced active development in the last years as computational capacity has increased and become widely available [4]. The application of the same techniques to the extended system of hyperbolic equations describing the motion of solids seems plausible, especially for cases of extreme loading where shocks appear. Eulerian methods have the advantage of neither being affected by the grid distortion that naturally occurs in Lagrangian methods as particles move nor needing the design of a remapping algorithm like in the case of arbitrary Lagrangian–Eulerian formulations (respectively, Chapters 4 and 7 in [13]). These advantages become apparent in some of the applications described in forthcoming chapters, in which strong shocks and vorticity naturally appear and would result in extreme distortion of a Lagrangian mesh to the extent of requiring very small time-steps or even making the algorithm fail. In addition, these numerical methods do not require explicit artificial viscosity and are expected to converge to the correct entropy-producing weak solutions. As a major disadvantage, the computational cost that involves solving an extended system of 13 to 23 equations in multi-dimensions is still relevant and has postponed the implementation of these methods until parallel massive computing has become widely available.

General elastic–plastic solid motion algorithms in Eulerian frameworks were developed by Miller and Collela [78] and Hill et al. [49] but lacked the capability of handling multi-material or free-surface problems. A literature search on the topic suggests that multi-material formulations are, in fact, an open field [1, 17, 35, 88]. A natural division among the multiple suggested implementations is to differentiate between those which allow mixing, and therefore can also account for chemical reaction phenomena, and formulations that assume that materials are non-miscible and that a well-defined interface lies between them. A second distinction can be made based on the use of the volume fraction of the materials (commonly used in mixing models) and the use of a level-set function, which is commonly used for non-miscible materials, as a way of tracking the interface position. More complex methods are still under development, such as interface reconstruction in volume-of-fluid (VOF) methods [3], which attempts to estimate the position of an interface not only based on the volume fraction of the materials in a particular cell but also considering the neighboring ones, or moment-of-fluid (MOF) methods [31].

The numerical method used for the different applications described in this thesis is constructed upon the AMROC framework [25], a parallel, adaptive mesh refinement (in space and time) scheme [18] written in C++ for solving generic systems of hyperbolic partial differential equations. The extension of this framework to solid mechanics and multi-material problems by means of the use of level-set functions is described in the work of Barton et al. [8]. The current version of the code includes some improvements with respect to the latter, which will be described in the course of this chapter. In a multi-material simulation in AMROC, each different material is contained in the region where an associated level-set function is positive. This level-set function is defined at all times as a smooth distance function to the closest boundary. Boundary conditions across material interfaces are imposed by the combined use of the modified ghost fluid method (M-GFM) [65] and the solution of a Riemann problem based on the states of the materials in contact. The updated version of the algorithm employs a robust algebraic HLLD solver, derived from the scheme widely used in magnetohydrodynamics [80] for wall flux computation, while the original version in [8] relied on the Riemann problem being approximated using a characteristic linear solver. After boundary conditions at material interfaces are imposed, each material can be solved independently. This chapter focuses on the implementation of the algorithm for each of the patches (i.e., rectangular computational domains given to a particular processor), first discussing a single-material case and consequently describing the implementation of multi-material capabilities through the level-set and ghost fluid method. Details on the parallel implementation and communication between patches can be found in [18, 25].

3.2 Single-material implementation

The set of equations to be solved can be written as

$$\frac{\partial \mathbf{U}}{\partial t} + \frac{\partial \mathbf{D^i}}{\partial x_i} = \mathbf{S} + \mathbf{P}, \tag{3.1}$$

where $\mathbf{U}$ is the vector of conserved variables, $\mathbf{D}$ is the flux vector, and $\mathbf{S}$ and $\mathbf{P}$ are source terms associated with kinematic constraints and the plastic update respectively.

All the possible conservative formulations for solid mechanics, regardless of whether they are based on the deformation $\mathbf{F}$ or inverse deformation tensor $\mathbf{g}$, must contain the equations for linear momentum and total energy,

$$\mathbf{U}_{1:4} = \begin{pmatrix} \rho u_{1:3} \\ \rho E \end{pmatrix}, \mathbf{D^i}_{1:4} = \begin{pmatrix} \rho u_{1:3} u_i - \sigma_{1:3,i} \\ \rho E u_i - \sigma_{ij} u_j \end{pmatrix}, \mathbf{S}_{1:4} = 0, \mathbf{P}_{1:4} = 0. \tag{3.2}$$

Three different approaches to the way the state and flux vectors are completed to form a close system of equations are subsequently described in this section.

3.2.1 $\mathbf{F}^e$ formulation

This approach was implemented in the first version of the AMROC multi-material algorithm for solid mechanics [8] and follows previous work in [10, 42, 7]. It uses the evolution equations for the nine components of the elastic deformation tensor $\mathbf{F}^e$ (Eq. (2.36)) and neglects the computation of the continuity equation since density can be obtained from

$$\frac{\rho_0}{\rho} = \det\left(\mathbf{F}^e\right). \tag{3.3}$$

An alternate implementation in two-dimensional problems substitutes the component F^e_{33} by the mass conservation equation when components F^e_{13}, F^e_{23}, F^e_{31}, F^e_{32} are identically zero (i.e., plane strain conditions). F^e_{33} can be obtained afterwards from Eq. (3.3). Assuming the plastic law described in Eqs. (2.44)-(2.45), the additional components of the system of equations are given by:

$$\mathbf{U}_{5:13} = \begin{pmatrix} \rho F^e_{1,1:3} \\ \rho F^e_{2,1:3} \\ \rho F^e_{3,1:3} \end{pmatrix}, \tag{3.4a}$$

$$\mathbf{D^i}_{5:13} = \begin{pmatrix} \rho F^e_{1,1:3} u_i - \rho F^e_{i,1:3} u_1 \\ \rho F^e_{2,1:3} u_i - \rho F^e_{i,1:3} u_2 \\ \rho F^e_{3,1:3} u_i - \rho F^e_{i,1:3} u_3 \end{pmatrix}, \tag{3.4b}$$

$$\mathbf{S}_{5:13} = \begin{pmatrix} -u_1 \frac{\partial \rho F^e_{k,1:3}}{\partial x_k} \\ -u_2 \frac{\partial \rho F^e_{k,1:3}}{\partial x_k} \\ -u_3 \frac{\partial \rho F^e_{k,1:3}}{\partial x_k} \end{pmatrix}. \tag{3.4c}$$

$$\mathbf{P}_{5:13} = \begin{pmatrix} -\frac{\rho}{2\mu\tau} {\sigma'}_{1k} F^e_{k,1:3} \\ -\frac{\rho}{2\mu\tau} {\sigma'}_{2k} F^e_{k,1:3} \\ -\frac{\rho}{2\mu\tau} {\sigma'}_{3k} F^e_{k,1:3} \end{pmatrix} \tag{3.4d}$$

In two-dimensional cases where the continuity equation is used, the thirteenth component of the system of equations is substituted by:

$$\mathbf{U}_{13} = \rho, \ \mathbf{D}^i_{13} = \rho u_i, \ \mathbf{S}_{13} = 0, \ \mathbf{P}_{13} = 0. \tag{3.5}$$

3.2.2 Inverse deformation tensor–plastic deformation tensor formulation

This approach includes $\mathbf{g}$ and $\mathbf{F}^p$ in the system of equations and was first implemented in the solvers developed by Miller and Colella [78] and Hill et al. [49]. The method considers all the components of the inverse deformation and plastic deformation tensors and also includes the continuity equation. A density penalty term is introduced to reduce deviations from the mass conservation equation when computing the density through the determinant of $\mathbf{g}$. Finally, a curl diffusion term corrects possible deviations from the initial curl free condition of the inverse deformation tensor (Eq. (2.9)). The linear momentum and energy equations (Eq. 3.2) are complemented with,

$$\mathbf{U}_{5:23} = \begin{pmatrix} g_{1:3,1} \\ g_{1:3,2} \\ g_{1:3,3} \\ \rho F^p_{1,1:3} \\ \rho F^p_{2,1:3} \\ \rho F^p_{3,1:3} \\ \rho \end{pmatrix}, \tag{3.6a}$$

$$\mathbf{D^i}_{5:23} = \begin{pmatrix} g_{1:3,k} u_k \delta_{1i} \\ g_{1:3,k} u_k \delta_{2i} \\ g_{1:3,k} u_k \delta_{3i} \\ \rho F^p_{1,1:3} u_i \\ \rho F^p_{2,1:3} u_i \\ \rho F^p_{3,1:3} u_i \\ \rho u_i \end{pmatrix}, \tag{3.6b}$$

$$\mathbf{S}_{5:23} = \begin{pmatrix} \epsilon_{1mn} u_m G_{1:3,n} - D\epsilon_{1mn} \frac{\partial G_{1:3,n}}{\partial x_m} + \eta \left(\frac{\rho}{\rho_0} \frac{1}{\det \mathbf{g}} - 1 \right) g_{1:3,1} \\ \epsilon_{2mn} u_m G_{1:3,n} - D\epsilon_{2mn} \frac{\partial G_{1:3,n}}{\partial x_m} + \eta \left(\frac{\rho}{\rho_0} \frac{1}{\det \mathbf{g}} - 1 \right) g_{1:3,2} \\ \epsilon_{3mn} u_m G_{1:3,n} - D\epsilon_{3mn} \frac{\partial G_{1:3,n}}{\partial x_m} + \eta \left(\frac{\rho}{\rho_0} \frac{1}{\det \mathbf{g}} - 1 \right) g_{1:3,3} \\ 0 \end{pmatrix}, \tag{3.6c}$$

$$\mathbf{P}_{14:22} = \begin{pmatrix} \frac{\rho}{2\mu\tau} g^e_{1:3,a} {\sigma'}_{ab} F_{b1} \\ \frac{\rho}{2\mu\tau} g^e_{1:3,a} {\sigma'}_{ab} F_{b2} \\ \frac{\rho}{2\mu\tau} g^e_{1:3,a} {\sigma'}_{ab} F_{b3} \end{pmatrix}, \tag{3.6d}$$

where $\mathbf{g}^e = \mathbf{F}^p\mathbf{g}$ and $\mathbf{F} = \mathbf{g}^{-1}$. The curl diffusion term and the density penalty term are, respectively, the second and third terms in the source vector $\mathbf{S}$, where D and η are coefficients with set values that depend on the mesh and time-stepping characteristics (see [78] for more details),

$$D = \frac{\Delta x^2}{4d\Delta t}, \;\; \eta = \frac{1}{6\Delta t}. \tag{3.7}$$

3.2.3 Elastic inverse deformation tensor formulation

A novel formulation that lies in between the previously described approaches is presented here. In this case, mass conservation and the evolution of the nine components of the elastic inverse deformation tensor $\mathbf{g}^e$ (2.37) are considered for a total of 14 equations (down from 23 in the inverse deformation tensor–plastic deformation tensor approach). These equations are similar to the evolution relations for $\mathbf{g}$ but the plastic source term is included in the evolution of $\mathbf{g}^e$ (as happened in the formulation based on $\mathbf{F}^e$) and the source curl diffusion term cannot be applied since the $\mathbf{g}^e$ is not curl free in general. An advantage with respect to the $\mathbf{F}^e$ formulation is that the mass conservation penalty term can still be enforced, controlling deviations from the density computed as the determinant of $\mathbf{g}^e$ with respect to the density computed from mass conservation. Deliberately neglecting one of the equations and obtaining the missing value employing Eq. 3.3 often leads to unphysical results (e.g., a negative density or F_{33} component) when numerical errors arise in extreme compression problems. The summary of the equations for this approach is,

$$\mathbf{U}_{5:14} \;\; = \;\; \begin{pmatrix} g^e_{1:3,1} \\ g^e_{1:3,2} \\ g^e_{1:3,3} \\ \rho \end{pmatrix}, \tag{3.8a}$$

$$\mathbf{D^i}_{5:14} \;\; = \;\; \begin{pmatrix} g^e_{1:3,k} u_k \delta_{1i} \\ g^e_{1:3,k} u_k \delta_{2i} \\ g^e_{1:3,k} u_k \delta_{3i} \\ \rho u_i \end{pmatrix}, \tag{3.8b}$$

$$\mathbf{S}_{5:14} \;\; = \;\; \begin{pmatrix} \epsilon_{1mn} u_m G^e_{1:3,n} + \eta \left(\frac{\rho}{\rho_0} \frac{1}{\det \mathbf{g}^e} - 1 \right) g^e_{1:3,1} \\ \epsilon_{2mn} u_m G^e_{1:3,n} + \eta \left(\frac{\rho}{\rho_0} \frac{1}{\det \mathbf{g}^e} - 1 \right) g^e_{1:3,2} \\ \epsilon_{3mn} u_m G^e_{1:3,n} + \eta \left(\frac{\rho}{\rho_0} \frac{1}{\det \mathbf{g}^e} - 1 \right) g^e_{1:3,3} \\ 0 \end{pmatrix}, \tag{3.8c}$$

$$\mathbf{P}_{5:14} = \begin{pmatrix} \frac{\rho}{2\mu\tau} g^e_{1:3,k} {\sigma'}_{k1} \\ \frac{\rho}{2\mu\tau} g^e_{1:3,k} {\sigma'}_{k2} \\ \frac{\rho}{2\mu\tau} g^e_{1:3,k} {\sigma'}_{k3} \\ 0 \end{pmatrix} \tag{3.8d}$$

where G^e represents the curl of $\mathbf{g}^e$.

3.2.4 Use of the stretch tensor

This subsection introduces a variation of the previous formulations that makes use of the stretch tensor and offers computational advantages in certain problems. As was specified in Chapter 2, the deformation tensor has a polar decomposition $\mathbf{F} = \mathbf{VR}$ and, conversely, $\mathbf{g} = \mathbf{R}^T\mathbf{V}^{-1}$. The same decomposition can be applied to their elastic counterparts $\mathbf{F}^e$ and $\mathbf{g}^e$. Assuming a general multiplicative decomposition $\rho\mathbf{F}^e = \mathbf{MN}$ and the form of the plastic deformation rate tensor $\mathbf{L}^p$ given in (2.44), Eq. (2.36) reads

$$A\left(\mathbf{M}\right)_{iK} N_{KJ} + M_{iK}\frac{DN_{KJ}}{Dt} = 0, \tag{3.9}$$

where

$$A\left(\mathbf{M}\right)_{iJ} = \frac{\partial M_{iJ}}{\partial t} + \frac{\partial\left(M_{iJ}u_k - M_{kJ}u_i\right)}{\partial x_k} + u_i\frac{\partial M_{kJ}}{\partial x_k} + \frac{1}{2\mu\tau}{\sigma'}_{ik}M_{kJ}. \tag{3.10}$$

Note that $\mathbf{A}\left(\rho\mathbf{F}^e\right) = 0$. Alternatively, for a similar decomposition of the inverse deformation tensor, $\mathbf{g}^e = \mathbf{pq}$, one obtains

$$p_{IK}B\left(\mathbf{q}\right)_{Kj} + \frac{Dp_{IK}}{Dt}q_{Kj} = 0, \tag{3.11a}$$

$$B\left(\mathbf{q}\right)_{Ij} = \frac{\partial q_{Ij}}{\partial t} + \frac{\partial\left(q_{Ik}u_k\right)}{\partial x_j} - \epsilon_{jmn}u_m Q_{In} - \frac{1}{2\mu\tau}q_{Ik}{\sigma'}_{kj}, \tag{3.11b}$$

$$\mathbf{B}\left(\mathbf{g}^e\right) = 0, \tag{3.11c}$$

where $Q_{Ij} \equiv \epsilon_{jmn}\frac{\partial q_{In}}{\partial x_m}$. $\mathbf{A}$ and $\mathbf{B}$ for identical decompositions of $\rho\mathbf{F}$ and $\mathbf{g}$ take the same form with the exclusion of the plastic source term. A solution to Eqs. (3.9,3.11a) can be obtained by simply setting:

$$\mathbf{A}(\mathbf{M}) = 0 \quad , \quad \frac{D\mathbf{N}}{Dt} = 0, \tag{3.12a}$$

$$\mathbf{B}(\mathbf{q}) = 0 \quad , \quad \frac{D\mathbf{p}}{Dt} = 0. \tag{3.12b}$$

Consider now a spatial field of symmetric, definite positive matrices $\mathbf{V}_n$ and a second one of orthogonal rotation matrices $\mathbf{R}_n$ such that they constitute the polar decomposition of the elastic deformation tensor (i.e., $\mathbf{F}^e_n = \mathbf{V}_n\mathbf{R}_n$ or $\mathbf{g}^e_n = {\mathbf{R}^T}_n{\mathbf{V}^{-1}}_n$, with $\mathbf{M} = \rho\mathbf{V}_n$, $\mathbf{N} = \mathbf{R}_n$, $\mathbf{p} = {\mathbf{R}^T}_n$, and

$\mathbf{q} = \mathbf{V}^{-1}{}_n$) at a particular time-step n. The deformation field at time-step $n+1$ can be obtained by solving Eq. (3.12) for the values of $\mathbf{V}_{n+1}$ and $\mathbf{R}_{n+1}$ such that $\mathbf{F}^e_{n+1} = \mathbf{g}^{e\,-1}_{\;n+1} = \mathbf{V}_{n+1}\mathbf{R}_{n+1}$. In general, $\mathbf{V}_{n+1}$ is not the stretch tensor of $\mathbf{F}^e_{n+1}$ since the symmetry condition is never enforced when Eq. (3.12) is solved. In contrast, the rotation matrix field at $n+1$ is preserved by the advection equation. This enables the construction of the stretch matrix at the new time-step:

$$\widetilde{\mathbf{V}}_{n+1} = \sqrt{\mathbf{b}_{n+1}} = \sqrt{\mathbf{F}^e_{n+1}\mathbf{F}^{eT}_{n+1}} = \sqrt{\mathbf{V}_{n+1}\mathbf{V}^T_{n+1}}, \tag{3.13}$$

with its associated rotation matrix determined from

$$\widetilde{\mathbf{R}}_{n+1} = \widetilde{\mathbf{V}}^{-1}_{n+1}\mathbf{F}^e_{n+1} = \widetilde{\mathbf{V}}^{-1}_{n+1}\mathbf{V}_{n+1}\mathbf{R}_{n+1} = \left(\sqrt{\mathbf{V}_{n+1}\mathbf{V}^T_{n+1}}\right)^{-1}\mathbf{V}_{n+1}\mathbf{R}_{n+1}. \tag{3.14}$$

The values of $\mathbf{V}_{n+1}$ and $\mathbf{R}_{n+1}$ can now be updated for their use in the next computational time-step with the real stretch and rotation matrix values,

$$\mathbf{V}_{n+1} \leftarrow \widetilde{\mathbf{V}}_{n+1}, \tag{3.15a}$$

$$\mathbf{R}_{n+1} \leftarrow \widetilde{\mathbf{R}}_{n+1}. \tag{3.15b}$$

The same approach is directly applicable to the formulations that make use of the deformation or inverse deformation tensor instead of keeping track of their elastic contributions. It is important to note that knowing the evolution of the rotation matrix is not needed for the computation of the new stretch matrix $\widetilde{\mathbf{V}}_{n+1}$, which is the only required element for formulating constitutive laws for solid materials (i.e., $e = e(\mathbf{V}^2, \varsigma)$). A summary of the proposed algorithm is:

- ◇ At t_0, given the initial deformation state in terms of inverse deformation or deformation gradients, compute $\mathbf{V}_0$. (e.g., $\mathbf{V}_0 = \sqrt{\mathbf{F}^e_0\mathbf{F}^{eT}_0}$ or $\mathbf{V}_0 = \sqrt{\mathbf{g}^{e-T}_0\mathbf{g}^{e-1}_0}$).
- ◇ At each time-step $\{t_0, t_f\}$

    1. Evaluate $\mathbf{V}_{n+1}$ given $\mathbf{V}_n$ through an appropriate discretization of $\mathbf{A}(\mathbf{V}) = 0$ or $\mathbf{B}(\mathbf{V}^{-1}) = 0$ (3.12) concurrently with the mass conservation, linear momentum and energy equations.
    2. Since $\mathbf{V}_{n+1}$ is not symmetric in general, obtain a new stretch tensor $\widetilde{\mathbf{V}}_{n+1} = \sqrt{\mathbf{V}_{n+1}\mathbf{V}^T_{n+1}}$.
    3. Substitute $\mathbf{V}_{n+1}$ with $\widetilde{\mathbf{V}}_{n+1}$.

- ◇ End

This algorithm, in the case of being applied to $\mathbf{F}$ or $\mathbf{g}$ and not just to the elastic contributions $\mathbf{F}^e$ or $\mathbf{g}^e$, can also be regarded as an arbitrary Lagrangian-Eulerian (ALE) approach in which an intermediate frame $\widetilde{X}_I$ of reference is chosen in such a way that it is neither Eulerian nor Lagrangian and there exist three maps $x_i = x_i\left(\widetilde{X}_J, t\right)$, $\widetilde{X}_I = \widetilde{X}_I\left(X_J, t\right)$, and $x_i = x_i\left(X_J, t\right)$ that satisfy:

$$V_{iJ} = \frac{\partial x_i}{\partial \widetilde{X}_J},\ R_{IJ} = \frac{\partial \widetilde{X}_I}{\partial X_J},\ F_{iJ} = \frac{\partial x_i}{\partial X_J},\ \text{with}\ \mathbf{F} = \mathbf{VR}. \tag{3.16}$$

A second interpretation stems from the fact that F_{iJ} is a contravariant–covariant tensor. Thus, a rigorous way of writing the tensor is $\mathbf{F} = F^i_J \mathbf{e}_i \otimes \mathbf{e}^J = \partial x^i / \partial X^J \mathbf{e}_i \otimes \mathbf{e}^J$. In this notation, $\otimes$ is the dyadic product, superscripts and subscripts denote, respectively, contravariant and covariant properties, and $\mathbf{e}_i$ and $\mathbf{e}^J$ are, respectively, the basis co-vectors and vectors. Vectors (for instance, the position vectors $\mathbf{X}$ and $\mathbf{x}$) have contravariant properties, which means that under a rotation of the coordinate system, they must be multiplied from the left by the rotation matrix in order to remain basis-independent. Co-vectors are covariant, and under the same rotation, must be multiplied from the right. Since F^i_J is covariant with respect to rotations of the Lagrangian coordinates X^J, $\mathbf{V}$ can be interpreted as a symmetric deformation tensor that results from a covariant rotation of the Lagrangian frame of reference such that $\mathbf{FR}^T = \mathbf{V}$.

The main consequence of evolving the stretch tensor instead of $\mathbf{F}$ or $\mathbf{g}$ without keeping track of the rigid-body rotations is the loss of information about particle paths contained in the deformation gradients (which can be recovered nonetheless by integration of the velocity field). This algorithm effectively "re-initializes" the Lagrangian frame of reference at each time step to be aligned with the directions of principal stretches at each point of the domain. A second consequence is that the kinematic constraints (i.e., divergence and curl constraints) cannot be imposed over $\mathbf{V}$. These disadvantages are not especially relevant when the stretch tensor substitutes for the elastic parts of the deformation or inverse deformation tensors. In this case, kinematic constraints cannot even be imposed over $\mathbf{F}^e$ and $\mathbf{g}^e$ since these fields are not divergence and curl free, respectively, and information on particle paths is already lost by not keeping track of the plastic deformations.

This approach offers several advantages related to the properties of $\mathbf{V}$ without increasing the size of the system or introducing new equations (i.e., $\mathbf{A} = 0$ and $\mathbf{B} = 0$ are the equations of motion for the deformation tensor and inverse deformation tensor, respectively). In some multi-material simulation examples, it was observed that impacts between sections of material contained in the same level set (i.e., different spikes in cylindrical Richtmyer–Meshkov instability simulations converging near the origin) were not well handled by a numerical implementation where any of the three approaches described in subsections 3.2.1, 3.2.2, or 3.2.3 was employed. This was because, even when the two states had similar strain states, the associated deformation tensors varied largely as one could be rotated with respect to the other, leading in many occasions to unphysical results (i.e., negative densities, very high wave speeds) when numerically solving equations (3.4), (3.6), or (3.8). Stretch tensors are symmetric and definite positive, and do not reflect rigid-body rotations. In consequence, between two colliding pieces of material, the differences in the state vector are reduced, leading to

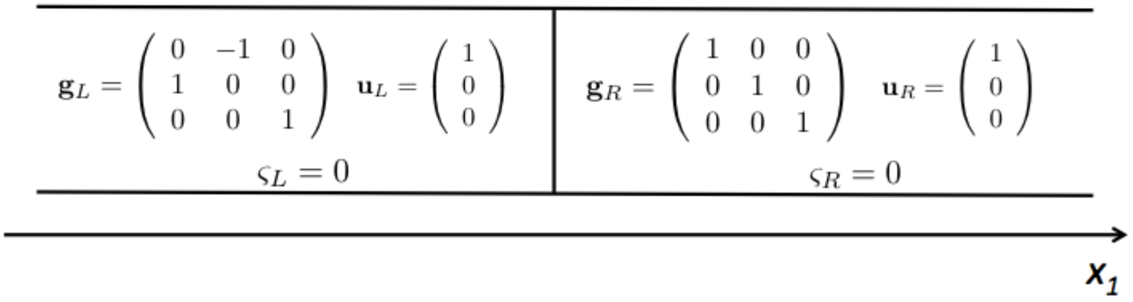

Figure 3.1: Initial condition for a one-dimensional problem in which two pieces of the same unstressed elastic material are rotated $\frac{\pi}{2}$ with respect to each other

smoother solutions for impacts and reconnections.

To illustrate this point, consider the one-dimensional initial value problem described in Fig. 3.1. At $t = 0$, two pieces of the same unstressed elastic material become attached and move with constant velocity. The left piece of the material has been rotated with respect to the other by $\frac{\pi}{2}$. The boundary conditions between the two portions are satisfied (i.e., normal velocity and stress are constant, tangential velocity and stress are zero). The solution of this initial value problem in time is that the two pieces move together at constant velocity without any change in their stress state. As shown in Fig. 3.2, the Eulerian algorithm evolves the deformation tensor creating a smooth transition between the rotated deformation tensor states. In the third time-step, the smoothing of the deformation tensor effectively decreases the density to about 0.6 or 0.85 of its initial value depending on the method used, which also affects the stress state and linear momentum and energy equations. The method employed in Fig. 3.2(a,b) is the inverse deformation tensor formulation (Section 3.2.2) that includes the density penalty term, which stabilizes the density defects as can be appreciated in Fig. 3.2(b). An identical test performed with the same formulation but disabling the density penalty term leads to a more unstable solution (as observed in Fig. 3.2(c,d)). Failure of the algorithm is possible in more demanding problems. When the stretch tensor is used, the rotated deformation tensor of the left material is replaced by the identity tensor and all the variables of the initial state vector are constant fields, which suffer no modification in time and prescribe the correct solution of the problem. The only disadvantage of the use of the stretch tensor is losing track of the position of the interface between the rotated and non-rotated pieces but this information can be recovered from the velocity field.

3.2.5 Time and spatial discretization

This paragraph summarizes the numerical implementation of the equations of motion and is largely based on [8]. The finite-difference spatial discretization employed considers the state vector at the center (denoted by the subscript i, j, k) of cells of dimensions $(\Delta x_1, \Delta x_2, \Delta x_3)$ contained in the

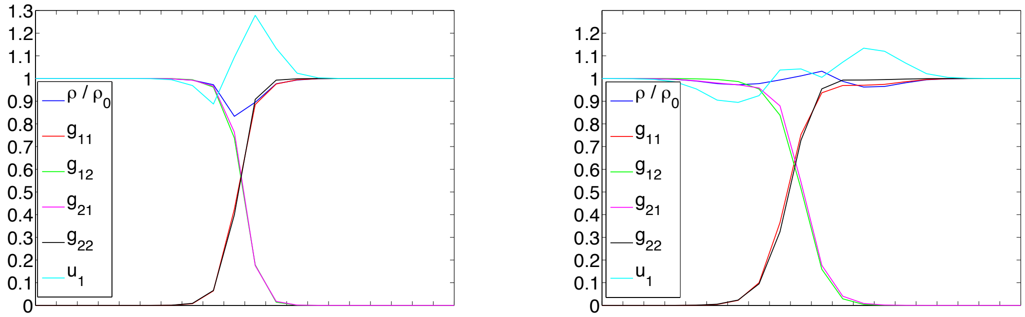

(a) time-step 3, with density penalty term

(b) time-step 8, with density penalty term

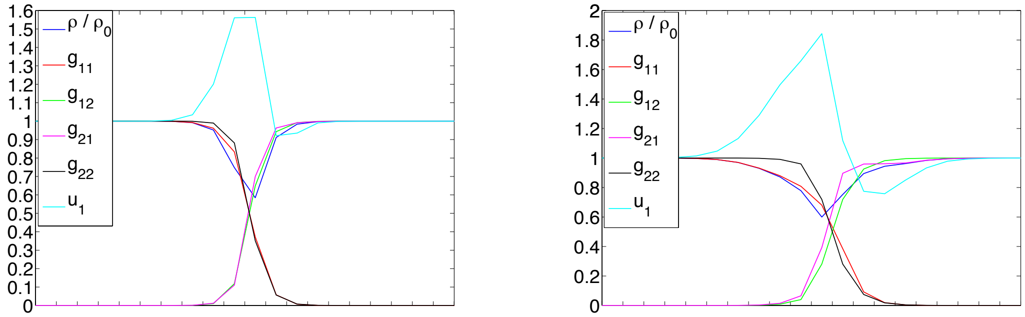

(c) time-step 3, without density penalty term

(d) time-step 8, without density penalty term

Figure 3.2: Density, components of the inverse deformation tensor, and velocity after 3 and 8 time-steps for the initial problem described in Fig. 3.1 using the **g** formulation with and without density penalty terms. Each tick in the x-axis represents a cell boundary.

computational domain D. The method of fractional steps is used whenever inelastic terms are present in Eq.(3.1). The first fractional step corresponds to the elastic update and makes use of explicit evaluation. The second involves the plastic update in pseudo-time. This is done implicitly since the problem can become locally stiff if the strain rates are high enough,

$$\widetilde{\mathbf{U}}_{i,j,k} = \mathbf{U}^n_{i,j,k} - \int_{t_n}^{\widetilde{t}} \mathbf{H}_{i,j,k}\left(\mathbf{U}\right)\, dt, \tag{3.17a}$$

$$\mathbf{U}^{n+1}_{i,j,k} = \widetilde{\mathbf{U}}_{i,j,k} + \int_{\widetilde{t}}^{t_{n+1}} \mathbf{P}_{i,j,k}\left(\mathbf{U}\right)\, dt, \tag{3.17b}$$

where

$$\begin{aligned}\mathbf{H}_{i,j,k} = \frac{1}{\Delta x_1}\left(\mathbf{D}^1_{i+1/2,j,k} - \mathbf{D}^1_{i-1/2,j,k}\right) + \frac{1}{\Delta x_2}\left(\mathbf{D}^2_{i,j+1/2,k} - \mathbf{D}^2_{i,j-1/2,k}\right) \ldots \\ + \frac{1}{\Delta x_3}\left(\mathbf{D}^3_{i,j,k+1/2} - \mathbf{D}^3_{i,j,k-1/2}\right) - \mathbf{S}_{i,j,k}.\end{aligned} \tag{3.18}$$

The discretization of the elastic and plastic updates are described in this and the following paragraph, respectively. Along x_1, $\mathbf{D}^1_{i+1/2,j,k}$ in Eq. (3.18) represents the intercell numerical flux function between the cells collocated at (i,j,k) and $(i+1,j,k)$. Equivalent notation applies to the other Cartesian directions. These fluxes are formed through polynomial reconstruction from cell centered flux values $\mathbf{D}_{i,j,k} = \mathbf{D}\left(\mathbf{U}_{i,j,k}\right)$ by use of the third-order weighted essentially non-oscillatory (WENO) method for finite-difference schemes [57]. This method constructs high-order approximations of a given scalar field in locally smooth flow regions and reduces to a monotone first-order scheme in the vicinity of discontinuities. The method achieves this goal by constructing a convex combination of lower order candidate stencils, with nonlinear weights assigned as functions of local smoothness indicators. For systems of equations, WENO methods can be applied in a number of ways [99]. The easiest approach (and the one considered in this implementation) is to treat each component of $\mathbf{D}$ as a scalar field. For the purposes of this exposition, a simplified notation $\mathbf{D}_{i+1/2}$, which can be taken as $\mathbf{D}^1_{i+1/2,j,k}$, $\mathbf{D}^2_{i,j+1/2,k}$ or $\mathbf{D}^3_{i,j,k+1/2}$ as needed, is used. First, the intercell flux is considered as the sum of the right- and left-going fluxes,

$$\mathbf{D}_{i+1/2} = \mathbf{D}^+_{i+1/2} + \mathbf{D}^-_{i+1/2}, \tag{3.19}$$

associated to positive and negative wave speeds, which are taken to be respectively left and right WENO reconstructed values. The third-order left reconstructed value for each component of $\mathbf{D}^+_{i+1/2}$ is found according to:

$$D^+_{i+1/2} = \sum_{j=0}^{1} \omega_j D^{+,(j)}_{i+1/2}, \tag{3.20}$$

where the candidate low-order stencils are,

$$D^{+,(j)}_{i+1/2} = \sum_{k=0}^{1} \gamma_{jk} D^+_{i-j+k}, \;\; j = 0,1, \tag{3.21}$$

and

$$\omega_j = \frac{c_j/(\beta_j+\epsilon)^2}{\sum_{k=0}^{1} c_k/(\beta_k+\epsilon)^2}, \;\; j = 0,1, \tag{3.22}$$

are the nonlinear weights. Values for c_j and γ_{jk} are presented in Table 3.1. ϵ is a small number taken to avoid division by zero. Smoothness coefficients β_i are given by

$$\beta_0 = \left(D^+_{i+1} - D^+_i\right)^2, \;\; \beta_1 = \left(D^+_{i-1} - D^+_i\right)^2. \tag{3.23}$$

A similar formulation is obtained for the right WENO reconstruction of $\mathbf{D}^-_{i+1/2}$ by mirroring the stencils around $i+1/2$. Finally, the cell centered positive and negative fluxes D^+_i are given by the

Lax-Friedrichs (LLF) splitting,

$$\mathbf{D}_i^{\pm} = \frac{1}{2}\left(\mathbf{D}_i \pm S_{max}\mathbf{U}_i\right), \tag{3.24}$$

where S_{max} is the maximum (in absolute value) characteristic speed (Eq. (2.50)) across the range of interest of $\mathbf{U}$ such that all the eigenvalues of $\partial\mathbf{D}_i^{\pm}/\partial\mathbf{U}_i$ are strictly positive and negative for $\mathbf{D}_i^{+}$ and $\mathbf{D}_i^{-}$ respectively. The LLF flux is simple and does not require the computation of characteristic equations. As a negative effect, this method introduces excess dissipation, whose effects can be minimized by increasing the order of the wall flux reconstruction.

Table 3.1: Coefficients of third-order WENO finite-difference method

i	c_i	γ_{i0}	γ_{i1}
0	2/3	1/2	1/2
1	1/3	-1/2	3/2

With respect to time-stepping, the integral in Eq. (3.17a) is approximated by the third-order total variation diminishing (TVD) Runge-Kutta method from [57],

$$\int_{t_n}^{\tilde{t}} \mathbf{H}\left(\mathbf{U}\right)\, dt \approx \Delta t \sum_{i=1}^{3} \omega_i \mathbf{H}\left(\mathbf{U}^n - \sum_{j=1}^{i} \beta_{ij}\mathbf{H}\left(\mathbf{U}^{(j-1)}\right)\right), \ \mathbf{U}^{(0)} = \mathbf{U}^n. \tag{3.25}$$

Coefficients for this method are shown in Table 3.4.

Table 3.2: Coefficients of third-order TVD Runge-Kutta method

i	ω_i	β_{i1}	β_{i2}
1	1/6	0	
2	1/6	1	
3	2/3	1/4	1/4

3.2.6 Inelastic update

The implicit evaluation of Eq. (3.17b) can prove to be computationally intensive if the strain rates are high enough such that the problem becomes stiff. In [8], it was shown that, given a particular choice of constitutive laws and inelastic models the problem could be reduced to the solution of two algebraic equations, in an approach that resembles a radial return algorithm. This procedure is described here given its importance as a key element within the code in reducing computation time.

A singular value decomposition of $\mathbf{F}^e$ is given by:

$$\mathbf{F}^e = \mathbf{g}^{e^{-1}} = \mathbf{U}\mathbf{K}^e\mathbf{W}, \tag{3.26}$$

where $\mathbf{U}$, $\mathbf{W}$ are orthogonal rotation matrices, and $\mathbf{K}^e = \mathrm{diag}(k^e)$ is the diagonal matrix of principal elastic stretches k_i^e, with $i = 1, 2, 3$. If the stretch tensor formulation is used, $\mathbf{W} = \mathbf{U}^T$ and k_i^e are, respectively, the eigenvectors and eigenvalues of $\mathbf{V}^e$. As a consequence of plasticity being modeled as independent of changes in volume, the density Jacobian $\det(\mathbf{K}^e)$, and the rotation matrices $\mathbf{U}$ and $\mathbf{W}$, remain constant. This way, given $\widetilde{\mathbf{F}}^e = \widetilde{\mathbf{U}}\widetilde{\mathbf{K}}^e\widetilde{\mathbf{W}}$, the updated elastic deformation tensor reads $\mathbf{F}^{e\,n+1} = \widetilde{\mathbf{U}}\mathbf{K}^{e\,n+1}\widetilde{\mathbf{W}}$ and the problem is reduced to solving for the increment in entropy and the updated principal stretches.

In order to being able to further reduce the complexity of the problem, a specific constitutive law is considered. Given an additive decomposition for $e = e_s + e_h$, e_s is expressed as a function of the invariants of the elastic Hencky's strain tensor $\mathbf{H^e}$,

$$\mathbf{H^e} = \frac{1}{2}\log\left(\mathbf{F^e}\mathbf{F^e}^T\right), \tag{3.27}$$

such that,

$$e_s = 2c_s(\rho)^2 I^2, \;\; I^2 = \left(I_1^{\mathbf{H^e}}\right)^2/3 - I_2^{\mathbf{H^e}}. \tag{3.28}$$

where $c_s(\rho) = \sqrt{\mu/\rho}$ is the shear wave speed. Note that $I_1^{\mathbf{H^e}} = \log(\rho/\rho_0)$ and $I = ||\mathbf{H^e}'||$. Derivation of the Cauchy stress for this particular equation of state using Eq. (2.33b) shows that:

$$\sigma = \left(\rho\frac{\partial e_h}{\partial I_1^{\mathbf{H^e}}} - \frac{2}{3}\mu I_1^{\mathbf{H^e}}\right) + 2\mu\mathbf{H^e}. \tag{3.29}$$

In consequence, the deviatoric stress σ' becomes linear with $\mathbf{H^e}'$, and Eq. (3.17b) can be reformulated in terms of the principal stretches as:

$$\mathbf{k^e}^{n+1} = \widetilde{\mathbf{k^e}} - \int_{\widetilde{t}}^{t_{n+1}} \frac{1}{\tau}\mathrm{diag}\left(\mathbf{h^e}'\mathbf{k^e}^T\right) dt, \tag{3.30}$$

where $\mathbf{h^e}' = \log(k^e) + \log(\rho/\rho_0)/3$ is the vector of principal Hencky's deviatoric stresses. From this last expression, it can be shown that,

$$\mathbf{h^e}'^{n+1} = \widetilde{\mathbf{h}^{e'}} - \int_{\widetilde{t}}^{t_{n+1}} \frac{1}{\tau}\mathbf{h}^{e'}\, dt, \tag{3.31a}$$

$$I^{n+1} = \widetilde{I} - \int_{\widetilde{t}}^{t_{n+1}} \frac{1}{\tau} I\, dt, \tag{3.31b}$$

from which,

$$\mathbf{h^e}'^{n+1} = \widetilde{\mathbf{h}^{e'}}\left(\frac{I^{n+1}}{\widetilde{I}}\right). \tag{3.32}$$

Known $\mathbf{h^e}'^{n+1}$ and I^{n+1}, the principal stretches are recovered as,

$$\mathbf{k^e}^{n+1} = \exp\left(\mathbf{h^e}'^{n+1} - \log(\widetilde{\rho}/\rho_0)/3\right). \tag{3.33}$$

In [9], it is shown that the increment in plastic entropy is given by:

$$\theta(\widetilde{\rho}) \exp\left(\frac{1}{c_v}(\widetilde{\varsigma} - \widetilde{\varsigma}^p)\right)\left(\exp\left(\frac{\varsigma^{p n+1}}{c_v}\right) - \exp\left(\frac{\widetilde{\varsigma}^p}{c_v}\right)\right) = -\frac{\widetilde{c_s}^2}{2}\left({I^{n+1}}^2 - \widetilde{I}^2\right) \tag{3.34}$$

where $\theta(\rho) = \partial e / \partial \exp(\frac{\varsigma}{c_v})$ and the shear wave velocity c_s is considered a function of ρ only (i.e., $\widetilde{c_s} = c_s\left(\widetilde{\rho}\right)$) . Under certain circumstances, a linearization of Eq. (2.46), such that:

$$\tau = \tau_0 \left(\frac{\sigma_0 f_H(\widetilde{\sigma_m}, \widetilde{\varsigma}) f_T(\widetilde{\rho}, \widetilde{\varsigma})}{\sigma_m}\right)^{n_1} = \tau_0 \left(\frac{\widetilde{\sigma_Y}}{\sigma_m}\right)^{n_1}. \tag{3.35}$$

is sufficient to accurately model the visco-plastic response of a material and allows the analytical determination of I^{n+1}. $\widetilde{\sigma_Y}$ can be considered the "instantaneous" yield stress for the particular state $\widetilde{\mathbf{U}}$. In the case of perfect plasticity, $\widetilde{\sigma_Y}$ reduces to simply σ_Y. Given that $I = \frac{||\sigma'||}{2\mu}$ and $\sigma_m = \sqrt{3}\mu I$, Eq. (3.31b) becomes:

$$\int_{\widetilde{I}}^{I^{n+1}} \frac{1}{I^{n_1+1}} dI = -\int_{\widetilde{t}}^{t_{n+1}} \frac{1}{\tau_0}\left(\frac{\sqrt{3}\mu}{\widetilde{\sigma_Y}}\right)^{n_1} dt, \tag{3.36}$$

which leads to the analytical result:

$$I^{n+1} = \left(\widetilde{I}^{-n_1} + \Delta t \frac{n_1}{\tau_0}\left(\frac{\sqrt{3}\mu}{\widetilde{\sigma_Y}}\right)^{n_1}\right)^{-1/n_1}, \tag{3.37}$$

representing the relaxation of a visco-elastic material. In the limit of immediate relaxation of stresses ($n_1 \to \infty$), Eq. 3.37 becomes discontinuous. If $\sigma_m < \widetilde{\sigma_Y}$, $I^{n+1} = \widetilde{I}$ and the material is in the elastic regime, otherwise

$$I^{n+1} = \frac{\widetilde{\sigma_Y}}{\sqrt{3}\mu}, \tag{3.38}$$

which is consistent with the classical theory of plasticity. If the equations of state used cannot be expressed in terms of the Hencky strain tensor invariants (3.28), an implicit algorithm can always be used for the computation of the principal stretches. In that case, robustness and computational cost of the algorithm become a concern.

3.3 Multi-material implementation

As mentioned in Section 3.1, the proposed approaches to the problem of multi-material interactions are varied and no agreement exists on which method produces better results. The adoption of a particular method rather depends on the characteristics of the problem to be solved and the properties that one would like to preserve. In the case of solid mechanics, a level-set implementation appears to be the most convenient since it allows the description of the sharp interfaces normally observed between elastic–plastic materials. However, level-set methods are generally non-conservative since the fluxes at one side and the other of a material interface are not matched exactly. Some conservative fixes have been proposed but are limited to particular types of problems [83]. As a result, acceptable mass conservation can only be achieved in well-posed problems and under extensive refinement of the computational domain. It is worth noting that, in the case of extreme temperature conditions, in which materials can melt and subsequently behave like a fluid, the conservative volume-of-fluid (VOF) approach may look more appealing since it allows modeling of phenomena normally appreciated in fluids, such as mixing. Given the general scope of the problems encountered in this application, the level-set implementation of [8] is closely followed, with some modifications targeted at improving the overall behavior of the method.

3.3.1 Level-set advection and reinitialization

For each material M_l in the computational domain D, a level-set function ϕ^l is defined at time $t = 0$ to be a signed distance to the closest material boundary in the initial configuration (i.e., interface, free surface) such that a simple evaluation of its sign allows one to determine whether a point $\mathbf{x}$ away from the interface belongs to the material. The criterion normally assumed is $\phi^l(x_i, t) > 0, \forall \mathbf{x} \in M_l$ with the condition that two level-set functions cannot be positive at the same point. Level-set functions satisfy the Eikonal condition

$$|\nabla \phi^l| = 1, \tag{3.39}$$

and easily provide geometric information, such as the local unit normals,

$$n^l = \frac{\nabla \phi^l}{|\nabla \phi^l|} = \nabla \phi^l, \tag{3.40}$$

as long as they remain signed distance functions.

The evolution in time of a level-set function is determined by the solution of the advection equation:

$$\frac{\partial \phi^l}{\partial t} + v_i \frac{\partial \phi^l}{\partial x_i} = 0, \tag{3.41}$$

where $\mathbf{v}$ is a given velocity field. For each level set, Eq. (3.41) is discretized with values at the cell centers (i, j, k) and solved concurrently in time with the equations of motion, using the third-order TVD Runge-Kutta method described in Eq. (3.25). High-order spatial accuracy is achieved by the application of a fifth-order WENO reconstruction method [99] for $\frac{\partial \phi^l}{\partial x_i}$. The discrete velocity field $\mathbf{v}_{i,j,k}$ is directly obtained from the state vector $\mathbf{U}_{i,j,k}$ of the material M_l for which $\phi^l_{i,j,k} > 0$. In the case of all level-sets being negative at a particular cell center, the state vector resulting from the application of the M-GFM method described in the next paragraph is employed. The same velocity field is used for all ϕ^l, thus avoiding the artificial formation of gaps or superpositions among different level-sets. This is different from the approach in [8], which uses a velocity field interpolated from the solution of a Riemann problem at the material interface which is not the same for all level-set functions and thus leads to the formation of gaps in some extreme cases, unless a corrective algorithm is enforced.

Given that the velocity field $\mathbf{v}$ describes particle paths, it will only accurately describe the motion of a particular level set at material boundaries (i.e., where $\phi^l_{i,j,k} = 0$). In addition, numerical inaccuracies may lead to further deviation of the level-set functions from satisfying Eq. (3.39) as time progresses. Since the ghost-fluid method relies extensively on an accurate computation of normals and distances to material boundaries, the Eikonal condition is reestablished at the end of each sub-step of the Runge-Kutta method (3.25) using Min's approach [79] for solving to equilibrium the Hamilton-Jacobi equation,

$$\frac{\partial \phi^l}{\partial \tau} + \operatorname{sgn}\left(\phi^l\right)\left(|\nabla \phi^l| - 1\right) = 0. \tag{3.42}$$

in pseudo-time. This method approximates the second term in Eq. (3.42) considering a discretization subcell fix for the level-set values in cells which are adjacent to the material boundary such that the interpolated position for which $\phi^l(\mathbf{x}, \tau = 0) = 0$ does not drift for $\tau > 0$. Numerical tests show that this method produces better results for applications described in upcoming chapters than the original method in [8], where the level-set function in the inner band adjacent to the boundary was kept fixed. For instance, the original method tends to produce numerical Kelvin-Helmholtz instability in planar geometry Richtmyer-Meshkov interfaces after the passage of a strong shock.

3.3.2 Boundary conditions at material interfaces and free surfaces

The modified ghost fluid method (M-GFM) of Liu et al. [65] is used to set boundary conditions at material interfaces. Given a material M^l, the aim of this approach is to populate a subset of cells, i.e., ghost cells, $B(s) = \{C_{i,j,k} : \phi^l_{i,j,k} < 0 \bigcup \phi^l_{i,j,k} > s|\Delta x|\}$, where s is related to the numerical stencil, with state variables such that the interior cells $\{C_{i,j,k} : x_{i,j,k} \in M^l\}$ reflect the desired boundary conditions. M-GFM bases the algorithm for setting the state of the ghost cells on the solution of a Riemann problem whose initial conditions contain information on the state at both sides of the interface. M-GFM was developed to overcome the difficulties that the original GFM method of Fedkiw et al. [32], which sets the state of a particular ghost cell $C_{i,j,k}$ using the normal velocity and stress state from the actual state in $C_{i,j,k}$, i.e., the state for material M_m such that $\phi^m_{i,j,k} > 0$, and the tangential velocity and entropy extrapolated from the interior cells of M^l, encountered when it was applied to problems involving interactions of strong shocks with interfaces, such as Richtmyer–Meshkov flow.

In this particular implementation of M-GFM, an inner layer of cells $A \in B$ defined as $A = B(1)$ adjacent to the interface are prescribed states resulting from solving multi-material one-dimensional

Riemann problems defined locally and directed along the normal to the interface in the approximate way described in the next paragraph. For a given ghost cell $C_{i,j,k}$ in the inner band, the initial states of such Riemann problem consist of an extrapolated state $\widetilde{\mathbf{U}}$ and the state vector $\mathbf{U}_{i,j,k}$ of the material M_m such that $\phi^m_{i,j,k} > 0$. In the case of material–vacuum interactions, a second state is not needed. State variables are rotated onto a local orthogonal coordinate system defined by the interface normal $\mathbf{n}^l$. The extrapolated state $\widetilde{\mathbf{U}}$ is given by interpolation of the interior cells of material M^l to give $\widetilde{\mathbf{U}} = \mathbf{U}(\widetilde{\mathbf{x}})$, where $\widetilde{\mathbf{x}}$ is the closest boundary point to the ghost cell $C_{i,j,k}$ and can by determined as

$$\widetilde{\mathbf{x}} = \mathbf{x}_{i,j,k} + d\mathbf{n}^l_{i,j,k}, \tag{3.43}$$

where $d = |\phi^l_{i,j,k}|$ is the distance to the interface, provided that $\phi^l_{i,j,k}$ remains a signed distance function. In the case of this assumption being not entirely correct (i.e., reinitialization of the level-set was not effective), $\widetilde{\mathbf{x}}$ is determined using the trajectory tracing method of [117]. Finally, all other cells $C_{i,j,k} \in (B \setminus A)$ take an extrapolated state from those in A.

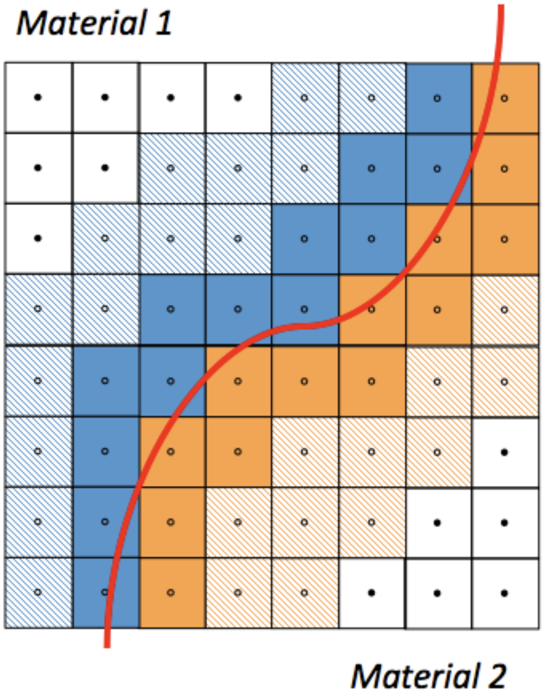

Figure 3.3: Diagram of ghost cells around a two-material interface. Orange-flagged cells represent ghost cells for material 1, with solid color and diagonal lines marking the inner band, populated by the solution of a Riemann problem, and the outer region, populated by extrapolation from inner band, respectively. The same pattern is used for the ghost cells of material 2, colored in blue.

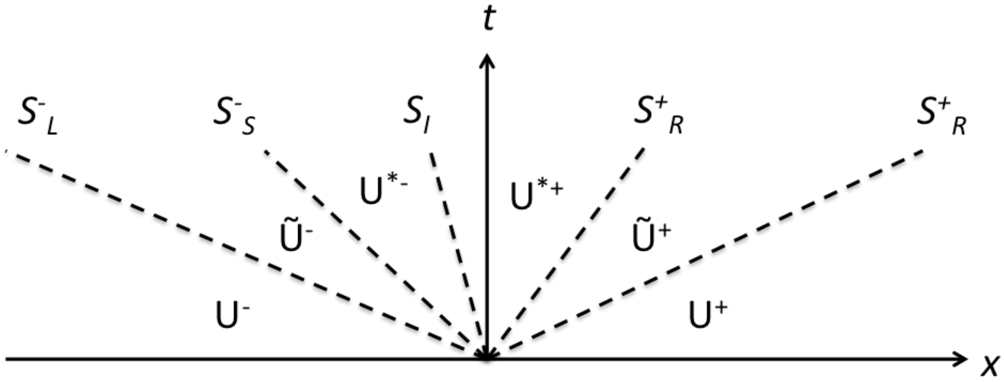

Figure 3.4: Waves and states in the approximate HLLD multi-material Riemann problem

3.3.3 HLLD Multi-material Riemann solver

The central idea in the Harten, Lax and van Leer (HLL) approximate Riemann solver [48], from which the HLLD method is a derivative, is to assume a wave configuration for the solution that consists of two waves separating three constant states. Assuming that the wave speeds are given by some algorithm, application of the integral form of the conservation laws gives a closed-form, approximate expression for the central state. This method was then modified to become the HLL-contact (HLLC) scheme [109], which handles four states, the two central ones being separated by a contact discontinuity. This method, although appropriate for fluids since the three waves separating the states can be assimilated to the three families of characteristics $(u-a, u, u+a)$, cannot reflect the fact that, in an elastic solid, additional families of characteristics defined by the shear wave speeds exist. The same problem is found in the field of magnetohydrodynamics [80], where Alfvén waves travel more slowly than longitudinal compression waves.

The HLLD approach assumes the existence of a number of slow waves between the fastest waves in each direction and the contact discontinuity. Here, the two-dimensional version is described, in which only one slow wave is placed between the fast wave and the interface. The core assumption for this method is that jumps in density and normal stress can occur across fast waves, but not across slow waves. Along the interface, normal velocity and stress are continuous. The third and fourth interface conditions depend on the modeling of friction between materials. For the case of free-slip, the tangential stresses are set to zero, while for no-slip, continuity of tangential velocities and stresses is enforced.

As shown in Figure 3.4 for each material $-,+$, the fastest (longitudinal) waves $S_L^{\pm}$ separates the states $\mathbf{U}^{\pm}$ and $\widetilde{\mathbf{U}}^{\pm}$. The slow shear waves in between $\widetilde{\mathbf{U}}^{\pm}$ and $\mathbf{U}^{*\pm}$ are denoted $S_S^{\pm}$. Across these discontinuities, the following relations are satisfied:

$$S_L^{\pm}(\mathbf{U} \pm -\widetilde{\mathbf{U}}^{\pm}) = \mathbf{D}\left(\mathbf{U}^{\pm}\right) - \mathbf{D}(\widetilde{\mathbf{U}}^{\pm}), \tag{3.44a}$$

$$S_S^{\pm}(\widetilde{\mathbf{U}}^{\pm} - \mathbf{U}^{*\pm}) = \mathbf{D}(\widetilde{\mathbf{U}}^{\pm}) - \mathbf{D}(\mathbf{U}^{*\pm}), \tag{3.44b}$$

where $\mathbf{D}$ is the appropriate flux vector for the formulation being used as described in Section 3.2. Finally, S_I is the interface wave speed. In this paragraph, we assume that all wave speeds are known. Methods for wavespeed estimation are given later. Equation (3.44a) can be solved for the set of primitive variables $\left(\widetilde{\rho}^{\pm}, \widetilde{\mathbf{u}}^{\pm}, \widetilde{\rho\mathbf{F}}^{\pm}, \widetilde{\mathbf{g}}^{\pm}, \widetilde{E}^{\pm}\right)$ without knowing the specific boundary conditions at the interface when the simplifications assumed in this method are considered. For each material i, the $\widetilde{\mathbf{U}}$ state can be constructed from,

$$\widetilde{u}_1^{\pm} = S_I, \tag{3.45a}$$

$$\widetilde{u}_{2,3}^{\pm} = u_{2,3}^{\pm}, \tag{3.45b}$$

$$\widetilde{\rho}^{\pm} = \rho^{\pm}\frac{S_L^{\pm} - u_1^{\pm}}{S_L^{\pm} - S_I}, \tag{3.45c}$$

$$\widetilde{E}^{\pm} = E^{\pm} + \left(S_I - u_1^{\pm}\right)\left(S_I - \frac{\sigma_{11}^{\pm}}{\rho^{\pm}\left(S_L^{\pm} - u_1^{\pm}\right)}\right), \tag{3.45d}$$

$$\widetilde{\rho F_{1J}}^{\pm} = \left(\rho F_{1J}\right)^{\pm}, \tag{3.45e}$$

$$\widetilde{\rho F_{2J}}^{\pm} = \left(\rho F_{2J}\right)^{\pm}\frac{S_L^{\pm} - u_1^{\pm}}{S_L^{\pm} - S_I}, \tag{3.45f}$$

$$\widetilde{\rho F_{3J}}^{\pm} = \left(\rho F_{3J}\right)^{\pm}\frac{S_L^{\pm} - u_1^{\pm}}{S_L^{\pm} - S_I}, \tag{3.45g}$$

$$\widetilde{g}_{J1}^{\pm} = g_{J1}^{\pm}\frac{S_L^{\pm} - u_1^{\pm}}{S_L^{\pm} - S_I}, \tag{3.45h}$$

$$\widetilde{g}_{J2}^{\pm} = g_{J2}^{\pm}, \tag{3.45i}$$

$$\widetilde{g}_{J3}^{\pm} = g_{J3}^{\pm}, \tag{3.45j}$$

where $J = 1, 2, 3$ and the expressions for $\mathbf{F}$ and $\mathbf{g}$ can be used for the elastic, plastic or total tensors depending on the formulation used.

In order to determine the $\mathbf{U}^{*\pm}$ states, Eq. (3.44b) must be solved taking into account the desired interface boundary conditions. For a free-slip, solid–fluid, or solid–vacuum discontinuity, the following expressions are obtained,

$$u^{*\pm}_2 = u_2^{\pm} + \frac{\sigma_{12}^{\pm}}{\widetilde{\rho}^{\pm}(S_S^{\pm} - S_I)}, \tag{3.46a}$$

$$u^{*\pm}_3 = u_3^{\pm} + \frac{\sigma_{13}^{\pm}}{\widetilde{\rho}^{\pm}(S_S^{\pm} - S_I)}, \tag{3.46b}$$

$$E^{*\pm} = \widetilde{E}^{\pm} + \frac{\sigma_{12}^{\pm}u_2^{\pm} + \sigma_{13}^{\pm}u_3^{\pm}}{\widetilde{\rho}^{\pm}(S_S^{\pm} - S_I)}. \tag{3.46c}$$

And in the case of no-slip boundary conditions,

$$u^{*-}_{2} = u^{*+}_{2} = \frac{\sigma_{12}^{-} - \sigma_{12}^{+} + \widetilde{\rho}^{-}(S_S^{-} - S_I)u_2^{-} - \widetilde{\rho}^{+}(S_S^{+} - S_I)u_2^{+}}{\widetilde{\rho}^{-}(S_S^{-} - S_I) - \widetilde{\rho}^{+}(S_S^{+} - S_I)}, \tag{3.47a}$$

$$u^{*-}_{3} = u^{*+}_{3} = \frac{\sigma_{13}^{-} - \sigma_{13}^{+} + \widetilde{\rho}^{-}(S_S^{-} - S_I)u_3^{-} - \widetilde{\rho}^{+}(S_S^{+} - S_I)u_3^{+}}{\widetilde{\rho}^{-}(S_S^{-} - S_I) - \widetilde{\rho}^{+}(S_S^{+} - S_I)}, \tag{3.47b}$$

$$\begin{aligned} E^{*\pm} &= \widetilde{E}^{\pm} + \left(u^{*\pm}_{2} - u_2^{\pm}\right)\left(u^{*\pm}_{2} - \frac{\sigma_{12}^{\pm}}{\widetilde{\rho}^{\pm}\left(S_S^{\pm} - S_I\right)}\right) + \ldots \\ &+ \left(u^{*\pm}_{3} - u_3^{\pm}\right)\left(u^{*\pm}_{3} - \frac{\sigma_{13}^{\pm}}{\widetilde{\rho}^{\pm}\left(S_S^{\pm} - S_I\right)}\right), \end{aligned} \tag{3.47c}$$

The remainder of variables can be expressed in the same way regardless of the interface conditions used:

$$u^{*\pm}_{1} = S_I, \tag{3.48a}$$

$$\rho^{*\pm} = \widetilde{\rho}^{\pm}, \tag{3.48b}$$

$$(\rho F_{1J})^{*\pm} = (\rho F_{1J})^{\pm}, \tag{3.48c}$$

$$(\rho F_{2J})^{*\pm} = \widetilde{\rho F_{2J}}^{\pm} + (\rho F_{1J})^{\pm}\frac{u_2^{\pm} - u^{*\pm}_{2}}{S_S^{\pm} - S_I}, \tag{3.48d}$$

$$(\rho F_{3J})^{*\pm} = \widetilde{\rho F_{3J}}^{\pm} + (\rho F_{1J})^{\pm}\frac{u_3^{\pm} - u^{*\pm}_{3}}{S_S^{\pm} - S_I}, \tag{3.48e}$$

$$g_{J1}^{*\pm} = \widetilde{g}_{J1}^{\pm} - \frac{g_{J2}^{\pm}(u_2^{\pm} - u^{*\pm}_{2}) - g_{J3}^{\pm}(u_3^{\pm} - u^{*\pm}_{3})}{S_S^{\pm} - S_I}, \tag{3.48f}$$

$$g_{J2}^{*\pm} = g_{J2}^{\pm}, \tag{3.48g}$$

$$g_{J3}^{*\pm} = g_{J3}^{\pm}, \tag{3.48h}$$

where $\mathbf{g}$ and $\mathbf{F}$ can be elastic or total deformations depending on the formulation used. In the case of plastic deformations, $(\rho\mathbf{F}^p)^* = \widetilde{\rho\mathbf{F}^p}$, since this yields $\mathbf{F}^{p*} = \mathbf{F}^p$. Some simplifications exist for the case of solid–fluid interfaces. If material i is a compressible fluid, the slow waves are neglected and only the first set of equations (3.45) applies, with $\sigma_{11}^{\pm} = -p$, where p is the pressure and $\sigma_{12}^{\pm} = \sigma_{13}^{\pm} = 0$. The presented scheme reduces in this case to the HLLC method.

A more accurate solution to the Riemann problem can be obtained by using the $\mathbf{U}^{*\pm}$ states as the new initial values in a multiple-pass algorithm. In most applications, three to four iterations are enough to achieve convergence in the solution.

3.3.3.1 Wave speed estimation

Since the HLL solver was developed, multiple ideas for estimating the velocity of the fastest waves have been proposed (see Chapter 10 in [108]). The fact that this solver deals with two materials that can have very different properties makes the task of obtaining a robust estimate even more challenging. The method used in this algorithm uses information from the original states to obtain the left and right fastest wave speeds such that,

$$S_L^- = \min\left(u_1^- - c_l^-, u_1^+ - c_{lg}^+\right), \tag{3.49a}$$

$$S_L^+ = \max\left(u_1^+ + c_l^+, u_1^- + c_{lg}^-\right), \tag{3.49b}$$

where $c_l^\pm = \max\left(\sqrt{\omega_k}\right)$, with $k = 1, 2, 3$, is obtained from the square root of the largest eigenvalue of the acoustic tensor $\mathbf{\Omega}(\mathbf{e}_1)$ (see Eq. (2.49)) given by the state $\mathbf{U}^\pm$. $c_{lg}^\pm$ is computed in the same way from an "artificial" state $\mathbf{U}_g^\pm$, such that,

$$\mathbf{U}_g^\pm = \mathbf{U}_g^\pm\left(\mathbf{u}^\pm, \sigma_{ij}^\mp, \varsigma^\pm\right). \tag{3.50}$$

The interface wave velocity is constructed in such a way that enforces continuity of normal stresses across the material interface. Extracting the relation associated to linear normal momentum from Eq. (3.44a),

$$S_L^\pm \widetilde{\rho}^\pm S_I - \widetilde{\rho}^\pm S_I^2 - \widetilde{\sigma}_{11}^\pm = S_L^\pm \rho^\pm u_1^\pm - \rho^\pm\left(u_1^\pm\right)^2 - \sigma_{11}^\pm, \tag{3.51}$$

and equating the normal stresses at the tilde state (which are equal to the normal stresses at the interface considering the simplifications adopted in the method) for each material, the following relation for S_I is found,

$$S_I = \frac{\sigma_{11}^- - \sigma_{11}^+ + \rho^+(S_L^- - u_1^-)u_1^- - \rho^+(S_L^+ - u_1^+)u_1^+}{\rho^-(S_L^- - u_1^-) - \rho^+(S_L^+ - u_1^+)}. \tag{3.52}$$

In the particular case of a solid–vacuum interface, this expression is greatly simplified to:

$$S_I = u_1 + \frac{\sigma_{11}}{\rho(S_L - u_1)}. \tag{3.53}$$

Since the slow wave speeds are not used in the first set of equations (3.45), they can be estimated once the states $\widetilde{\mathbf{U}}^\pm$ are known. A simple choice, inspired by the approach adopted in [80], is:

$$S_S^\pm = \widetilde{u}_1^\pm \pm \widetilde{c_s}^\pm, \tag{3.54}$$

where $\widetilde{c_s}^\pm = \min\left(\sqrt{\omega_\pm}\right)$ is the slowest acoustic speed given by the eigenvalues of the acoustic tensor in the normal direction $\mathbf{\Omega}(\mathbf{e}_1)$ associated to the state $\widetilde{\mathbf{U}}^{\pm}$.

3.3.3.2 Numerical examples

To conclude the analysis of the newly developed HLLD multi-material Riemann solver, two different cases of interest for two-dimensional elastic solid–gas interfaces are considered and compared with results obtained by the characteristic-based Riemann solver in [8] and an exact multi-material Riemann solver which uses an iterative process involving multiple Newton–Raphson evaluations. This last solver cannot be practically implemented in the numerical code given the high computational cost of the iterations and its reliance on an accurate initial guess.

The elastic solid employed is defined by the Godunov-Romenski equation of state [30, 107],

$$
\begin{aligned}
e &= e_s + e_h, && (3.55a)\\
e_s &= 2c_s(\rho)^2 I^2, \;\; I^2 = \left(I_1^{\mathbf{H}}\right)^2/3 - I_2^{\mathbf{H}}, && (3.55b)\\
e_h &= \frac{K}{2\alpha^2}\left(\left(\frac{\rho}{\rho_0}\right)^{\alpha} - 1\right)^2 + c_v T_0 \left(\frac{\rho}{\rho_0}\right)^{\gamma_s}\left(\exp\left(\frac{\varsigma}{c_v}\right) - 1\right), && (3.55c)
\end{aligned}
$$

with $c_s(\rho) = \frac{\mu}{\rho} = \frac{\mu_0}{\rho_0}\left(\frac{\rho}{\rho_0}\right)^{\beta}$, the Hencky strain tensor $\mathbf{H} = \frac{1}{2}\log\left(\mathbf{F}\mathbf{F}^T\right)$ and typical parameters for copper, $\rho_0 = 8.93\,\mathrm{g/cm^3}$, $K = 15.28\cdot 10^6\,\mathrm{m^2/s^2}$, $c_v = 3.9\cdot 10^2\,\mathrm{J/kgK}$, $T_0 = 300\,\mathrm{K}$, $\mu_0 = 39.38\,\mathrm{GPa}$, $\alpha = 1$, $\beta = 3$, $\gamma_s = 2$. The perfect gas is defined by its heat capacity ratio $\gamma_g = 5/3$.

The interface is collocated at $x = 0$ at $t = 0$ with the solid and gas materials occupying the right and left half-plane and being denoted by s and g, respectively. For the first initial value problem, a purely hydrostatic state is prescribed for the solid. The solution of the Riemann problem with initial conditions,

$$
\begin{aligned}
&\mathbf{F}_s = \begin{pmatrix} 0.8 & 0 & 0\\ 0 & 0.8 & 0\\ 0 & 0 & 0.8\end{pmatrix}, \qquad \varsigma_s/c_v = 0.5, \qquad \mathbf{u}_g = \begin{pmatrix} -10\\ 0\end{pmatrix}\,\mathrm{km/s},\\
&\rho_g = 0.1\,\mathrm{kg/m^3}, \qquad p_g = 0.05\,\mathrm{GPa}, \qquad \mathbf{u}_g = \begin{pmatrix} 0\\ 0\end{pmatrix}\,\mathrm{km/s},
\end{aligned}
\tag{3.56}
$$

involves a longitudinal expansion in the solid and a shock propagating through the fluid and represents a typical Riemann problem that originates from a one-dimensional shock–interface interaction. Since the free-slip boundary condition is already satisfied in the initial state and the expansion does not modify the tangential stresses when the tangential velocity is zero, the problem is purely one-dimensional and shear waves do not appear. Table 3.3 shows results for the adjacent states to the interface for: a) exact Riemann solver, b) HLLD solver, c) HLLD solver with multiple passes in which the $\mathbf{U}^*$ states are used as initial conditions for the following pass, d) characteristic-based

Table 3.3: Comparison between results of approximate Riemann solvers and exact solution for a one-dimensional solid–gas interface Riemann problem involving an expansion wave in the solid and a compression shock in the gas. The solid follows the constitutive law (3.58) and the gas is considered perfectly caloric. The approximate methods considered are: a) HLLD single-pass, b) HLLD with multiple passes, c) characteristic-based single-pass, d) characteristic-based with multiple passes.

Variable	Initial condition	Exact	HLLD		characteristic	
			single-pass	multi-pass	single-pass	multi-passes
			SOLID			
$\rho\,(\mathrm{g/cm^3})$	17.441	10.423	15.412	10.767	14.779	9.844
F_{11}	0.8	1.339	0.905	1.296	0.944	1.417
$\sigma_{11}\,(\mathrm{GPa})$	-506.271	-23.750	-255.065	-28.375	-201.883	-12.487
$\sigma_{22}\,(\mathrm{GPa})$	-506.271	-97.081	-341.503	-108.660	-299.757	-79.011
$e\,(\mathrm{km^2/s^2})$	7.230	1.556	5.248	1.633	3.851	1.461
$u_1\,(\mathrm{km/s})$	-10.000	-13.893	-11.918	-14.873	-12.284	-15.233
			FLUID			
$\rho\,(\mathrm{g/cm^3})$	0.1	0.397	0.409	0.506	1.445	7.479
$p\,(\mathrm{GPa})$	0.05	23.750	19.676	28.375	1.171	12.487
$u_1\,(\mathrm{km/s})$	0	-13.893	-11.918	-14.873	-12.284	-15.233
			WAVESPEEDS			
$S_L^s\,(\mathrm{km/s})$		-9.653	4.568	-8.982	2.678	-11.442
$S_L^g\,(\mathrm{km/s})$		-18.510	-15.774	-26.826	-0.913	-16.901

solver, and e) characteristic-based with multiple passes. Wave speeds are also provided. The intermediate state $\widetilde{\mathbf{U}_s}$ is not shown since it corresponds identically to $\mathbf{U}_s^*$ where shear waves are not present. The first conclusion extracted from the analysis of Table 3.3 is that the multiple-pass algorithm is advantageous compared to the single-pass. In particular, the result of the expansion is underestimated by the latter. In addition, multiple-pass algorithms converge towards satisfying the normal stress continuity condition across the interface, which cannot be directly enforced with just one pass of the algorithm. Finally, the HLLD solver gives a result which is closer to the exact, especially for the values of densities, stresses, and velocities at each side of the interface.

The second example considers an initial solid state in which tangential stresses are present. A shear wave is then required in order to adapt the stress state to the free-slip interface conditions. The initial configuration,

$$\begin{gathered}\mathbf{F}_s = \begin{pmatrix} 0.8 & -0.1 & 0 \\ -0.1 & 0.9 & 0 \\ 0 & 0 & 0.9 \end{pmatrix}, \qquad \varsigma_s/c_v = 0.5, \qquad \mathbf{u}_g = \begin{pmatrix} -10 \\ 1 \end{pmatrix}\ \mathrm{km/s}, \\ \rho_g = 0.1\,\mathrm{kg/m^3}, \qquad\qquad p_g = 0.05\,\mathrm{GPa}, \qquad \mathbf{u}_g = \begin{pmatrix} 0 \\ 0 \end{pmatrix}\ \mathrm{km/s},\end{gathered} \tag{3.57}$$

produces a Riemann problem in which a longitudinal expansion followed by a shear shock occurs in the solid and a pressure shock develops in the fluid and mimics the start-up process of a Richtmyer-

Table 3.4: Comparison between results of approximate Riemann solvers and exact solution for a solid–gas interface Riemann problem involving an expansion wave and a shear shock in the solid and a compression shock in the gas. The solid follows the constitutive law (3.58) and the gas is considered perfectly caloric. The approximate methods considered are: a) HLLD single-pass, b) HLLD with multiple passes, c) characteristic-based single-pass, d) characteristic-based with multiple passes.

Variable	Initial condition	Exact	HLLD		characteristic	
			single-pass	multi-pass	single-pass	multi-pass
			SOLID			
$\rho\,(\mathrm{g/cm^3})$	13.975	10.339	12.919	10.498	12.211	9.754
F_{11}	0.800	1.081	0.865	1.065	0.916	1.146
F_{12}	-0.100	-0.135	-0.108	-0.133	-0.114	-0.143
F_{21}	-0.100	0.109	0.252	0.109	-0.009	0.109
F_{22}	0.900	0.874	0.856	0.874	0.889	0.874
F_{33}	0.900	0.900	0.900	0.900	0.900	0.900
g_{11}	1.268	0.911	1.115	0.925	1.094	0.859
g_{12}	0.141	0.141	0.141	0.141	0.141	0.141
g_{21}	0.141	-0.114	-0.328	-0.116	0.011	-0.107
g_{22}	1.127	1.127	1.127	1.127	1.127	1.127
g_{33}	1.111	1.111	1.111	1.111	1.111	1.111
σ_{11} (GPa)	-259.168	-19.852	-145.911	-21.871	-95.872	-4.972
σ_{12} (GPa)	-55.9012	0.000	0.28922	0.000	-0.18507	0.000
σ_{22} (GPa)	-203.266	-47.939	-135.957	-51.625	-106.298	-35.387
σ_{33} (GPa)	-200.093	-44.863	-132.759	-48.355	-101.521	-32.950
$e\,(\mathrm{km^2/s^2})$	3.265	0.483	2.458	0.509	1.283	0.417
u_1 (km/s)	-10.000	-12.363	-11.191	-12.881	-11.669	-13.259
u_2 (km/s)	1.000	0.145	-0.326	0.162	0.417	-0.057
			FLUID			
$\rho\,(\mathrm{g/cm^3})$	0.1	0.396	0.402	0.465	1.378	3.780
p (GPa)	0.05	19.852	17.101	21.871	1.115	4.972
u_1 (km/s)	0.000	-12.363	-11.191	-12.881	-11.669	-13.259
u_2 (km/s)	0.000	0.000	0.000	0.000	0.000	0.000
			WAVESPEEDS			
S_L^s (km/s)		-7.162	4.568	-7.238	0.850	-8.936
S_S^s (km/s)		-9.654	-7.928	-9.936	-6.459	-10.530
S_L^g (km/s)		-16.518	-14.8913	-22.902	-0.913	-14.740

Meshkov flow in which the shock and the interface are not aligned, hence resulting in tangential stresses in the direction normal to the interface. Table 3.4 shows results for the adjacent states to the interface in fluid and gas in the same fashion as the previous example. The intermediate state $\widetilde{\mathbf{U}_s}$ in the solid is not shown since the multiple-pass algorithms do not offer a solution for it and the only output of the multi-material Riemann solver needed for its implementation within the M-GFM method are the $\mathbf{U}^*$ states. Results are in agreement with the previous example (Table 3.3) with respect to differences between the multi-pass and single-pass algorithms. Moreover, the zero tangential stress condition is not fully enforced with just one pass. As in the one-dimensional case, HLLD is closer to the exact solution, especially for the normal stress across the interface which is severely underestimated by the characteristic solver, fluid and gas densities, and normal velocity.

In conclusion, the HLLD approximate Riemann solver offers results that are closer to the exact result when compared to the characteristic-based solver for two cases of interest that mimic strong-shock–interface interactions. A possible explanation for this is that the linearized-characteristic solver considers infinitely weak shocks and therefore does not handle well the state in the gas, which is processed by a shock wave of $M \approx 18$. The HLLD solver in contrast considers all the waves (shocks or expansions) as discontinuities, giving a better result in the fluid. On the other hand, expansion waves in the solid are better represented by the linearized solver and as a result, in the single-pass scheme, the results in the solid are closer to the exact solution for this method. However, the implementation in multiple passes makes the HLLD a better scheme overall. It is worth noting that, when these solvers are included in the proposed numerical scheme, they will not be submitted in general to such strong-shock–interface interactions, as shocks are captured in a few computational cells.

3.3.4 Effect of the Cartesian grid on the level-set method

The effect of a discretized domain on the accuracy of the level-set method is investigated in these last two subsections devoted to the multi-material implementation. The shell collapse test proposed in [8] is replicated here in order to examine the deviations from radial symmetry that appear in the level-set method when a rectangular grid is employed. This test is of paramount importance to the study of the converging Richtmyer–Meshkov instability in converging geometries (Chapter 6) as it examines the evolution of numerically induced perturbations under mesh refinement. The next subsection will focus on the impact of the level-set method and AMR on mass conservation.

The initial conditions specified in [8] are followed. A radially symmetric shell is described by its inner and outer radius, respectively, $R_{i0} = 0.8\,\mathrm{cm}$ and $R_{o0} = 1.0\,\mathrm{cm}$. The motion is started by a radial velocity field $u_{r0} = U_0 R_{i0}/r$, where $r = \sqrt{x_1^2 + x_2^2}$. The shell is unstressed at $t = 0$ ($g_{Ij} = \delta_{Ij}$ and $\varsigma = 0$) and made of aluminum, modeled here as an elastic–perfectly plastic material with $\sigma_Y = 0.2976\mathrm{GPa}$ and equation of state:

$$e = e_s(\mathbf{H}^e) + e_h(\rho, \varsigma), \tag{3.58a}$$

$$e_s = 2c_s(\rho)^2 I^2, \;\; I^2 = \left(I_1^{\mathbf{H}^e}\right)^2/3 - I_2^{\mathbf{H}^e}, \tag{3.58b}$$

$$e_h = \frac{K}{2\alpha^2}\left(\left(\frac{\rho}{\rho_0}\right)^{\alpha} - 1\right)^2 + c_v T_0 \theta(\rho)\left(\exp\left(\frac{\varsigma}{c_v}\right) - 1\right) \tag{3.58c}$$

$$\theta(\rho) = \left(\frac{\rho}{\rho_0}\right)^{\Gamma_\infty} \exp\left[3\Gamma_1\left(1 - \left(\frac{\rho}{\rho_0}\right)^{-1/3}\right) + \frac{\Gamma_2}{\gamma}\left(1 - \left(\frac{\rho}{\rho_0}\right)^{-\gamma}\right)\right]. \tag{3.58d}$$

This constitutive law is an extension of (3.58) where the density contribution to the thermal part of the hydrostatic energy is modeled by the relative Debye temperature determined through the analytic Grüneisen function found in [22]. Parameters for aluminum are: $\rho_0 = 2.703\,\mathrm{g/cm^3}$, $K = 28.27 \cdot 10^6\,\mathrm{m^2/s^2}$, $c_v = 9.0 \cdot 10^2\,\mathrm{J/kgK}$, $T_0 = 300\,\mathrm{K}$, $\mu_0 = 26.7\,\mathrm{GPa}$, $\alpha = 0.627$, $\Gamma_\infty = 1/2$, $\Gamma_1 = 3/5$, $\Gamma_2 = 3.2$, and $\gamma = 7/2$.

With this setup, the initial kinetic energy in the solid is gradually reduced by plastic dissipation and converted in internal energy until the converging motion is stopped. Following the analytical solution in [56] for an incompressible and perfectly plastic material, a shell with an initial radial velocity $U_0 = 0.427\,\mathrm{km/s}$ and the initial conditions and material parameters indicated above comes to rest when the inner radius is $R_{if} = 0.3$.

In order to analyze the effect of the Cartesian grid on the radial symmetry of the material boundaries, a square two-dimensional computational domain with dimensions $\{0, 1.1\} \times \{0, 1.1\}\,\mathrm{cm}$ (containing one quadrant of the shell) is defined. Grid resolution is increased by factors of 2 from 55×55 to 1760×1760 cells. At each time t, the average position of the material boundaries is computed as

$$\overline{R_j}(t) = \frac{1}{N}\sum_{n=1}^{N} R_{j_n}(t), \tag{3.59}$$

where $j = i, o$ for the inner and outer boundaries respectively, R_{j_n} identifies the position of the material boundary at a particular ray $\theta_n = \arctan(x_2/x_1) = C_n$, and N is the total number of rays. The error in radial symmetry as a function of time is measured by:

$$L_2 - \mathrm{error}_j(t, \overline{R}_j(t)) = \frac{1}{\overline{R}_j(t)}\sqrt{\frac{1}{N}\sum_{n=1}^{N}\left(R_{j_n}(t) - \overline{R}_j(t)\right)^2}. \tag{3.60}$$

Figure 3.5 shows the evolution of this quantity as a function of time for the different resolutions examined. First-order convergence is achieved as the number of cells is progressively increased, with low-resolutions exhibiting a fractional convergence rate. This suggests that for avoiding large errors in maintaining radial symmetry, simulations need to be run with a considerable number of cells. It is important to remark that the errors for the inner radius are almost an order of magnitude higher than for the outer radius. This can be attributed to the fact that the inner material boundary intersects less cells, making the effects of employing a radial level set more noticeable. For instance, the change in the interface normal direction from cell to cell is more acute.

Figure 3.6 shows the azimuthal change in interface position at the final simulation time $t_f = 3\,\mu\mathrm{s}$. It can be clearly observed that the excursions from the average position are not considerably reduced until the resolution is high enough. In contrast, the average position seems to converge faster towards the exact solution. To measure this, the analytical solution in [56] is employed for computing (a) the mean position difference $|\overline{R}_i(t_f) - R_{if}|$ and (b) the deviation from radial symmetry, now considering

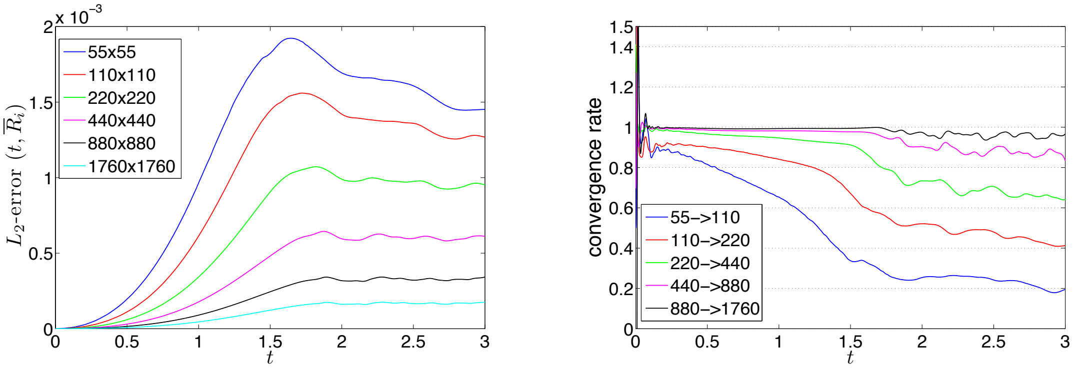

(a) Inner radius. L_2-error.

(b) Inner radius. Convergence rate

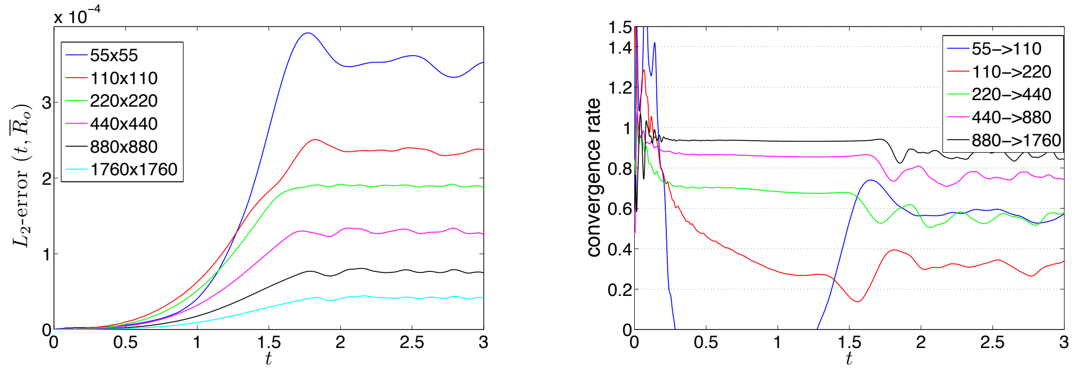

(c) Outer radius. L_2-error.

(d) Outer radius. Convergence rate

Figure 3.5: L_2-error computed using Eq. (6.7) for the inner and outer material boundary as a function of time for the examined grid resolutions. The convergence rate is also shown.

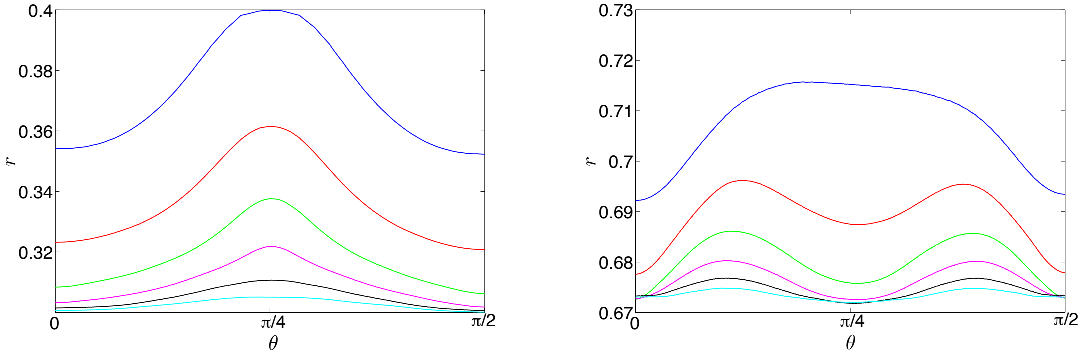

(a) Inner radius

(b) Outer radius

Figure 3.6: Position of the interface as a function of the azimuthal position for $t = t_f = 3\,\mu$s. Different colors are used to describe the results produced by the examined grid resolutions. For the color legend, see Fig. 3.5(a).

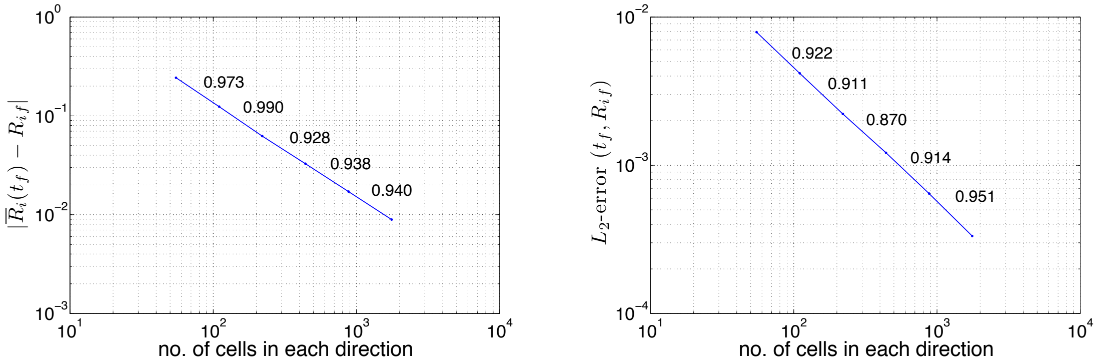

(a) Error in mean position

(b) Deviation from radial symmetry

Figure 3.7: Errors in 2D simulations for different grid resolutions taking as reference the analytical result in [56] at $t = t_f = 3\,\mu$s. The error in the mean position of the interface is represented in (a). Azimuthally averaged deviations from radial symmetry are shown in (b).

the analytical solution as a reference value:

$$L_2 - \text{error}_i(t_f, R_{if}) = \frac{1}{R_{if}} \sqrt{\frac{1}{N} \sum_{n=1}^{N} \left(R_{in}(t_f) - R_{if}\right)^2}. \tag{3.61}$$

In Fig. 3.7, the results for this analysis are depicted. Both measures indicate an approximately constant convergence rate that is close to first-order.

In summary, computational simulations involving level-sets that are not aligned with Cartesian grids suffer from distortion. The errors can be reduced when a small cell-size is employed since first-order convergence is expected. In Chapter 6, results are shown for a similar analysis performed for the problem of a radial solid–gas material interface processed by a radial shock wave.

3.3.5 Mass conservation in the level-set method

To close the study of the multi-material implementation, a general analysis of the effect of the level-set method on mass conservation is performed. Although the proposed numerical scheme is strictly conservative in each single-material patch, adaptive mesh refinement and the usage of the level-set method for multi-material implementations introduce mass conservation errors. The purpose of this section is to examine the source and importance of the lack of mass conservation and how it evolves as grid size parameters are changed. The elastic inverse deformation tensor formulation of Subsection 3.2.3 is considered in this test along with a purely elastic material which follows the Godunov-Romenski equation of state (3.58) with the typical parameters for copper described in paragraph 3.3.3.2 . Two different two-dimensional test cases are defined on a square grid $[0,4] \times [0,4]$ composed of square cells with reflective boundary conditions at all four edges.

3.3.5.1 IVP 1

For the first problem, a sinusoidal density field,

$$\mathbf{g} = \begin{pmatrix} 1/(0.75+0.25\cos(\pi x_1)\cos(\pi x_2)) & 0 & 0 \\ 0 & 1/(0.75+0.25\cos(\pi x_1)\cos(\pi x_2)) & 0 \\ 0 & 0 & 1 \end{pmatrix}, \tag{3.62a}$$

$$\mathbf{u} = \begin{pmatrix} 0 \\ 0 \end{pmatrix}, \tag{3.62b}$$

$$\varsigma = 0, \tag{3.62c}$$

is considered. A level set can be defined in a way such that different regions of the computational domain are considered as distinct materials, even if they are de-facto the same. With this arrangement, the multi-material Riemann solver is used across the interface defined by the signed distance function and errors due to this can be quantified. The initial material interface is defined by

$$r = 2 + 0.5\cos(4\theta), \tag{3.63}$$

where $r = \sqrt{x_1^2 + x_2^2}$ and $\theta = \arctan \frac{x_2}{x_1}$.

3.3.5.2 IVP 2

The second initial value problem is defined by a Riemann problem,

$$\text{if } x_1 < 2 \begin{cases} \mathbf{g} &= \begin{pmatrix} 1 & 0 & 0 \\ 0 & 1 & 0 \\ 0 & 0 & 1 \end{pmatrix} \\ \mathbf{u} &= \begin{pmatrix} 0 \\ 0 \end{pmatrix} \\ \varsigma &= 0 \end{cases} , \text{if } x_1 > 2 \begin{cases} \mathbf{g} &= \begin{pmatrix} 1.655 & 0 & 0 \\ 0 & 1 & 0 \\ 0 & 0 & 1 \end{pmatrix} \\ \mathbf{u} &= \begin{pmatrix} 0 \\ 0 \end{pmatrix} \\ \varsigma &= 2.004 \end{cases} , \tag{3.64}$$

which produces a shock of $M_s \approx 2.03$ to the left and an expansion to the right. Density is matched at the contact discontinuity, with $g_{11} = 1.3640$ on both sides. The level-sets for this problem are set so the "artificial" initial material interface is located at

$$r = 3 + 0.8\cos(4\theta), \tag{3.65}$$

with $r = \sqrt{x_1^2 + x_2^2}$ and $\theta = \arctan \frac{x_2}{x_1}$.

3.3.5.3 Test results

Below, different tests are performed using the two initial value problems previously described. Firstly, the influence of the adaptive mesh refinement algorithm is quantified in a series of simulations in which level-sets are not used, i.e., we perform strictly single-material simulations. This is followed by convergence analyses in which the number of refinement levels are fixed while the base grid is successively refined.

Influence of adaptive mesh refinement. Adaptive mesh refinement is a source of conservation errors since the fluxes at the patch boundaries (i.e., the boundaries separating different levels of refinement) do not generally match. This issue can be corrected by a fix-up algorithm, which reassigns fluxes at the end of each time-step in a way such that they are equal across patch boundaries. However, in the case of the equations of motion for solid mechanics, this fix is not exact as it applies individually to each component of the deformation or inverse deformation tensor and, in consequence, the reconstruction of density using the determinant of the tensors is, in general, not strictly conservative. Another drawback of the fix-up algorithm is that, in elastic–plastic simulations, a change in the deformation tensor components caused by the rearrangement of fluxes leads to states that do not satisfy the plasticity constraint imposed. For instance, in the case of perfect plasticity, the von Mises stress after correction may not be equal to the yield stress.

In order to quantify these errors, Figure 3.8 shows the total mass with respect to time for IVP 2 when a purely single-material simulation is considered (i.e., a level-set function has not been defined and the computational domain is treated as containing an unique material). Mass conservation is exact when uni-grid (1 level) simulations are used and degrade by 0.05% when an extra level of refinement is added. The usage of the fix-up algorithm reduces the mass error drastically but not to the level of uni-grid simulations. This analysis reveals that convergence studies that look at mass errors with respect to cell size should be performed with constant levels of refinement and increasing the number of cells in the coarsest grid in order to minimize the influence of adaptive mesh refinement errors and highlight the mass conservation errors coming from the use of a level-set approach.

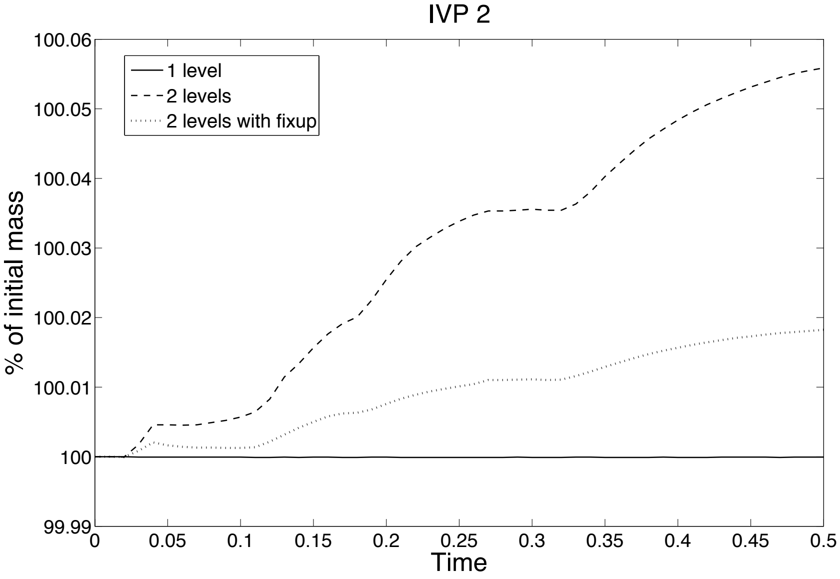

Figure 3.8: Mass percentage with respect to the initial mass as a function of time for IVP 2 in a single-material simulation (no level set). Uni-grid and two-level simulations with and without fix-up algorithm are also shown. Uni-grid produces exact conservation of mass. The addition of an extra level of refinement degrades the solution, an effect that can be partially fixed by the use of the fix-up algorithm.

Convergence studies. The influence of separating the computational domain in two level-sets and using the multi-material algorithm is tested following the conclusions of the previous paragraph. A series of simulations are shown in which the number of levels is kept constant (2 for IVP 1 and 3 for IVP 2) and the base grid is successively refined by a factor of 2. The refinement criteria employed flags a determined number of cells at each side of the material interface and also cells in which the density gradient exceeds a threshold value.

Table 3.5: L_2-errors and convergence rate for IVP 1

2 levels	total mass		mass LS 1		mass LS 2	
resolution	L_2-error	**C.R.**	L_2-error	**C.R.**	L_2-error	**C.R.**
32	0.845e-2		1.281e-2		1.546e-2	
64	0.663e-2	**0.351**	1.027e-2	**0.318**	1.122e-2	**0.462**
128	4.687e-2	**-2.822**	4.855e-2	**-2.241**	3.980e-2	**-1.827**
256	5.599e-2	**-0.256**	5.553e-2	**-0.194**	5.806e-2	**-0.545**
512	4.090e-2	**0.453**	3.914e-2	**0.504**	4.852e-2	**0.259**
1024	2.175e-2	**0.911**	2.065e-2	**0.923**	2.652e-2	**0.871**

Figure 3.9 presents results for IVP 1. The L_2 mass error is computed using the expression:

$$\varepsilon_{L_2} = \sqrt{\frac{1}{n_f}\sum_{n=1}^{n_f}\left(\frac{|m_n - m_0|}{m_0}\right)^2}, \tag{3.66}$$

where n_f is the number of time samples, m_n is the mass for each of the samples n, and m_0 is the initial mass. For simulations using a small number of cells, mass conservation errors are very low. This is due to the fact that the vast majority of the computational domain gets refined up to the finest level since the layer around the interface that gets flagged for refinement is set to have a width that comprises a fixed number of cells, rather than being based on physical distance. Therefore, refinement will extend further from the interface when the cell size is large. It can also be observed that time oscillations in the mass value are high for low resolutions. As the base cell size is decreased, the mass conservation error increases as the width of the flagged strip decreases. After achieving a maximum for $n = 256$, the mass error actually starts decreasing with approximately first-order convergence rate (i.e., L_2 error slope approaches 0.9 when going from $n = 512$ to $n = 1024$, as seen in Table 3.5).

A similar trend is appreciated in the results for IVP 2 shown in Fig. 3.10. In this case, mass fluctuations are also more acute for cases with a lower number of cells. As in IVP 1, the total mass conservation error in the L_2-norm initially increases as the base grid is refined. After achieving a maximum, it starts decreasing at slightly less than first-order convergence rate as shown in Table 3.6.

In conclusion, a convergence rate close to first-order for mass conservation can be expected when this level-set method is used and the problem is well-posed. Richtmyer–Meshkov instability is however generally ill-posed in the nonlinear regime, especially if free-slip interface conditions where tangential velocities can be largely different at each side of the interface are imposed. Additional mass conservation studies are performed in Chapter 6 when the solid–gas converging Richtmyer–Meshkov instability is presented and in Appendix C.

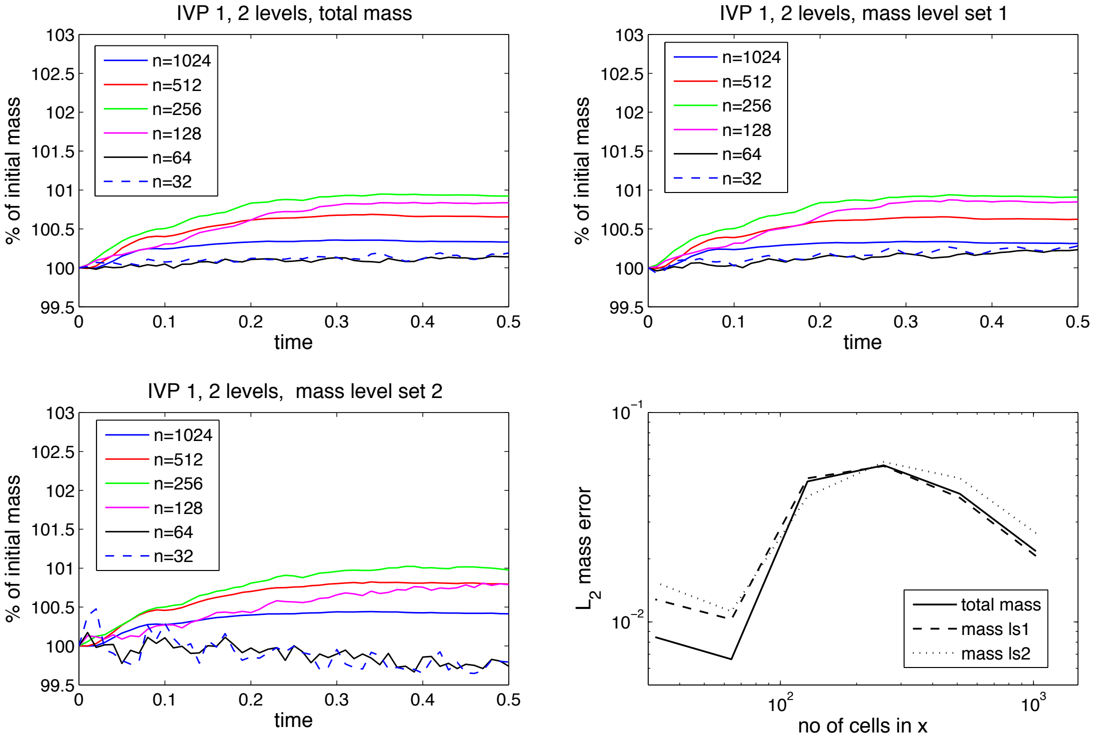

Figure 3.9: Mass percentage with respect to initial mass as a function of time for IVP 1. Results are depicted for the mass contained in each of the two level-sets and the total mass. The last figure represents the mass errors evolution in the L_2-norm with the number of cells in each direction of the base grid.

3.4 Summary

The numerical implementation of the extended set of Euler equations for solid mechanics described in Chapter 2, which involve the solution of mass, linear momentum and energy concurrently with an appropriate hyper-elastic constitutive law and equations of motion for describing the deformation and inelastic state of the material, was described in this chapter. The approach follows closely the work of Barton et al. [8] but expands the number of formulations included in the code by adding the inverse deformation tensor–plastic deformation tensor methodology of Miller and Colella [78] and Hill et al. [49], requiring the solution of 23 equations, and a novel approach based on the elastic inverse deformation tensor in which only 14 equations are needed. In addition, all the mentioned formulations can be easily adapted to the use of the stretch tensor, which leads to a more robust algorithm for dealing with impacts between portions of a same material (i.e., reconnection, topology changes). Some upgrades were introduced in the multi-material part of the solver. In particular, a different reinitialization strategy in which a subcell fix for cells adjacent to the boundary and a robust algebraic approximate Riemann solver for material interfaces based on the HLLD method for

Table 3.6: L_2-errors and convergence rate for IVP 2

3 levels	total mass		mass LS 1		mass LS 2	
resolution	L_2-error	**C.R.**	L_2-error	**C.R.**	L_2-error	**C.R.**
16	2.401e-3		5.892e-3		12.69e-3	
32	2.620e-3	**-0.126**	2.414e-3	**1.287**	4.809e-3	**1.400**
64	5.332e-3	**-1.025**	5.329e-3	**-1.142**	5.734e-3	**-0.254**
128	5.394e-3	**-0.016**	5.589e-3	**-0.069**	5.144e-3	**0.157**
256	3.554e-3	**0.602**	3.426e-3	**0.706**	3.774e-3	**0.447**
512	1.955e-3	**0.862**	1.775e-3	**0.949**	2.253e-3	**0.744**
1024	1.109e-3	**0.817**	0.992e-3	**0.839**	1.302e-3	**0.791**

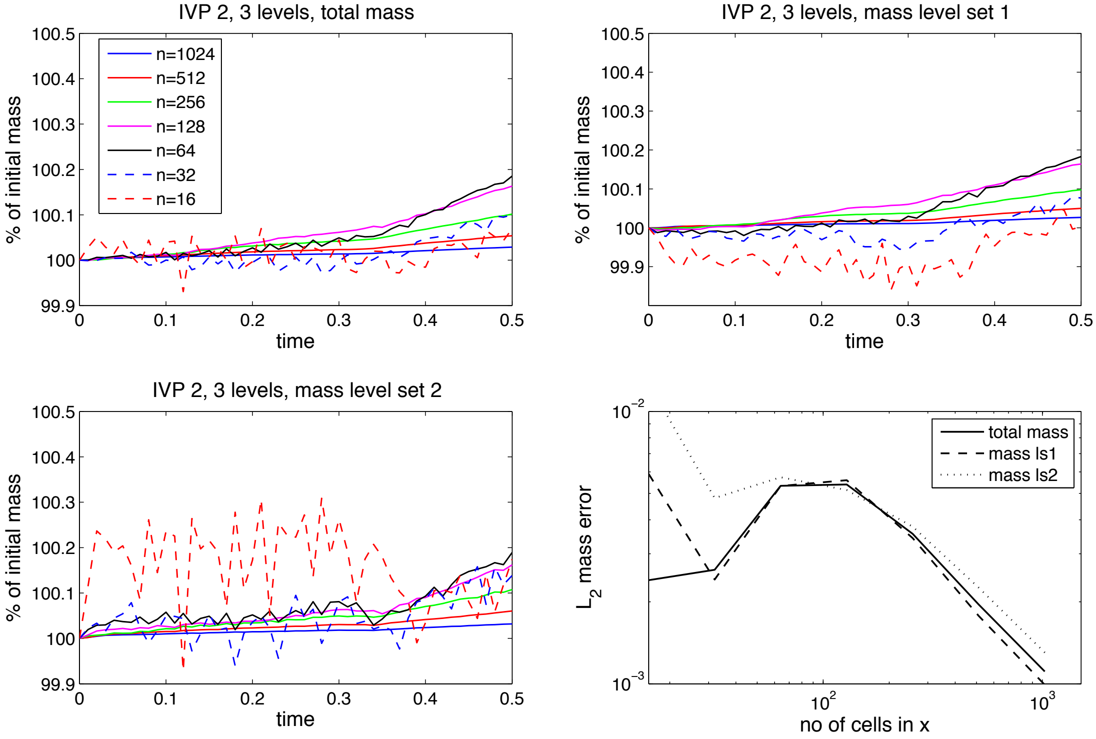

Figure 3.10: Mass percentage with respect to initial mass as a function of time for IVP 2. Results are depicted for the mass contained in each of the two level-sets and the total mass. The last figure represents the mass errors evolution in the L_2-norm with the number of cells in each direction of the base grid.

MHD were implemented.

In the next two chapters, the capabilities of the algorithm are tested against analytical results and models. In Chapter 4, an approximate theory for the motion of shocks in converging geometries is developed. This theory is then contrasted with one-dimensional numerical Eulerian simulations that can replicate the behavior of converging geometries by the addition of the appropriate geometric source terms to the equations of motion. Chapter 5 describes an analytical model for the Richtmyer–Meshkov flow in elastic solids. At the end of the chapter, comparisons with numerical results for the cases of free-slip and no-slip boundary conditions are shown. Finally, in Chapter 6, computations for analyzing Richtmyer–Meshkov problems involving an interface separating elastic–plastic solids from other media (i.e., gas, vacuum) in different geometrical configurations are presented.

Chapter 4

Converging shocks in elastic–plastic solids

4.1 Introduction

Cylindrical and spherical shock waves propagating in solid materials have been recently the focus of attention in applied physics and engineering, starting with the problem of an outgoing (exploding) wave forced by a moving cylinder/sphere [72], as occurs in projectile penetration. The particular study of converging shocks in solids is relevant to the production of high temperatures and pressures in condensed matter, with possible applications to inertial confinement fusion [62]. Recent work has actually suggested the utilization of ultra-dense deuterium with density $\approx 140\,\mathrm{kg/cm^3}$ for fusion experiments [11, 5]. However, experimental studies reveal complications inherent in the measurement techniques and the difficulty of producing a quasi-radially symmetric flow with minimal excursions from circularity.

Guderley [46] originally considered cylindrically and spherically symmetric converging shock waves in an inviscid ideal gas and showed that, if the shock wave is initially already strong, there exist similarity solutions in which the radial location $R(t)$ of the shock is proportional to a power of the time measured from the instant when the shock has imploded to $r = 0$. The Guderley implosion problem has been addressed using Whitham's shock dynamics (WSD) theory [122], which gives good approximations to the values of the Guderley exponent. WSD was also extended to imploding shocks initially infinitesimally weak [54] and applied to two-dimensional gas dynamics problems [14] such as shock diffraction by a wedge and shock stability [121].

Yadav & Singh [125] studied the propagation of spherically converging shocks in metals using WSD and employing a Mie–Gruneisen equation of state for the hydrostatic part of the energy that does not account for the effects of shear. Their solution for the post-shock pressure approaches an inverse power of R, the exponent varying with the effective specific heat ratio of the metal. In that study, a distinction was also made between the behavior of light metals like aluminum, which behave like gases in the strong-shock limit, and heavier materials like copper, which exhibit a slight variation of the gas-like behavior. A similar equation of state was used by Hiroe, Matsuo & Fujiwara [50] who simulated a cylindrically imploding shock (and its subsequent reflection off the axis) using a random choice numerical method. They observed that the flow only falls within the self-similar regime commonly observed with gases in extreme proximity of the axis.

This chapter presents an approximate description of the behavior of an elastic–plastic material processed by a cylindrically/spherically symmetric converging shock, following Whitham's shock dynamics theory. Unique to this analysis is the introduction of shear deformations through the use of hyper-elastic equations of state. The examined constitutive laws share a compressible neo-Hookean [61] structure for the internal energy $e = e_s(I_1) + e_h(\rho, \varsigma)$, where e_s accounts for shear through the first invariant of the Cauchy–Green strain tensors. The hydrostatic contribution to the internal energy is represented by e_h. In particular, an isothermal (i.e., $e_h = e_h(\rho)$) and a non-isothermal (i.e., $e_h = e_h(\rho, \varsigma)$) form of this term are employed in this study. This rather simple approach reduces the complexity of the problem to the point where analytical solutions can be obtained. More general laws, in which the shear part depends on the three invariants of the Cauchy–Green tensors and the material properties can vary with the density and entropy, have been formulated [37, 77] and adapt well to a variety of stress states conditions. A summary of other constitutive laws specific to high-compression shocks in different media (e.g., porous materials) can be found in [2], with an emphasis on hydrostatic terms of the Mie–Grüneisen type.

To describe the large deformations in a highly compressed material, the Eulerian description of the conservation laws governing the finite-deformation evolution of a purely elastic material under radially symmetric conditions is introduced in Section 4.2 . After describing the general compressible neo-Hookean hyper-elastic constitutive law employed, a WSD analytical solution is constructed and compared against high-resolution numerical simulations for both isothermal and non-isothermal constitutive laws. The strong-shock limits are derived analytically from the WSD solution, along with estimations of the density, radial velocity, pressure, and sound speed immediately behind the shock. Section 4.3 extends the study to finite-deformation plasticity and provides similar comparisons between numerical and analytical results. This section also includes a study of the effect of the shear modulus and yield stress on the shock trajectory. Finally, a characterization of the elastic–plastic transition in converging shocks, which involves an elastic precursor and a plastic compression region, is exposed by means of numerical simulations as it exceeds the scope of WSD.

4.2 Elastic motion

4.2.1 Governing equations for radially symmetric motion

The radially symmetric motion of a continuum elastic medium induced by the collapse of cylindrical and spherical imploding shock waves is described here. The equations for mass, linear momentum and energy conservation (Eqs. (2.1) expressed in curvilinear coordinates and specialized to radial motion take the form

$$\begin{aligned}
\frac{\partial \rho}{\partial t} + u\frac{\partial \rho}{\partial r} + \rho\frac{\partial u}{\partial r} &= -(s-1)\frac{\rho u}{r}, && \text{(4.1a)}\\
\frac{\partial u}{\partial t} + u\frac{\partial u}{\partial r} - \frac{1}{\rho}\frac{\partial \sigma_{rr}}{\partial r} &= (s-1)\frac{\sigma_{rr}-\sigma_{\theta\theta}}{\rho r}, && \text{(4.1b)}\\
\frac{\partial e}{\partial t} + u\frac{\partial e}{\partial r} - \frac{\sigma_{rr}}{\rho}\frac{\partial u}{\partial r} &= (s-1)\frac{u\sigma_{\theta\theta}}{\rho r}, && \text{(4.1c)}
\end{aligned}$$

where r is the distance to the axis/origin, u the radial component of velocity vector and s the space index, with $s = 1$ for planar symmetry, $s = 2$ for cylindrical symmetry and $s = 3$ for spherical symmetry.

In cylindrical symmetry ($s = 2$), the inverse deformation tensor reduces to a diagonal form $\mathbf{g} = \mathrm{diag}(g_{Rr}, g_{\Theta\theta}, 1)$, where plane strain is assumed (no deformation in the z direction). Similarly, $\mathbf{g} = \mathrm{diag}(g_{Rr}, g_{\Theta\theta}, g_{\Phi\phi})$ for $s = 3$. The density constraint $J \equiv \rho_0/\rho = 1/\det(\mathbf{g})$, where ρ_0 is the density of the undeformed material, reduces the complexity of the problem as the non-radial components of $\mathbf{g}$ are functions of g_{Rr} and ρ:

$$g_{\Theta\theta} = \frac{1}{J g_{Rr}} \quad \text{for } s = 2, \qquad \text{(4.2a)}$$

$$g_{\Theta\theta} = g_{\Phi\phi} = \sqrt{\frac{1}{J g_{Rr}}} \quad \text{for } s = 3. \qquad \text{(4.2b)}$$

At this point, the system of equations (4.1) can be closed by the choice of a specific constitutive law of the form $e(I_1^{\mathbf{C}}, I_2^{\mathbf{C}}, I_3^{\mathbf{C}}, \varsigma)$, which would then be used to determine σ_{rr} and $\sigma_{\theta\theta}$ as a function of the inverse deformation tensor components and e. Noting (4.2), only the equation of evolution of the inverse deformation tensor component g_{Rr} is needed,

$$\frac{\partial g_{Rr}}{\partial t} + g_{Rr}\frac{\partial u}{\partial r} + u\frac{\partial g_{Rr}}{\partial r} = 0. \qquad \text{(4.3)}$$

4.2.2 Numerical method and computational geometry

A radially symmetric problem can be computed as one-dimensional when appropriate geometrical source terms are included. The equations of motion (4.1) and (4.3) can be rewritten in a conservative form as functions of r for the different formulations described in Chapter 3,

$$\begin{aligned}
\frac{\partial \rho}{\partial t} + \frac{\partial \rho u}{\partial r} &= -(s-1)\frac{\rho u}{r}, && (4.4a)\\
\frac{\partial \rho u}{\partial t} + \frac{\partial \rho u^2 - \sigma_{rr}}{\partial r} &= (s-1)\frac{\sigma_{rr} - \sigma_{\theta\theta} - \rho u^2}{r}, && (4.4b)\\
\frac{\partial \rho E}{\partial t} + \frac{\partial (\rho E - \sigma_{rr}) u}{\partial r} &= -(s-1)\frac{(\rho E - \sigma_{rr}) u}{\rho r}, && (4.4c)\\
\frac{\partial g_{Rr}}{\partial t} + \frac{\partial g_{Rr} u}{\partial r} &= 0, && (4.4d)\\
\frac{\partial \rho F_{rR}}{\partial t} &= -(s-1)\frac{\rho F_{rR}}{r}. && (4.4e)
\end{aligned}$$

The geometric source terms on the right-hand side are evaluated at the cell centers and added concurrently with the wall fluxes. To this extent, the matrix $\mathbf{H}$ in Eq. (3.18) can be simplified for the one-dimensional radial case to become

$$\mathbf{H}_i = \frac{1}{\Delta x_1}\left(D^1_{i+1/2} - D^1_{i-1/2}\right) - \mathbf{S}_i + \mathbf{G}_i, \tag{4.5}$$

where $\mathbf{G_i}$ is the vector of geometric source terms resulting from Eq. (4.4). In order to being able to investigate the strong-shock limit, simulations were performed using the built-in adaptive mesh refinement (AMR) as described in [49, 8]. Three levels of refinement, each one increasing resolution by four, over an initial grid of 10^4 cells, were used.

The shock is initiated at the position R_i at the left boundary of the computational domain to avoid the calculation of $g_{\Theta\theta}$ at $t = 0$ for all r behind the shock (since $g_{\Theta\theta} = 0$ immediately behind the shock), and propagates from left to right. The value of the initial radius R_i is not relevant here since the problem does not have a characteristic length scale. The boundary condition at the left-end of the domain is transmissive (zero-gradient boundary condition), while reflective boundary conditions are applied at the axis/origin $r = 0$.

4.2.3 Whitham's shock dynamics and Rankine–Hugoniot jump conditions

To apply WSD, the system of PDEs (4.1) and (4.3) advecting the vector of primitive variables (ρ, u, e, g_{Rr}) can be first decoupled into a set of ordinary differential equations (ODEs) called the "characteristic" equations as derived in Appendix A. The essential assumption behind the WSD approach is based on the intuition that, as the converging shock is adjusting to changes in the geometry, the shock ignores its interaction with the flow behind it and its motion can be approximated by integrating the equation governing the flow along the $u + a$-characteristics, a being the sound speed. Numerical simulations confirm that the slope of the family of $u + a$-characteristics is indeed close to the slope of a converging shock trajectory, especially when the shock gets stronger (e.g., see Fig. 4.1(b)). This intuition can be motivated by a small-perturbation analysis of the shock propagation down a nonuniform shock tube of cross-sectional area $A(r)$ slowly varying from $A(r)$ to $A(r) + \mathrm{d}A$. Over the length of the shock tube, the errors might accumulate but they are neglected in the WSD theory.

Assume that the shock is located at the radial position $r = R(t)$ at time t. For the characteristic curve of slope $u + a$, the ODE relating the changes in the post-shock properties as r ($> R$) varies is further simplified by using the Rankine–Hugoniot (RH) jump conditions across the moving shock, which give the primitive variables immediately behind the shock in terms of the shock Mach number M. In the frame of reference of the shock imploding at the instantaneous speed $U(t) = -\mathrm{d}R/\mathrm{d}t > 0$, the weak formulation of the conservation equations (4.1) and (4.3) leads to the following jump conditions normal to the shock,

$$\begin{aligned}
\rho(U-u) &= \rho_0 U, && (4.6a)\\
\rho(U-u)^2 - \sigma_{rr} &= \rho_0 U^2 - \sigma_{rr0}, && (4.6b)\\
\rho(U-u)\left[e + \frac{1}{2}(U-u)^2\right] - \sigma_{rr}(U-u) &= \rho_0 U\left(e_0 + \frac{1}{2}U^2\right) - \sigma_{rr0}U, && (4.6c)\\
g_{Rr}(U-u) &= U, && (4.6d)
\end{aligned}$$

which relate the state immediately behind the shock ($r = R^+$) to the unshocked quiescent state '0'. These conditions can be reformulated as

$$\begin{aligned}
J &= \frac{1}{g_{Rr}}, && (4.7a)\\
u &= a_0(1-J)M, && (4.7b)\\
\sigma_{rr} &= \sigma_{rr0} - \rho_0 a_0^2(1-J)M^2, && (4.7c)\\
e &= e_0 - \frac{\sigma_{rr0}}{\rho_0}(1-J) + \frac{1}{2}a_0^2(1-J)^2 M^2, && (4.7d)
\end{aligned}$$

where $M = U/a_0 > 1$. Observe that $J < 1$ since the material is being compressed by the shock, and that Eq. (4.2) and (4.7a) imply that $g_{\Theta\theta}$ is unaltered by the shock. In the next sections, this theory is applied to different constitutive laws.

4.2.4 Neo-Hookean isothermal constitutive law

Assuming an isothermal constitutive law, i.e., e independent of ς, reduces the governing equations to Eq. (4.1a), (4.1b) and (4.3), with the jump conditions to (4.7a), (4.7b) and (4.7c), since the energy equation is now redundant. A fairly general isothermal constitutive law proposed by Blatz and Ko [19] is:

$$e(\mathbf{g}) = \frac{\mu}{2\rho_0}(I_1^{\mathbf{C}} - 3I_3^{\mathbf{C}\,1/3}) + \int_{\rho_0}^{\rho} \frac{p(\rho')}{\rho'^2}\, d\rho', \tag{4.8}$$

with the density constraint $I_3^{\mathbf{C}} = J^2 = (\rho_0/\rho)^2$,where μ is the shear modulus and the so-called hydrostatic pressure p was assumed to not depend on ς. Using the geometrical simplifications of the inverse deformation tensor described in Section 4.2.1 and transforming both inverse deformation tensor $\mathbf{g}$ and stress tensor $\boldsymbol{\sigma}$ to curvilinear coordinates, one obtains:

$$\sigma_{rr} = \frac{\mu}{J}\left(\frac{1}{{g_{Rr}}^2} - J^{2/3}\right) - p(\rho_0/J), \tag{4.9a}$$

$$\sigma_{\theta\theta} = \frac{\mu}{J}\left(J^{4-s}{g_{Rr}}^{4-s} - J^{2/3}\right) - p(\rho_0/J). \tag{4.9b}$$

Unlike gases, the sound speed a in solids depends on the deformation mode: for general three-dimensional deformations, compression (or longitudinal) waves and shear deformation waves exist, each propagating at a different velocity. In radially symmetric motion, the eigen-structure of a hyper-elastic material only involves compression waves traveling at speeds $u \pm a$ with a referring to the longitudinal sound speed, now simply called "sound speed". For the isothermal constitutive law (4.8), one obtains

$$a = \sqrt{a_\mu^2\left(\frac{1}{{g_{Rr}}^2} + \frac{1}{3}J^{2/3}\right) - \frac{J^2}{\rho_0}\frac{\mathrm{d}p}{\mathrm{d}J}}, \tag{4.10}$$

where the shear modulus-based wave speed has been defined by $a_\mu \equiv \sqrt{\mu/\rho_0}$.

The derivation of the equation for the $u + a$-characteristic curve and the application of the necessary shock jump conditions are described in Appendix A.1.1 and lead to the following ODE for any isothermal pressure form:

$$\frac{\mathrm{d}R}{R} = -\frac{1}{s-1}\frac{a\left[a + a_0(1-J)M\right]\left[-a/J + a_0(1-J)M'(J) - a_0 M\right]}{(1-J)\left[a_0\left(a^2 - 2a_\mu^2 J^2\right)M + a_\mu^2 a(1+J)\right]}\mathrm{d}J, \tag{4.11a}$$

$$M(J) = \frac{1}{a_0}\sqrt{\frac{1}{1-J}\left[\frac{p(\rho_0/J)}{\rho_0} - a_\mu^2\left(J - J^{-1/3}\right)\right]}, \tag{4.11b}$$

where $a(J)$ is given by Eq. (4.10) using Eq. (4.7a). This ODE can be integrated to obtain R as a function of J

$$\frac{R}{R_i} = \exp\left(-\frac{1}{s-1}\int_{J_i}^{J}\frac{a\left[a + a_0(1-J)M\right]\left[-a/J + a_0(1-J)M'(J) - a_0 M\right]}{(1-J)\left[a_0\left(a^2 - 2a_\mu^2 J^2\right)M + a_\mu^2 a(1+J)\right]}\mathrm{d}J\right), \tag{4.12}$$

with J_i and R_i the initial density ratio and position of the shock. The shock velocity $U = a_0 M$ is then found using Eq. (4.11b), and integrated to obtain the shock trajectory $r = R(t)$.

4.2.4.1 Polynomial dependence for $p(\rho)$

As a first example, the expression of the pressure proposed by Miller & Colella in [78] for the Wilkins' flying aluminum plate problem is considered:

$$p\left(\frac{\rho_0}{J}\right) = \sum_{\alpha=1}^{3} c_\alpha \left(\frac{1}{J} - 1\right)^{\alpha}, \tag{4.13}$$

where $\mu = 27.8\,\mathrm{GPa}$, $\rho_0 = 2.7\,\mathrm{kg.m^{-3}}$, $c_1 = 72\,\mathrm{GPa}$, $c_2 = 172\,\mathrm{GPa}$, and $c_3 = 40\,\mathrm{GPa}$. In the strong-shock limit $M \gg 1$, (4.11b) and (4.13) imply that J must tend to 0, which leads to an infinite density at $r = 0$. A more general power law $p = c_\alpha J^{-\alpha}$ with $\alpha > 1$, similar to the one given by (4.13) as $M \gg 1$, would simplify the ODE (4.11) to:

$$\frac{\mathrm{d}R}{R} \simeq \frac{\sqrt{\alpha}}{2(s-1)} \frac{\mathrm{d}J}{J^{3/2}}. \tag{4.14}$$

Solving Eq. (4.14), and using Eq. (4.7b) and (4.11b), the strong-shock limit gives, for a shock at $r = R$,

$$\begin{aligned} J &\simeq \left(a_0 \frac{\rho_0}{c_\alpha}\right)^{-2/\alpha} M^{-2/\alpha}, && (4.15a)\\ u &\simeq a_0\, M, && (4.15b)\\ p &\simeq \rho_0 a_0^2\, M^2, && (4.15c)\\ a &\simeq \sqrt{\frac{\alpha c_\alpha}{\rho_0}} \left(\frac{\rho_0 a_0^2}{c_\alpha}\right)^{(\alpha-1)/2\alpha} M^{(\alpha-1)/\alpha}, && (4.15d)\\ \text{with} \quad M &\simeq \frac{1}{a_0}\sqrt{\frac{c_\alpha}{\rho_0}} \left[\left(\frac{s-1}{\sqrt{\alpha}}\right) \log\left(\frac{R_i}{R}\right)\right]^{\alpha}. && (4.15e) \end{aligned}$$

It is interesting to notice that the power of $\log(1/R)$ does not depend on the space index. Also observe that for a pressure dependence $p = J^{-\alpha}$, the isentropic exponent defined by $\Gamma \equiv \partial \log p / \partial \log \rho$ is exactly equal to α.

As depicted in Fig. 4.1(a), the density ratio immediately behind the converging shock predicted by WSD compares favorably with the one obtained from high-resolution numerical simulations, even when the shock is weak. The $u + a$-characteristics obtained from the numerical simulation and the shock trajectory predicted by WSD are displayed in Fig. 4.1(b). The characteristics behind the shock follow a trajectory that is closer to that of the shock as one approaches the origin and the shock becomes stronger, confirming the underlying intuition behind WSD: only a small envelope of information carried by the $u + a$-characteristics can reach the shock, and as the shock strengthens, it has almost lost memory of the flow behind it. Figure 4.1(c) represents the shock Mach number M as a function of the shock location $R(t)/R_i$, down to dimensionless radii of 10^{-4}. The numerical simulation shows good agreement for low Mach numbers and small discrepancy arises at moderate

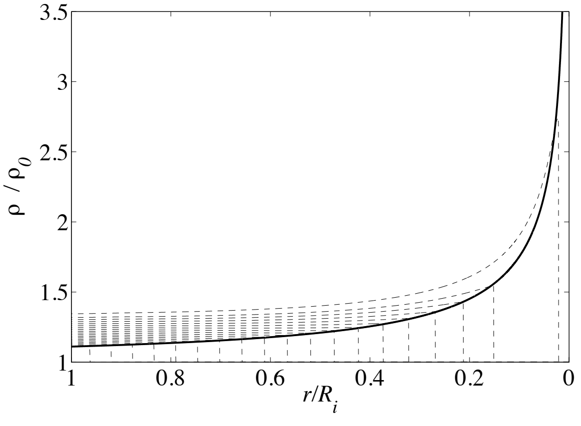

(a) ρ/ρ_0 vs r/R_i.

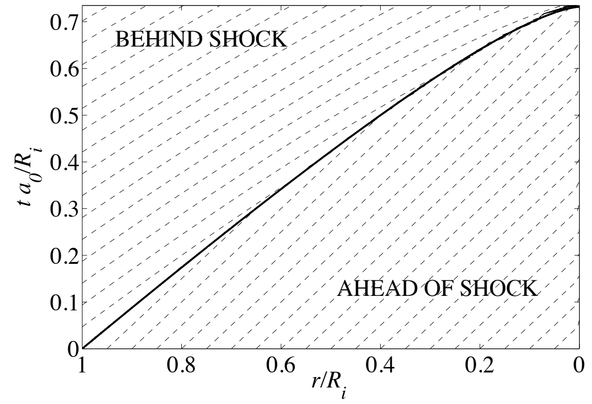

(b) $r - t$ diagram

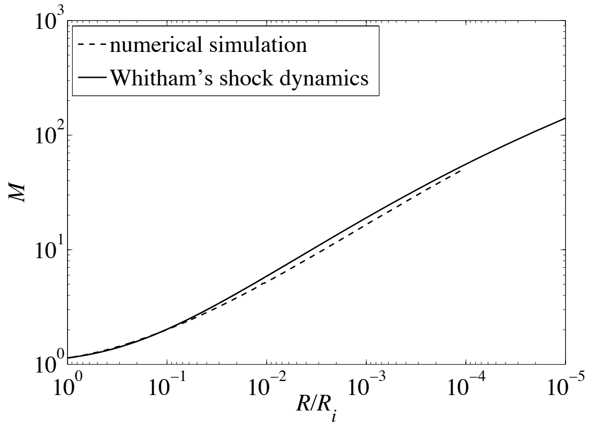

(c) $R/R_i - M$ logarithmic

Figure 4.1: Spherically symmetric ($s = 3$) converging shock initially started at $R = R_i$ with $J_i = 0.9$ (i.e., $M_i \approx 1.14$) and propagating from left to right into a purely elastic solid medium described by the isothermal constitutive law (4.8) with polynomial pressure form (4.13): (a) Density radial profiles obtained from the numerical simulation at equally spaced times (dashed lines) and density ratio immediately behind the shock ($r = R(t)^+$) given by WSD (solid line); (b) $u + a$-characteristics obtained from numerical simulation (dashed lines) and shock trajectory $r = R(t)$ vs t obtained from WSD (solid line); (c) Shock Mach number M as a function of the shock position $R(t)$ plotted in a log–log scale, from the simulation (dashed line) and WSD (solid line).

Mach numbers ($2 \lesssim M \lesssim 5$). At higher Mach numbers, the slope $\mathrm{d}M/\mathrm{d}R$ of both methods agree well until the shock has reached such small radii that the resolution of the computational grid is not sufficient to track the shock, which occurs at $M \approx 50$. As a reference for later comparison with the other constitutive laws tested, at $R/R_i = 10^{-1}, 10^{-2}$, and 10^{-3}, the shock Mach numbers obtained in the simulation are $M \approx 2.00$, 5.23, and 16.49, respectively.

4.2.4.2 Arctanh form for $p(\rho)$

In this subsection, an alternate pressure term for the constitutive law defined by Eq. (4.8) is investigated:

$$p\left(\frac{\rho_0}{J}\right) = p_0 \left(\frac{\mathrm{Arctanh}\,(J_\infty/J)}{\mathrm{Arctanh}\,(J_\infty)}\right)^{\beta}, \tag{4.16}$$

where p_0 is the unshocked pressure and β a positive integer. The material cannot be compressed more than a limit value J_∞ reached at the axis/origin which corresponds to infinite pressure. In contrast, for the same situation, the internal energy and density were unbounded for the polynomial pressure form (4.13). As J approaches J_∞, $p \sim (-\log(J - J_\infty))^{\beta}$, and Eq. (4.11) simplifies to

$$\frac{\mathrm{d}R}{R} \simeq -\frac{1}{s-1}\frac{\mathrm{d}M}{M}. \tag{4.17}$$

As a result, the strong-shock limit $M \gg 1$ for a shock at $r = R$ gives

$$\begin{aligned}
J - J_\infty &\propto e^{-2\psi M^{2/\beta}}, && (4.18\text{a})\\
u &\propto M, && (4.18\text{b})\\
p &\propto M^2, && (4.18\text{c})\\
a &\propto M^{(\beta-1)/\beta} e^{\psi M^{2/\beta}}, && (4.18\text{d})\\
\text{with } M &\propto R^{-(s-1)}, && (4.18\text{e})
\end{aligned}$$

where $\psi\,(J_\infty, a_\mu, p_0, \beta)$ is a positive coefficient. From (4.18e), the shock trajectory near the center follows $R \propto (t_\infty - t)^{1/s}$, where t_∞ defines the implosion time. The exponent in (4.18e) depends on the space index s only, not on the material properties or other parameters such as J_∞. In this case, the isentropic exponent Γ is not constant, in particular $\Gamma \propto e^{2\psi M^{2/\beta}}/M^{2/\beta}$ as $M \gg 1$.

Figure 4.2 shows numerical results superposed with the WSD solution. For low values of the integer $\beta = 1$ in (4.16), J approaches J_∞ at a very slow rate $\mathrm{d}J/\mathrm{d}R$ as $r \to 0$, and numerical inconsistencies ultimately arise when the Arctanh argument becomes greater than 1 due to machine precision-generated errors. This is corrected by choosing higher values of β, for example, $\beta = 5$ in the present case. As seen in Fig. 4.2(c), the WSD solution obtained using the Arctanh law for the pressure does not perform as well as the polynomial one because the strong-shock regime described

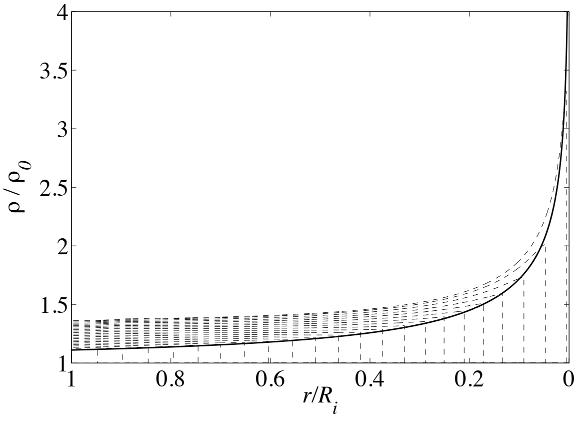

(a) ρ/ρ_0 vs r/R_i.

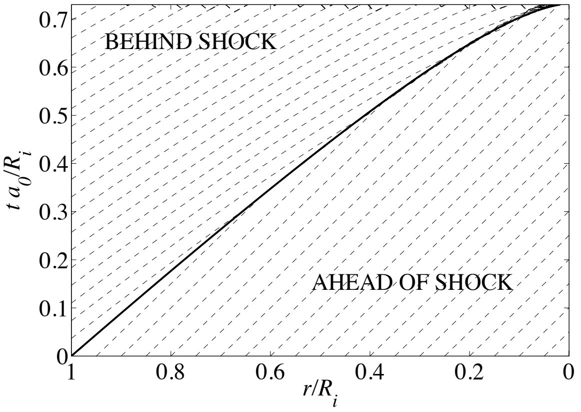

(b) $r - t$ diagram

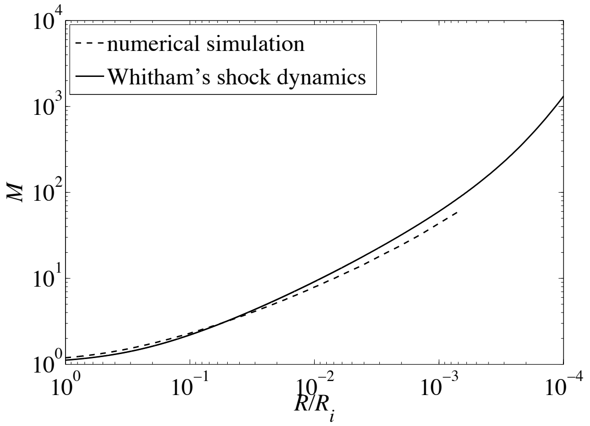

(c) $R/R_i - M$ logarithmic

Figure 4.2: Spherically symmetric ($s = 3$) converging shock initially started at $R = R_i$ with $J_i = 0.9$ (i.e., $M_i \approx 1.02$) and propagating from left to right into a purely elastic solid medium described by the isothermal constitutive law (4.8), using the Arctanh pressure form (4.16) with the choice $J_\infty = 1/6$, $p_0 = 10\,\mathrm{GPa}$ and $\beta = 5$. See Fig. 4.1 for keys.

by Eq. (4.18) (where WSD errors are expected to be minimal) is only reached for very small values of $J - J_\infty$ as second-order terms are close to the dominant terms (this can be appreciated in the figure as the power law is not reached for the WSD result until $R/R_i < 2 \cdot 10^{-4}$). Mach numbers $M \approx 2.23$, 8.29, and 43.27 are encountered at $R/R_i = 10^{-1}, 10^{-2}$, and 10^{-3}, respectively. For a given shock position, the Mach number of the shock is higher than when using a polynomial pressure form, essentially because of the large value of the exponent β chosen and the higher rate of increment of the Mach number with the radius.

4.2.5 Neo-Hookean non-isothermal constitutive law

Consider next the following simple non-isothermal constitutive law, to account for high-pressure effects near the axis/origin:

$$e(\mathbf{g}\,,\varsigma) = \frac{\mu}{2\rho_0} I_1^{\mathbf{C}} + c_v T_0 J^{1-\gamma} \exp\left(\frac{\varsigma - \varsigma_0}{c_v}\right), \tag{4.19}$$

where ρ_0, T_0 and ς_0 refer to the unshocked density, temperature and specific entropy, and c_v and γ are the specific heat at constant volume and specific heat ratio, respectively. The first part of this constitutive law represents the elastic shear deformation of the material, while the second part simply portrays the internal energy of an ideal gas. One can expect this material to behave like an ideal gas in the strong-shock limit (where the pressure term should be dominant) or as $\mu = 0$. The stress components σ_{rr} and $\sigma_{\theta\theta}$ are given by

$$\begin{aligned}
\sigma_{rr} &= \frac{\mu}{J {g_{Rr}}^2} - \frac{(\gamma-1)\rho_0}{J}\left\{e - \frac{\mu}{2\rho_0}\left[\frac{1}{{g_{Rr}}^2} + (s-1)J^{4-s}{g_{Rr}}^{4-s}\right]\right\}, && (4.20\text{a})\\
\sigma_{\theta\theta} &= \mu J^{3-s}{g_{Rr}}^{4-s} - \frac{(\gamma-1)\rho_0}{J}\left\{e - \frac{\mu}{2\rho_0}\left[\frac{1}{{g_{Rr}}^2} + (s-1)J^{4-s}{g_{Rr}}^{4-s}\right]\right\}, && (4.20\text{b})
\end{aligned}$$

and the sound speed reduces to:

$$a = \sqrt{-\frac{\gamma J \sigma_{rr}}{\rho_0} + (1+\gamma)\frac{a_\mu^2}{{g_{Rr}}^2}}. \tag{4.21}$$

As $\mu = 0$, Eq. (4.20a) indeed shows that $\sigma_{rr} = -(\gamma-1)\rho e$, and the ideal gas sound speed $a = \sqrt{\gamma p/\rho}$ is then recovered with the pressure defined by $p = -\sigma_{rr}$.

The derivation of the ODE resulting from WSD theory is more tedious than that of the isothermal constitutive law. The $u+a$-characteristic equation is reported in Appendix A.2. The combination of that expression with the RH jump conditions (4.7) gives a final ODE of the form $\mathrm{d}R/R = F(J)\mathrm{d}J$, which reduces in the strong-shock limit to

$$\frac{\mathrm{d}R}{R} \simeq -\frac{n(\gamma)}{s-1}\frac{\mathrm{d}M}{M}, \tag{4.22a}$$

$$\text{with} \quad n(\gamma) \quad = \quad 1 + \frac{2}{\gamma} + \sqrt{\frac{2\gamma}{\gamma - 1}}. \tag{4.22b}$$

Manipulating the jump conditions (4.7) further and using Eq. (4.20a), it can also be shown that J must tend to the finite value $J_\infty = (\gamma - 1)/(\gamma + 1)$ as $M \gg 1$ (similarly to the ideal gas case), and after integration of (4.22), one obtains for a shock at $r = R(t)$:

$$J - J_\infty \quad \propto \quad M^{-2}, \tag{4.23a}$$

$$u \quad \propto \quad M, \tag{4.23b}$$

$$p \quad \propto \quad M^2, \tag{4.23c}$$

$$a \quad \propto \quad M, \tag{4.23d}$$

$$\text{with} \quad M \quad \propto \quad R^{-(s-1)/n}. \tag{4.23e}$$

While γ has a clear physical meaning for ideal gases, it could be expressed in the constitutive law (4.19) as a function of the maximum compression ratio $1/J_\infty$ that the solid can reach. The scaling law (4.23e) corresponds exactly to the power law found by Whitham when applying his WSD method to ideal gases [122], and gives an approximate strong-shock trajectory $R \propto (t_\infty - t)^{n/(n+s-1)}$. Observe in particular that the exponent is independent of μ. In other words, in the strong-shock limit, the solid experiences a zero-shear behavior governed by the pressure part of the constitutive law (4.19). Moreover, $\Gamma \simeq \gamma$ only as $M \gg 1$, while $\Gamma = \gamma$ for an ideal gas independently of the conditions of compression.

The WSD prediction conforms to the numerical results at all the stages of the shock evolution (Fig. 4.3). This is confirmed by the observation that characteristics behind the shock follow very closely the trajectory of the shock. The shock Mach number plotted as a function of the shock position offers the best of agreement between WSD and numerical results of the three cases studied. At $R/R_i = 10^{-1}, 10^{-2}$, and 10^{-3}, the shock Mach number is $M \approx 3.17$, 7.71, and 19.02, respectively.

4.3 Plastic motion

In the present study, as the converging shock processes the solid with an increasing strength, the shocked material is expected to ultimately reach its intrinsic yield stress and enter the plastic regime. The results shown in the previous section were therefore only valid for some fictitious material with infinitely large yield stress.

As was shown in Chapter 2, the basic assumption in finite-deformation plasticity is the multiplicative decomposition of the inverse deformation tensor into elastic and a plastic deformation parts: $\mathbf{g} = \mathbf{g}^p\mathbf{g}^e$, where $\mathbf{g}^e$ and $\mathbf{g}^p$ are the elastic and plastic inverse deformation tensors. To meet

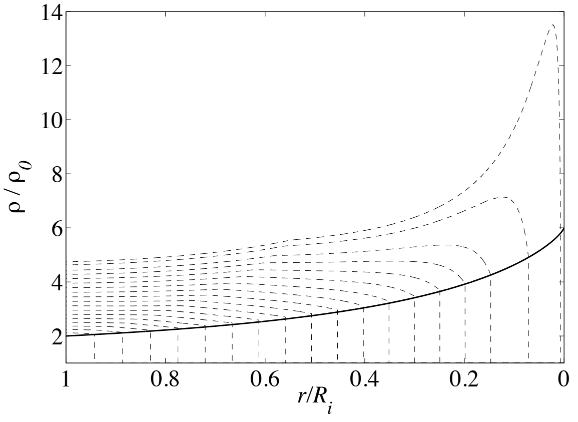

(a) ρ/ρ_0 vs r/R_i.

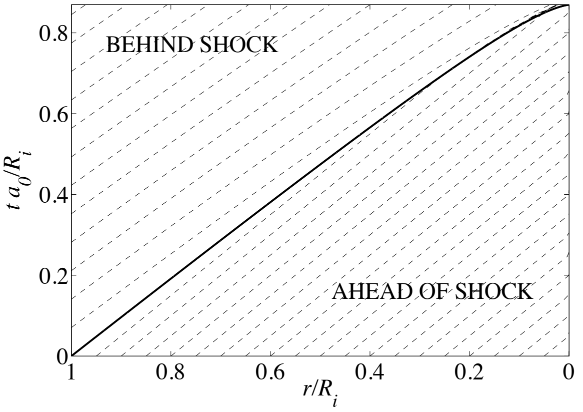

(b) $r - t$ diagram

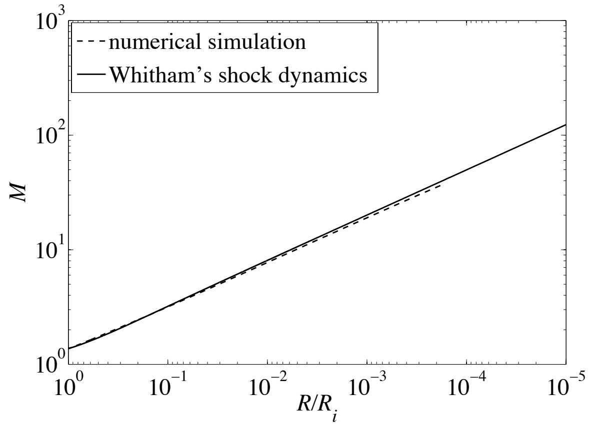

(c) $R/R_i - M$ logarithmic

Figure 4.3: Spherically symmetric ($s = 3$) converging shock initially started at $R = R_i$ with $J_i = 0.9$ (i.e., $M_i \approx 1.07$) and propagating from left to right into a purely elastic solid medium described by the non-isothermal constitutive law (4.19) with $\gamma = 1.4$ (i.e., $J_\infty = 1/6$). See Fig. 4.1 for keys.

the particular geometry constraints of this problem, only the diagonal components of these tensors are nonzero once transformed to curvilinear coordinates (as was argued in the elastic case). From the compressibility constraints $J = 1/\det \mathbf{g}$ and $J^p = 1/\det \mathbf{g}^p = 1$ (no change in volume for the plastic deformation), and because $J = J^e J^p$, the $\Theta\theta$- and $\Phi\phi$-components of the total, elastic and plastic inverse deformation tensors in spherical geometry can be expressed as functions of their radial counterpart and J:

$$g_{\Theta\theta} = g_{\Phi\phi} = \sqrt{\frac{1}{J g_{Rr}}}, \tag{4.24a}$$

$$g^e_{\Theta\theta} = g^e_{\Phi\phi} = \sqrt{\frac{1}{J g^e_{Rr}}}, \tag{4.24b}$$

$$g^p_{\Theta\Theta} = g^p_{\Phi\Phi} = \sqrt{\frac{1}{g^p_{RR}}}, \tag{4.24c}$$

where g^e_{Rr} is related the plastic inverse deformation tensor component by

$$g^e_{Rr} = \frac{g_{Rr}}{g^p_{RR}}. \tag{4.25}$$

For a cylindrical problem under plain strain however, no assumption about the components g^e_{Zz} and g^p_{ZZ} other than $g_{Zz} = g^p_{ZZ} g^e_{Zz} = 1$ can simplify the problem in a way that would express the non-radial components in terms of the radial ones. The focus is therefore set on the spherical geometry for the remaining part of the study.

To pursue the analysis further, consider the compressible neo-Hookean isothermal constitutive law given by Eq. (4.8). Although the energy equation is redundant, it would need to be included to evaluate the plastic dissipation. As was stated in Chapter 2, the internal energy equation is generally written for an elastic-plastic material as function of the elastic deformations as it accounts for the energy stored in the solid that can be released by mean of elastic deformation. Eq. (4.8) then becomes:

$$e(\mathbf{g}^e) = \frac{\mu}{2\rho_0}(I_1^{\mathbf{C}^e} - 3(I_3^{\mathbf{C}^e})^{1/3}) + \int_{\rho_0}^{\rho} \frac{p(\rho')}{\rho'^2}\, d\rho', \tag{4.26}$$

with $I_1^{\mathbf{C}^e}, I_2^{\mathbf{C}^e}, I_3^{\mathbf{C}^e}$ the invariants of the elastic Cauchy–Green tensor $\mathbf{C}^e = (\mathbf{g}^e)^{-T}(\mathbf{g}^e)^{-1}$. The stresses are computed from $\boldsymbol{\sigma} = -\rho \mathbf{g}^{e^T} \partial e / \partial \mathbf{g}^e$:

$$\sigma_{rr} = \frac{\mu}{J}\left(\frac{1}{{g^e_{Rr}}^2} - J^{2/3}\right) - p(\rho_0/J), \tag{4.27a}$$

$$\sigma_{\theta\theta} = \sigma_{\phi\phi} = \frac{\mu}{J}\left(J g^e_{Rr} - J^{2/3}\right) - p(\rho_0/J). \tag{4.27b}$$

In general, the system (4.1a), (4.1b), (4.3) and (4.27) must be completed by an evolution equation for g^p_{RR}, g^e_{Rr} being then computed using Eq. (4.25). In the following subsection, a simpler closure is derived for the case of perfect plasticity.

4.3.1 Perfectly plastic model

For simplicity, the material being processed by the converging shock is described by an elastic–perfectly plastic model. In uniaxial stress, this means that plasticity occurs at a constant stress equal to the yield stress σ_Y (i.e., no incremental stress is needed to achieve larger deformations). For more general stress conditions, this concept is extended to a yield criterion of the form $\sigma_{\text{eff}} = \sigma_Y$, where σ_{eff} is an effective stress function. For example, the von Mises constraint may be expressed as

$$\sigma_{\text{eff}} \equiv \sqrt{\frac{3}{2}\text{tr}\left(\boldsymbol{\Sigma}'^T\boldsymbol{\Sigma}'\right)} = \sigma_Y, \tag{4.28}$$

where $\boldsymbol{\Sigma}'$ is the deviatoric part of the Mandel stress tensor $\boldsymbol{\Sigma} = -(\rho_0/\rho)\,\mathbf{g}^{e^{-T}}\boldsymbol{\sigma}\,\mathbf{g}^{e^T}$ [23]. Applying this expression to a diagonal stress tensor $\boldsymbol{\sigma} = \text{diag}(\sigma_{rr}, \sigma_{\theta\theta}, \sigma_{\phi\phi})$ and $\sigma_{\phi\phi} = \sigma_{\theta\theta}$, as the one given by (4.27),

$$\sigma_Y = J|\sigma_{rr} - \sigma_{\theta\theta}|. \tag{4.29}$$

For the elastic solution behind a converging shock, $\sigma_{rr} - \sigma_{\theta\theta} = \mu\left(J^2 - 1\right)/J < 0$, since $J < 1$. Numerical results (see next subsection) shows that $\sigma_{rr} - \sigma_{\theta\theta} < 0$ in the plastic regime as well. Substituting the stresses by their expressions in terms of the elastic deformations given by Eq. (4.27), one finally obtains the following implicit dependence of g^e_{Rr} on J:

$$\frac{\sigma_Y}{\mu}{g^e_{Rr}}^2 - J{g^e_{Rr}}^3 + 1 = 0. \tag{4.30}$$

This relationship implies that the stresses (4.27) depend on J only, unlike the stresses for a purely elastic material which also depended on g_{Rr}. The system of governing equations for an elastic–perfectly plastic solid processed by a spherical converging shock then reduces to Eq. (4.1a), (4.1b), (4.27) and (4.30).

4.3.1.1 Shock dynamics for elastic–perfectly plastic solids

Derivation of the $u + a$-characteristic equation and utilization of the RH jump conditions (see Appendix A.1.2) leads to the final ODE:

$$\frac{\mathrm{d}R}{R} = -\frac{1}{2}\frac{\left[a + a_0(1-J)M\right]\left[-a/J + a_0(1-J)M'(J) - a_0M\right]}{\left[a_0a(1-J)M + \sigma_Y/\rho_0\right]}\mathrm{d}J, \tag{4.31a}$$

$$M(J) = \frac{1}{a_0}\sqrt{\frac{1}{1-J}\left[\frac{p(\rho_0/J)}{\rho_0} - a_\mu^2\left(\frac{1}{J{g^e_{Rr}}^2} - J^{-1/3}\right)\right]}, \tag{4.31b}$$

where $g^e_{R_r}$ is a function of J through Eq. (4.30). Integration of Eq. (4.31a) gives

$$\frac{R}{R_i} = \exp\left(-\frac{1}{2}\int_{J_i}^{J} \frac{[a + a_0(1-J)M]\,[-a/J + a_0(1-J)M'(J) - a_0 M]}{[a_0 a(1-J)M + \sigma_Y/\rho_0]}\mathrm{d}J\right). \tag{4.32}$$

For the polynomial law (4.13), the strong-shock limit corresponds to $J \ll 1$, for which $g^e_{Rr} \sim J^{-1} \gg 1$ according to the constraint (4.30). For the Arctanh law (4.16), large Mach numbers are obtained when J approaches J_∞, while g^e_{Rr} reaches a finite value given by Eq. (4.30) when $J = J_\infty$. For both isothermal laws, the compression effects are dominant over the shear deformation terms and the strong-shock limits are the same as for the purely elastic case (Eq. (4.15) and (4.18)). Comparisons with numerical simulations are provided in the following section.

4.3.2 Numerical simulation of elastic–plastic shocks

To gain generality, a numerical experiment was implemented allowing the material behind the shock to be initially elastic and to transition to a plastic regime when processed by a stronger shock. The system of equations (4.1a), (4.1b), (4.3), (4.25) and (4.27), which govern the deformation of an elastic–plastic solid following a compressible neo-Hookean isothermal constitutive law, is closed in this case following the inverse deformation tensor/plastic deformation tensor formulation described in Section 3.2.2. The radial evolution equation for the plastic deformation tensor is expressed in spherical coordinates as:

$$\frac{\partial \rho F^p_{RR}}{\partial t} + \frac{\partial \rho u F^p_{RR}}{\partial r} = -\frac{2\rho u F^p_{RR}}{r} + \rho F^p_{RR}\dot{\epsilon}\frac{\sigma_{rr} - \sigma_{\theta\theta}}{|\sigma_{rr} - \sigma_{\theta\theta}|}\left(\frac{J|\sigma_{rr} - \sigma_{\theta\theta}|}{\sigma_Y}\right)^N, \tag{4.33}$$

where the first term of the right-hand side is a geometric source term given by the transformation to spherical coordinates, while the second source term incorporates a form of the plastic deformation rate tensor $\mathbf{L}^p$ which models the perfectly plastic model of Eq. (4.29) (see [49]) where the exponent N is a large positive integer (i.e., $N > 10$) in order to obtain a fast relaxation towards the yield surface and $\dot{\epsilon}$ is a positive constant that can be assigned freely and symbolizes a reference strain rate. The plastic source term tends to zero rapidly when the effective stress $J|\sigma_{rr} - \sigma_{\theta\theta}|$ is smaller than the yield stress σ_Y (elastic regime) so the plastic deformation F^p_{RR} cannot increase. However, when the effective stress overtakes the yield value, this forcing term transforms F^p_{RR} such that the effective stress is brought back to the yield curve, given here by (4.30). Since the equation of state (4.26) is not expressed as a function of the logarithmic strains, an analytical solution in the way shown in Section 2.3 is not possible and the method of fractional steps with implicit evaluation of the plastic source terms is used instead, due to the stiffness of the problem for $N >> 1$.

Figure 4.4 reveals good agreement between the WSD solution described in paragraph 4.3.1.1 and the numerical simulation for a converging shock in aluminum described by an elastic–plastic material following the isothermal constitutive law (4.26) and (4.13). The value of the yield stress is so low that the material processed by the incident shock becomes purely plastic even for weak shock strengths (hence the appellation of 'plastic shock') and no elastic–plastic transition is visible here. It can be shown that this material enters the plastic regime for $J \lesssim 0.98$. Plasticity appears to have a positive effect on the agreement between the WSD and numerical simulations when compared to the purely elastic case for this same constitutive law (Fig. 4.1). Since plasticity is not dominant at the strong-shock limit, this effect should be attributed to better agreement at the medium range of Mach numbers ($2 < M_{shock} < 5$) that is where the small disagreement between WSD and simulations appears in the elastic case. At $R/R_i = 10^{-1}, 10^{-2}$, and 10^{-3}, the shock Mach numbers are $M \approx 1.86$, 4.98, and 15.57, respectively. These values are lower than the ones obtained for the purely elastic case with the same constitutive law, indicating that the shock travels at a slower velocity when a finite yield stress is introduced.

4.3.2.1 Elastic–plastic transition

To highlight the elastic–plastic transition for non-weak shock waves, the yield stress was artificially increased as the values of the coefficients in the pressure form (4.13) were decreased. Setting $\sigma_Y = 7\,\text{GPa}$ and $c_\alpha = 1$ GPa for $\alpha = 1, 2, 3$, the new material enters the plastic region at $J \approx 0.85$. As reported in Fig. 4.5(a), an initially elastic shock converges, and a plastic region forms behind as soon as the yield stress has been reached. As the coupled "elastic precursor–plastic region" converges towards the center, the plastic region becomes steeper and narrower while the elastic precursor keeps a constant strength. When approaching the center further, the elastic precursor disappears and a quasi-discontinuous plastic wave remains.

The elastic–plastic transition described in Fig. 4.5(a) can be tracked using the Hugoniot curve for the material, expressing the response σ_{eff} for smooth compression (Fig. 4.6). As the material is compressed along the radial direction, prior to reaching the yield point (segment OA in Fig. 4.6), the entropy remains constant and the restoring force greatly increases (elastic compression). The onset of plasticity is materialized by a kink in the Hugoniot (point A). During this elastic period, the shock Mach number increases from its initial value (in the case of the simulation, $M_i \approx 1.01$) to the elastic precursor Mach number (in this case, $M^e \approx 1.2$). Beyond the yield point, only a slight increase in normal stress is required to significantly compress the material as most of the additional work is converted to entropy instead of additional restoring stress (segment AB). As a result, for a final compression large enough that the yield point is exceeded, the initial state of the material can be linked to the corresponding final state only by an elastic compression of fixed strength up to the cusp (segment OA) and a plastic compression from the cusp to the final level (segment AB). The increment in the slope of the segment initiated at A as the strength of the shock increases is related to the acceleration of the plastic region. If the total compression is large enough, the initial state

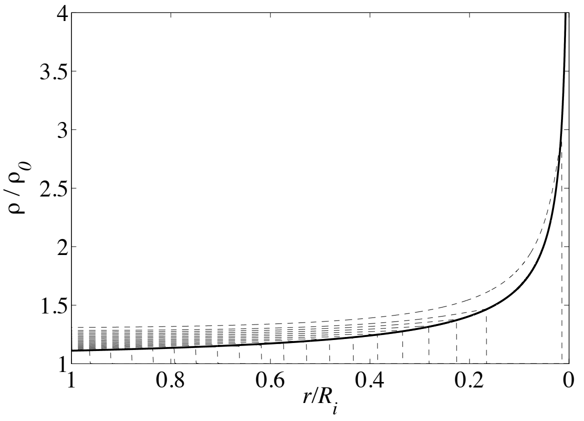

(a) ρ/ρ_0 vs r/R_i for plastic shock

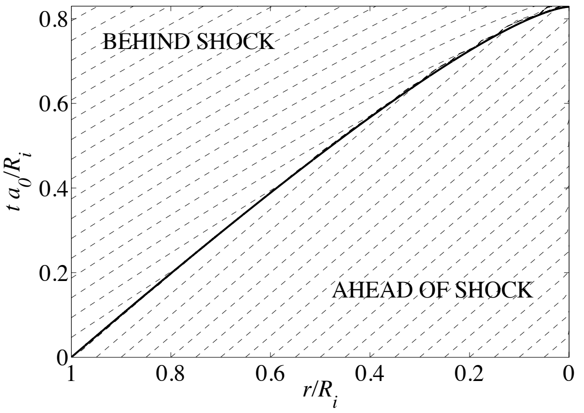

(b) $r - t$ diagram

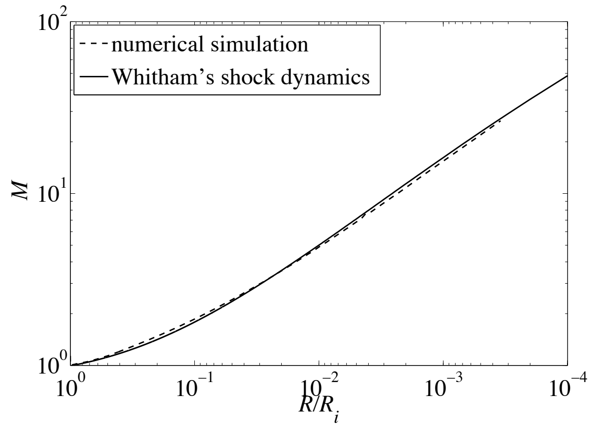

(c) $R/R_i - M$ logarithmic

Figure 4.4: Spherically symmetric ($s = 3$) converging shock initially started at $R = R_i$ with $J_i = 0.9$ (i.e., $M_i \approx 1.01$) and propagating from left to right into an elastic–plastic solid medium following the isothermal constitutive law (4.26) with the polynomial pressure form (4.13), and given the von Mises constraint (4.28) with $\sigma_Y = 0.29$ GPa (aluminum). See Fig. 4.1 for keys.

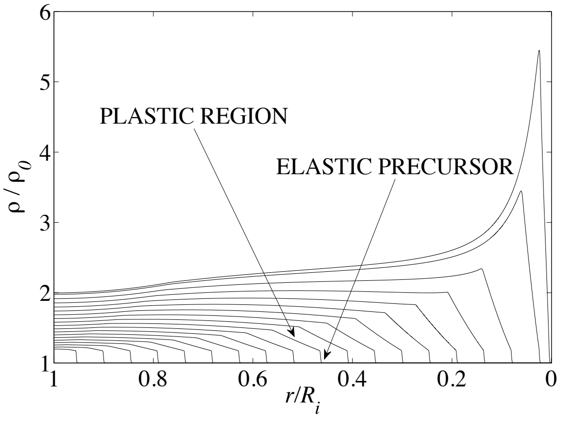

(a) Spherical $s = 3$, $J_i = 0.9$ ($M_i \approx 1.01$)

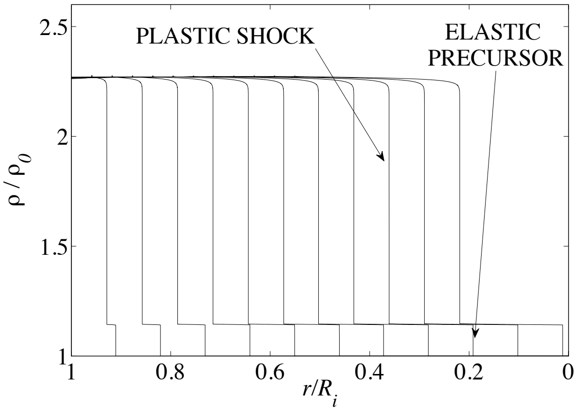

(b) Planar $s = 1$, $J_i = 0.48$

Figure 4.5: Density radial profiles obtained from the numerical simulation for (a) spherically symmetric converging and (b) planar motion. Elastic–plastic deformations follow the isothermal constitutive law (4.26), using the polynomial pressure form (4.13) with $c_1 = c_2 = c_3 = 1$GPa, and given the von Mises constraint (4.28) with $\sigma_Y = 7$GPa. Note that for the planar case an initial shock Mach number cannot be defined since the shock is started beyond the elastic–plastic transition. The elastic precursor Mach number is $M^e \approx 1.02$ for both simulations

can be directly connected to the final compressed state without going through the kink, in which case only a plastic compression occurs (segment OD). The path OAC represents the transition from the elastic–plastic to the purely plastic regime, in which the plastic region has overtaken the elastic precursor.

There exist differences with the elastic–plastic transition observed in planar geometry (see [73] for a detailed description of planar shocks in solids). In planar geometry (see Fig. 4.5(b)), a plastic discontinuity of constant strength is directly formed behind the elastic precursor (a discontinuous wave of constant strength as well) if the compression is such that the yield point is reached and that both waves can exist. In this case, the elastic precursor travels faster than the plastic shock. In

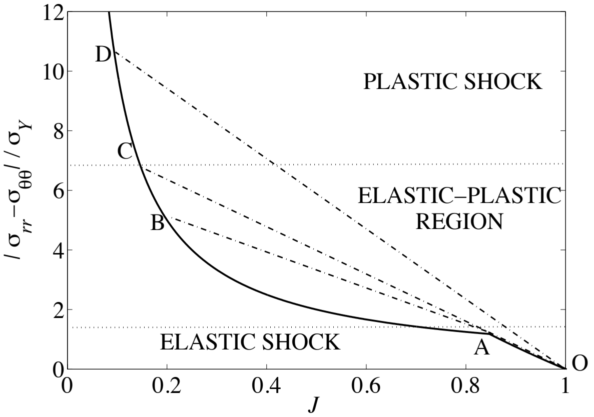

Figure 4.6: $|\sigma_{rr} - \sigma_{\theta\theta}|/\sigma_Y$ vs $J(= \rho_0/\rho)$ immediately behind the shock for an elastic–plastic material. The Hugoniot curve (i.e., the locus of the possible post-shock states of the material for a given initial condition) is completed by some Rayleigh lines (i.e., the thermodynamic path connecting the initial state with a post-shock state). Isothermal polynomial pressure form is considered, but the shape of the Hugoniot curve and the different regions can be reproduced for other constitutive laws.

the converging geometry however, as the compression increases, a plastic wave is ultimately formed with a compact radial extent, strengthens, narrows, accelerates, and ultimately overtakes the elastic precursor near the center.

4.3.3 Influence of the shear modulus and plasticity on the shock velocity

In this section, the behavior of three materials is considered: i) a purely elastic material of the aluminum kind, following the isothermal constitutive law (4.8) and (4.13); ii) its elastic–plastic equivalent, with $\sigma_Y = 0.29$ GPa; iii) the same material with 'zeroshear' ($\mu = 0$). Previous sections have confirmed that the compression term (as $\mu = 0$) becomes dominant as the shock strengthens, along with results for the converging problem that were obtained considering only the compression part of the stress [125, 50]. Figure 4.7(a) supports the form (4.11b): the shear-related deformations ($\mu \neq 0$) accelerate the shock. The existence of a finite yield stress limits this effect, giving results that are closer to the zero-shear material. This is because the existence of the finite yield stress decreases the value of the shear part of the Mach number (second term in the square root of (4.31b)) through the constraint (4.30). The time is not non-dimensionalized in this plot since a_0 depends on μ. According to Fig. 4.7(b), for a shock at a given radial location, a purely elastic material is slightly more compressed than its zero-shear and elastic–plastic equivalents due to a higher shock Mach number at a given position.

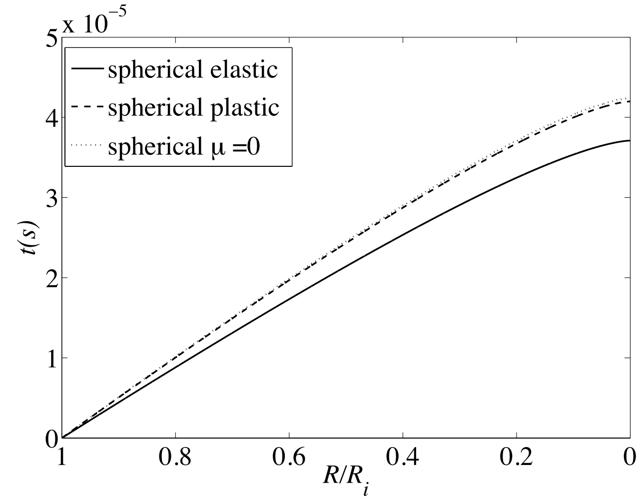

(a) Shock trajectory

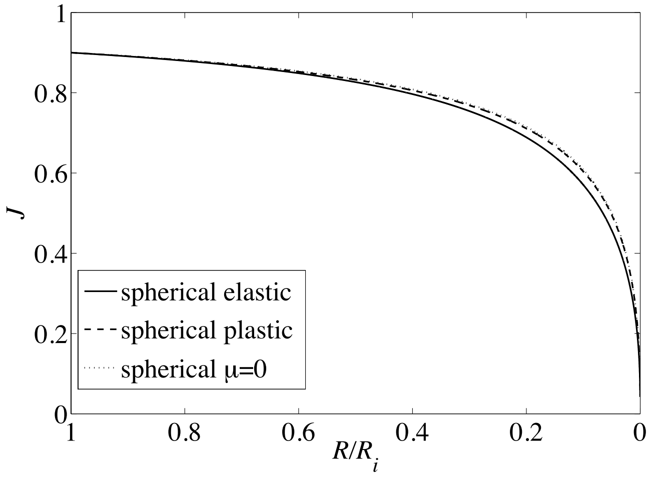

(b) $J(=\rho_0/\rho)$ at $r = R^+$ vs R/R_i

Figure 4.7: (a) Shock trajectory and (b) J immediately behind the shock vs R for a spherically symmetric ($s = 3$) converging shock initially stated at $r = R_i$ with $J_i = 0.9$. Comparisons between the purely elastic, elastic–plastic and zero-shear solid simulations using the isothermal constitutive law (4.8) or (4.26), with the polynomial pressure form (4.13). $\sigma_Y = 0.29$ GPa was used for the elastic–plastic case.

4.4 Summary

Exact solutions of Whitham's shock dynamics equations for compressible neo-Hookean elastic–plastic solids were derived. Closed expressions for the shock evolution can be obtained in terms of definite integrals. Results show that this method is a highly accurate tool for studying converging shocks, even when shear deformations and plasticity are considered in addition to the hydrostatic pressure contributions commonly used.

Analysis of the strong-shock limit reveals that the behavior of an elastic–plastic material close to the axis/origin $r = 0$ is highly dependent on the pressure law that is used. For an isothermal law with $p(\rho)$ of the type $p \propto \rho^{\alpha}$, with $\alpha > 1$, ρ is unbounded at $r = 0$ and $M \propto (\log(1/R))^{\alpha}$, where the exponent depends on α but nor on other material properties nor on the geometrical space index s. As the shock converges, its shock strength increases at a slower rate than for the two other equations of state investigated for which the density of the shocked material remains bounded close to the origin: $M \propto R^{-(s-1)}$ for an isothermal law with $p(\rho)$ of the Arctanh type, and $M \propto R^{-(s-1)/n(\gamma)}$ for the non-isothermal 'ideal gas'-like constitutive law. For both cases, the exponent depends on s, but the Arctanh strong-shock limit does not involve the maximum compression ratio ρ_{∞}/ρ_0 that the material can reach at $r = 0$, unlike the ideal gas-like material where ρ_{∞}/ρ_0 indirectly appears in $n(\gamma)$. The study of more complex constitutive laws remains open for future research.

It has been shown that the existence of shear deformation terms accelerates the shock with respect to the same material with a shear modulus artificially set to zero (i.e., with deformations induced by isotropic stresses only). However, limiting the stresses by a yield value attenuates this effect, reaching a result closer to the zero-shear case. Because weak shocks are usually sufficient to overcome the yield stress of common materials and initiate plastic deformations behind them, one can therefore conclude that isotropic stresses could be solely considered to describe the state of an elastic–plastic solid processed by converging shocks.

Finally, the transition from an elastic to a plastic shock exhibits a complex structure of two compression waves moving at different velocities that falls beyond the capabilities of Whitham's shock dynamics. Numerical simulations showed that the converging geometry modifies the elastic precursor–plastic shock structure usually observed in planar symmetry, making the converging plastic shock travel faster than the elastic precursor.

The next two chapters examine the Richtmyer–Meshkov flow in solid media. Although the topic of converging shocks may appear disconnected from the latter, aspects of the results derived from the analysis performed here are especially relevant for Chapter 6, where the effects of a converging geometry are included in the study of the shock-driven motion of an interface separating an elastic–plastic solid from a gas.

Chapter 5

Analytical model for linearized impulsive-driven Richtmyer–Meshkov flow in elastic solids

5.1 Introduction

The original Richtmyer–Meshkov problem [96] [74] describes the instability, caused by the passage of a shock wave, of the interface separating two fluids. This problem has been the subject of study in many fields [20], including inertial confinement fusion [63], astrophysical phenomena [6], magnetohydrodynamics [120] and solid mechanics [95].

In the field of solid mechanics, Plohr and Plohr [95] performed an analysis based on linearized compressible elasticity, using free-slip boundary conditions and neo-Hookean stress-strain relations. The numerical solution of the resulting equations for a discrete range of initial conditions and material parameters revealed that the behavior of the interface separating two solids was oscillatory and stable after the shock wave– interface interaction, with shear waves advecting vorticity from the interface.

Piriz et al. [90] performed both local analysis and simulations to derive an approximate result for the long time behavior of the interface. They provide a long time approximation for the amplitude and frequency of the interface oscillations. However, it is unclear what boundary conditions exactly were applied.

Richtmyer–Meshkov flow has similarities with other types of flows that are unstable for fluids, such as the Rayleigh–Taylor problem. In the field of solid mechanics, this flow has been studied too. Plohr and Sharp in 1998 [94] used Laplace transform methods to study the instability of an incompressible metal plate to derive an expression for the critical wavelength beyond which the flow is unstable. They also demonstrate the existence of shear waves in the solids, which dissipate the vorticity deposited at the interface by an impulse. Other contributions come from Piriz et al. [89] and Terrones [105].

In this chapter, the stability of the Richtmyer–Meshkov problem for elastic solids using an incompressible, linearized and impulse-driven model to obtain a simple time-dependent solution is demonstrated. Using transform techniques, the stability calculation reduces to an analysis of the locations of singularities in the complex plane. Two distinct long-term types of behavior are identified for both free-slip and no-slip boundary conditions: decaying oscillations and standing waves. An analysis of the vorticity distribution shows that the shear stiffness of the solids is responsible both for the stabilization of the interface, and also for the period of the interface oscillations. Finally, comparisons with previous results in the literature and numerical simulations are discussed.

5.2 Problem description

The impulsive Richtmyer–Meshkov problem for solids is formulated using linearization of small perturbations and two-dimensional, plane-strain conditions for both materials. Fig. 5.1 shows the initial configuration and the parameters that influence the problem. The shock wave that initiates the motion of the system in the compressible Richtmyer–Meshkov problem is replaced by an impulsive acceleration $V\delta(t)$. The interface is described as perpendicular to the direction of the impulse with the addition of a sinusoidal perturbation of wavelength $2\pi/k$ and initial amplitude η_0. Both materials ($j = -, +$) are described by their density ρ_j and their shear wave speeds $c_j = \sqrt{\mu_j/\rho_j}$, where μ_j is the material shear modulus. The materials are taken to be purely elastic and incompressible.

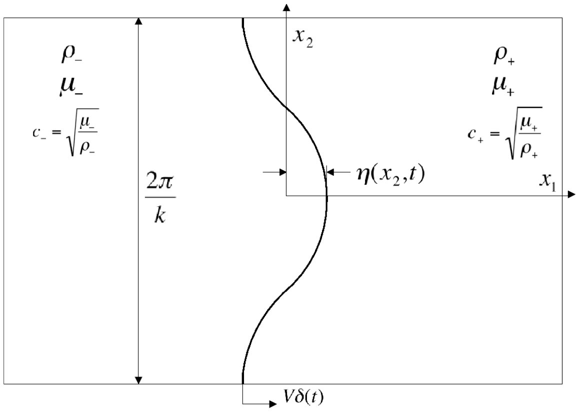

Figure 5.1: Description of the problem. The interface is $x_1 = \eta(x_2, t)$. Left and right states are denoted "$-$" and "$+$", respectively.

Limitations to this model are given essentially by the amplitude–wavelength interface parameter $\eta_0 k$. In the first place, a shock takes a finite time to completely cross a perturbed interface, which will produce discrepancies between the early time behavior of the model and that of a numerical simulation using the compressible Euler equations. In addition, the interface amplitude changes as the shock goes through it, although this effect can be corrected by estimating the final amplitude after shock passage and providing that value as input for the analytical model. $\eta_0 k$ is directly responsible as well for the strength of the shock waves, which can deviate from linearity as the interface parameter increases. To this effect, when comparing to numerical simulations, $\eta_0 k < 0.1$ is generally chosen. Another source of inaccuracies is the assumption of incompressibility. In the case of a shock-driven motion, material density is changed. For comparison with numerical simulations, the density observed after shock passage assuming an unperturbed interface is used as input for the analytical model. Another effect of compressibility is the formation of acoustic waves resulting from the distortion of the shock wave after crossing a perturbed interface, which cannot be captured by an incompressible model. These waves are less noticeable when the shock is weak and $\eta_0 k$ small and as the shock moves away from the interface. With this considerations, one can predict that the assumptions made have a large influence in the start-up and short-term behavior but that the long-term behavior must be closer to the one observed in compressible solids.

Mass conservation and momentum equations are applied to each material in order to obtain a system of partial differential equations for evolution of the perturbed flow while boundary conditions relate the velocities and stresses at the interface between materials. The system is transformed in time by a Laplace transform, and in one spatial dimension by a normal-mode assumption. The resulting fourth-order ordinary differential equation for the transform of the velocity field in each material is then solved. From this expression, other useful variables, such as amplitude of the interface and the vorticity, can be calculated.

5.3 Equations of motion and boundary conditions

The general form of the conservation equations (Eqs.(2.1) and (2.7)) as functions of the set of primitive variables $(\rho, \mathbf{u}, \mathbf{g})$ is described here along with the incompressibility and plane-strain constraints. These equations are specialized in the following sections to describe the base flow and the perturbed flow.

Mass conservation and conservation of linear momentum are expressed in Eulerian form as

$$\frac{\partial u_i}{\partial x_i} = 0 \tag{5.1}$$

and

$$\rho \frac{\partial u_i}{\partial t} + \rho u_j \frac{\partial u_i}{\partial x_j} - \frac{\partial \sigma_{ij}}{\partial x_j} = 0. \tag{5.2}$$

The evolution of the inverse deformation tensor follows:

$$\frac{\partial g_{Ij}}{\partial t} + \frac{\partial}{\partial x_j}(g_{Ik} u_k) = 0. \tag{5.3}$$

Finally, the kinematic equation that describes the evolution of the interface $\eta(x_2, t) - x_1 = 0$ is given by

$$\frac{D}{Dt}\left(\eta(x_2, t) - x_1\right) = 0, \tag{5.4}$$

where $D/Dt = \partial/\partial t + u_j \partial/\partial x_j$ is the material derivative.

The assumptions of plane strain and incompressibility impose relations between the elements of the inverse deformation tensor $\mathbf{g}$. From the two-dimensionality of plane strain, these simplifications follow:

$$g_{13} = g_{23} = g_{31} = g_{32} = 0, \quad g_{33} = 1. \tag{5.5}$$

This may be combined with conservation of mass expressed as $\det(\mathbf{g}) = \rho/\rho_0$ to give

$$g_{11}g_{22} - g_{21}g_{12} = 1, \tag{5.6}$$

for an incompressible material.

To close the problem, a constitutive law relating stresses to the material deformation is defined. Both materials are modeled following a neo-Hookean [61] constitutive relation:

$$\sigma_{ij} = -p\delta_{ij} + \mu F_{iK}F_{jK}, \tag{5.7}$$

where pressure p is a Lagrange multiplier that enforces incompressibility, i.e., p satisfies

$$\frac{\partial^2 p}{\partial {x_i}^2} = \frac{\partial^2}{\partial x_i \partial x_j}(-\rho u_i u_j + \mu F_{iK}F_{jK}), \tag{5.8}$$

for uniform ρ. Additionally one can show in this case that $\partial^2/\partial x_i \partial x_j (F_{iK}F_{jK}) = 0$, leaving an equation equivalent to its hydrodynamic counterpart.

5.3.1 Boundary conditions

Boundary conditions at the interface η relate variables from each material. Defining $\mathbf{n}$ and $\mathbf{t}$ as the unit normal and tangent at the boundary, in a free-slip interface, the four boundary conditions are, respectively, continuity of normal velocity, continuity of normal stress, and zero tangential stress,

$$\begin{aligned} [|u_i|]n_i &= 0, && (5.9)\\ n_i[|\sigma_{ij}|]n_j &= 0, && (5.10)\\ t_i\sigma^-_{ij}n_j = {} & 0 = t_i\sigma^+_{ij}n_j, && (5.11) \end{aligned}$$

where $[|q|]$ indicates the jump $q^+ - q^-$. In the case of no-slip boundary conditions, continuity of tangential velocities and stresses is enforced,

$$\begin{aligned} [|u_i|]t_i &= 0, & (5.12) \\ t_i[|\sigma_{ij}|]n_j &= 0. & (5.13) \end{aligned}$$

in addition to Eqs. (5.9–5.10). Boundary conditions at infinity are imposed as radiation conditions, requiring all waves at infinity to be outgoing.

5.4 Base flow and linearization

The trivial base flow assumes a planar interface aligned with the x_2 axis and perpendicular to the direction of the impulse. The resulting one-dimensional motion depends on x_1, t only and does not deform the material. The reference frame is chosen with the unperturbed interface located at $x_1 = 0$ after the impulse at $t = 0$, so that

$$\eta = -Vt\,(H(t) - 1)\,, \tag{5.14}$$

where V is the impulsive velocity and $H(t)$ is the Heavyside function. In each material the velocity, deformation and pressure fields are given by

$$\begin{aligned} u_1 &= -V\,(H(t) - 1)\,, & (5.15) \\ u_2 &= 0, & (5.16) \\ g_{Ij} &= \delta_{Ij}, & (5.17) \\ p &= \rho V \delta(t) x_1 + \mu, & (5.18) \end{aligned}$$

where the resulting Cauchy stress $\sigma_{ij} = -\rho V \delta(t) x_1 \delta_{ij}$ represents the fact that for this special geometry the material is in an unstressed state before and after the impulse.

5.4.1 Linearization

Once the base flow variables are known, the complete value of each variable q defining the problem is calculated by adding a perturbation term q' to the base flow result $\overline{q}$, i.e., Eqs. (5.14–5.18). Substituting $q = \overline{q} + q'$ in the equations of motion, Eqs. (5.1–5.4), and retaining terms that are at most linear in perturbation quantities gives the following system of linear equations for the perturbed variables:

$$\frac{\partial u'_j}{\partial x_j} = 0, \tag{5.19}$$

$$\rho\frac{\partial u'_j}{\partial t}+\overline{u_1}\frac{\partial u'_i}{\partial x_1}-\frac{\partial \sigma'_{ij}}{\partial x_i}=0, \tag{5.20}$$

$$\frac{\partial \eta'}{\partial t}-u'_1=0, \tag{5.21}$$

$$\frac{\partial g'_{Ij}}{\partial t}+\overline{u_1}\frac{\partial g'_{I1}}{\partial x_j}+\frac{\partial u'_i}{\partial x_j}=0, \tag{5.22}$$

where $\overline{u_1}$ is given by equation (5.15).

Linearization of the neo-Hookean stress-strain relations, Eq. (5.7), produces

$$\sigma'_{ij}=-p'\delta_{ij}-\mu(g'_{ij}+g'_{ji}), \tag{5.23}$$

the familiar relation for a Hookean material of linear elasticity with Lamé's first parameter $\lambda = 0$.

The boundary conditions for the normal velocity, normal stress and free-slip conditions, Eqs. (5.9–5.13), respectively, become,

$$\begin{aligned} [|u'_1|] &= 0, && (5.24)\\ [|\sigma'_{11}|] &= -[|\rho|]\,V\eta'\delta(t), && (5.25)\\ \sigma'^{-}_{21} = & \; 0 \; = \sigma'^{+}_{21}, && (5.26) \end{aligned}$$

and are applied on the unperturbed interface (i.e., at $x_1 = 0$ for $t \geq 0$). In the case of no-slip boundary conditions, the following relation is used in place of (5.26):

$$\begin{aligned} [|u'_2|] &= 0, && (5.27)\\ [|\sigma'_{21}|] &= 0, && (5.28) \end{aligned}$$

5.5 Solution of the problem

When assuming that the interfacial perturbation is initially sinusoidal in x_2, the resulting perturbation solutions may be expressed as Fourier modes in x_2, $q'(t, x_1, x_2) = \hat{q}(x_1, t)\exp(ikx_2)$. In addition, the differential expressions that have time dependence are converted to algebraic relations using the Laplace transform. The initial conditions for the perturbations precede the impulse and are thus zero.

Denoting the Laplace transforms of a variable $\hat{q}$ with capital letters (e.g., $G_{Ij} = \mathcal{L}[\hat{g}_{Ij}]$), the linearized equations (5.19–5.22) become

$$\frac{d}{dx_1}U_1+ikU_2=0, \tag{5.29}$$

$$\rho sU_1+2\mu\frac{d}{dx_1}G_{11}+\frac{d}{dx_1}P+\mu ik(G_{12}+G_{21})=0, \tag{5.30}$$

$$\rho s U_2 + 2\mu i k G_{22} + ikP + \mu \frac{d}{dx_1}(G_{12} + G_{21}) = 0, \tag{5.31}$$

$$sG_{I1} + \frac{d}{dx_1} U_i = 0, \tag{5.32}$$

$$sG_{i2} + ikU_i = 0. \tag{5.33}$$

This system of equations is manipulated to obtain an expression for U_1, which is a fourth-order ordinary differential equation to be solved separately in each material (i.e., $x_1 < 0$ and $x_1 > 0$)

$$\frac{d^4}{dx_1{}^4} U_1 - \left(\frac{s^2}{c^2} - 2k^2\right) \frac{d^2}{dx_1{}^2} U_1 + \left(\frac{k^2 s^2}{c^2} + k^4\right) U_1 = 0, \tag{5.34}$$

where $c^2 = \mu/\rho$. The general solution for U_1 is spanned by the fundamental solutions

$$\{e^{kx_1}, e^{-kx_1}, e^{\sqrt{\frac{s^2}{c^2}+k^2}x_1}, e^{-\sqrt{\frac{s^2}{c^2}+k^2}x_1}\}. \tag{5.35}$$

Apart from the four boundary conditions imposed at the interface (5.24–5.28), regular boundary conditions at infinity are imposed after a suitable definition of the generally multi-valued square root. Recalling that the inverse Laplace transform is defined by a vertical contour of integration in the complex s-plane located to the right of all singularities, the square roots are explicitly defined to have positive real parts in the right half-plane. Boundary conditions at $x_1 \to \pm\infty$ then imply

$$U_1^{\pm}(s, x_1) = A_{\pm}(s) e^{\mp k x_1} + B_{\pm}(s) e^{\mp\sqrt{\frac{s^2}{c_{\pm}^2}+k^2}x_1}, \tag{5.36}$$

where the upper sign is taken for $x_1 > 0$ and the lower sign for $x_1 < 0$.

The four unknowns, $A_{\pm}(s), B_{\pm}(s)$, are determined by application of the four interface boundary conditions equation transformed into Laplace space. Solving the resulting linear system in the case of free-slip gives

$$A_{\pm}^{fs}(s) = \frac{(r-1)V\eta_0 ks(2c_{\pm}^2 k^2 + s^2)}{\Omega^{fs}(s)}, \tag{5.37}$$

$$B_{\pm}^{fs}(s) = -\frac{(r-1)V\eta_0 ks 2c_{\pm}^2 k^2}{\Omega^{fs}(s)}, \tag{5.38}$$

where $\Omega^{fs}(s)$ is given by

$$\Omega^{fs}(s) = (1+r)s^4 + 4c_-^2 k^2 s^2 + 4c_+^2 k^2 r s^2 - 4c_-^4 k^4 \left(-1 + \sqrt{1 + \frac{s^2}{c_-^2 k^2}}\right) - 4c_+^4 k^4 r \left(-1 + \sqrt{1 + \frac{s^2}{c_+^2 k^2}}\right) \tag{5.39}$$

and $r = \rho_+/\rho_-$. The expression obtained for no-slip boundary conditions is more complex,

$$A_-^{ns}(s)\Omega^{ns}(s) \quad = \quad (r-1)V\eta_0 ks(c_+^2 k^2 r(2 - 2G^+(s)) + ...$$

$$\begin{aligned} &+ \quad s^2(-1+r+rG^-(s)+G^+(s)) + c_-^2k^2(-2+2G^+(s))), && (5.40) \\ B_-^{ns}(s)\Omega^{ns}(s) \quad &= \quad -(r-1)V\eta_0 k2s(c_-^2k^2(-1+G^+(s)) + ... \\ &+ \quad r(s^2 + c_+^2k^2(1-G^+(s)))), && (5.41) \\ A_+^{ns}(s)\Omega^{ns}(s) \quad &= \quad (r-1)V\eta_0 ks(c_-^2k^2(2-2G^-(s)) + ... \\ &+ \quad 2c_+^2k^2r(-1+G^-(s)) + s^2(1+G^+(s)+r(-1+G^-(s)))), && (5.42) \\ B_+^{ns}(s)\Omega^{ns}(s) \quad &= \quad -(r-1)V\eta_0 k2s(s^2 + c_-^2k^2(1-G^-(s)) + ... \\ &+ \quad c_+^2k^2r(-1+G^-(s))), && (5.43) \end{aligned}$$

where $G^{\pm}(s)$ and $\Omega^{ns}(s)$ are given by

$$G^{\pm}(s) = \sqrt{1+\frac{s^2}{c_{\pm}^2k^2}}, \tag{5.44}$$

$$\Omega^{ns}(s) = C(s) + D(s)G^-(s) + E(s)G^+(s) + F(s)G^-(s)G^+(s), \tag{5.45}$$

$$\tag{5.46}$$

with components

$$C(s) = -\left(s^2(1-r) - 2(c_+^2k^2r - c_-^2k^2)\right)^2, \tag{5.47a}$$

$$D(s) = 4(c_-^2k^2 - c_+^2k^2r)^2 + 4s^2(c_+^2k^2r^2 - c_-^2k^2r) + s^4(r+r^2), \tag{5.47b}$$

$$E(s) = 4(c_-^2k^2 - c_+^2k^2r)^2 + 4s^2(-c_+^2k^2r + c_-^2k^2) + s^4(1+r), \tag{5.47c}$$

$$F(s) = -4(c_-^2k^2 - c_+^2k^2r)^2. \tag{5.47d}$$

From the expression for the normal velocity, the problem is solved in the complex s-plane. All other transformed variables may be obtained from $U_1(x_1, s)$ by manipulation of Eqs. (5.29–5.33).

Before analyzing the solutions in detail, physical insight is obtained by examining the evolution of vorticity, defined for a two-dimensional flow as $\omega = \partial u_2/\partial x_1 - \partial u_1/\partial x_2$. By taking the curl of the linearized momentum equation (5.20) to eliminate the hydrodynamic pressure and then differentiating in time to expresses the time derivative of the stress in terms of the rate of strain with the aid of Eq. (5.22), one finds that the vorticity due to the linear perturbations satisfies the second-order wave equation,

$$\frac{\partial^2\omega'}{\partial t^2} = c^2\frac{\partial^2\omega'}{\partial {x_i}^2} \tag{5.48}$$

in each material for $t > 0$. The fourth-order ODE, Eq. (5.34), is simply the Laplace transform of this equation cast in terms of $\hat{u}_1$ after the normal-mode assumption has been made: $u'(t, x_1, x_2) = \hat{u}(t, x_1)\exp(ikx_2)$.

Using incompressibility (5.19), vorticity can be expressed solely in terms of the velocity perturbation $\hat{u_1}$ as

$$\omega'(t,x_1,x_2) = \hat{\omega}(t,x_1)e^{ikx_2} = i\left(-k\hat{u}_1 + \frac{1}{k}\frac{\partial^2 \hat{u}_1}{\partial {x_1}^2}\right)e^{ikx_2}. \tag{5.49}$$

From this one may readily verify that the $A_\pm(s)$ solution in Eq. (5.36) corresponds to an irrotational velocity field, while the $B_\pm(s)$ solution identifies shear waves. Note that expression (5.49) holds within each solid but not at the interface, where a finite jump of the tangential velocity u_2 produces an additional vortex sheet if free-slip boundary conditions are imposed. In the free-slip case, the Laplace transform of Eq. (5.49) may be written as,

$$\omega_\pm(s,x_1) = -2ikU_1(s,0)e^{\mp\sqrt{\frac{s^2}{c_\pm^2 k^2}+1}\ kx_1}, \tag{5.50}$$

where $U_1(s,0) = U_1^+(s,0) = U_1^-(s,0)$ is the transform of the normal velocity at the interface. Excluding the vortex sheet the remaining vorticity ω is continuous at the interface. Alternatively, vorticity is discontinuous at $x_1 = 0$ when no-slip boundary conditions are imposed

$$\omega_-(s,x_1<0) = -2ik^2V\eta_0\frac{(r-1)s^3G(s)}{\Omega^{ns}(s)}e^{\sqrt{\frac{s^2}{c_\pm^2 k^2}+1}\ kx_1}, \tag{5.51a}$$

$$\omega_+(s,x_1>0) = 2ik^2V\eta_0\frac{(r-1)s^3H(s)}{\Omega^{ns}(s)}e^{-\sqrt{\frac{s^2}{c_\pm^2 k^2}+1}\ kx_1}, \tag{5.51b}$$

with

$$G(s) = \left(c_-^2k^2\left(-1+\sqrt{1+\frac{s^2}{c_+^2k^2}}\right)+r\left(s^2+c_+^2k^2\left(1-\sqrt{1+\frac{s^2}{c_+^2k^2}}\right)\right)\right), \tag{5.52a}$$

$$H(s) = \left(s^2+c_-^2k^2\left(1-\sqrt{1+\frac{s^2}{c_-^2k^2}}\right)+c_+^2k^2r\left(-1+\sqrt{1+\frac{s^2}{c_-^2k^2}}\right)\right). \tag{5.52b}$$

Using the convolution theorem, the vorticity mode in physical space $\hat{\omega}(t,x_1)$ can be computed as,

$$\hat{\omega}_\pm(x_1,t) = \int_0^t \hat{\omega}(\tau,x_1=0)\hat{g}_\pm(t-\tau,x_1)\ d\tau, \tag{5.53}$$

where $\hat{g}_\pm(t,x_1) = \mathcal{L}^{-1}[\exp(\mp\sqrt{\frac{s^2}{c_\pm^2k^2}+1}\ kx_1)]$ and $\hat{g}_\pm(t,x_1)\exp(ikx_2)$ satisfies the second-order wave equation (5.48) as outward radiating waves. This convolution expression shows how the vorticity that is deposited at the interface is transported by the shear waves into the materials for $t > 0$.

5.6 Analysis of the interface behavior

To determine the time-dependent behavior of the velocity field, interface amplitude, or other quantities of interest, the inverse Laplace transform of the s-dependent expressions is performed. The

Bromwich integral offers a general way of performing this operation,

$$f(t) = \mathcal{L}^{-1}\{F(s)\} \equiv \frac{1}{2\pi i} \lim_{T\to\infty} \int_{\gamma-iT}^{\gamma+iT} e^{st} F(s)\, ds, \tag{5.54}$$

where γ is a real value situated to the right of all singularities of the function $F(s)$.

Expression (5.54) can be calculated numerically to obtain the complete evolution of the interface η in time and such results are reported in the next section. Here, the tools of complex analysis and asymptotics are used to examine analytically both the initial growth rate and the long-term behavior of the interface.

5.6.1 Short-time interface behavior

From Eq. (5.21) (i.e., $\partial\eta'/\partial t = u_1'(0, x_2, t)$), one can see that the growth rate of the linearized interface may be computed by calculating the inverse Laplace transform of $U_1(s, x_1 = 0)$. Using Eq. (5.36), this quantity may be computed as

$$\frac{\partial\hat{\eta}}{\partial t} = \mathcal{L}^{-1}\left[\frac{(r-1)V\eta_0 k s^3}{\Omega^{fs}(s)}\right], \tag{5.55}$$

for free-slip boundary conditions, or alternatively as

$$\frac{\partial\hat{\eta}}{\partial t} = \mathcal{L}^{-1}\left[\frac{(r-1)V\eta_0 k s^3 \left(-1+\sqrt{1+\frac{s^2}{c_+^2 k^2}} + r\left(-1+\sqrt{1+\frac{s^2}{c_-^2 k^2}}\right)\right)}{\Omega^{ns}(s)}\right], \tag{5.56}$$

when no-slip boundary conditions are enforced. The familiar impulsive Richtmyer-Meshkov result for inviscid fluids can be recovered by eliminating the shear strength $\mu_\pm$ of the materials (i.e., $c_\pm = 0$). This reduces Eqs. (5.55–5.56) to

$$\frac{\partial\hat{\eta}}{\partial t} = \mathcal{L}^{-1}\left[\frac{(r-1)}{(r+1)}\frac{V\eta_0 k}{s}\right] = \frac{(r-1)}{(r+1)} V\eta_0 k, \tag{5.57}$$

from which one sees that the perturbation amplitude grows linearly in time. The ratio $(r-1)/(r+1)$ is the Atwood number A_t.

For the case of elastic solids, the initial growth rate for *any value of shear strength* is also given by Eq. (5.57) as can be seen by examining the large s limit $U_1(0, s) \sim A_t V\eta_0 k/s$. Physically for times much shorter than the characteristic shear wave speeds $t \ll 1/(kc)$ the vorticity is located approximately at the interface and the interface initially evolves as in the fluid example.

5.6.2 Long-time interface behavior

From Eq. (5.55), the time-dependent behavior of the interface amplitude $\hat{\eta}(t)$ is:

$$\hat{\eta}(t) = \eta_0 + \mathcal{L}^{-1}[N_i(s)], \tag{5.58}$$

where i takes the values fs or ns for free or no-slip boundary conditions respectively, and

$$N_{fs}(s) = \frac{(r-1)V\eta_0 k s^4}{\Omega^{fs}(s)}, \tag{5.59a}$$

$$N_{ns}(s) = \frac{(r-1)V\eta_0 k s^4\left(-1+\sqrt{1+\frac{s^2}{c_+^2k^2}}+r\left(-1+\sqrt{1+\frac{s^2}{c_-^2k^2}}\right)\right)}{\Omega^{ns}(s)}. \tag{5.59b}$$

$\Omega^i(s)$ is as defined in Eqs. (5.39) and (5.45). In performing the inverse transform, the analytic properties of the denominator Ω^i determine the time dependence of the solution.

With the aim of obtaining the long-time behavior of the interface, a specific representation of Ω^i is constructed and the Bromwich integral is deformed around the possible singularities.

While the square roots in Ω^i have been defined to have a positive real part in $Re(s) > 0$, there are several possibilities for the specific locations of the branch cuts. Fig. 5.2 shows the set of branch cuts that was used for our analysis. This choice offers the possibility of applying linearization techniques to calculate the long-term behavior, as is shown later in this section.

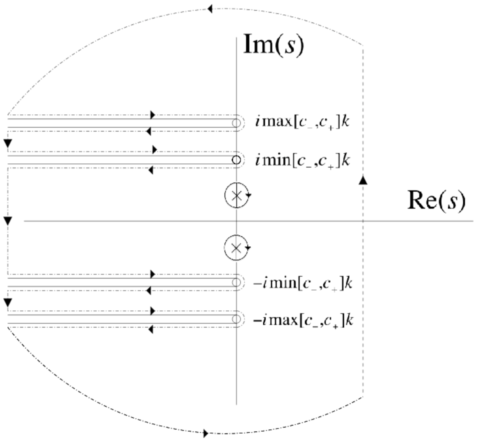

Figure 5.2: Set of branch cuts used for the analysis and deformation of the Bromwich integral. Two poles are shown in the imaginary axis, which is not a general case. For any pole found, the contour is deformed to surround it.

Using this disposition of branch cuts, the Bromwich integral for η can be closed in the left half-plane for $t > 0$ and computed as:

$$\hat{\eta}(t) = \eta_0 + \frac{1}{2\pi i}\sum_n Res(N(s_n))e^{s_n t}$$
$$+$$
$$\frac{1}{2\pi i}\sum_{l=-}^{+}\int_0^\infty e^{-x_1 t + ic_l t}\left[N(-x_1 + ic_l^b k) - N(-x_1 + ic_l^a k)\right] dx \tag{5.60}$$
$$+$$
$$\frac{1}{2\pi i}\sum_{l=-}^{+}\int_0^\infty e^{-x_1 t - ic_l t}\left[N(-x_1 - ic_l^b k) - N(-x_1 - ic_l^a k)\right] dx,$$

where s_n are the possible zeros of the denominator; the superscripts "a" and "b" determine the value of the function right above and below of the branch cut respectively. The part of the contour that lies at infinity has no contribution according to Jordan's lemma and the turning-integrals around the branch points can be shown to contribute nothing as their radius goes to zero.

Hence, the behavior of the interface is determined by the residue of the amplitude function in the complex s-plane at the zeros of Ω^i and by the integration around the branch cuts.

5.6.2.1 The contributions of the branch cuts

It can be seen directly that the oscillatory exponentials may be taken out of the integrals in Eq. (5.60). In addition, it can be shown that the magnitude of the integrals decays with time. This follows from the fact that functions $|N(s)|$ are, in general, bounded along the branch cuts, although there are certain discrete parametric exceptions that correspond to poles of $N(s)$ crossing a branch cut and onto a separate sheet. In such a case, the poles are simple poles and the principal value of the integrals is well defined.

The long-time asymptotic contributions from the branch integrals to $\hat{\eta}(t)$ may be computed using Watson's lemma [15]. Essentially for large t, an expansion of $[N(-x_1 \pm ic^b k) - N(-x_1 \pm ic^a k)]$ about $x_1 = 0$ is used. Note that care must be taken in treating the various square roots with respect to the disposition of the branch cuts. Local to a given branch-point, such a procedure gives an expression of the form

$$N(-x_1 \pm ic^b k) - N(-x_1 \pm ic^a k) = \sqrt{x_1}\sum_{j=0}^{\infty} a_j {x_1}^j, \tag{5.61}$$

where $\sqrt{x_1}$ denotes the usual real square root. Then, expression (5.61) multiplied by $\exp(-x_1 t)$ and integrated gives terms in $1/t^{3/2}$, $1/t^{5/2}$, $1/t^{7/2}, \ldots$ When the exponentials $\exp(\pm ickt)$ are included, the resulting terms clearly oscillate with the shear wave frequency while decaying to 0 as $t \to \infty$. Appendix B develops an approximation for the growth rate using the first term ($a_0\sqrt{x_1}$) of this approximation.

5.6.2.2 The contributions of the poles

The denominator Ω^i is a single-valued sheet of a multi-valued function containing square roots. A rationalization is performed by forming the product of all sheets to obtain a polynomial of degree 16 and 20 respectively for the cases of free-slip and no-slip. The roots of this polynomial are computed numerically but only a few are real zeros of Ω^i. A simple evaluation of the denominator at the roots allows one to determine which residues need to be computed. The number of these poles varies depending on the parameters of the problem.

The analysis reveals that all the zeros of Ω^i correspond to simple poles of $N(s)$ and lie in $Re(s) \leq 0$, which combined with our analysis of the branch-cut integrals indicates that the interface may be classified as stable. The positions of the poles depend on the ratio of shear wave velocities c_-/c_+ and the density ratio r.

Exploring this parameter space, regions are found where there are a pair of conjugate poles that lie in the imaginary axis (oscillatory) and regions where all poles lie in $Re(s) < 0$. Fig. 5.3 shows the region in parameter space where the dominant poles produce pure oscillatory behavior and in the region where the poles contribute at most exponentially decaying oscillatory behavior.

Oscillatory behavior is obtained when both materials have a similar shear wave speed. The region around $c_-/c_+ = 1$ where this happens depends on the density ratio r. As the ratio c_-/c_+ separates from 1, the pure imaginary poles travel along the imaginary axis towards the lowest pair of branch points. As this happens, the amplitude of the oscillations decreases, representing a smooth transition towards decaying oscillatory behavior. After a certain critical value of the shear wave velocity ratio, which depends on the density ratio, the poles reach the lowest branch cut and disappear and for such parameters, the interface amplitude oscillates while decaying with time to η_0. Some differences arise between the free-slip and no-slip cases as the region of oscillatory behavior is narrower in the latter. In particular, one can appreciate that, in the neighborhood of $r = 1$, the oscillatory behavior is restricted to situations in which the shear wave speeds are extremely close to each other.

A particular case, represented in Fig. 5.3(a), that gives oscillatory behavior of the interface is that of one shear wave velocity being zero and the other finite (or one being finite and the other infinite). This case is the asymptotic result of the decaying behavior and will be explained by monitoring the location of the poles closest to the imaginary axis.

Fig. 5.4 shows the position of the closest pole with respect to the imaginary axis and relative to the position of the branch cuts with $c_- \geq c_+$. First, the poles lie in the imaginary axis for $c_- = c_+$ and they approach the lower branch cut as c_- increases. After that, if c_- keeps increasing, the poles reappear from the superior branch cut and separate from it approaching the imaginary axis.

In conclusion, when our shear wave velocities are far from $c_- = c_+$, the behavior of the interface is decaying. As the values of the shear wave velocities separate from each other, a pair of conjugate

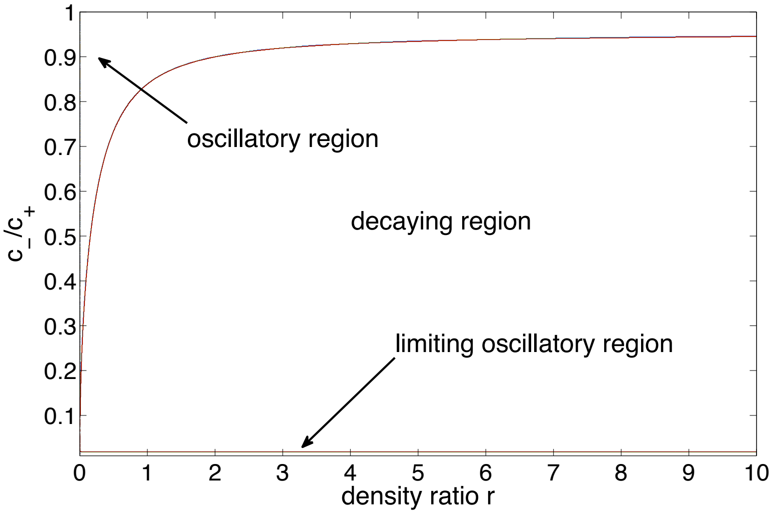

(a) Free-slip

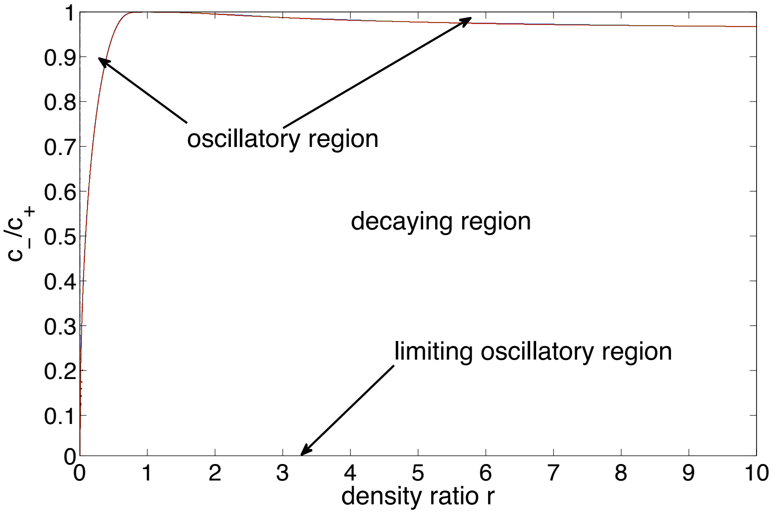

(b) No slip

Figure 5.3: Regions of existence / non-existence of pure imaginary poles. A parametric set that lies in the first / second region produces an oscillatory / decaying behavior of the interface, respectively.

poles tend to approach the imaginary axis. This means that the interface behavior in time looks like an oscillatory exponential decay that decays more slowly as the values of the shear wave velocity are more distinct. Finally, when one of them becomes 0, the pole reaches the imaginary axis and the behavior of the interface is oscillatory in time.

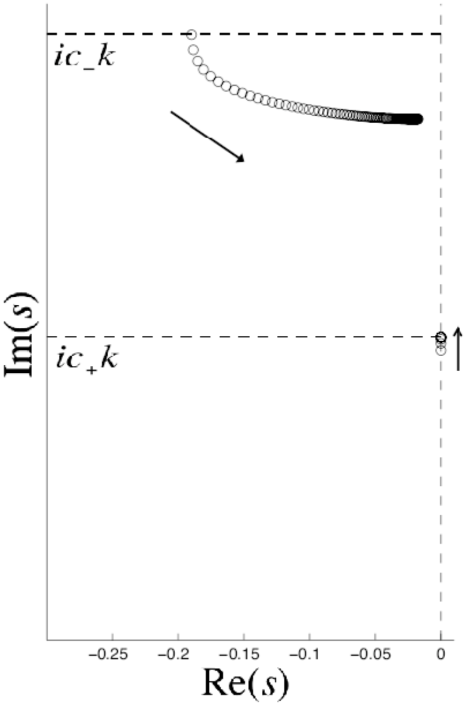

Figure 5.4: Position of the closest pole with respect to the imaginary axis and relative to the branch cuts (horizontal dashed lines). Another conjugate pole lies in $Im(s) < 0$. Arrows show the direction the poles follow when incrementing c_- leaving c_+ and r unchanged. When both velocities are similar, the poles lie on the imaginary axis and the interface oscillates. After reaching the branch cut, the pole reappears and tends to the imaginary axis as $c_- \to \infty$.

5.6.3 Conclusions of the analysis

Two different long-term types of behavior for the interface amplitude $\hat{\eta}(t)$ are identified: pure oscillatory and oscillatory decay. When discussed in terms of the interface $\eta(t, x_2) = \hat{\eta}(t)\exp(ikx_2)$ these correspond to standing oscillatory waves and decaying waves.

As the branch cut integration always results in algebraically decaying waves oscillating at the two shear speeds, the classification of the late-time behavior is a function of the locations of poles, i.e., the zeros of Ω. For the oscillatory case, after an initial transient due to the branch cuts, the interfacial waves oscillate at a frequency determined by the position of the poles on the imaginary axis. The relative amplitude of this wave depends on the position of the poles too through the calculation of residues. This amplitude decreases as the critical value of c_-/c_+ is parametrically approached. After that, the behavior changes to time-dependent decay.

Physically the free-slip condition allows interfacial shear waves to persist when the shear speeds are similar in both materials, but when these nonzero speeds differ too greatly (Fig. (5.3(a))) such waves decay.

The other case that gives a late-time oscillatory behavior for $\hat{\eta}(t)$ is the extreme case of one of the shear wave velocities being zero (which indicates that this material is unaffected by shear stresses, equivalent to a inviscid fluid-like material). For this case, vorticity can only be carried off the interface by the material with a nonzero-shear modulus.

Oscillatory decaying behavior occurs when the shear wave velocities are sufficiently different and no poles exist on the imaginary axis. To analyze this region, the position of the pair of conjugate poles that is closest to the imaginary axis is important. If the pole is very close to this axis (which occurs when the two shear wave velocities are very different) the subdominant exponentially decaying traveling wave may be present for some time as the characteristic decay rate of the resulting wave is very small. On the other hand, when this pair of poles is far from the imaginary axis, which happens just after reaching the critical shear wave speed ratio that separates oscillatory from decaying behavior, the evolution of the interface is controlled by the integral around the branch cuts and exhibits a $1/t^{3/2}$ decay.

5.7 Results

In this section, some specific results from the solution of the linearized Richtmyer-Meshkov flow are presented with the aim of visualizing the general conclusions extracted from the analytic approach to the problem.

The most representative variable to discuss the stability of the system is the amplitude of the interface. For that reason, the first group of results shows the behavior of the amplitude under changes of the parameters that control the problem. A second group describes the frequency behavior of the long-time oscillations, comparing it with previously published approximate results [90]. The way the vorticity is carried away from the interface and the evolution of tangential slip velocity at the interface is shown next. The section ends with a comparison for a particular set of parameters with fully compressible numerical simulations. These results serve as verification of the accuracy of the analytical model and numerical algorithm and show important differences caused by compressibility effects and the different way in which the motion is initiated.

5.7.1 Interface behavior

Fig. 5.5 shows the amplitude of the interface in time (conveniently non-dimensionalized with the shear wave speed of the + material, the initial amplitude, and impulsive velocity) when the shear wave velocity ratio c_-/c_+ is in the range $1 \leq c_-/c_+ \leq 3$, leaving the density ratio fixed. As expected, after the transient, the interface amplitude $\hat{\eta}(t)$ oscillates for the case $c_-/c_+ = 1$. For the other cases the interface amplitude decays faster as c_-/c_+ is increased. A faster decay rate is observed in the no-slip case but the frequency of oscillations for a given shear wave speed ratio is very similar in both cases.

Fig. 5.6 shows the amplitude of the interface when c_-/c_+ is increased from 0.2 to 1. A practically oscillatory behavior is observed for $c_-/c_+ = 0.2$ and $c_-/c_+ = 0.4$. As it was already pointed out, the interface oscillates for $c_-/c_+ = 0$. Therefore, values 0.2 and 0.4 are close enough to 0 to exhibit a very low rate of decay. For the intermediate values ($c_-/c_+ = 0.6$, 0.8) in the free-slip case, the amplitude of the interface decays faster, but it returns to oscillatory for $c_-/c_+ = 1$. Important differences are noticed between the free- and no-slip for this range of parameters. In the second case, the decay rate does not change much, with all the curves showing a behavior close to oscillatory. As a result, it can be said that the decay rate for a given shear wave speed ratio is slower in the no-slip rate for this particular set of parameters. This contrasts with results obtained for $c_-/c_+ > 1$ (Fig. 5.5), in which the no-slip amplitude exhibited a faster decay rate. For $c_-/c_+ = 1$, both cases exhibit oscillatory behavior, but the amplitude of oscillations is higher in the free-slip case. The frequency at which the amplitude oscillates is again very similar, independently of the set of boundary conditions used.

5.7.2 Oscillation period

An attempt to perform a long-time ($s \to 0$) approximation of Eq. (5.36) leads to the following expression

$$U(s,0) = \frac{(r-1)V\eta_0 ks}{2(1+r)\left(s + ik\sqrt{\frac{\mu_-+\mu_+}{\rho_-+\rho_+}}\right)\left(s - ik\sqrt{\frac{\mu_-+\mu_+}{\rho_-+\rho_+}}\right)} \tag{5.62}$$

From this last expression, the oscillation period is:

$$\frac{T}{T_0} = \sqrt{\frac{1+r}{1+\frac{\mu_+}{\mu_-}}}, \tag{5.63}$$

with $T_0 = (2\pi/k)\sqrt{\rho_-/\mu_-}$. This value is of the order of $\max[c_-, c_+]k$, which formally contradicts our principal assumption in performing the long-time approximation, $s << (c_-k, c_+k)$. As a consequence, performing an inverse Laplace transform of Eq. (5.62) leads to an inaccurate value for the amplitude and does not reflect a possible decaying behavior. In fact, it predicts that the long-time amplitude of the oscillations scales as $1/T$ (i.e., as $\sqrt{(1+\mu_+/\mu_-)\,/\,(1+r)}$) and therefore does not decay to zero for any combination of material parameters.

Piriz et al. [90] provide a similar expression

$$\frac{T}{T_0} = \frac{1.55}{\sqrt{2}}\sqrt{\frac{1+r}{1+\frac{\mu_+}{\mu_-}}}, \tag{5.64}$$

obtained by a mixture of local analysis and simulation. They also predict pure oscillation irrespective of the material parameters, with the amplitude scaling as $1/T$ for the long-time behavior. This is

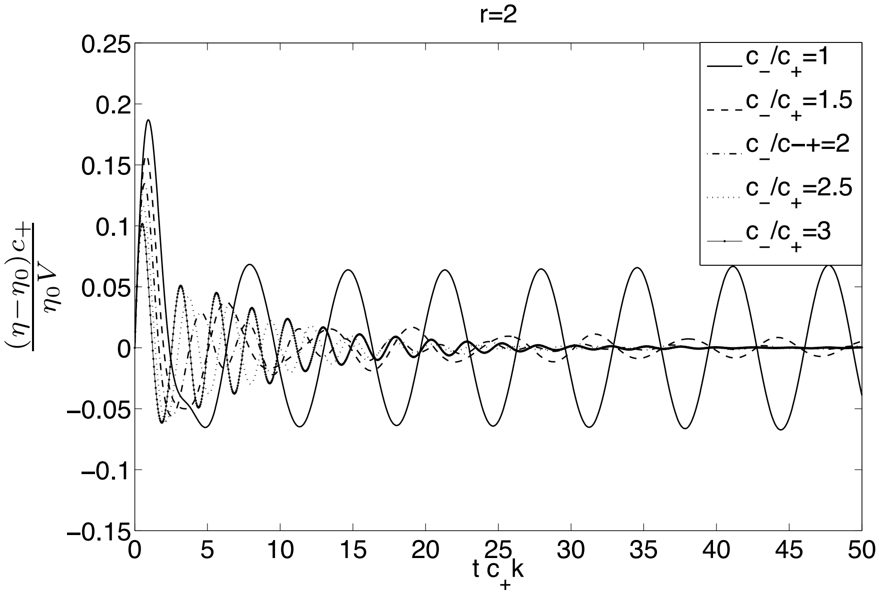

(a) Free-slip

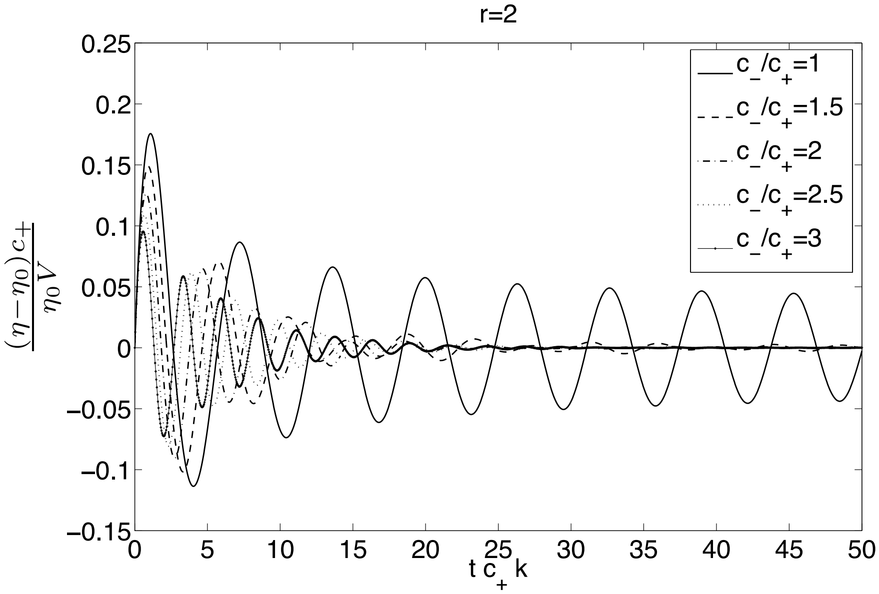

(b) No-slip

Figure 5.5: Interface amplitude varying c_-/c_+ from 1 to 3 and r

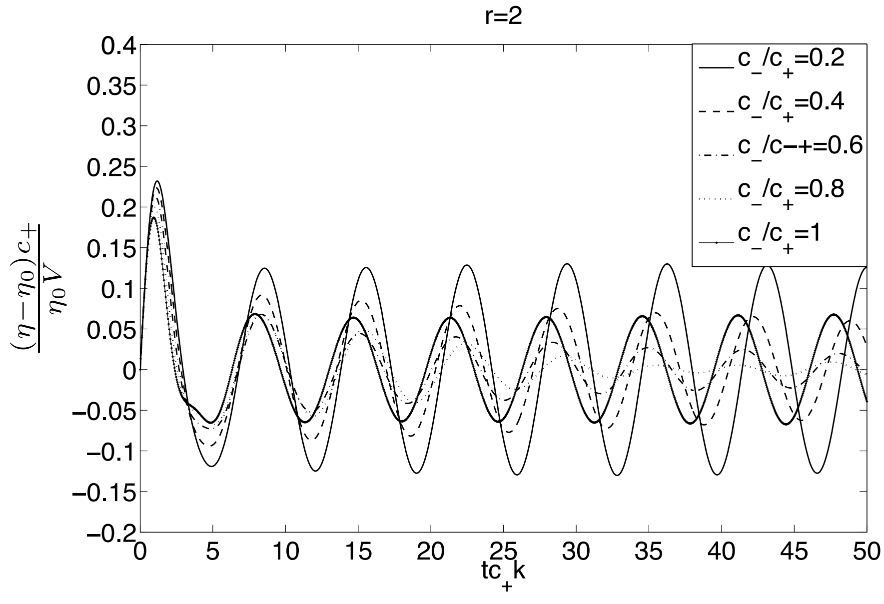

(a) Free-slip

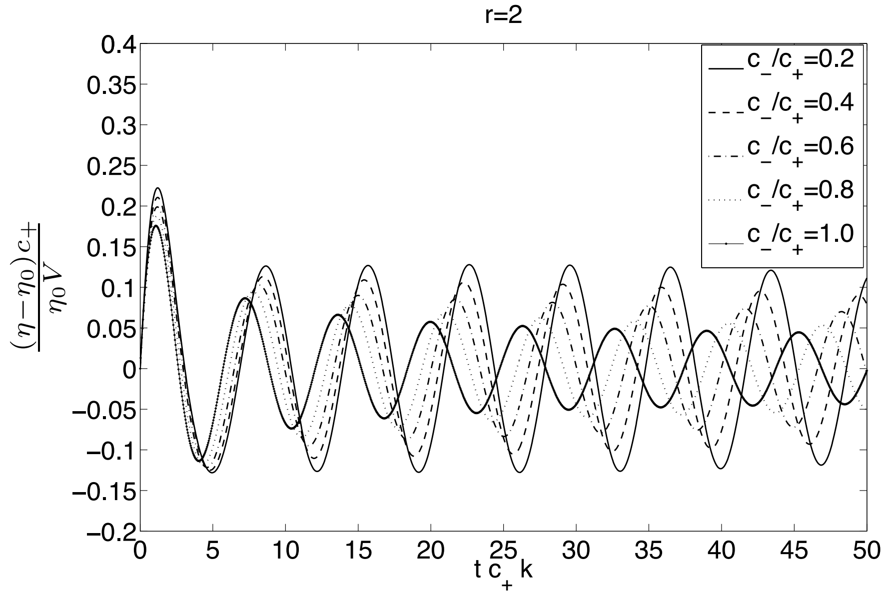

(b) No-slip

Figure 5.6: Interface amplitude varying c_-/c_+ from 0.2 to 1 and fixed r

because the simple analytic model proposed in [90] computes the interface behavior using Newton's second law with a forcing term that is proportional to the amplitude of the interface and a mass term that is proportional to its acceleration. The resulting equivalent mass-spring system does not capture decaying oscillations.

Figs. 5.7 and 5.8 show a comparison between these approximations and the result calculated from the complete model. The oscillation period arising from the pole that is closer to the imaginary axis (the imaginary part of the pole position) is also compared. In spite of the inaccuracy for calculating the expected behavior of the system (oscillating decay or pure oscillatory), the long-term approximation in fact gives a very good result for the oscillation frequency. As expected, as the ratio c_+/c_- separates from 1, the oscillation period of the complete system is closer to that associated with the pole that is closer to the imaginary axis.

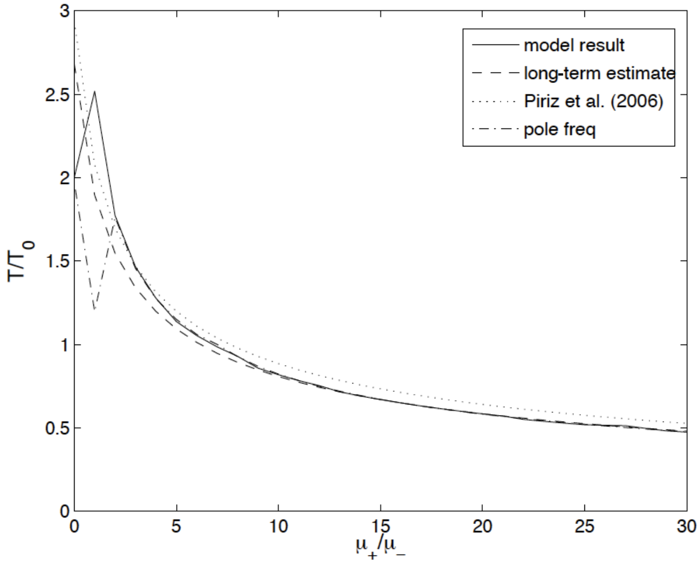

Figure 5.7: Oscillation period for fixed density ratio 6.182 and varying shear modulus. The complete model result is calculated performing numerically the inverse Laplace transform of the interface amplitude and counting the time between oscillations. The long-term estimate uses Eq. (5.63). The estimate of Piriz et al. uses Eq. (5.64). The pole frequency is calculated by locating the pole in the complex plane.

5.7.3 Vorticity

Vorticity is controlled by a wave equation. For the free-slip case at $t = 0$, the impulse produces an instantaneous tangential velocity that is equal in magnitude and opposite in direction in the materials. In the no-slip case, the analysis of Eq. (5.51) for $s \to \infty$ reveals that the vorticity is a

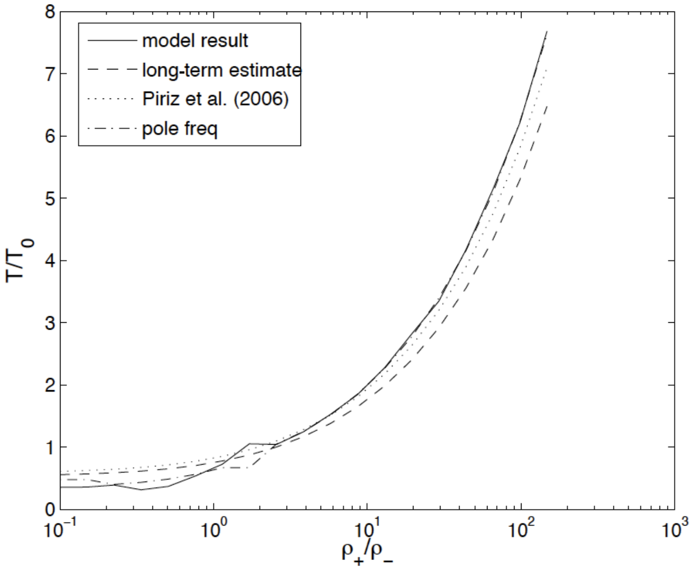

Figure 5.8: Oscillation period for varying density ratio and fixed ratio of shear modulus μ_+/μ_-. The complete model result is calculated performing numerically the inverse Laplace transform of the interface amplitude and counting the time between oscillations. The long-term estimate uses Eq. (5.63). The estimate of Piriz et al. uses Eq. (5.64). The pole frequency is calculated by locating the pole in the complex plane.

delta function at $t = 0$:

$$\hat{\omega}(x_1 = 0^-, t = 0) = \mathcal{L}^{-1}\left[-2ik^2 V\eta_0 \frac{(r-1)r}{(r+1)\left(\frac{r}{c_-k} + \frac{1}{c_+k}\right)}\right], \tag{5.65a}$$

$$\omega(x_1 = 0^+, t = 0) = \mathcal{L}^{-1}\left[-2ik^2 V\eta_0 \frac{r-1}{(r+1)\left(\frac{r}{c_-k} + \frac{1}{c_+k}\right)}\right]. \tag{5.65b}$$

This spike in vorticity can be regarded as the effect of attempting to achieve continuous tangential velocities across the interface immediately after the impulse occurs. For an incompressible inviscid fluid, vorticity lies at the interface and cannot be dissipated or transported. Therefore, the growth rate of the interface is constant ($U(t, 0) = A_t V\eta_0 k$, r being the density ratio). This growth rate is observed for our solution at $t = 0^+$. After that moment, shear waves carry the vorticity away from the interface. Figs. 5.9 and 5.10 show how the initial vorticity is carried off the interface for two cases: solids with equal shear wave velocity (Fig. 5.9) and solids with different shear wave velocities (Fig. 5.10). The delta function in the no-slip cases has been truncated for better appreciation of the rest of the curves. It can be observed that, even if no large differences are apparent in the interface amplitude between free- and no-slip boundary conditions, the distribution of vorticity is drastically different. In addition to not being continuous across the interface and exhibiting a delta function for $x_1 = 0, t = 0$ which gets advected into the materials by the shear waves, one can appreciate that the amount of vorticity transported into each material under no-slip boundary conditions is not symmetric and hence depends on a function of r. This becomes evident for the case in which $c_- = c_+$ and can be also observed by examining Eq. (5.65).

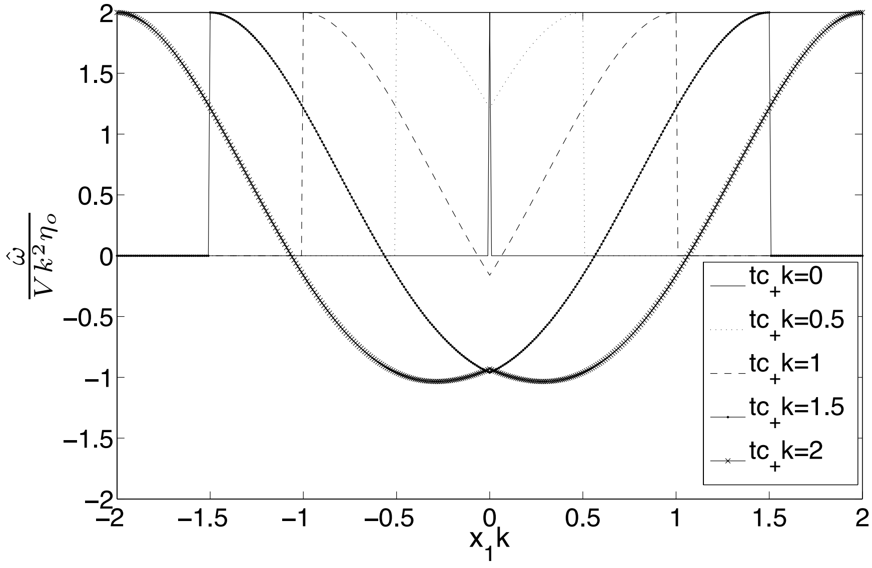

(a) Free-slip

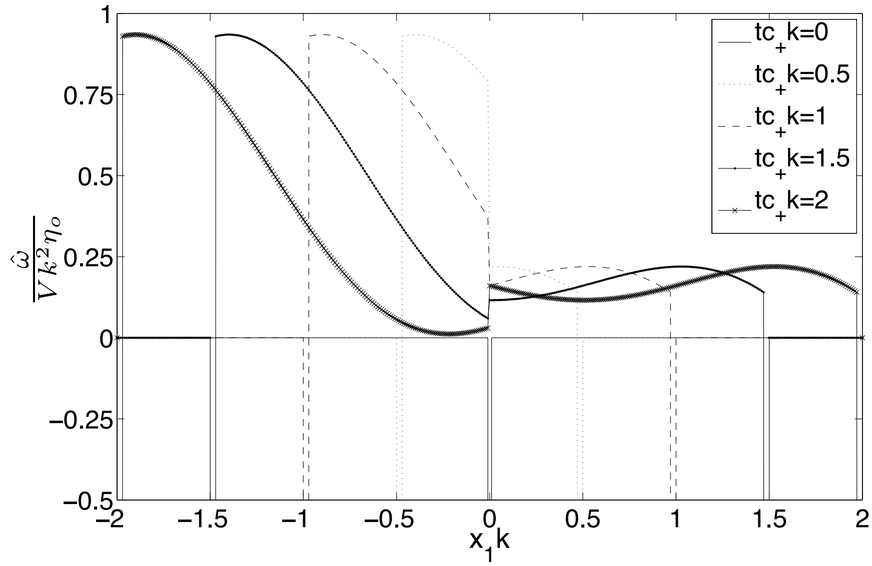

(b) No-slip

Figure 5.9: Amplitude of vorticity at different times for $c_-/c_+ = 1$, $r = 2$. Equal shear wave velocities produce a symmetric distribution of vorticity at each time.

To close the study of vorticity, under free-slip boundary conditions, a vortex sheet is produced by the jump in tangential velocity across the interface. Using the incompressibility condition (5.19), it

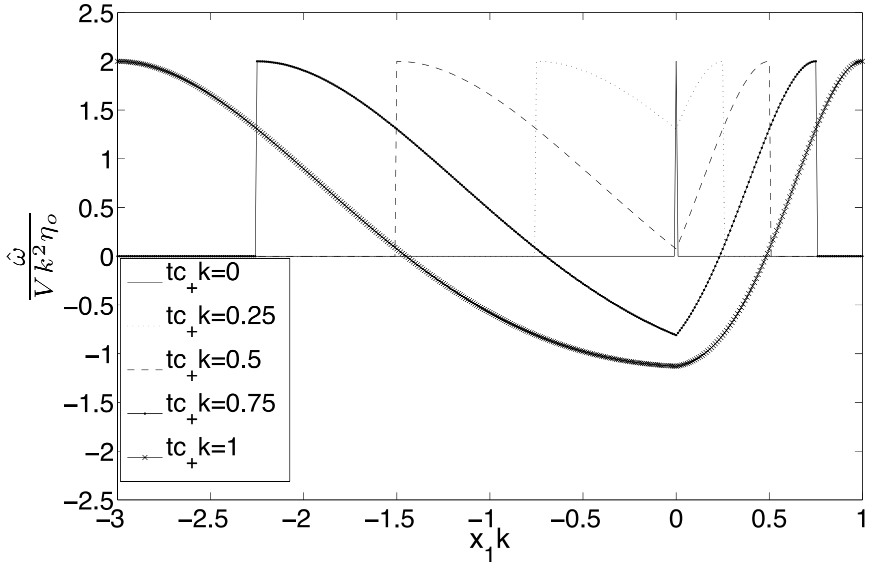

(a) Free-slip

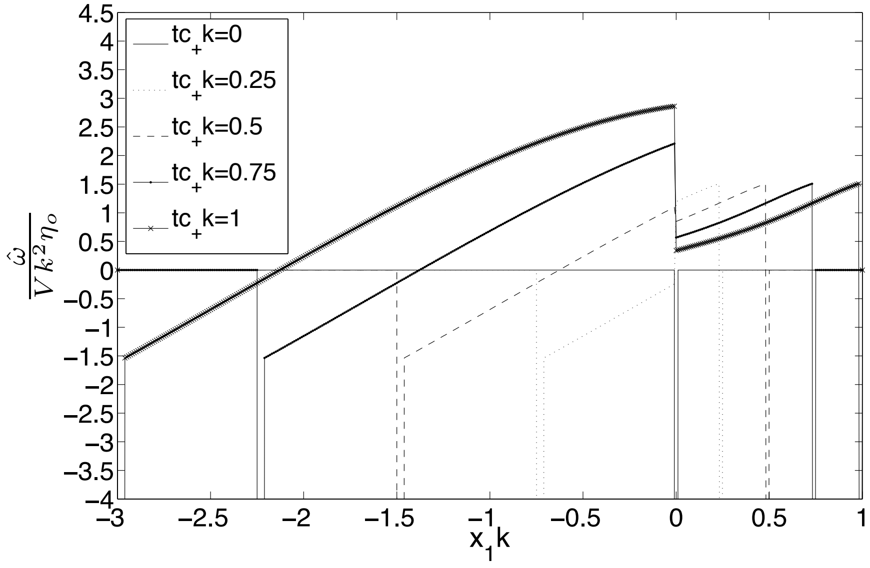

(b) No-slip

Figure 5.10: Amplitude of vorticity at different times for $c_-/c_+ = 3$, $r = 2$. Vorticity is carried off the interface faster in the material with higher wave velocity

is easy to derive the expressions for the tangential velocities from the normal velocity. This reveals that the behavior is similar to that of the growth rate (the parametric regions of oscillatory and decaying behavior are the same). Fig. 5.11 shows the evolution of the jump in time for two different sets of parameters (case 1: $c_-/c_+ = 1$ and $r = 2$; case 2 : $c_-/c_+ = 3$ and $r = 2$).

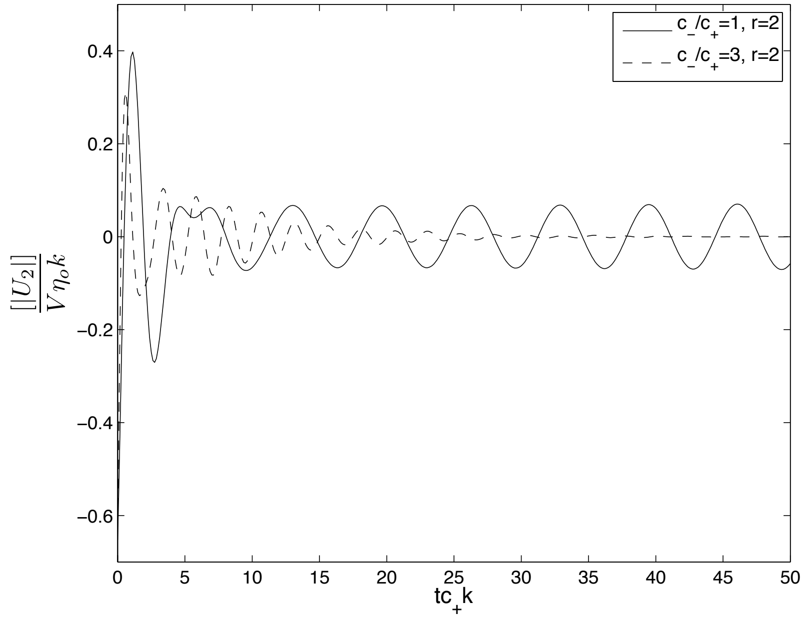

Figure 5.11: Evolution of the tangential velocity jump across the interface for two different sets of parameters. The first set (continuous line) corresponds to an oscillatory long-term behavior while the second one (dashed line) corresponds to a decaying behavior.

5.7.4 Comparison with numerical results

The fully compressible numerical method described in Chapter 3 is used to test the accuracy of the results predicted by the linear incompressible model. To this effect, the compressible neo-Hookean [61] equation of state

$$e(\mathbf{g}\,,\varsigma) = \frac{\mu}{2\rho_0}\mathrm{tr}(\mathbf{C}) + c_v T_0 \left(\frac{\rho_0}{\rho}\right)^{1-\gamma} \exp\left(\frac{\varsigma - \varsigma_0}{c_v}\right), \tag{5.66}$$

was used to model the left and right materials. Parameters in this equation are the specific heat $c_v = 0.011\,\mathrm{J\,kg^{-1}\,K^{-1}}$, reference temperature $T_0 = 300\,\mathrm{K}$, shear modulus $\mu_- = 9\,\mathrm{GPa}$, $\mu_+ = 11.43\,\mathrm{GPa}$ and reference density $\rho_{0-} = 2.7\,\mathrm{kg\,m^{-3}}$, $\rho_{0+} = 3.375\,\mathrm{kg\,m^{-3}}$. The reference entropy ς_0 is set to zero. These particular values were selected so the initial normal stress across the perturbed interface is continuous and the shear wave speeds in both materials are similar after the shock–interface interaction. This constitutive law can be regarded as a model for an ideal gas (hydrostatic term) which has some resistance to shear. The motion is initiated by a weak shock of compression ratio $J = 0.95$ and the interface is perturbed with a sinusoidal wave of non-dimensional amplitude $\eta_0^i k = 0.03\pi \approx 0.1$. The shock wave–interface interaction affects the initial states, particularly by changing the density and the amplitude of the interface. Using the hypothesis of small perturbations, a one-dimensional Riemann problem can be solved to determine the disturbed states, and the velocity and amplitude of the interface after shock passage. These new parameters are used as initial conditions for the linear model. For this particular case, $c_-/c_+ = 0.992$, $r = 1.2567$, $V/c_+ = 0.5329$ and $\eta_0 k = 0.0897$.

Results in Fig. 5.12 show good agreement between numerical and analytical predictions for the no-slip case. After a short transitional period, which is produced by the effect of having a shock wave instead of an impulse initiating the motion and the finite time required for the shock to fully cross the interface [68], results match for the frequency and amplitude of oscillations in the long-term behavior. A series of faster oscillations are observed and an analysis of their frequency shows that they are related to the longitudinal wave speeds. These are acoustic waves emitted by the distortion of the shock after the interface interaction.

In contrast, for the free-slip condition, a phase-lag is encountered for oscillations in the long-term behavior. This phenomenon is produced by the effect of a shock passing through a free-slip boundary condition. It can be shown that the shock interaction with an interface separating two materials with the same properties and same state, and collocated at an angle, is very different depending on the conditions assumed at the interface. For no-slip conditions, the shock passes through the interface and it neither gets deformed nor are shear waves produced as a result, much as if the interface did not exist. On the other hand, free-slip conditions induce the formation of shear waves since they allow discontinuous tangential velocities. These additional “start-up” shear waves are present in the results obtained in the compressible free-slip numerical example but they cannot be captured by the impulsive analytical model. In consequence, the amount of vorticity deposited at the interface is very different when comparing the two results in the short-term range and this affects the long-term behavior in the way observed in Fig. 5.12(a).

5.8 Summary

An analytic approach to the Richtmyer-Meshkov flow for elastic solids allowed a simple determination of the parametric dependence of the problem. The incompressible and linear assumptions reduce the number of parameters under consideration to two: the shear wave velocity ratio and the density ratio. The parameter space is then explored easily despite the complexity of the expressions encountered.

The analysis reveals the following conclusions concerning the amplitude and rate of growth of the interface between two elastic solids with frictionless contact:

1. Solutions show a transitory period close to $t = 0$ followed by a regular behavior. The rate of growth of the interface at $t = 0$ corresponds to the Richtmyer-Meshkov result for fluids.

2. Two different patterns are identified for the long-time behavior. The first one is purely oscillatory and appears when the two solids in contact have a very similar shear wave velocity or

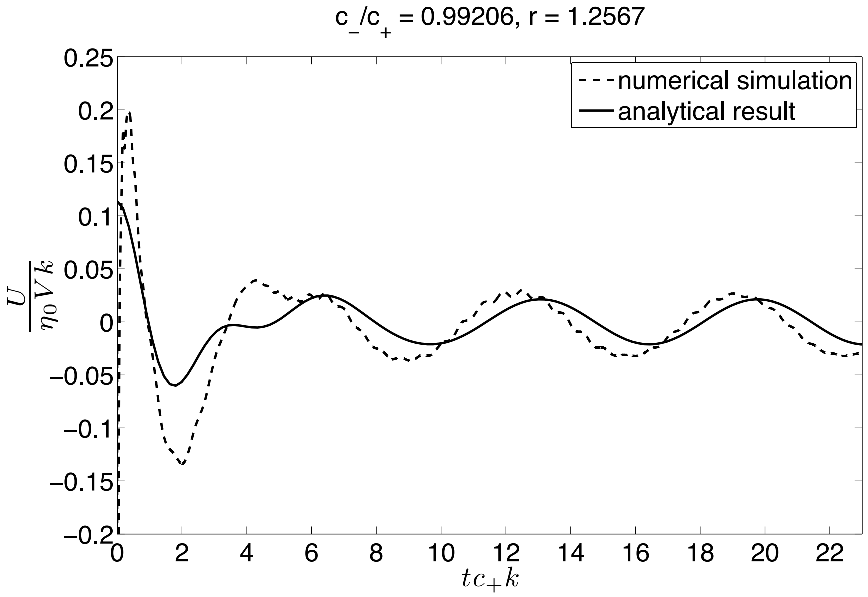

(a) Free-slip

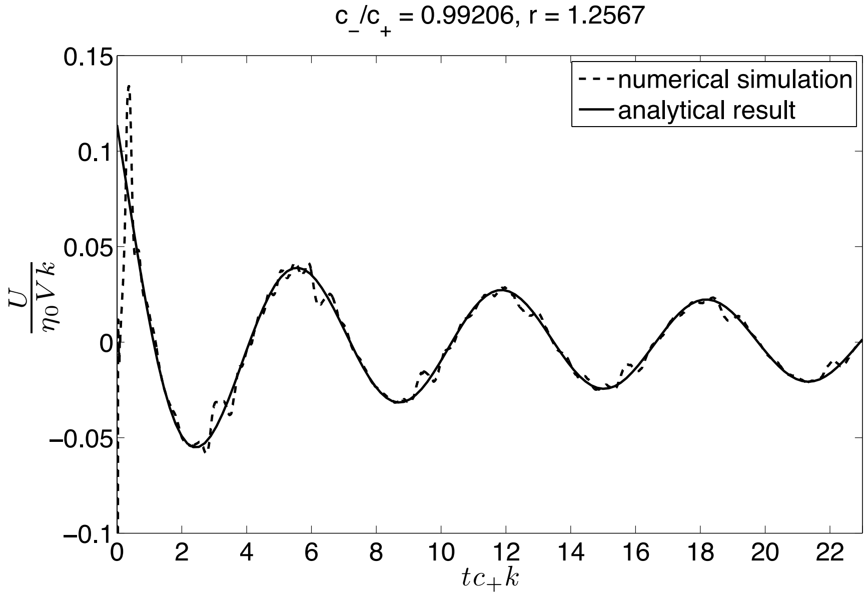

(b) No-slip

Figure 5.12: Comparison of interface growth rate, defined as $U(0,t)$ between the analytical model prediction and numerical simulation results.

when one of the solids has no shear strength. The second behavior is described as an oscillatory decay that parametrically varies in oscillation frequency and rate of decay. As the ratio c_-/c_+ separates from 1, the decaying rate increases and then decreases as c_-/c_+ becomes very large or very small, tending to the asymptotic oscillatory behavior when $c_-/c_+ \to 0$ or $c_-/c_+ \to \infty$

3. While the model of [90] accurately predicts the oscillation frequency of the interfacial waves, it incorrectly predicts the long-time amplitude. The amplitude should be computed using the full expression or performing a more accurate long-time approximation considering true pole locations and the branch cuts of the Laplace transform.

Finally, the second-order wave equation with the shear wave velocity governs the vorticity within each material. Shear waves carry the initial vorticity deposited by the impulse at the interface at $t = 0$ to the interior of the solid and away from interface. The tangential slip velocity at the interface either oscillates or decays while oscillating, as determined by the nature of the interfacial wave $\eta(t, x_2)$.

The next chapter extends the analysis of the Richtmyer–Meshkov flow in solids to cases that consider more realistic phenomena, such as compressibility and plasticity, which exceed the scope of this analytical model. However, it will be shown that regions of an elastic–plastic solid remain in the elastic regime under some particular conditions. In these situations, the model derived in this chapter is useful for characterizing the motion of the interface.

Chapter 6

Numerical simulations of Richtmyer–Meshkov instability in multiple material interfaces

6.1 Introduction

The problem of examining the Richtmyer–Meshkov flow in elastic–plastic solids is of special relevance since shocks often stress materials beyond their yield point. Unfortunately, plasticity theory is intrinsically nonlinear due to yield criteria being based on norms (e.g., von Mises) or differences in absolute value (e.g., Tresca) of shear stresses. For this reason, purely analytical models are extremely difficult to formulate and the study of the problem using numerical techniques becomes necessary. This chapter analyzes, making use of computer simulations, two relevant Richtmyer–Meshkov problems involving the behavior of the interface separating an elastic–plastic solid from other media: the solid–vacuum and solid–gas cases in planar and cylindrical geometries, respectively.

The study of the Ritchmyer–Meshkov flow in a solid–vacuum planar configuration is motivated by previous numerical and experimental work by Dimonte et al. [27] and Piriz et al. [91], which make use of this problem to postulate a way of determining the yield stress of a material by means of measuring the conditions at the interface after relaxation of stresses occurs in the solid and the interface evolution deviates from the initial fluid-like behavior. Results suggest a linear relation between the yield stress, the maximum amplitude reached by the interface perturbation and the square of the maximum growth rate. In some cases, the material interface never abandons the plastic state and the growth becomes unbounded, leading to the formation of ejecta. The study of this problem also serves as a way of validating the code by comparison with the cited references before attempting the more demanding case involving a cylindrical geometry and a solid–gas interface.

The converging Richtmyer–Meshkov flow appears in experiments aiming to achieve inertial confinement fusion (ICF) [62], plasma generation [60], and in astrophysical phenomena such as supernova formation [36]. It represents a more complex problem due to the acceleration of the shock and interface as they approach the axis, the second shock–interface interaction (re-shock) after the transmitted shock in the fluid reaches the axis, and the presence of secondary instabilities such as Rayleigh–Taylor [127, 76] (interface acceleration) and Kelvin-Helmholtz (discontinuity in tangential velocities in a non-viscous gas–solid interface). The problem has been studied extensively in the field of fluid mechanics, starting with the classical paper of Zhang and Graham [129] in which the four possible configurations spanned by the density ratio across the material interface (heavy–light, light–heavy) and the direction of the shock (imploding, exploding) are qualitatively explored by means of numerical simulations. Lombardini et al. [67, 66] studied the influence of initial parameters (shock strength, wave number of the interface perturbation) of heavy–light and light–heavy systems in the imploding configuration. The study of this problem in the field of solid mechanics is of interest for multiple reasons. In the first place, the existence of shear modifies the behavior of the solid even when the material is in a plastic state. Moreover, a typical solid–gas configuration exhibits an initial Atwood ratio larger than those commonly studied in fluid–fluid systems. Beyond the physical interest, this problem represents an excellent testbed for the capabilities and limits of the numerical implementation described in Chapter 3 and it is the reason for which the formulation based on stretches (3.2.4) was developed after observing that simulations using the formulations based on deformations gradients fail shortly after impacts between reconnecting regions of the same material begin to occur.

6.2 Constitutive laws

The hyper-elastic constitutive law of Godunov–Romenski [30, 107]:

$$e = e_s + e_h, \tag{6.1a}$$

$$e_s = 2c_s(\rho)^2 I^2, \;\; I^2 = \frac{\left(I_1^{\mathbf{H}^e}\right)^2}{3} - I_2^{\mathbf{H}^e}, \tag{6.1b}$$

$$e_h = \frac{K}{2\alpha^2}\left(\left(\frac{\rho}{\rho_0}\right)^{\alpha} - 1\right)^2 + c_v T_0 \left(\frac{\rho}{\rho_0}\right)^{\gamma_s}\left(\exp\left(\frac{\varsigma}{c_v}\right) - 1\right), \tag{6.1c}$$

with $c_s(\rho) = \frac{\mu}{\rho} = \frac{\mu_0}{\rho_0}\left(\frac{\rho}{\rho_0}\right)^{\beta}$ and the Hencky elastic strain tensor $\mathbf{H}^e = \frac{1}{2}\log\left(\mathbf{F}^e\mathbf{F}^{eT}\right)$ is used for the two problems analyzed in this chapter. The material considered is copper with parameters $\rho_0 = 8.93\,\mathrm{g/cm^3}$, $K = 15.28 \cdot 10^6\,\mathrm{m^2/s^2}$, $c_v = 3.9 \cdot 10^2\,\mathrm{J/kgK}$, $T_0 = 300\,\mathrm{K}$, $\mu_0 = 39.38\,\mathrm{GPa}$, $\alpha = 1$, $\beta = 3$, $\gamma_s = 2$. As stated in Chapter 3, the use of this particular equation of state admits algebraic solutions for the plastic update that are similar to a radial return algorithm, decreasing the computation time since an implicit algorithm is not needed. J_2-perfect plasticity is considered with a typical yield stress $\sigma_Y = 0.12\,\mathrm{GPa}$ for copper. In some examples, this value can be modified in order to match existing results in the literature or for the purpose of a parametric analysis. More complex behavior, such as hardening and thermal softening can also be considered in the model but the assumption of perfect plasticity is normally better suited for studying the effect of the plastic model on the results. The model for gases is a simple calorically perfect model $p = \rho RT$ with $R = c_p - c_v$, completely characterized by the ratio of specific heats $\gamma_g = \frac{c_p}{c_v} = 5/3$.

6.3 Planar Richtmyer–Meshkov instability in solid–vacuum interfaces

The first problem to be examined in this chapter is the Ritchmyer–Meshkov instability which develops in an interface separating an elastic–plastic material from vacuum. This analysis is motivated by previously published results in [91] and [27]. In the first publication, a semi-analytical model for a solid–vacuum interface is developed and complemented with finite-element simulations. In the latter article, the authors make use of a multidisciplinary approach involving simulations run with the Eulerian hydrodynamics software PAGOSA [119], molecular dynamics algorithms, and experiments to characterize the behavior of a solid–gas interface (which mimics the solid–vacuum case for very small values of the gas density). Both studies suggest the existence of a linear correlation between the yield stress in an elastic–perfectly plastic solid and a non-dimensional parameter which relates the wavelength, maximum amplitude and growth rate of the interface, and the reference density of the material. This relation appears to be material independent since it is based on the idea that the solid after a moderate to strong-shock–interface interaction behaves like a fluid until the stresses at the interface are sufficiently relaxed for the effect of shear to become apparent. This effect will appear in the form of oscillatory motion, as occurred in the elastic analytical model of Chapter 5. In addition, results seem to indicate the existence of a threshold value of the initial amplitude, given an initial shock strength and yield stress, for which the interface grows indefinitely leading to formation of ejecta in a fluid-like fashion, and for which the previously stated linear relation with yield stress does not apply since a maximum amplitude of the interface cannot be properly defined.

The study of the behavior of the interface for a range of initial conditions and material parameters performed by Dimonte et al. [27] is replicated here using the AMROC multi-material implementation described in Chapter 3 and substituting the solid–gas interface employed in Dimonte et al.'s simulations by a solid–vacuum interface. There exist two reasons that support this last decision. In the first place, the solid–gas case is used in [27] to mimic a solid–vacuum interface, which may be difficult to model in PAGOSA. Finally, making use of a solid–vacuum interface represents an opportunity to test the capabilities of the multi-material HLLD solid–vacuum solver.

Copper is used in all the test cases and modeled following the constitutive law (6.1). A perfectly plastic model with yield stress of 0.5 GPa, the same that is used in [27], is considered for the first baseline test case. In this example, the motion is started by the Riemann problem produced by the impact of two blocks of unstressed copper approaching with a relative velocity of 5 km/s. For copper material parameters, the solution of such a Riemann problem involves two plastic shock waves traveling in opposite directions with velocity $U_s = 7.6\,\mathrm{km/s}$ ($M_s = 1.67$) with respect to the material discontinuity. The jump in normal velocity and stress across the shocks is $\Delta u = 2.5\,\mathrm{km/s}$ and $\Delta\sigma_{xx} = -174.8\,\mathrm{GPa}$, respectively. The value of the velocity jump matches that in [27]. However, the value of the increment in normal stress, which is reported to be 160 GPa in [27] cannot be exactly matched. This indicates a deviation of approximately 10% that can be attributed to different constitutive laws being employed. In the case of a non-perturbed interface, i.e., a one-dimensional problem, the solution of the Riemann problem after the shock–interface interaction yields a copper density of $7.9\,\mathrm{g/cm^3}$ and an initial interface velocity $V_0 = 5.2\,\mathrm{km/s}$. These values match reasonably well those reported by Dimonte et al. ($8.3\,\mathrm{g/cm^3}$ and 5.26 km/s, respectively). It is important to note that the release temperature obtained in our example is close to 1900 K while a value of 1300 K is obtained in [27]. The latter temperature value is barely below the melting temperature for copper, while the value obtained in our simulations is well above the melting threshold. Since melting is not included in this particular plasticity model, the yield stress value remains unmodified but the observed large discrepancies for this temperature value raise the question of the accuracy of constitutive laws used by both sets of simulations. Additional simulations run by Dr. Julian Cummings of the PSAAP CFD group using Sandia National Laboratories CTH hydro-code indicate an approximate value of 1800 K when the same initial conditions are considered.

Figure 6.1(a) shows the rectangular computational domain and initial disposition of vacuum (blue) and solid (red). The solid is initially placed on the right side of the computational domain. With this setup, one of the shocks originated by the initial Riemann problem travels to the right and exits the computational domain while the other moves towards the interface. A start-up glitch is produced due to the discrete treatment of the Riemann problem and for this reason the initial position of the shock is chosen far from the interface in order to avoid excessive wave perturbations due to the glitch (Fig. 6.1(b)). A constant velocity field is added to the whole domain in a way such that an unperturbed interface would remain stationary upon the shock-interface interaction. The interface is perturbed with a sinusoidal wave $\eta = \eta_0 \cos(kx_2)$ with k chosen in a way such that two full waves are included in the computational domain.

In Fig. 6.1 density contour plots at different times for a numerical simulation using $\sigma_Y = 0.5\,\mathrm{GPa}$ and $\eta_0 k = 0.4$ are shown. The first two figures are used to show the initial conditions and shock propagation towards the interface. After the shock reaches the interface, an expansion fan develops in the solid as a result of the Riemann problem originated at the free surface (with zero normal and tangential stress boundary conditions). As expected in a heavy–light Richtmyer–Meshkov problem, the interface experiences a phase reversal (Fig. 6.1(c)). In this particular simulation, the spike

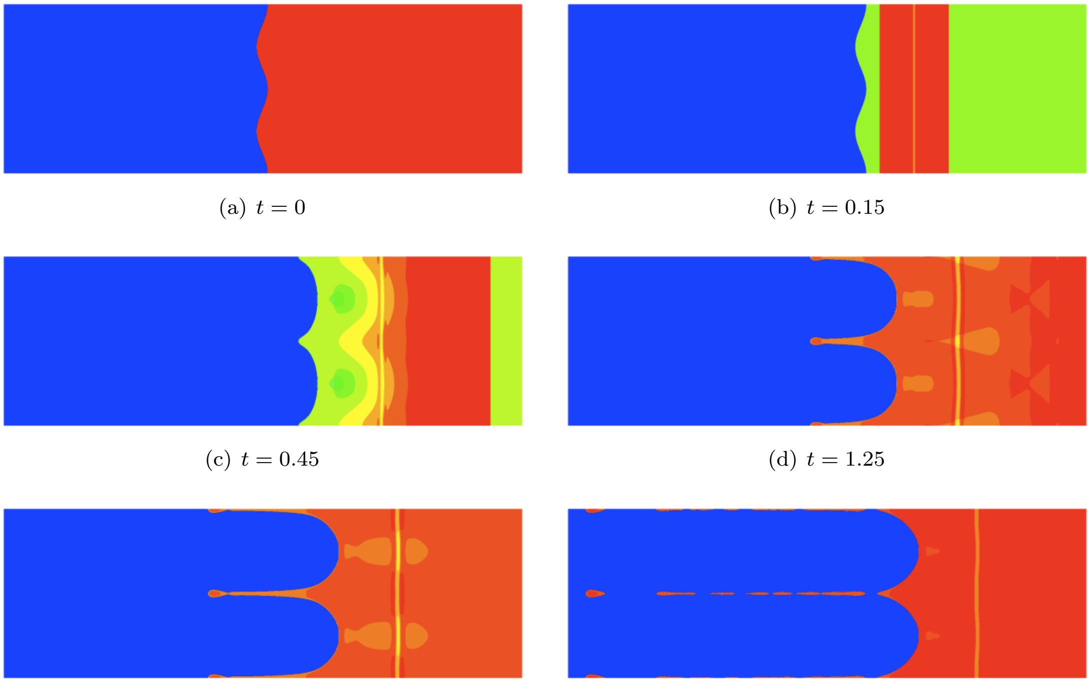

(a) $t = 0$

(b) $t = 0.15$

(c) $t = 0.45$

(d) $t = 1.25$

(e) $t = 1.9$

(f) $t = 5.2$

Figure 6.1: Time evolution of density contours for a solid–vacuum Richtmyer-Meshkov problem with parameters for copper, $\sigma_Y = 0.5\,\text{GPa}$, $\eta_0 k = 0.4$, and $M_s = 1.67$. (a,b) show initial conditions and propagation of the shock, (c) depicts the state after shock–interface interaction with interface phase reversal, (d,e,f) show unbounded spike growth and break-up.

amplitude is unbounded and grows until the spikes break due to grid resolution and regularization (a fracture model has not been included in the numerical implementation yet), as shown in Fig 6.1(d,e). Finally, in the last frame, the ejected droplets, which move at constant velocity, are about to exit the computational domain through the left boundary.

Figure 6.2 offers the first comparison with results in [27] by showing the evolution of spike and bubble amplitudes with respect to time for different initial amplitudes $\eta_0 k = \{0.125, 0.18, 0.22, 0.4\}$. Perturbation amplitudes are computed as differences from the interface position in time of an additional simulation run with initial parameter $\eta_0 k = 0$. Time is conveniently non-dimensionalized with $k|V_{bu}|t$ with V_{bu} being the maximum growth rate of the bubbles. $t = 0$ is taken at the initial shock–interface interaction. Following an initial growth period produced by the material being in the plastic regime, the characteristic oscillatory (or decaying oscillatory) behavior described in the analytical elastic model appears after the shear stresses are relaxed to a state below the yield surface. In this long-term limit, shear waves and not plasticity control the evolution of the bubble interface, whose amplitude converges to a mean value proportional to the initial interface amplitude in the four cases examined.

The spikes, on the other hand, exhibit a more pronounced growth rate at early times. A lower initial amplitude produces a behavior close to that of the bubbles, with interface amplitudes saturating around a mean value in the long term. However, a sufficiently large initial amplitude produces continuous growth of the interface as the material never abandons the plastic regime. As shown in Fig. 6.2, comparison with Dimonte et al.'s results reveal good agreement in the description of the bubble amplitudes and discrepancies for the spike amplitudes that become larger as the initial perturbation amplitude increases, especially for the cases where ejecta are formed. These differences may be attributed to different constitutive laws and algorithms being used since they become more noticeable in the large deformation, nonlinear regime. Moreover, figures in [27] are small in size and it is not easy to identify how exactly the initial time is chosen (beginning or end of shock-interface interaction, phase reversal) and which state is used as a reference for computing spike and bubble amplitudes. These uncertainties lead to misaligned curves in the start-up process between the two sets of results. However, a visual examination of the maximum amplitude slope reveals similar growth rate values in both methods and they seem to agree at the time of predicting whether ejecta are formed or the interface reaches a constant amplitude.

Finally, in Fig. 6.3, the linear relation between the yield stress and the saturation interface amplitude postulated in [27, 91] is constructed from discrete data points. A series of simulations were run varying the values of $\eta_0 k = \{0.125,\ 0.18,\ 0.22,\ 0.4\}$ and $\sigma_Y = \{0.25,\ 0.5,\ 0.75,\ 1\}$ GPa. For all the cases in which the interface reaches a constant mean value in the long-term, this value and the square of the maximum spike velocity are represented in the y- and x-axis, respectively, conveniently non-dimensionalized as $k\eta_{sp}^{max}$ and $\rho_0|V_{sp}|^2/\sigma_Y$. A linear fit of the data is performed revealing that

$$\sigma_Y \approx K\rho_0 \frac{|V_{sp}|^2}{k\eta_{sp}^{max}}, \tag{6.2}$$

with $K = 0.2$ and $K = 0.24$ for our simulations and Dimonte et al.'s results respectively. The difference in slope may look large at first but a closer examination of the data points reveals that for small initial amplitudes, i.e., results closer to a linear regime, the values obtained are very similar. It is only as the saturation amplitude grows that the obtained results exhibit an underestimation of the linear fit while those of Dimonte et al. are consistently above the linear regression function. If only data points with $k\eta_{sp}^{max} < 2$ are considered, the gap in slopes of the linear fits becomes smaller, with $K = 0.205$ and $K = 0.215$, respectively. Finally, it is worth mentioning that the value reported in [91] is $K = 0.29$. However, the case examined there is a light–heavy, i.e., vacuum–solid, problem with Atwood ratio $A_t \approx 1$ instead of a heavy–light interface (with $A_t = -1$). Under that condition, the interface does not experience phase reversal and higher saturation amplitudes are obtained for similar growth rates.

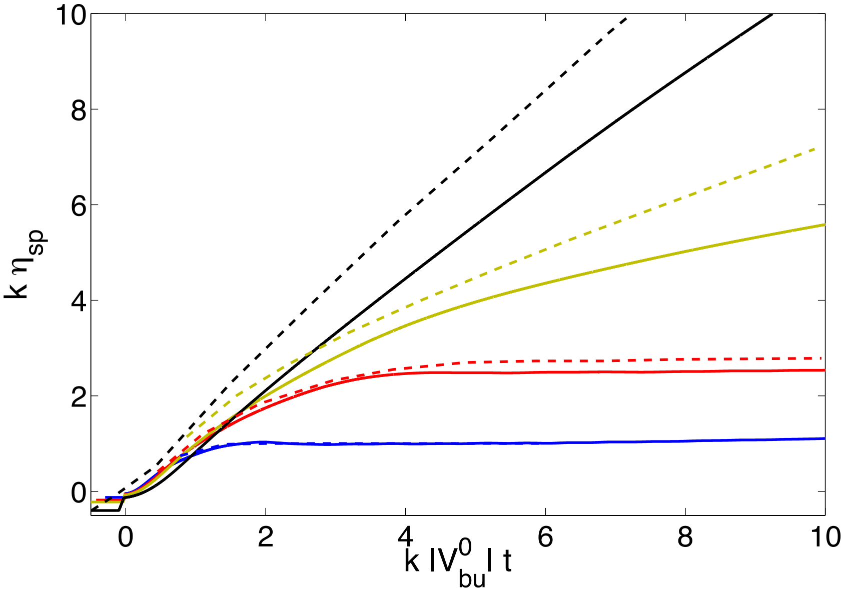

(a) Spike amplitude

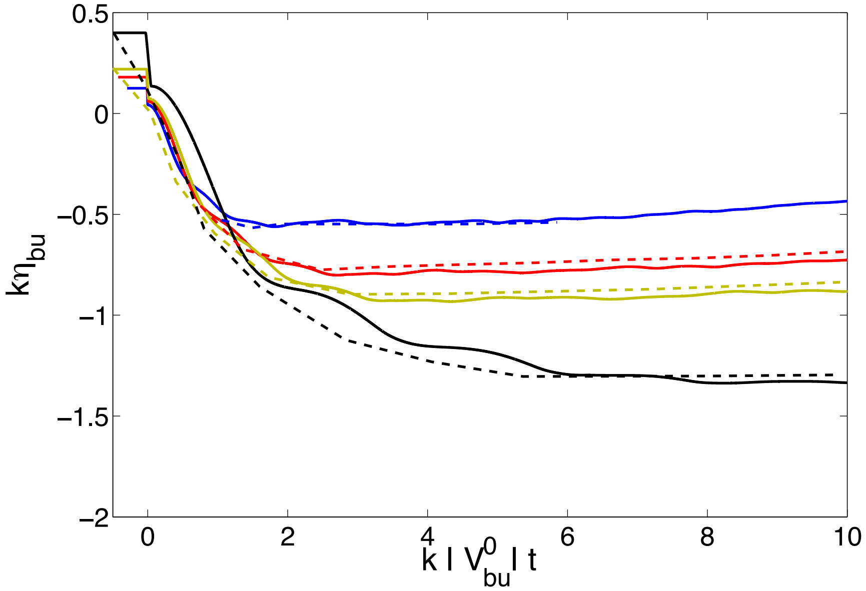

(b) Bubble amplitude

Figure 6.2: Comparison between spike and bubble amplitudes with time obtained from AMROC simulations (continuous lines) and Dimonte et al. (PAGOSA) results [27] (dashed lines) for four different values of the initial amplitude of the interface $k\eta_0 = 0.125$ (blue), 0.18 (red), 0.22 (brown), and 0.4 (black). Material used is copper with initial shock strength $M_s = 1.67$ and $\sigma_Y = 0.5\,\text{GPa}$.

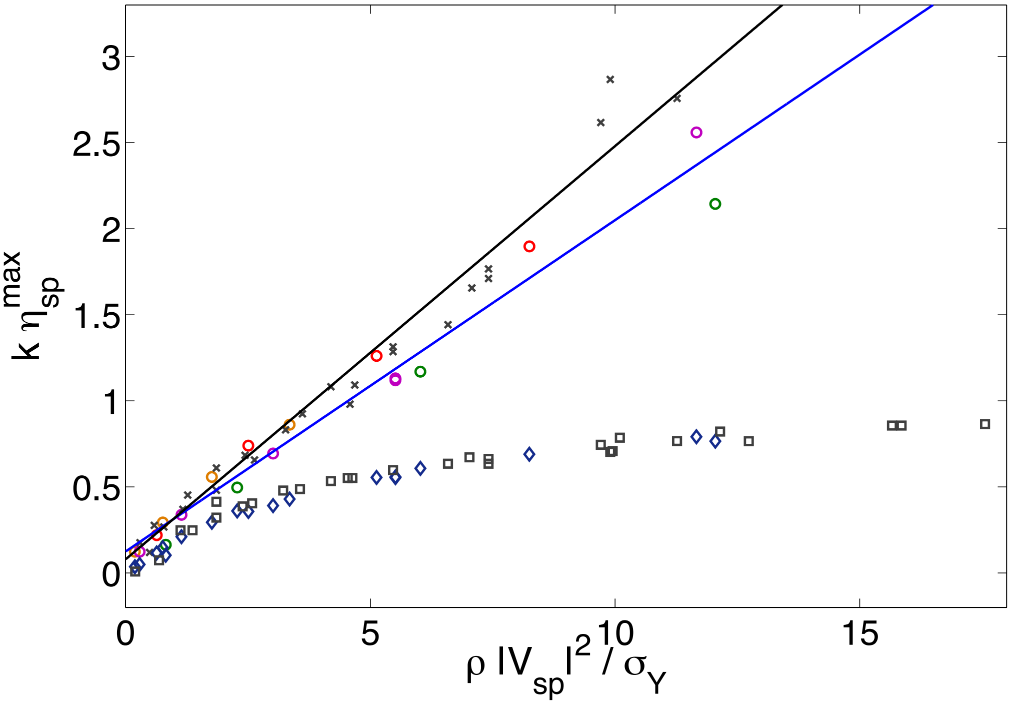

Figure 6.3: Maximum non-dimensional spike amplitude ($k\eta_{sp}^{max}$) vs. maximum non-dimensional spike growth rate squared ($\rho_0|V^{sp}|^2/\sigma_Y$) for different initial conditions and yield stresses. Circles represent AMROC spike results with $\sigma_Y = 0.25$ (green), 0.5 (magenta), 0.75 (red) and 1 (orange) GPa. Dimonte et al. results [27] for spikes are denoted by crosses. The blue and black continuous lines are the linear fits obtained from the data points for AMROC and PAGOSA simulations, respectively. Finally, maximum bubble amplitudes are also shown using black squares and blue diamonds for AMROC and Dimonte et al.'s results, respectively. Material used is copper with equation of state (6.1).

6.4 Cylindrical Richtmyer–Meshkov instability in solid–gas interfaces

The problem of solid–gas interfaces accelerated by an imploding shock in cylindrical geometries is described and analyzed in this section with the main goal of studying the effect of diverse initial conditions and material parameters on the interface stability and behavior. Parameters of interest describing the initial geometry of the interface are given by the wave number n and amplitude η_0 of the perturbations and the initial mean position R_0. The initial material state is defined by the initial density solid-gas density ratio $r_i = \frac{\rho_s}{\rho_g}$, the incoming shock Mach number M_s. A perfect plasticity model is considered for the solid, defined by the yield stress σ_Y. Table 6.1 summarizes the range of parameters used in the numerical simulations.

The first part of the section introduces the initial setup and boundary conditions for the problem. This paragraph is followed by the description of the evolution in time of a simulation run with the

Table 6.1: Parametric study of the Ritchmyer–Meshkov flow for solid–gas interfaces in cylindrical geometry

wave number	n	**4**, 8 ,12, 16
initial perturbation amplitude parameter	$C \equiv \eta_0 n/R_0$	**0.05**, 0.1
solid–gas density ratio	r_i	10, **100**, 1000
initial shock Mach number	M_s	1.16, 1.31, 1.48, **1.65**, 1.83
yield stress	σ_Y	0, **0.12**, 0.5, 1.0 GPa

parameters marked in bold in Table 6.1. The purpose of this paragraph is to explain the general features observed in the Richtmyer–Meshkov flow for solid–gas interfaces and establish a baseline problem that serves as a reference for the parametric study. This goal is accomplished by the extensive use of density contour plots and wave diagrams that support the explanation of relevant events, such as the initial shock–interface interaction, phase reversal, and re-shock. The third part of the section presents convergence studies based on the conservation of mass in the fluid and its evolution at each of the phases of the problem and on the deviation from radial symmetry of a cylindrical and unperturbed solid–gas interface. These studies are of key importance for trusting numerical results and determining their validity. Errors close to 2% in mass conservation are demonstrated for a problem with initial density ratio $r_i = 100$ when the maximum resolution available given current computational constraints is used. For higher density ratios, mass conservation becomes a major issue as the volume occupied by the fluid diminishes. Deviation from radial symmetry is a known drawback of the algorithm already reported in [8] for a different test case and it is therefore important to quantify is effect in the converging Richtmyer–Meshkov problem. The last part of the section is rather extensive and contains the results of the parametric study separated in different paragraphs (geometry parameters, density ratio, initial shock Mach number, and yield stress) that contain tables and time evolution and contour plots in order to illustrate the main conclusions of the analysis.

6.4.1 Computational domain. Boundary and initial conditions

A square computational domain $\{0, 10\} \times \{0, 10\}$ with grid cells of aspect ratio unity is employed for simulating a quadrant of a full cylindrical simulation. To achieve this purpose, reflective conditions are imposed in the left and bottom edges while zero-gradient boundary conditions are enforced in the upper and right edges in a way such that the axis is located at $(0, 0)$.

Figure 6.4 shows a typical initial configuration of the problem. The solid–fluid interface is initially located at $R_{int}(\theta) = R_0 + \eta_0 \cos(n\theta)$, with $r = \sqrt{{x_1}^2 + {x_2}^2}$ and $\theta = \arctan(x_2/x_1)$. The value $R_0 = 5$ is used in all the simulations considered in this section. At $t = 0$ the system is at rest. The fluid is modeled as a perfect gas with $\gamma_g = 5/3$, $\rho_0^g = 8.93/r_i\,\mathrm{g/cm^3}$ and $p_0^g = 0.05\,\mathrm{GPa}$, which is very small compared to the typical shock driving stress in the solid. The solid between the interface and the discontinuity originating the shock has an uniform state given by $\mathbf{g} = \mathbf{I}$ and $\varsigma/c_v = 2.365 \cdot 10^{-2}$, which produces a hydrostatic compression state of 0.05 GPa such that normal stresses are continuous across the solid–gas interface. The shock is initiated by a Riemann problem set by a discontinuity in density and radial stress in the solid at $r = R_s \equiv 7$ that depends on the desired shock strength. For $r > R_s$, the initial state must be adapted to comply with the linear momentum equation and curl constraint in cylindrical coordinates:

$$\frac{\partial \sigma_{rr}}{\partial r} + \frac{\sigma_{rr} - \sigma_{\theta\theta}}{r} = 0, \tag{6.3a}$$

$$\frac{\partial g_{\Theta\theta}}{\partial r} + \frac{g_{\Theta\theta} - g_{Rr}}{r} = 0. \tag{6.3b}$$

This can be achieved by keeping the entropy constant and employing an explicit ODE scheme to solve for the inverse deformation tensor components g_{Rr} and $g_{\Theta\theta}$. Note that an implementation of the Newton–Raphson method is needed to obtain g_{Rr} once $g_{\Theta\theta}$ and σ_{rr} are known. Plane strain conditions are always considered in the z direction.

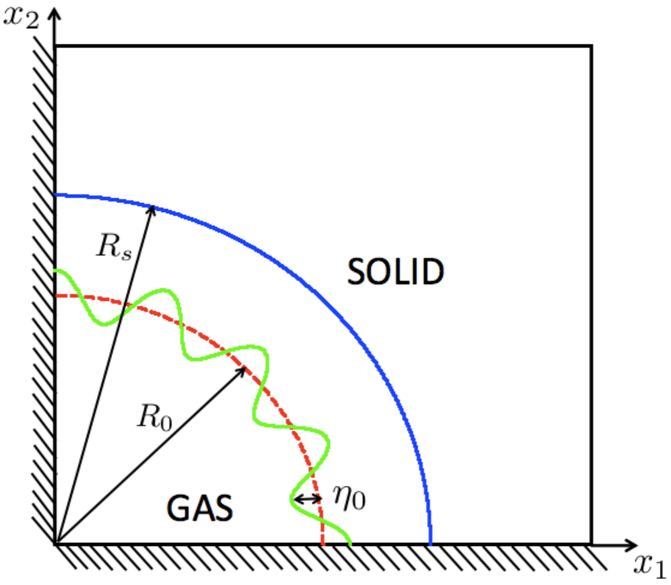

Figure 6.4: Schematic representation of boundary conditions, initial fluid and solid regions, material interfaces, and position of the incoming shock for the converging Richtmyer–Meshkov flow in a solid–gas interface with $n = 16$.

6.4.2 Baseline problem description

This paragraph describes the time evolution of a reference problem with initial parameters $n = 4$, $C \equiv \frac{\eta_0 n}{R_0} = 0.05$, $r_i = 100$, $M_s = 1.65$, and $\sigma_Y = 0.12\,\text{GPa}$. In order to achieve the desired initial

Mach number, the inverse deformation tensor in cylindrical coordinates at $r = R_s$ is

$$\mathbf{g} = \mathrm{diag}\{g_{Rr}, g_{\Theta\theta}, g_{Zz}\} = \{1.655, 1, 1\}, \tag{6.4}$$

and $\varsigma/c_v = 2.004$. This state produces an elastic stress tensor,

$$\sigma = \mathrm{diag}\{\sigma_{rr}, \sigma_{\theta\theta}, \sigma_{zz}\} = \{-655.1, -356.9, -356.9\}\mathrm{GPa}. \tag{6.5}$$

The previous values were computed to obtain a shock traveling at $M_s \approx 2$ in an elastic solid. However, since the perfect plasticity model is enforced, the stress conditions behind the shock are modified to meet the yield criterion after the first time-step and a slower plastic shock ($M_s = 1.65$) develops towards the solid–gas interface followed by a density (contact) discontinuity and an expansion traveling outwards. Figure 6.6(b) shows the configuration just after the shock is produced. Going outwards, the solid–gas interface (blue to green), incoming shock (green to orange), contact discontinuity in solid (orange to yellow) and expansion (yellow to red) can be observed. The plastic shock initially moves with velocity $U_s = 7.4\,\mathrm{km/s}$ ($M_s = 1.65$) and accelerates due to its converging imploding motion. The jump in radial velocity and stress across the shock is $\Delta u_r = 2.19\,\mathrm{km/s}$ and $\Delta\sigma_{rr} = -142.1\,\mathrm{GPa}$ where the minus sign indicates compression.

The state in the solid and fluid just after the shock–interface interaction varies azimuthally. However, if one considers a purely radial problem with $\eta_0 = 0$, the interface moves inwards with velocity $\dot{R}_{int} = 5.14\,\mathrm{km/s}$ and normal stress $\sigma_{rr} = -3.64\,\mathrm{GPa}$ at both sides. The solid-gas density ratio is reduced to 23.6 and continues to decrease as the interface moves inwards. A shock with Mach number $M_s^g = 7.5$ propagates in the fluid and an expansion is sent outwards in the solid, which presents a release density at the interface of $7.95\,\mathrm{g/cm^3}$ (see Fig. 6.6(c), where the transmitted shock in the fluid cannot be observed since the density jump is not enough to trigger a change in color in the contour plot).

The evolution of the different discontinuities after the first shock–interface interaction for the radial case ($\eta_0 = 0$) can be tracked in detail in Fig. 6.5, a $r - t$ wave diagram constructed upon the density (grey) and stress (black) gradients. The evolution depicted in the diagram can be directly translated to the perturbed interface case when the perturbation amplitude is sufficiently small. The transmitted shock is accelerated, as is the interface, by the effect of the converging geometry. The interface experiences the typical phase reversal of heavy–light Richtmyer–Meshkov configurations (Fig. 6.6(d)). The growth rate of the interface increases with time as well. At this point, numerical Kelvin-Helmholtz instability becomes noticeable as there exists a discontinuity in tangential velocity across the free-slip solid–gas interface. This new phenomenon can be observed in Fig. 6.7(a) as it creates interface oscillations of smaller wavelength and amplitude. After the transmitted shock reaches the origin, a reflected shock travels outwards and reaches the interface producing a first re-shock (Fig. 6.7(b)), which makes the Kelvin–Helmholtz instability grow larger. This second shock–interface interaction produces a bifurcation of transmitted (outwards) and reflected (inwards) shocks. The inward-moving shock reaches the axis and reflects producing in this way a series of re-shocks (Fig. 6.7(c)), which slow down the solid–gas interface until it finally sets in a long-term equilibrium mean position. The deceleration process is Rayleigh–Taylor unstable. Each outward shock moves faster than its predecessors and at the end, a single outward shock is obtained (Fig. 6.7(d)). At this point, the effects of the multiple shock–interface interactions and instabilities described cause the mixing zone, defined as the zone between the minimum and maximum circumferences for which fluid and solid can be found to grow. At the end of the simulation, fluid has been confined to a small region near the axis in pockets surrounded by solid (Figs. 6.6(e,f) and 6.7(e,f)).

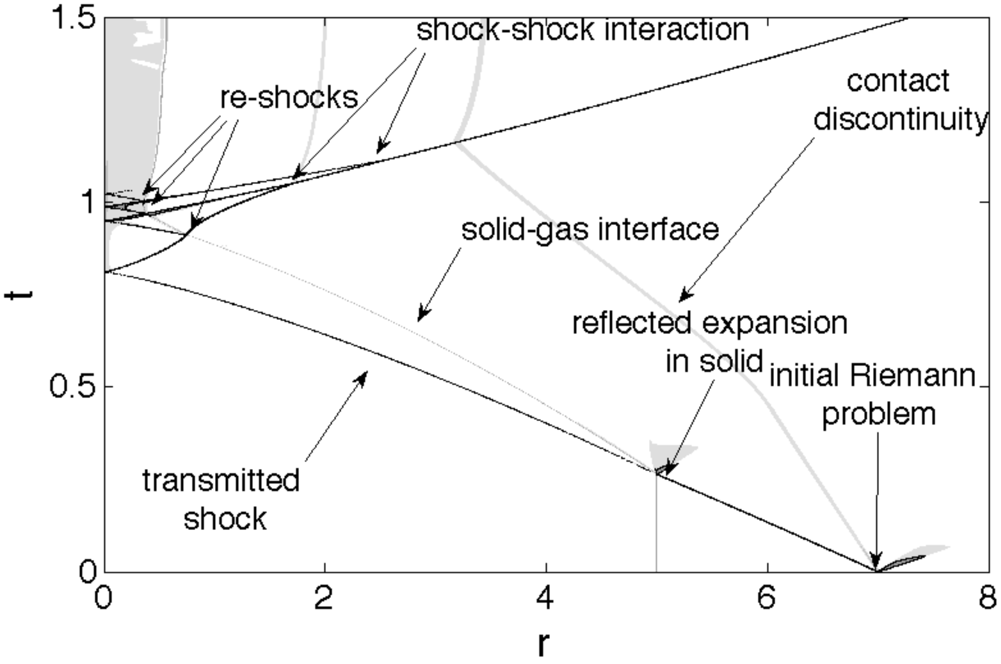

Figure 6.5: $r-t$ wave diagram for radially converging solid–gas flow constructed using density (grey) and pressure (black) gradients. The initial Riemann problem in the solid produces a shock towards the solid–gas interface, a contact discontinuity and an expansion. The shock–interface interaction produces a transmitted shock in the fluid and a reflected expansion in the solid. The interface starts moving towards the axis. As the transmitted shock reaches the axis, it is reflected as a stronger shock which produces a secondary interaction with the interface. As a result, shocks appear in both fluid and solid. This process is repeated with weaker shocks at each time, until the solid–gas interface reaches an stationary position. The series of transmitted shocks in the solid finally merge in a single outwards shock.

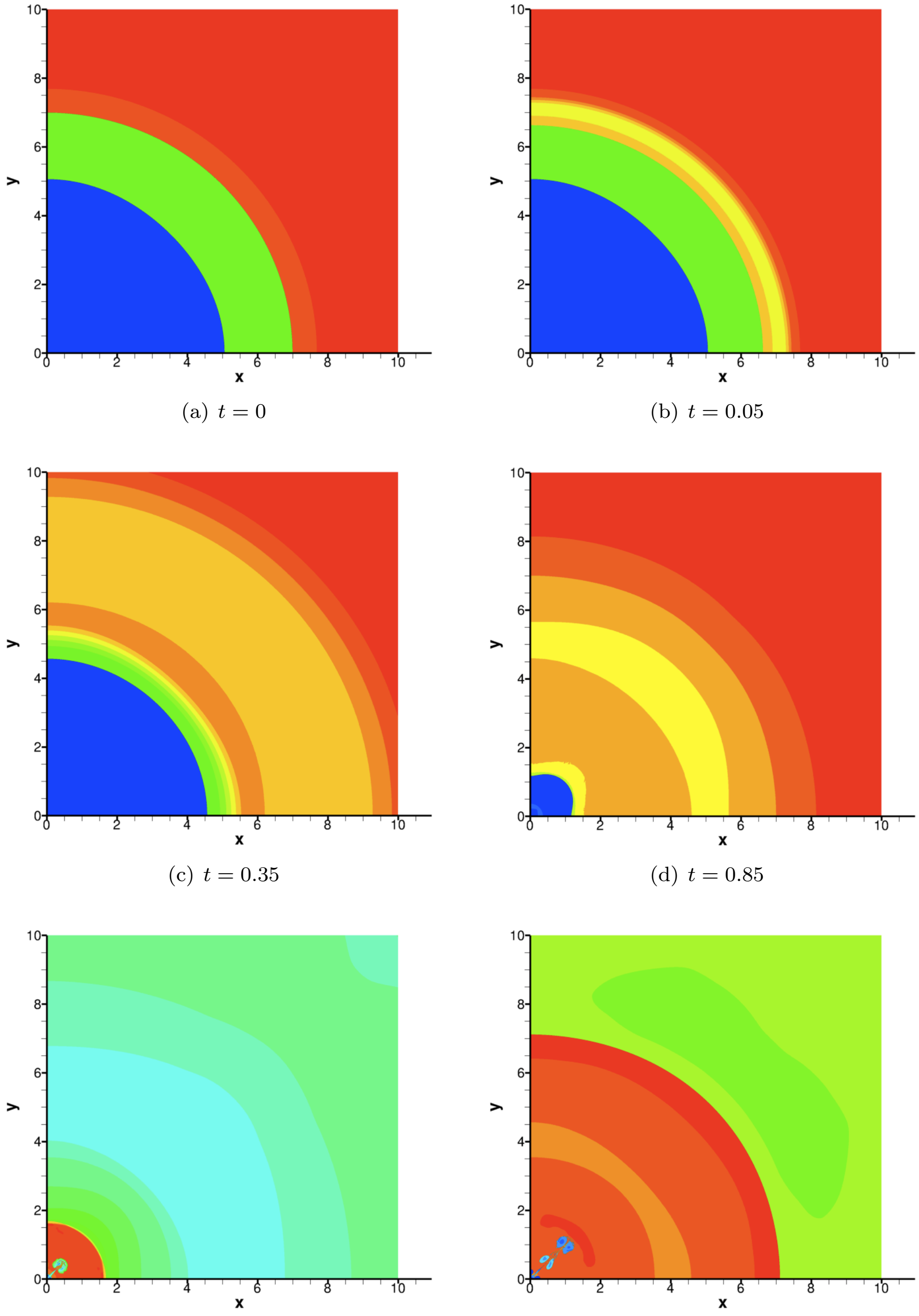

(a) $t = 0$

(b) $t = 0.05$

(c) $t = 0.35$

(d) $t = 0.85$

(e) $t = 1.05$

(f) $t = 1.5$

Figure 6.6: Time evolution of density contours for the baseline solid–gas Richtmyer–Meshkov problem with parameters for copper, $\sigma_Y = 0.12\,\mathrm{GPa}$, $\eta_0 n/R_0 = 0.05$, and $M_s = 1.65$. Individual frames show: (a,b) initial conditions and propagation of the shock, (c) state after shock–interface interaction, (d) reflected shock at the axis and growth of instability before first re-shock, (e,f) state after re-shocks and outbound shock.

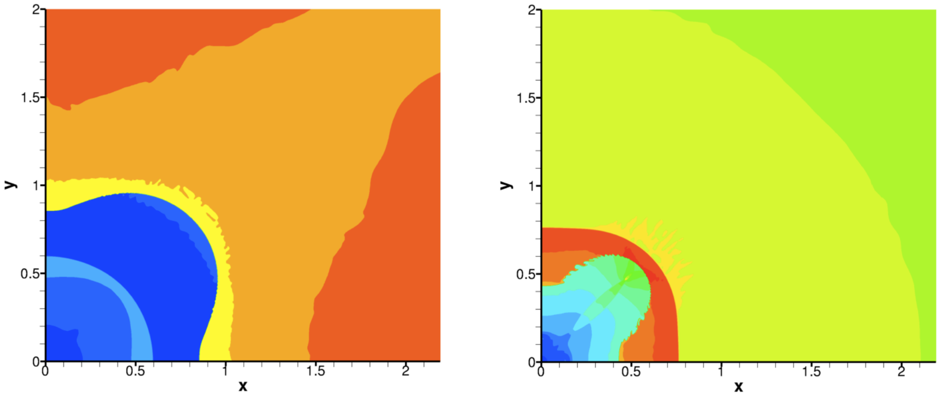

(a) $t = 0.9$ (b) $t = 0.933$

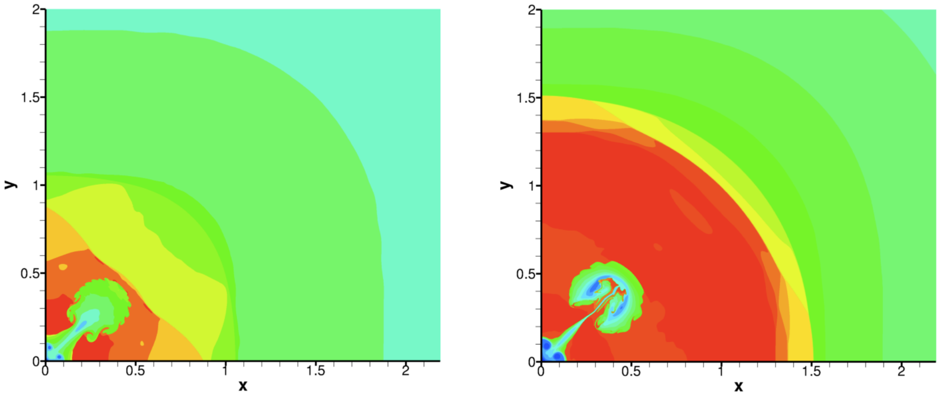

(c) $t = 0.383$ (d) $t = 1.033$

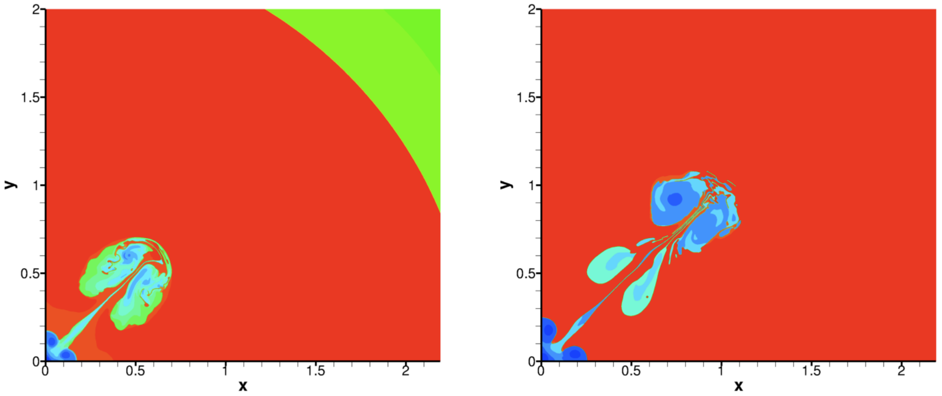

(e) $t = 1.1$ (f) $t = 1.3$

Figure 6.7: Time evolution of density contours for the baseline solid–gas Richtmyer-Meshkov problem with parameters for copper, $\sigma_Y = 0.12\,\mathrm{GPa}$, $\eta_0 n/R_0 = 0.05$, and $M_s = 1.65$ with emphasis on the region close to the axis. Individual frames show: (a) Kelvin-Helmholtz instability and outbound shock after imploding shock reaches the axis, (c,d) structure of various shocks and interface instability growth, (e,f) state after re-shocks with growing of mixing zone. Roughness in the density contours of the first frames are due to use of rectangular grid, limitations of the approximate Riemann problem and numerical errors when computing normals at the interface once Kelvin-Helmholtz instability appears.

6.4.3 Convergence studies

This section presents two convergence studies that are important in the determination of the minimum mesh resolution required for running accurate simulations. The first example focuses on conservation of the mass of fluid, which is required given that the level-set method is in general non-conservative. The second test quantifies another known inaccuracy of the level-set algorithm, which is the deviation for radial symmetry at an initially cylindrical material interface as a simulation progresses. This problem becomes more relevant in the case of inward motions (like the one occurring in the converging Richtmyer–Meshkov instability with a solid–gas interface) as the number of cells bisected by the material interface decreases with time.

6.4.3.1 Fluid mass conservation

Keeping an acceptable conservation of mass in the lighter material in a generally non-conservative level-set method becomes of paramount importance for the accurate analysis of multi-material Richtmyer–Meshkov flows. Solid–gas problems are more prone to suffer from poor mass conservation since the fluid is generally more compressible than the solid. For instance, in the baseline problem, the incoming shock propagates in the solid at $M_s \approx 1.65$ but the transmitted shock propagates in a fluid with a density 10 to 100 times lower than the solid at $M_s \approx 8$. This effect is aggravated by a converging geometry which accelerates the shock and increases its compression ratio until it tends to extremely large values at the axis. In consequence, the volume occupied by the fluid abruptly decreases in time and for very large density ratios (typically greater than 1000), the final volume occupied becomes comparable to the smallest cell size that can be afforded with the current available computational power, leading to large mass conservation errors. A second concern is the fact that the problem with slip at the interface is ill-posed. This means that, as the mesh resolution is increased, new and more complex scales appear, increasing the contact surface between the two materials and therefore increasing the chance of mass conservation errors.

This paragraph is focused on mass conservation in cylindrical geometry Richtmyer–Meshkov flow for solid–gas interfaces. For other test cases, such as solid–solid or solid–gas in planar geometry, the reader may refer to Appendix C. A slightly modified version of the baseline problem is considered for this example, with the only difference being an initial amplitude parameter $\eta_0 n/R_0 = 0.0318$. Series of simulations of the same initial, boundary value problem were run for different base-grid resolutions and number of levels of refinement. The total mass of fluid at multiple time-steps was computed by direct evaluation of the density field and material volumes with the help of the two-dimensional quadrature feature integrated in the visualization software package Tecplot. Mass errors where computed in the L_2-norm:

$$\varepsilon_{mass}(t_{n_f}) = \sqrt{\frac{1}{n_f}\sum_{n=1}^{n_f}\left(\frac{|m_n - m_{n-1}|}{m_{n-1}}\right)^2}, \tag{6.6}$$

where m_n is the mass at time-step n, with $t_0 = 0$. Multiple values of the final time $t_{n_f} = \{0.5, 0.75, 1, 1.25, 1.5\}$ were considered so the effect of the ill-posedness of the problem as time evolves and interface instabilities develop can be described. Thus, this method considers that the change in mass between time-steps gives a more accurate measure of mass conservation than computing the difference in mass with respect to the initial value. This can be attributed to the fact that the latter method can cancel errors due to oscillations and is not accurate in cases in which there is an abrupt increment in mass followed by an equally abrupt loss (for instance, caused by shocks passing through the interface). If the loss is comparable to the gain, the final mass value will be very close to the initial value and the mass changes will be underestimated. Computing the absolute value of the change in mass with respect to the previous time-step adequately captures the effect of the jumps.

Figure 6.8 shows the mass conservation evolution in time. Simulations with 5 levels of refinement are chosen with equivalent number of cells (number of cells that a uni-grid simulation would require to equal the resolution of the finest level) in each direction ranging from 512 to 16384. The total mass of fluid increases after the first shock–interface interaction (around $t \approx 0.25$). This increment is reduced as the mesh resolution is increased. At this point, interface perturbations are quasi-linear and the problem is well-posed. Mass values remain stable until the first re-shock ($t \approx 0.9$). After this point, as described in Subsection 6.4.2, the interface exhibits a nonlinear behavior and the level of detail in which flow features appear depends on the resolution used, with lower resolutions not describing the effects of smaller wavelengths. Figure 6.9 shows how the shape of the interface for a given time after re-shocks is clearly dependent on grid resolution. In this region, it is not clear whether mass conservation monotonically improves with higher resolution.

Tables 6.2–6.3 and the series of plots in Fig. 6.10 illustrate with numerical results, the conclusions drawn from the previous analysis. In the figures, different numbers of refinement levels and base-grid resolutions are considered. In order to unify the results, the equivalent number of cells in one direction is used in the x-axis of the plots. The mass error (6.6) is computed for different final times, ranging from 0.5 to 1.5. For the sake of simplicity, mass errors for cases with the same equivalent resolutions but different levels of refinement are averaged in Tables 6.2-6.3. At $t = 0.5$ closely after the first shock passage through the interface, first-order convergence is achieved for the mass error as resolution is increased. Shortly after, at $t = 0.75$, first-order convergence rate is maintained for coarse grids but it drops below first-order for the finer grids. This can be attributed to the existence of numerical Kelvin–Helmholtz instability caused by the discontinuous tangential

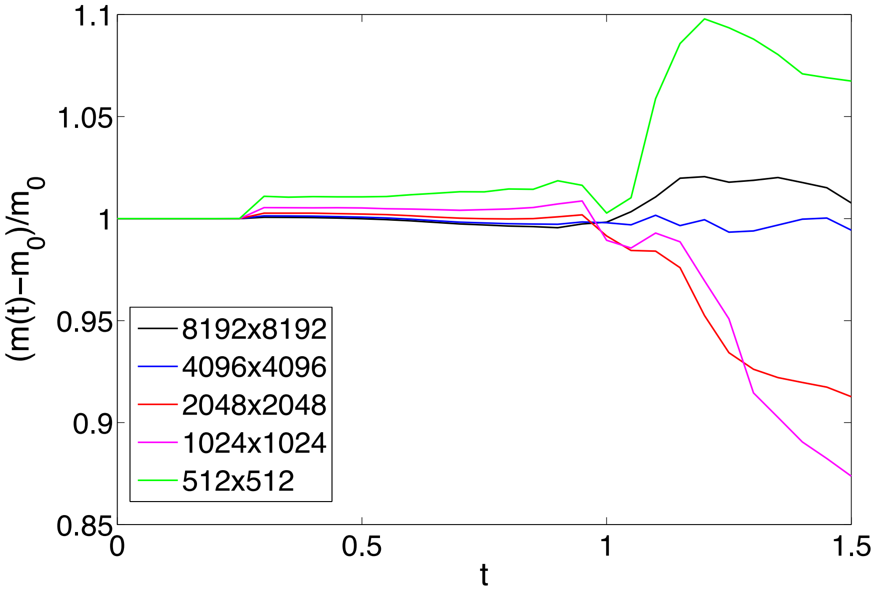

Figure 6.8: Mass of fluid evolution with respect to initial mass for simulations with 5 levels of refinement and variable base-grid size. The legend values represent the equivalent number of cells (cells in one direction that an uni-grid simulation needs in order to match the resolution of the finest level)

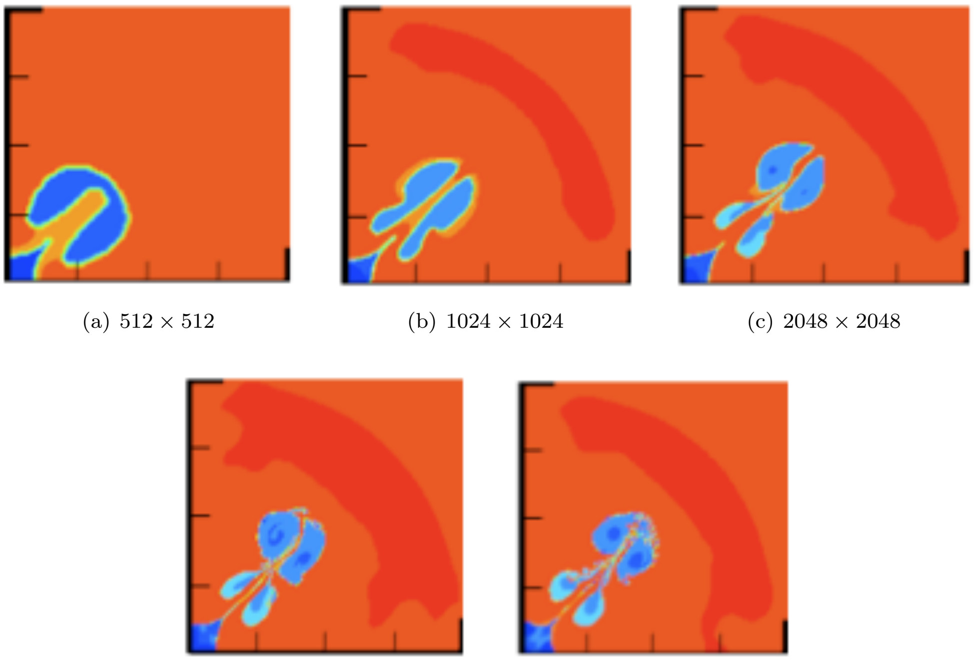

(a) 512 × 512

(b) 1024 × 1024

(c) 2048 × 2048

(d) 4096 × 4096

(e) 8192 × 8192

Figure 6.9: Density color-contour plots highlighting the mixing zone for five different resolutions at $t = 1.5$

velocity at the interface. This effect depends on grid resolution and is more relevant as the cell size decreases. For results after the re-shock, first-order convergence is no longer achieved. Plateaus and steep decrements in mass errors occur as the resolution is increased and smaller scales progressively appear. For instance, mass error is sharply reduced from 128 × 128 to 512 × 512 and from 1024 × 1024 to 4096 × 4096 equivalent cells, with plateaus in between and afterwards. An explanation for this phenomenon can be inferred from Fig. 6.9: between 512 × 512 and 1024 × 1024, the shape of the interface changes drastically, leading to a stagnation in mass error even if resolution is increased as a result of the increment in total length of the interface. After that, the general shape of the interface remains relatively unchanged until the 4096 × 4096 case. As resolution is increased to 8192 × 8192, more detailed features appear in the interface, specifically tiny pockets of fluid, which lead to the second plateau in mass conservation. It is worth noting that results become more dependent on the number of levels of refinement used for a given equivalent resolution but a trend cannot be easily identified (for instance, it cannot be said that, in general, lower levels of refinement for a given equivalent resolution lead to better mass conservation).

Table 6.2: L_2-errors and convergence rate for $t = \{0.5, 0.75, 1.0\}$. Cases with the same equivalent resolution but run with different levels of refinement have been averaged.

eq.resolution	$\mathbf{t_{n_f} = 0.5}$		$\mathbf{t_{n_f} = 0.75}$		$\mathbf{t_{n_f} = 1.0}$	
	$\epsilon(t_{n_f})$	**C.R.**	$\epsilon(t_{n_f})$	**C.R.**	$\epsilon(t_{n_f})$	**C.R.**
64	5.052e-3		3.662e-3		8.672e-3	
128	3.562e-3	**0.504**	2.435e-3	**0.589**	10.17e-3	**-0.229**
256	1.991e-3	**0.839**	1.381e-3	**0.818**	3.695e-3	**1.460**
512	1.096e-3	**0.862**	0.736e-3	**0.909**	1.009e-3	**1.873**
1024	0.538e-3	**1.026**	0.361e-3	**1.025**	1.003e-3	**0.009**
2048	0.265e-3	**1.023**	0.185e-3	**0.963**	0.607e-3	**0.723**
4096	0.136e-3	**0.960**	0.113e-3	**0.708**	0.127e-3	**2.260**
8192	0.076e-3	**0.841**	0.097e-3	**0.225**	0.176e-3	**-0.469**
16384	0.052e-3	**0.539**	0.103e-3	**-0.089**	0.180e-3	**-0.039**

Table 6.3: L_2-errors and convergence rate averaged for $t = \{1.25, 1.5\}$. Cases with the same equivalent resolution but run with different levels of refinement have been averaged.

eq.resolution	$\mathbf{t_{n_f} = 1.25}$		$\mathbf{t_{n_f} = 1.5}$	
	$\epsilon(t_{n_f})$	**C.R.**	$\epsilon(t_{n_f})$	**C.R.**
64	10.10e-3		9.267e-3	
128	9.599e-3	**0.074**	8.198e-3	**0.177**
256	3.104e-3	**1.629**	2.660e-3	**1.624**
512	2.259e-3	**0.458**	1.934e-3	**0.460**
1024	1.604e-3	**0.494**	1.723e-3	**0.163**
2048	1.090e-3	**0.557**	0.885e-3	**0.965**
4096	0.523e-3	**1.060**	0.507e-3	**0.804**
8192	0.508e-3	**0.042**	0.491e-3	**0.0459**
16384	0.576e-3	**-0.181**	0.631e-3	**-0.361**

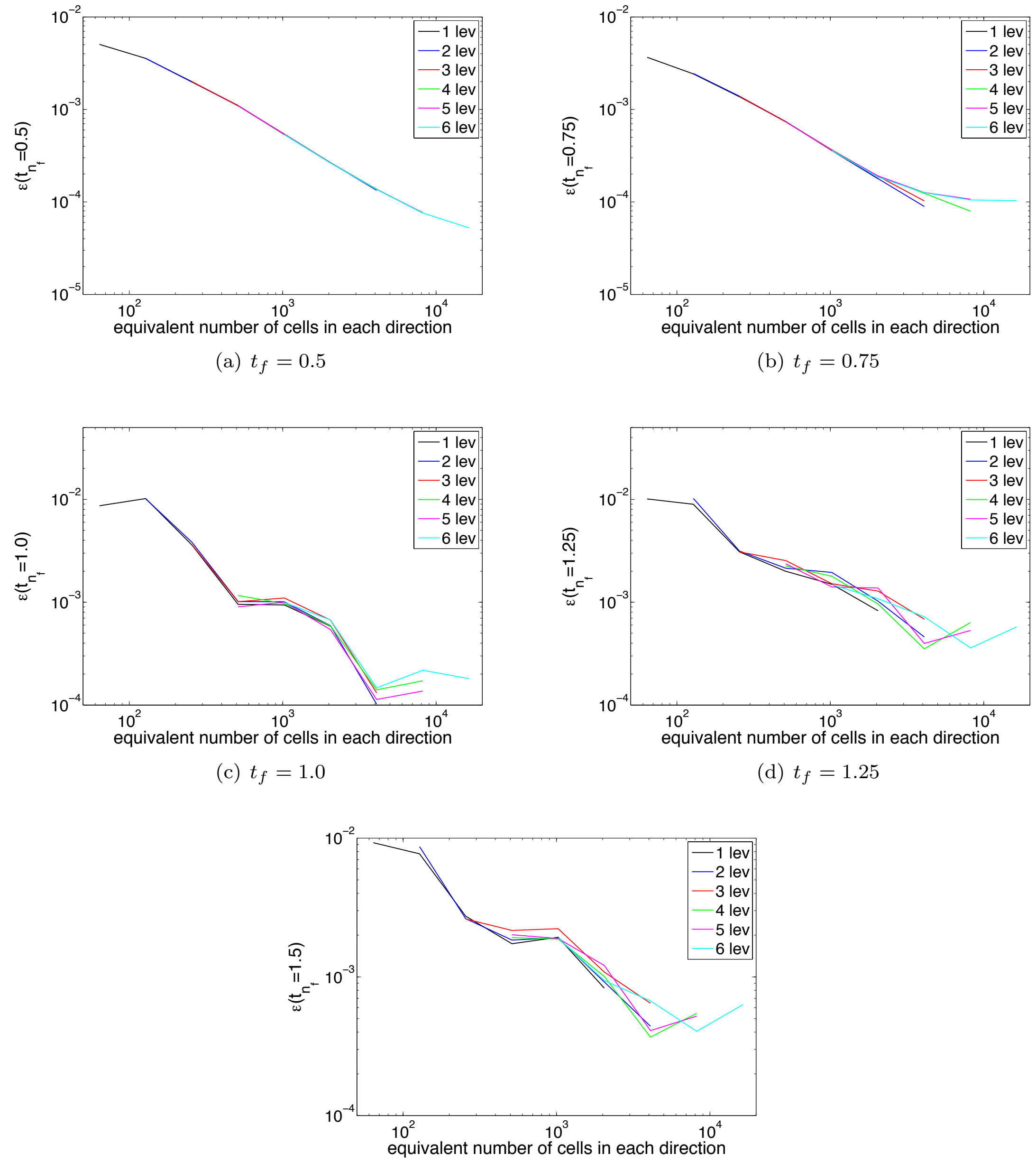

(a) $t_f = 0.5$

(b) $t_f = 0.75$

(c) $t_f = 1.0$

(d) $t_f = 1.25$

(e) $t_f = 1.5$

Figure 6.10: Mass conservation errors given by Eq. (6.6) for multiple final times $t_f = \{0.5, 0.75, 1, 1.25, 1.5\}$. Different number of total levels (with 1 level corresponding to uni-grid) and base-grid resolutions are considered, with results unified using the equivalent number of cells (number of cells needed in an uni-grid simulation to match the resolution of the finest AMR level) in each direction. First-order convergence is obtained for early times as the problem is well posed. For later times, as multiple source of instability are present, the problem is ill-posed and an increment in resolution does not monotonically decrease conservation errors.

6.4.3.2 Preservation of cylindrical geometry in a multi-material level-set algorithm

Numerical limitations of the level-set advection and reinitialization algorithm (see Section 3.3) have an effect on the time evolution of the perturbed material interface. This problem is well documented in the test case described in Subsection 3.3.4, in which an initially cylindrical shell moves inwards with a radial velocity field. The shell enters the plastic state and a transfer between kinetic and internal energy occurs under the effect of plastic dissipation until the solid comes to a rest. In the process, the cylindrical geometry is distorted as the solid moves inwards and less cells are bisected by the material boundary. The distortion is heavily dependent on the grid resolution used but exhibits first-order convergence rate for small cell-sizes.

In order to test the magnitude of this known effect in the simulations of the cylindrical Richtmyer–Meshkov flow for solid–gas interfaces, a series of simulations with $\eta_0 = 0$ are considered. The first six cases are run with a single-grid, starting at 64×64 cells and increasing resolution by a factor of two until 2048×2048. After this point, uni-grid computations are not practical due to computation time constraints and simulations with 4 levels of refinement are employed, with effective grid resolutions spanning from 4096 effective cells in each direction (i.e., number of cells that uni-grid simulations need in order to match the resolution of a multi-level simulation) to 16384 cells. The rest of initial parameters and material properties are similar to those used in the baseline problem.

In Fig. 6.11, the deviation from the cylindrical geometry is measured by:

$$L_2 - \text{error}(t, \overline{R}) = \frac{1}{\overline{R}(t)} \sqrt{\frac{1}{N} \sum_{n=1}^{N} \left(R_n(t) - \overline{R}(t)\right)^2}, \tag{6.7}$$

where R_n is the solid–gas boundary position at a particular ray $\theta_n = \arctan(x_2/x_1) = C_n$, N is the total number of rays, and $\overline{R}$ is the mean radial position of the interface

$$\overline{R}(t) = \frac{1}{N} \sum_{n=1}^{N} R_n(t). \tag{6.8}$$

Results are shown from the time interval $t = \{0.26, 0.8\}$. The initial shock–interface interaction ($t \approx 0.26$) produces the first deviations from the radial symmetry. The convergence rate of the errors in this period is below first-order due to the discontinuous velocity field as the shock arrives at the interface. A second region is appreciated between $t = 0.3$ and $t = 0.5$ where the error does not increase at a high rate, specially in high-resolution simulations. As the interface continues to move inwards (after $t > 0.5$), the deviation from radial symmetry increases. This phenomenon is accelerated as the interface approaches the origin and less cells are intersected by the material boundary. At the same time, the numerical Kelvin–Helmholtz instability appears at the material boundary since small perturbations from the radial symmetry produce discontinuities of tangential velocities between the solid and the gas. The convergence rate in this region approaches first-order in uni-grid computations. However, it is observed that the error in AMR simulations (represented by dashed lines) increases at a higher rate than for uni-grid computations. For instance, the error measured for the 2048 × 2048 uni-grid case is similar to that for an effective cell size of 4096 × 4096 with four levels of refinement. During this period the interface is Rayleigh–Taylor stable since the interface accelerates (see Fig. 6.5) and all the perturbations can be attributed to the effect of the level-set advection and reinitialization algorithms in a converging geometry and the subsequent numerical Kelvin–Helmholtz instability. Results are not shown for the time after the first re-shock as a shock interaction with an already perturbed interface produces a strong Richtmyer–Meshkov instability and the deceleration of the interface causes the inception of Rayleigh–Taylor instabilities.

6.4.3.3 Summary of convergence studies

The test cases analyzed suggest that very small cell sizes are required to reduce the errors in mass conservation and deviation from radial symmetry up to acceptable limits. AMR is completely necessary to achieve high-resolution with reasonable computation times, even when refinement produces a lower convergence rate of the deviations from radial symmetry. The fact that first-order convergence rate is only achieved for a small period of time reveals that an increment in grid resolution is not accompanied by a proportionally accurate result in many phases of the simulation. With these results, an equivalent resolution of 8192 × 8192 with $\Delta x_1 = \Delta x_2 = 1.2207 \cdot 10^{-3}$ is chosen for the parametric analysis. This is motivated by the typical simulation time (around 18 hours for an equivalent resolution of 8192 × 8192 with 4 levels of refinement and running on 56 cores compared to 36 hours for 16384 × 16384 with 5 levels of refinement and running on 72 cores) and the small difference in mass conservation between the two largest resolutions tested (i.e., in the case examined for mass conservation, 8192 × 8192 has a lower mass conservation error than 16384 × 16384 for the period of time after the re-shock).

6.4.4 Interface parametric analysis

This section describes the behavior of the solid–gas interface under different initial and material parameters. The study of the interface evolution in the impulsive and linearized analytical model for elastic solids (Chapter 5) reveals that the growth rate of the interface is mainly affected by the initial geometry (wave number and amplitude), the density ratio of the materials, and the initial velocity of the impulse (which can be substituted in the shock-driven case by the Mach number of the incoming shock). In particular, just after the impulse occurs, the interface growth rate in an elastic solid follows the classical idealized results for fluids obtained by Richtmyer [96]:

$$U = A_t V_0 \eta_0 k. \tag{6.9}$$

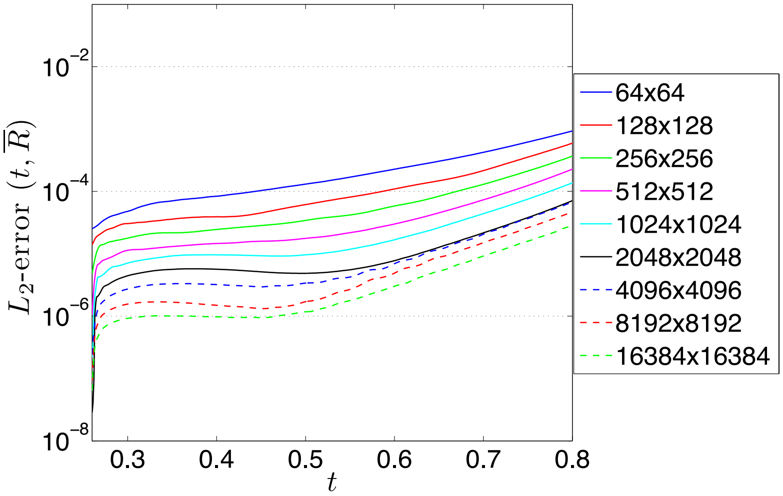

(a) L_2-error

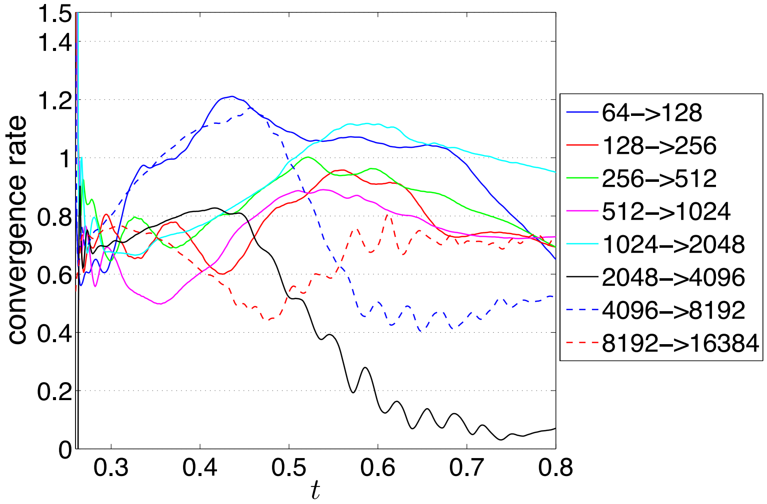

(b) Convergence rate

Figure 6.11: L_2-error and convergence rate for the preservation of radial symmetry in a solid–gas cylindrical interface processed by a shock wave. Continuous and dashed lines represent uni-grid and AMR computations respectively. The number of cells in the legend represent the effective resolution.

For a solid–gas interface, the Atwood ratio is defined as $A_t = \frac{\rho_g - \rho_s}{\rho_g + \rho_s}$, with ρ_s and ρ_g the densities after the shock–interface interaction of solid and gas, respectively. In the cylindrical case, $k = n/R(t)$ or $k = n/R_0$ for analysis far or close to the initial interface position, respectively. In addition to the elastic analysis, the results for the elastic–plastic solid–vacuum planar case revealed that the yield stress is the key parameter that controls the transition between the fluid-like and the elastic behavior. In the forthcoming paragraphs, the effect of each of these parameters is described using plots depicting the temporal evolution of interface parameters. The amplitude of the interface η and the growth rate $\mathbf{U} \equiv \dot{\eta}$ of the perturbations can be computed by knowing at each time the volume fraction at each point of the domain for fluid and solid. In the level-set approach, the volume fraction can be easily computed as $X_i = \frac{\phi_i}{|\phi_i|}$. The amplitude is subsequently derived as

$$\eta(t) = \max\left(r \ni |\int_0^{\frac{\pi}{2}} X_i(r,\theta,t)\,d\theta| \leq 1\right) - \min\left(r \ni |\int_0^{\frac{\pi}{2}} X_i(r,\theta,t)\,d\theta| \leq 1\right). \tag{6.10}$$

This expression is valid for the initial small-perturbation regime but also helps to describe the mixing zone formed after the re-shocks. The growth rate can be directly computed from differentiation of perturbation amplitude with respect to time. In addition to time evolution of the interface parameters, selected contour plots sequences are employed to visualize the observed phenomena. A complete set of these sequences for all the parametric cases can be found in Appendix D.

6.4.4.1 Influence of the initial geometry of the interface

Variations in the initial shape of the interface $R_{int}(\theta) = R_0 + \eta_0 \cos(n\theta)$ are considered in this first parametric analysis. The wave number takes values $n = \{4, 8, 12, 16\}$ and two initial amplitude parameter values are employed: $C \equiv \frac{\eta_0 n}{R_0} = \{0.05, 0.1\}$, resulting in eight different initial combinations. Values of the initial mean position R_0, shock strength and solid–gas initial density ratio remain constant and match those of the baseline problem.

Figure 6.12 is used to describe the behavior of the interface by looking at the amplitude and the growth rate conveniently non-dimensionalized by the initial perturbation amplitude, wave number, velocity of the interface after the shock–interface interaction, and mean position of the interface. Figures 6.12 (a,b) span the whole simulation time. After the first shock–interface interaction and the phase reversal, the amplitude grows for all cases. However, instead of growing unboundedly or saturating to a constant value like in the planar case, the interface amplitude reaches a peak and then decreases. This is clearly seen for the cases $n = \{12, 16\}$ in which a second interface phase reversal occurs before the first re-shock. For the simulations with $n = 8$, the trend is the same, but since the peak occurs at later times when decreasing n, the first re-shock happens before this phase reversal could be completed. Finally, for $n = 4$, the peak in amplitude is not reached in the period between the first and shock–interface interactions. In Fig. 6.13, a series of density contour plots

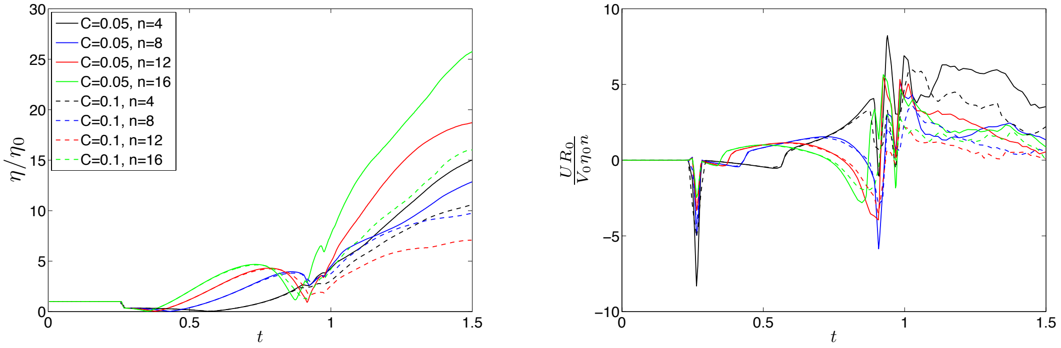

(a) Interface amplitude / time

(b) Growth rate / time

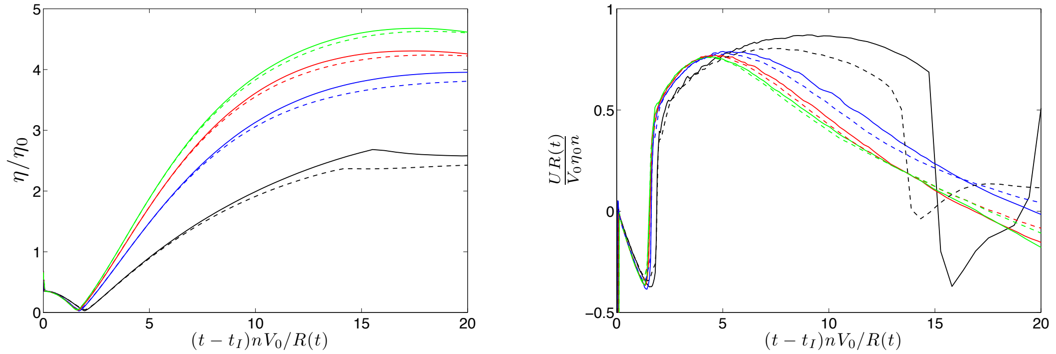

(c) Interface amplitude / non-dimensionalized time

(d) Growth rate / non-dimensionalized time

Figure 6.12: Interface evolution as a function of time for $n = \{4, 8, 12, 16\}$ and $C \equiv \frac{\eta_0 n}{R_0} = \{0.05, 0.1\}$ (see legend in (a)). Figures (a) and (b) show the whole simulation time, including events after re-shocks. Figures (c) and (d) focus on the short-term behavior after the first shock–interface interaction.

depict this phenomenon for $n = 16$ and $C = 0.1$. The new spikes form in the period between the time of the first and second plots, with previous spikes becoming bubbles. The decrease in interface amplitude can be clearly appreciated in the contour plots. Good collapse between the cases with different initial amplitudes in the time period before the re-shock is observed when the evolution of the perturbation amplitude is scaled with the initial perturbation value. After the series of re-shocks (marked clearly in Fig. 6.12(b) by sudden spikes in the growth rate from $t \approx 0.9$ to $t \approx 1.1$) the amplitude increases in a fluid-like fashion, exhibiting first an almost constant growth rate that slowly decays afterwards. In general, for this region, the cases with $C = 0.05$ achieve a higher value of the amplitude when scaled to the initial one than those with $C = 0.1$. The density contour plots for $n = 4$, $C = 0.05$ and $n = 16$, $C = 0.1$ (Figs 6.7 and 6.13, respectively) reveal that, at the time of re-shock, the interface shape is not sinusoidal anymore, especially for $n = 16$ after the second phase reversal. The behavior after re-shocks then resembles that of a turbulent mixing zone between the plastic solid and the gas.

In Figs. 6.12 (c,d), the initial behavior of the interface is characterized. Time is conveniently non-dimensionalized with the initial velocity of the interface, the position of the interface in time and the wave number. t_I is the time of the first shock–interface interaction. The growth rate is presented in a non-dimensional form such that the value of this parameter predicted by the first-order impulsive start-up theory (6.9) would be $A_t \approx 1$. Results show acceptable collapse for the maximum growth rate, with values becoming closer to each other as n increases. This is due to the fact that the effects of the converging geometry are reduced as n becomes larger, with $n \to \infty$ corresponding to a planar case. The maximum growth rate for $n = 4$ is largely affected by converging geometry effects, as it occurs at a time in which the mean position of the interface is closer to the axis.

6.4.4.2 Influence of the density ratio

The interfacial density ratio is an important parameter in the Richtmyer-Meshkov instability since it defines, together with the pressure gradient across the shock, the magnitude of the baroclinic vorticity deposited after the acceleration of the interface by the passage of the shock. For the purpose of the parametric study of the solid–gas initial density ratio, the values $r_i = \{10, 100, 500\}$ were selected. The initial density of the fluid is modified, keeping the solid state unchanged, in order to achieve these values. Since the previous section revealed important differences in the interface behavior depending on the wave number used, each density ratio is evaluated for $n = \{4, 16\}$ and $C = 0.05$ for a total of 6 different cases (in Appendix D, contour plots for cases with $C = 0.1$ are also shown).

The conditions resulting from the shock–interface interaction are modified due to different Riemann problems at the interface being developed with each initial value of the density ratio. Table 6.4 summarizes the initial interface velocity V_0, Atwood ratio after shock A_t (with a negative value

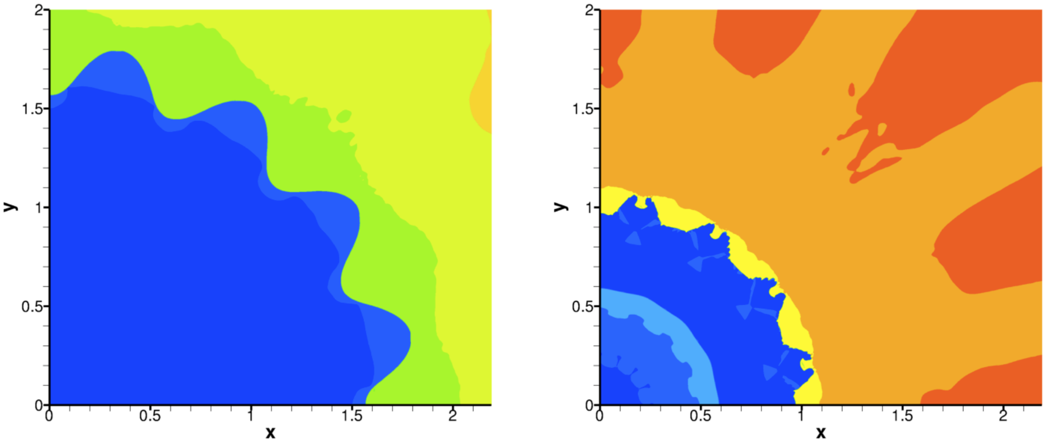

(a) $t = 0.8$ (b) $t = 0.883$

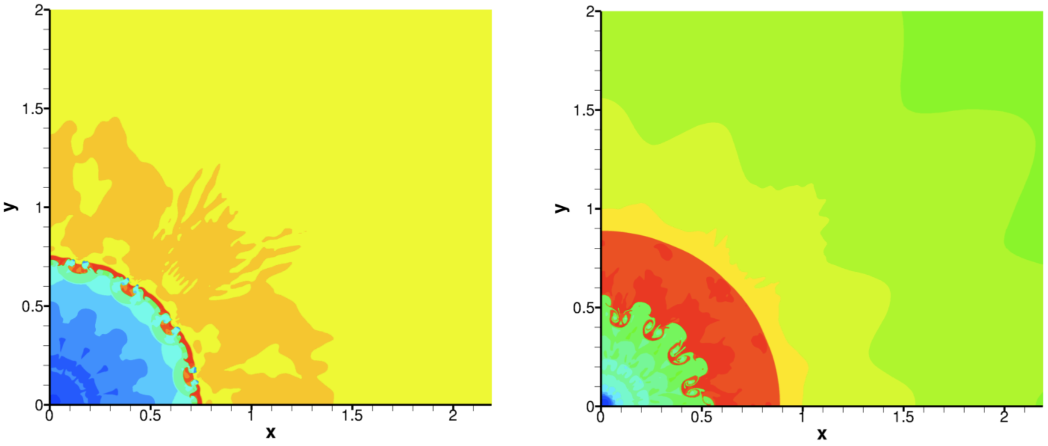

(c) $t = 0.917$ (d) $t = 0.95$

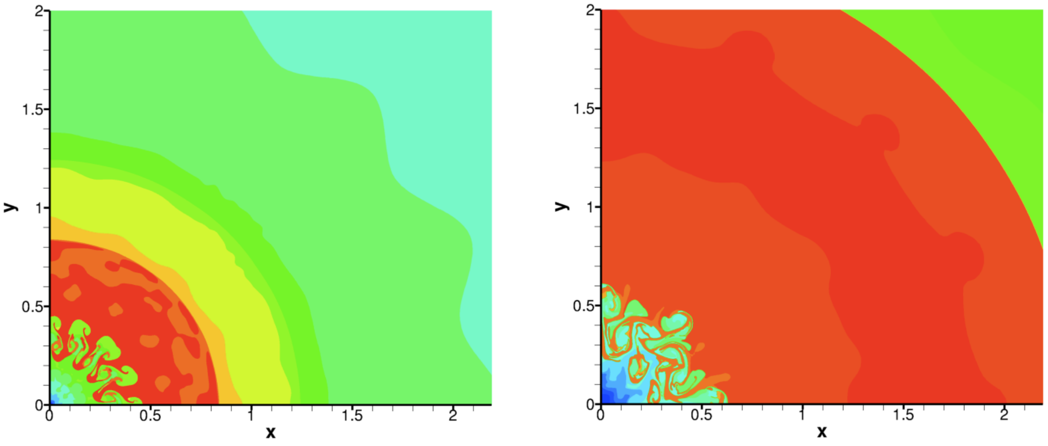

(e) $t = 1.0$ (f) $t = 1.1$

Figure 6.13: Density contour plots close to the axis for the case with initial parameters $n = 16$ and $C = 0.1$. New spikes form in the cusp of the bubbles in the period between $t = 0.8$ and $t = 0.883$ (Figures (a) and (b)). These new spikes grow producing a second phase reversal, with previous spikes becoming bubbles. The interface is re-shocked in (c) and a mixing zone typical of gas–gas Richtmyer–Meshkov instability is formed.

Table 6.4: Interface parameters in shock–interface problem with different initial density ratios

r_i	V_0(km/s)	σ_{rr}(GPa)	A_t
10	4.58	-25.4	-0.455
100	5.14	-3.64	-0.919
500	5.23	-0.88	-0.985

indicating a heavy–light interface), and normal stress σ_{rr} for each of the considered cases in an unperturbed interface problem ($C = 0$).

As a result of the converging cylindrical geometry, the conditions across the interface dynamically change as it approaches the axis. Figure 6.14 reveals that the velocity evolution is substantially modified as the initial density of the fluid varies. In particular, less velocity is achieved upon release as the fluid density is increased. The acceleration produced by the converging geometry is also lower and, in the $r_i = 10$ case, the velocity decreases when the fluid inside becomes denser than the solid moments before the first re-shock (Fig. 6.14(d)). The differences between the two cases with higher density ratio are less noticeable. The first re-shock occurs at a later time for lower r_i as a consequence of the slower motion of the interface and the transmitted shock in the fluid. The normal stress at the interface is always increased proportionally to its value after the shock passage by the converging motion.

Important features are found when comparing the interface evolution for the six considered cases. In the first place, as Fig. 6.15 shows, the cases $r_i = 100$ and $r_i = 500$ exhibit a very similar behavior, especially before the re-shock. This suggests the existence of a limiting case as the solid–vacuum situation ($A_t = -1$) is approached. Unfortunately, with no opposition from the presence of a gas, solid–vacuum converging simulations fail before the interface reaches the origin (since the value of the velocity at the interface tends to infinity), exceeding the capabilities of the level-set algorithm. A solid–gas interface with a low enough initial density ratio can be then sufficient to qualitatively predict the evolution of the pure solid–vacuum configuration.

The evolution after re-shock, as observed in Figs. 6.15 (a,b), exhibits some differences that are mainly a result of the volume occupied by the fluid. The case $r_i = 500$ contains five times less mass of fluid than the case $r_i = 100$. Inferring from Fig. 6.14(c) a similar pressure field in both cases after re-shock, the final volume of fluid has to be much smaller in the higher density ratio case. The comparison between the contour plots in Fig. 6.17 and their counterparts for $r_i = 100$ (Figs. 6.7(e) and 6.13(f)) reveals that the fluid pockets are more sparsely distributed in the first case. Recalling that the amplitude (size of the mixing zone) is computed as the difference between the smaller and larger radius for which fluid and solid are found when sweeping azimuthally, the obtained η is commonly larger in the higher density ratio case even when the volume fraction of fluid is generally lower at each radial position r. This is illustrated in Fig. 6.16, where the volume fraction of fluid for initial density ratios $r_i = \{100, 500\}$ and wave numbers $n = \{4, 16\}$ is shown at

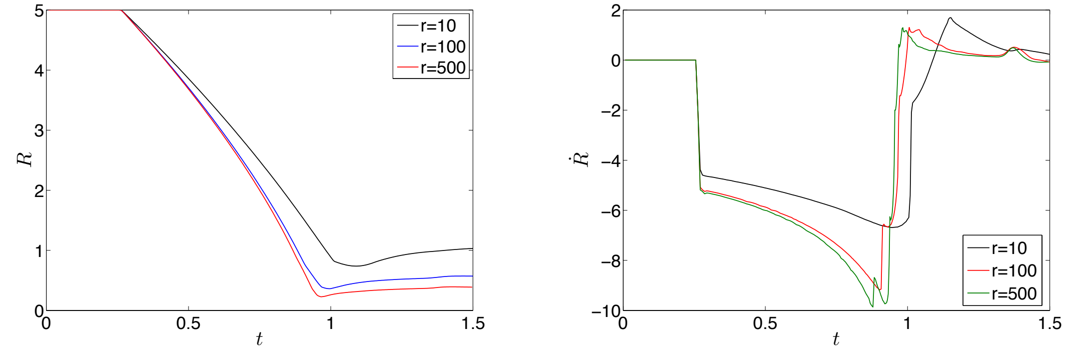

(a) Position (b) Velocity

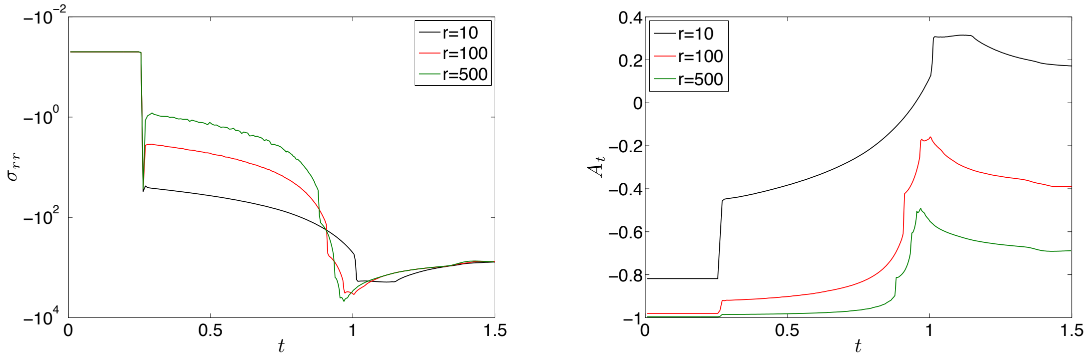

(c) Normal stress (d) Atwood ratio

Figure 6.14: Evolution of the interface position, normal velocity $\dot{R}$, normal stress σ_{rr}, and Atwood ratio A_t at the interface as a function of time for $r_i = \{10, 100, 500\}$ with $\eta_0 = 0$. A lower initial density ratio reduces the initial velocity of the interface and its acceleration before the first re-shock.

times $t = \{1.2,\, 1.4\}$. It is important to note that as the density ratio is increased, numerical mass conservation errors become higher.

The comparison of the baseline problem, with an initial density ratio of 100, to the case of lower density ratio, with an initial density ratio of 10, reveals substantial differences. In the first place, the lower (in absolute value) Atwood ratio makes the interface grow more slowly before the first re-shock (Fig. 6.16(c)). However, with respect to the start-up process, Fig. 6.16(b) reflects that the non-dimensional maximum growth rate divided by the Atwood ratio after the shock passage $UR(t)/(A_t V_0 \eta_0 n)$ is higher for $r_i = 10$ and closer to the first-order theory predicted value of 1. In the case with $n = 16$, the second interface inversion seen for $r_i = 100$ before the re-shock never occurs. This seems to indicate that the occurrence of this second interface phase inversion during the inwards motion of the interface depends heavily on the density of the lighter material. As the vacuum condition is approached by lowering the density of the fluid, the high compression generated by the converging motion makes the plastic solid achieve a lower energy configuration by creating new spikes in the bubbles. For a lower density ratio, this effect is restricted by the opposition of a more dense fluid. Figure 6.16(d) shows that the growth rate for $r_i = 10$, $n = 16$ remains approximately constant for the period of time of inwards motion of the interface while it increases progressively in the same period for $r_i = 10$ and $n = 4$. After re-shock, the fluid becomes more dense than the solid (Figs. 6.14(d) and 6.18(b,c)). The re-shock in this configuration is again a heavy–light Richtmyer–Meshkov case which produces an interface phase reversal for $n = 16$ as shown by the density color-contour plots in Fig. 6.14(d)(d,e,f). For $n = 4$, the phase reversal does not completely occur (see density contour plot in Appendix D) and the interface exhibits no growth in this period.

6.4.4.3 Influence of the initial shock Mach number

The incoming shock Mach number controls the initial velocity of the interface for a fixed density ratio. In this paragraph, five initial shock Mach numbers $M_s = \{1.16,\, 1.31,\, 1.48,\, 1.65,\, 1.83\}$ are examined for wave numbers $n = \{4, 16\}$, with all other parameters remaining fixed (initial density ratio $r = 100$ and interface amplitude parameter $C = 0.05$). Table 6.5 summarizes the initial interface conditions: velocity V_0 , Atwood ratio after shock A_t (with a negative value indicating a heavy–light interface), normal stress σ_{rr}, and time elapsed from the beginning of the simulation to shock–interface interaction t_I, for each of the considered cases.

As is shown in Fig. 6.19, the evolution of interface conditions with respect to time is scaled by the initial shock Mach number, with higher values increasing the values of velocity and normal stress. It is important to note that the Atwood ratio reaches a higher value with weaker shocks, with the gas becoming for an instant after the first re-shock more dense than the solid in the $M_s = 1.16$ case. Figure 6.20 shows the evolution of the interface conditions when time, velocity, and stress are conveniently scaled with the initial velocity of the interface. Results reflect that the acceleration of

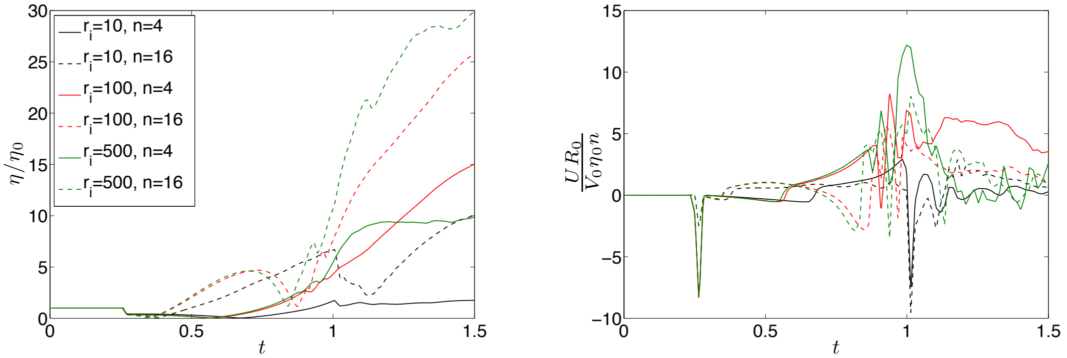

(a) Interface amplitude / time

(b) Growth rate / time

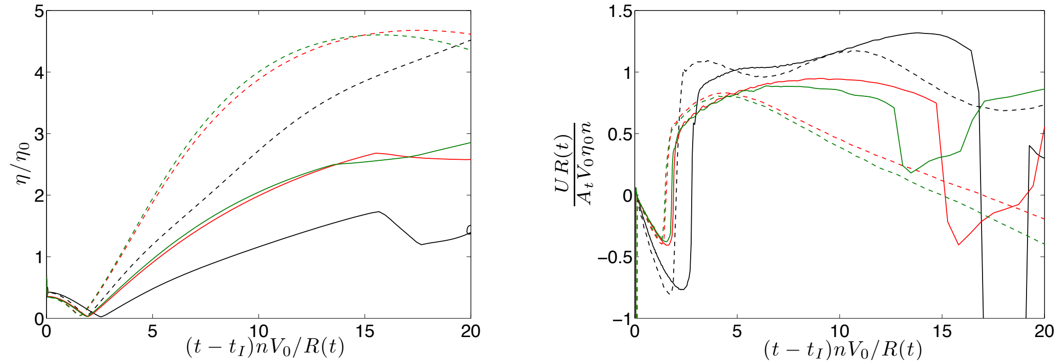

(c) Interface amplitude / non-dimensionalized time

(d) Growth rate / non-dimensionalized time

Figure 6.15: Interface evolution as a function of time for $r_i = \{10, 100, 500\}$, $n = \{4, 16\}$, and $C \equiv \frac{\eta_0 n}{R_0} = 0.05$ (see legend in (a)). Figures (a) and (b) show the whole simulation time, including events after re-shocks. Figures (c) and (d) focus on the short-term behavior after the first shock–interface interaction.

Table 6.5: Interface parameters in shock–interface problem with different initial shock Mach numbers

M_s	V_0(km/s)	σ_{rr}(GPa)	A_t	t_I
1.16	2.011	-0.661	-0.943	0.375
1.31	3.059	-1.302	-0.933	0.331
1.48	4.119	-2.174	-0.927	0.293
1.65	5.14	-3.64	-0.919	0.264
1.83	6.195	-4.768	-0.915	0.238

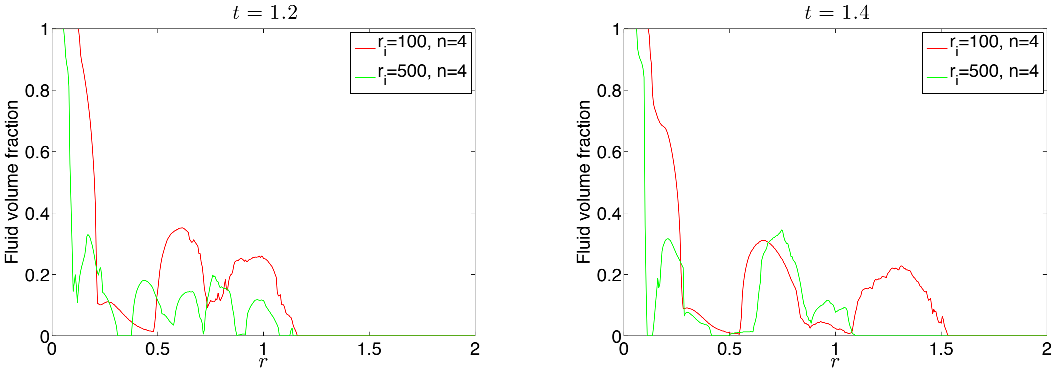

(a) $t = 1.2$, $n = 4$ (b) $t = 1.4$, $n = 4$

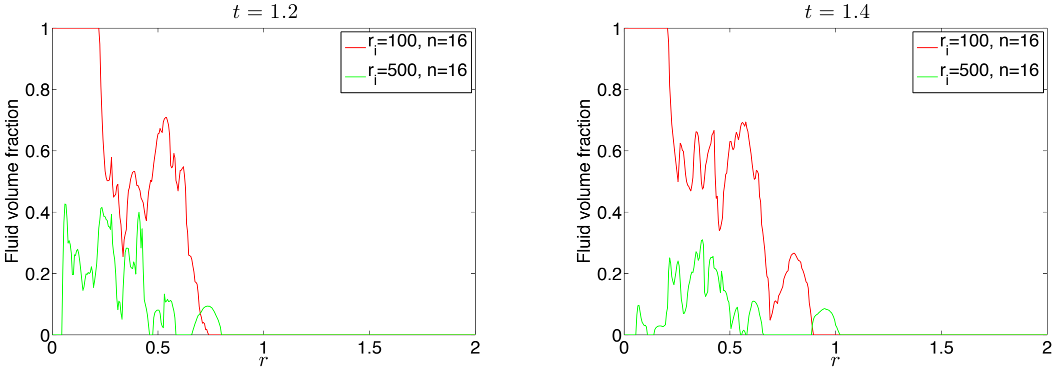

(c) $t = 1.2$, $n = 16$ (d) $t = 1.4$, $n = 16$

Figure 6.16: Volume fraction $\overline{X}_f(r,t)$ of fluid computed by sweeping azimuthally for each r: $\overline{X}_f(r,t) = \int_0^{\frac{\pi}{2}} X_f(r,\theta,t)\, d\theta$. Results are shown for $r_i = \{100,\ 500\}$, $n = \{4,\ 16\}$ and $t = \{1.2,\ 1.4\}$.

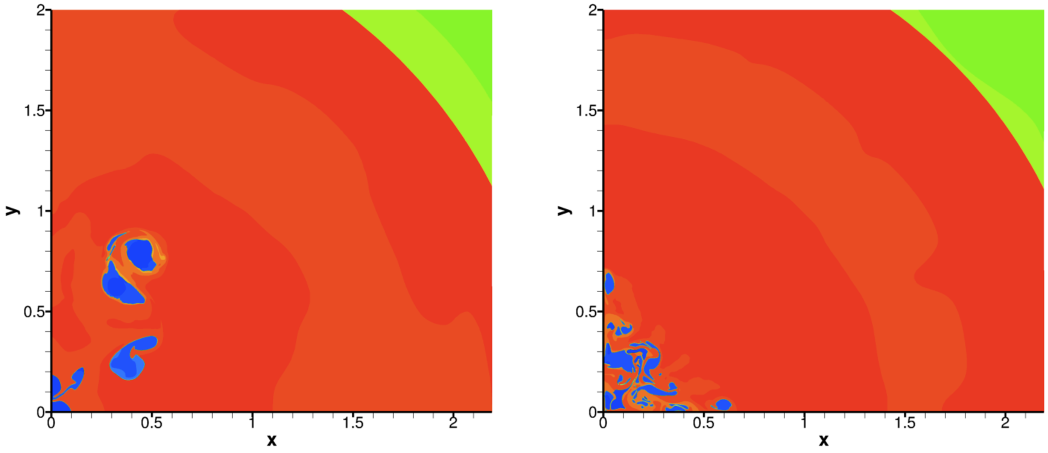

(a) $n = 4$ (b) $n = 16$

Figure 6.17: Density contour plots close to the axis at $t = 1.2$ for $r_i = 500$ and $n = \{4, 16\}$. Comparison with equivalent figures for $r_i = 100$ (Figs. 6.7(e) and 6.13(f)) shows that the volume of fluid is reduced due to its lower initial density. However, the fluid pockets are more sparsely distributed, leading to a higher value of the interface amplitude (computed as the size of the mixing zone).

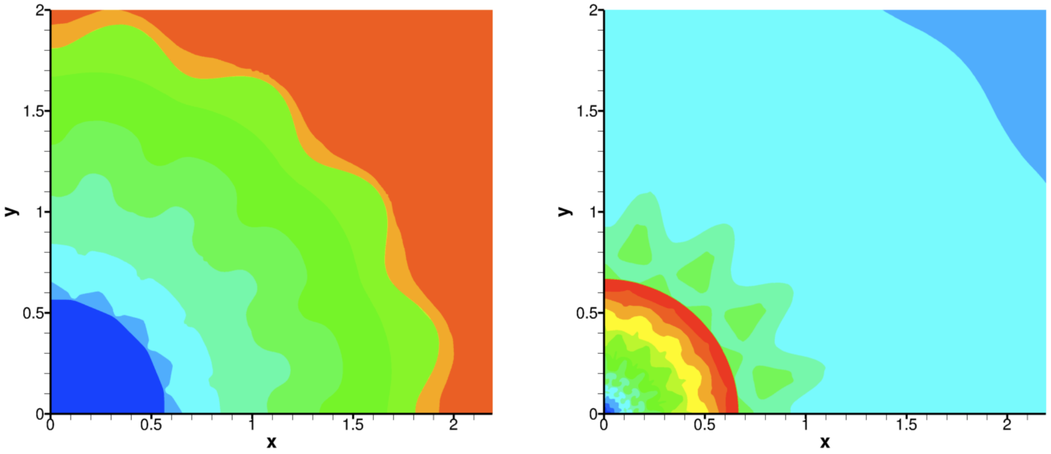

(a) $t = 0.85$ (b) $t = 0.983$

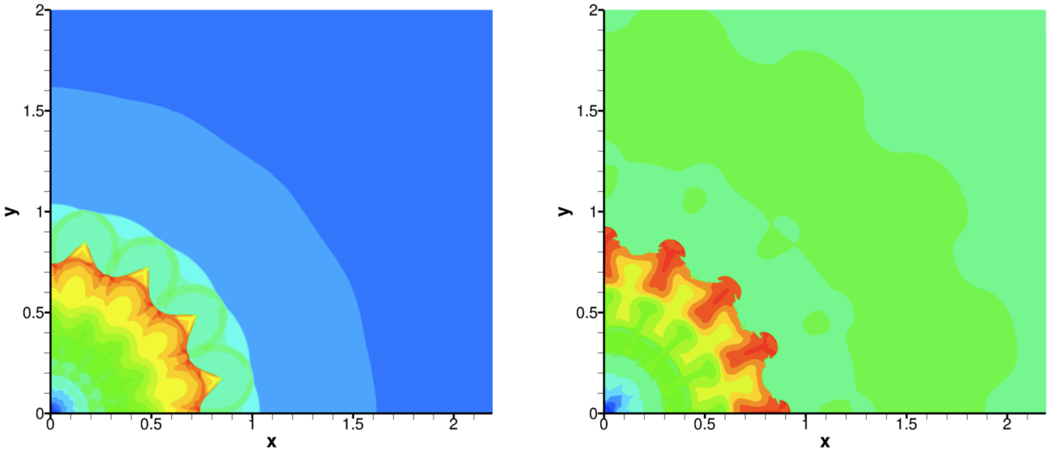

(c) $t = 1.033$ (d) $t = 1.2$

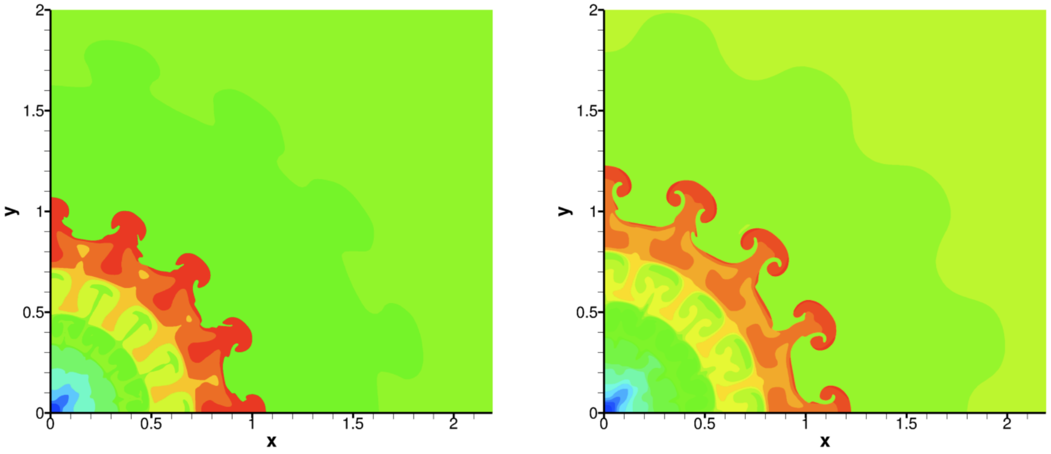

(e) $t = 1.3$ (f) $t = 1.5$

Figure 6.18: Density contour plots in the region close to the axis for the case with initial parameters $r_i = 10$, $n = 16$, and $C = 0.05$. The fluid is more compressible than the solid, which produces a positive A_t after the transmitted shock in the fluid is reflected at the axis (between figures (a) and (b)). The re-shock is then a heavy-light Richtmyer–Meshkov case, which produces an interface inversion ((d) et seq.).

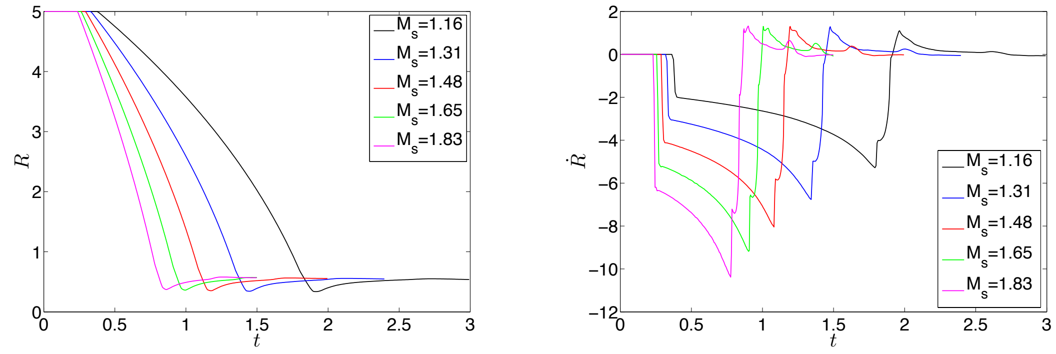

(a) Position (b) Velocity

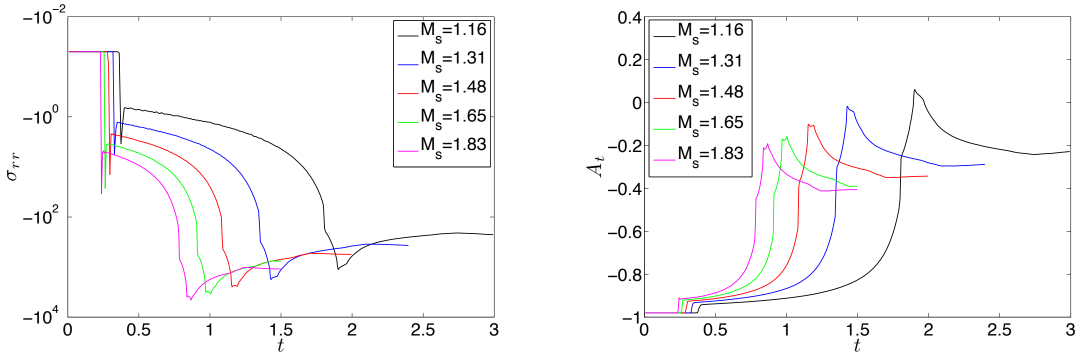

(c) Normal stress (d) Atwood ratio

Figure 6.19: Evolution of the interface position, normal velocity $\dot{R}$, normal stress σ_{rr}, and Atwood ratio A_t at the interface as a function of time for $M_s = \{1.16,\ 1.31,\ 1.48,\ 1.65,\ 1.83\}$ and $\eta_0 = 0$. A lower initial density ratio reduces the initial velocity of the interface and its acceleration before the first re-shock.

the interface scaled with the initial velocity is higher for weaker shocks (i.e., a low Mach number simulation is more sensible to the effect of the converging geometry), leading to the described more pronounced increment of the normal stress and Atwood ratio with respect to its original values. As a last remark, the final position of the interface after re-shocks is almost independent of the shock strength.

Figure 6.21 shows amplitude and growth rate of the interface perturbations, which exhibit a large dependence on the initial shock Mach number. The same features observed in the baseline problem are found, with accelerated growth of the interface and a second phase reversal as the interface converges towards the origin, respectively, for $n = 4$ and $n = 16$. With respect to the growth rate after the first shock passage, a larger value throughout the inwards motion of the interface when scaled with the initial interfacial velocity V_0 is observed for the weaker shocks. This can be appreciated in the values for phase inversion and maximum non-dimensional growth rate shown in Fig. 6.21(f).

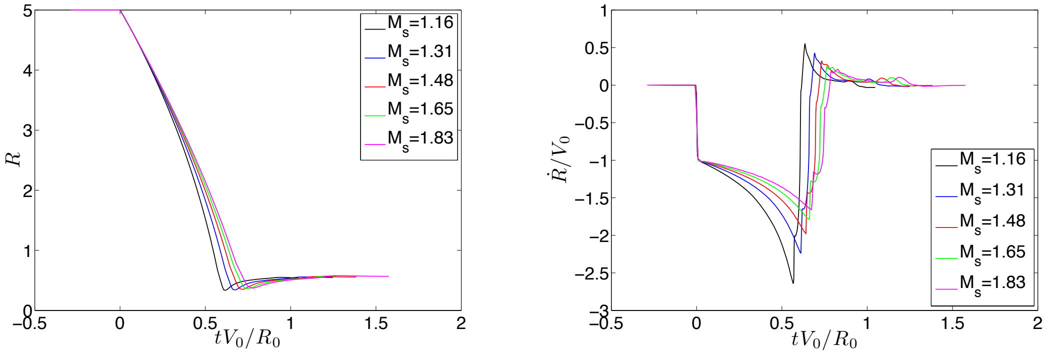

(a) Position (b) Velocity

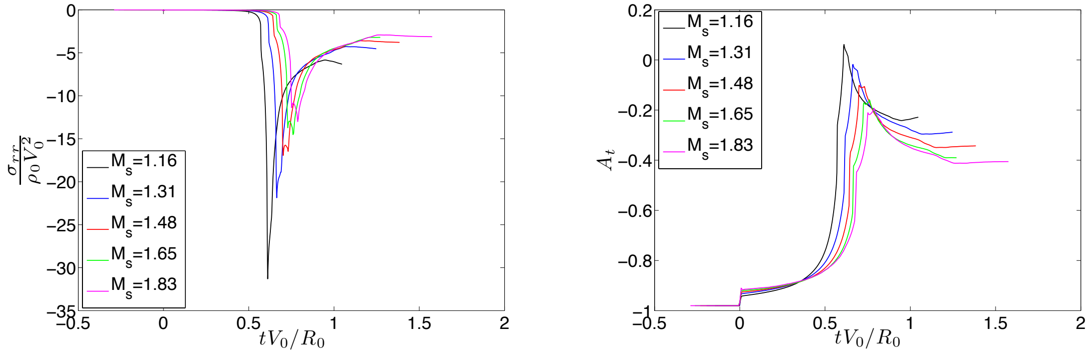

(c) Normal stress (d) Atwood ratio

Figure 6.20: Evolution of the interface position and non-dimensional normal velocity $\dot{R}$, normal stress σ_{rr}, and Atwood ratio A_t at the interface as a function of time scaled with V_0 for $M_s = \{1.16,\ 1.31,\ 1.48,\ 1.65,\ 1.83\}$ and $\eta_0 = 0$.

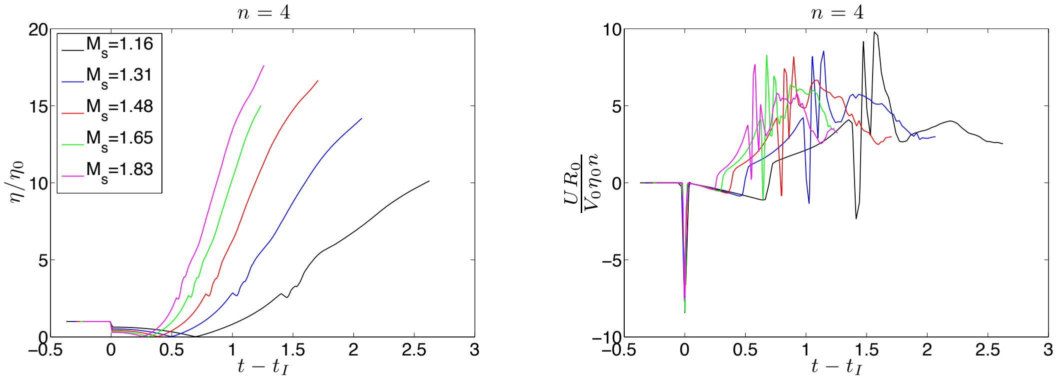

(a) Interface amplitude / time, $n = 4$ (b) Growth rate / time, $n = 4$

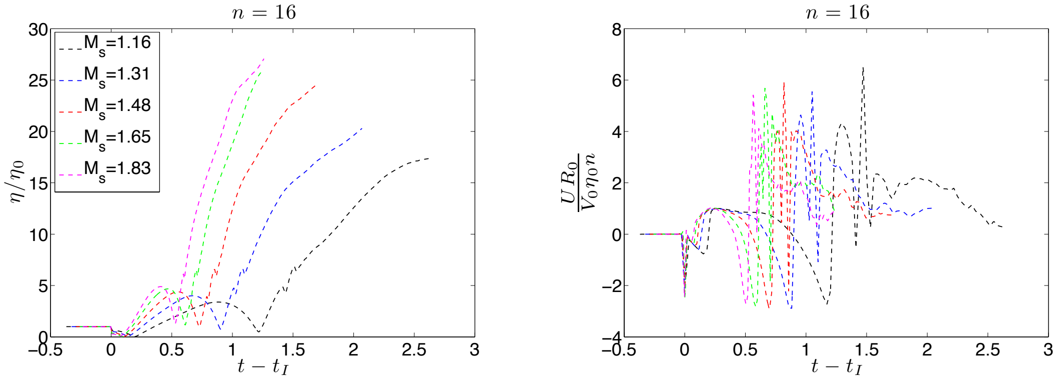

(c) Interface amplitude / time, $n = 16$ (d) Growth rate / time, $n = 16$

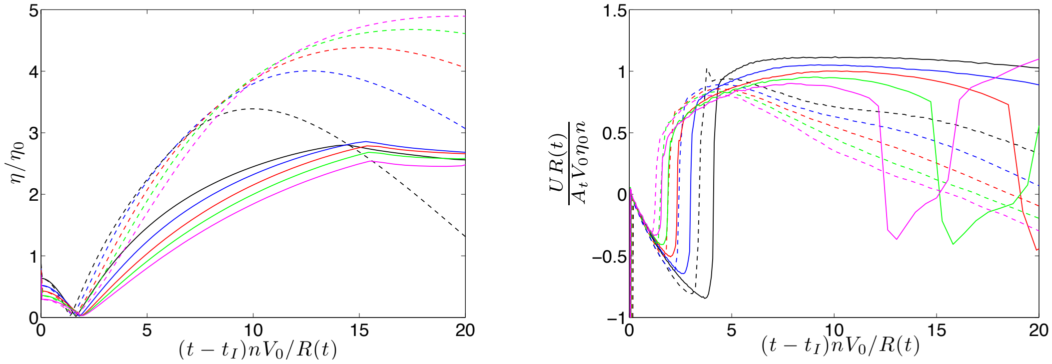

(e) Interface amplitude / non-dimensionalized time (f) Growth rate / non-dimensionalized time

Figure 6.21: Interface evolution as a function of time for $M_s = \{1.16,\ 1.31,\ 1.48,\ 1.65,\ 1.83\}$, $n = \{4,\ 16\}$, and $C \equiv \frac{\eta_0 n}{R_0} = 0.05$ (see legend in (a,c)). Figures (a,b,c,d) show the whole simulation time, including events after re-shocks. Figures (e) and (f) focus on the short-term behavior after the first shock–interface interaction.

On the behavior after re-shock, the fluid and elastic–plastic solid become more "mixed" as the strength of the incoming shock increases, as observed in Fig. 6.22. For $M_s = 1.16$, the initial structure of the perturbation remains with a number of observed spikes and bubbles equal to the original perturbation with $n = 16$. This periodicity is broken as the shock Mach number increases leading to a more "turbulent" mixing zone with lower length-scales appearing.

6.4.4.4 Influence of yield stress

The yield stress controls the strength of the solid. After this threshold value is exceeded, the solid behaves mostly like a fluid, with hydrostatic stresses being much higher than shear ones. Given the relatively strong shock of $M_s = 1.65$ that drives the Richtmyer–Meshkov instability in the baseline problem, a very high value of the yield stress is necessary for the solid to remain in the elastic regime. In order to remain close to physical values of yield stress normally measured for copper, this parametric study is performed with $\sigma_Y = \{0,\, 0.12,\, 0.5,\, 1\}\,\mathrm{GPa}$, values that keep the solid in the plastic regime. In particular, a zero yield stress corresponds to a solid with no ability to support shear, which performs exactly like a fluid subjected to hydrostatic pressure. Additional parameters of the problem are the wave number $n = \{4,\, 16\}$, the relative initial amplitude $C \equiv \frac{\eta_0 n}{R_0} = 0.05$ and the initial solid–gas density ratio $r_i = 100$.

Figure 6.23 shows the velocity of the interface with respect to time with $C = 0$ simulations for the values of the yield stress examined in this analysis. No noticeable change of the velocity evolution is appreciated when varying σ_Y. The same occurs with the rest of the interface conditions, such as Atwood ratio and the normal stress. These are not shown here since they do not provide any new relevant information.

The evolution of the interface perturbations is depicted in Fig. 6.24. In principle, no change in the general trends previously observed is appreciated: the amplitude increases between shock interactions for $n = 4$ and suffers a second phase reversal for $n = 16$. However, it is observed that decreasing the yield stress leads to higher values of the perturbation amplitude for a given time. This is especially noticeable for $n = 16$ after the re-shocks (Fig. 6.24(a)). The perturbations in the hydrostatic case with $\sigma_Y = 0\,\mathrm{GPa}$ grow faster (Fig. 6.24(b)) since no elastic behavior at all is experienced. When the yield stress is increased, the presence of some shear deformations that carry away from the interface some of the vorticity deposited in the shock passage reduces the growth rate. A lower yield stress also increases the initial maximum growth rate, as shown in Fig. 6.24(d).

With the aim of analyzing the mixing zone more closely, Fig. 6.25 shows the density contour plots for $n = 4$ at the final simulation time for the four examined cases. As the yield stress increases, the instability is less pronounced, as can be observed in the shape of the small fluid pocket surrounding the origin, which is almost axisymmetric for $\sigma_Y = 1\,\mathrm{GPa}$. The mixing zone for $n = 16$ is similarly depicted in Fig. 6.26. In this case, bigger pockets of fluid appear as the yield stress increases,

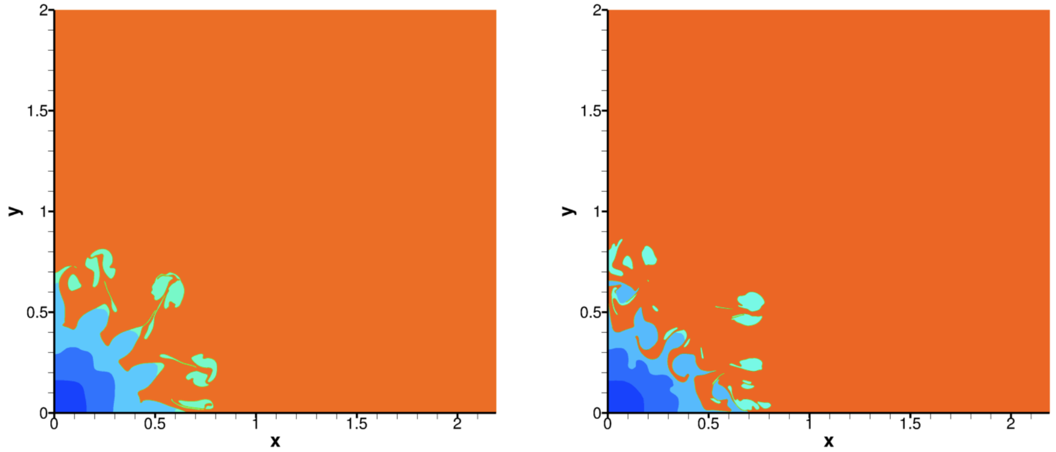

(a) $M_s = 1.16$ (b) $M_s = 1.31$

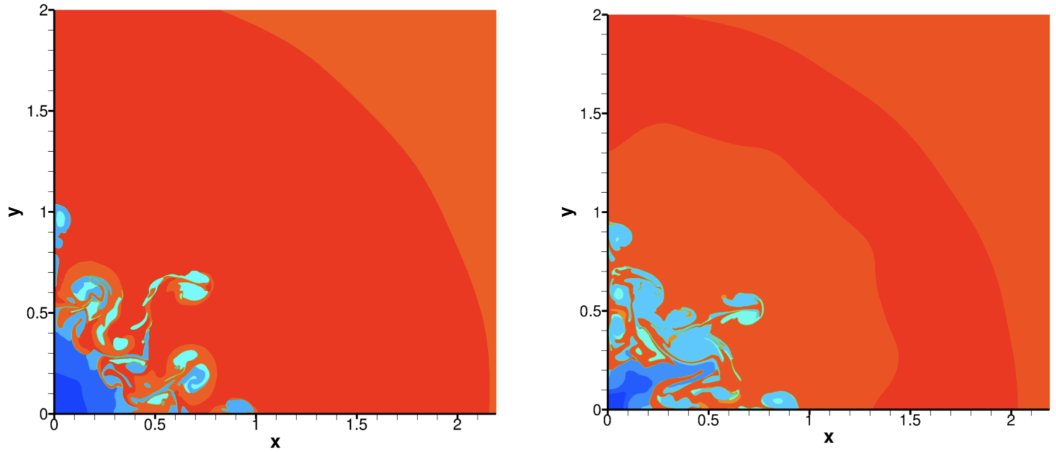

(c) $M_s = 1.48$ (d) $M_s = 1.65$

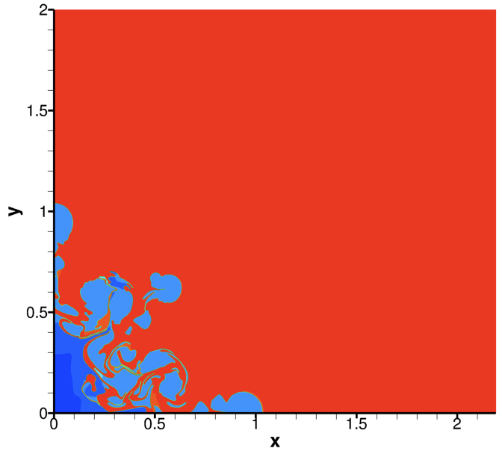

(e) $M_s = 1.83$

Figure 6.22: Density contours for $M_s = \{1.16, 1.31, 1.48, 1.65, 1.83\}$ and $n = 16$ at the end of the simulation time. The mixing zone expands and becomes more fluid-like when increasing the Mach number of the incoming shock.

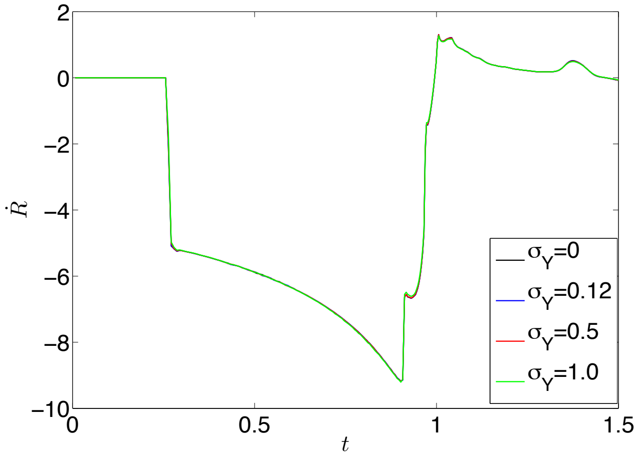

Figure 6.23: Evolution of normal velocity $\dot{R}$ as a function of time for $\sigma_Y = \{0,\ 0.12,\ 0.5,\ 1\}$ GPa and $\eta_0 = 0$. Differences in the evolution are indistinguishable.

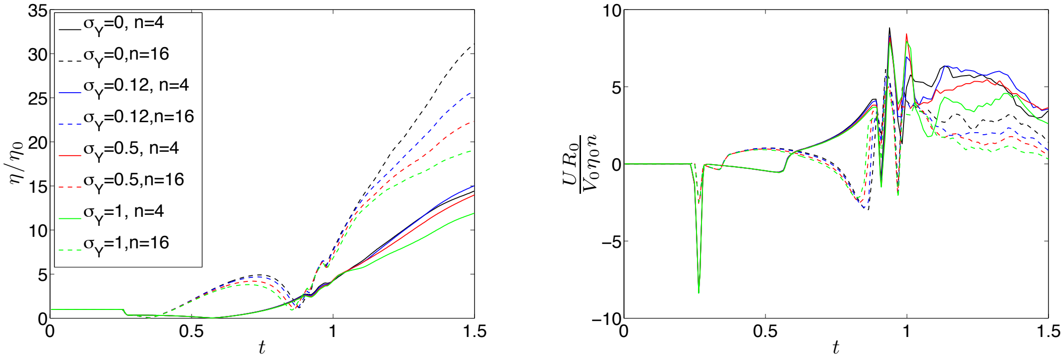

(a) Interface amplitude / time

(b) Growth rate / time

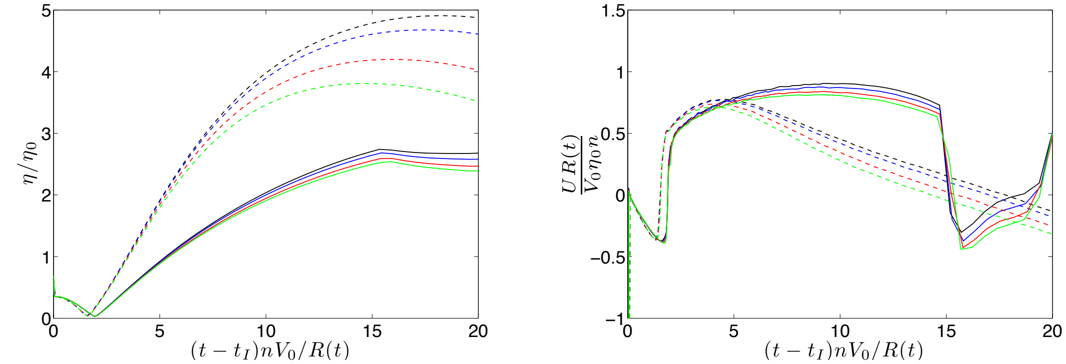

(c) Interface amplitude / non-dimensionalized time

(d) Growth rate / non-dimensionalized time

Figure 6.24: Interface evolution as a function of time for $\sigma_Y = \{0,\ 0.12,\ 0.5,\ 1\}$ GPa and $\eta_0 = 0$, $n = \{4, 16\}$, and $C \equiv \frac{\eta_0 n}{R_0} = 0.05$ (see legend in (a)). Figures (a,b) show the whole simulation time, including events after re-shocks. Figures (c) and (d) focus on the short-term behavior after the first shock–interface interaction.

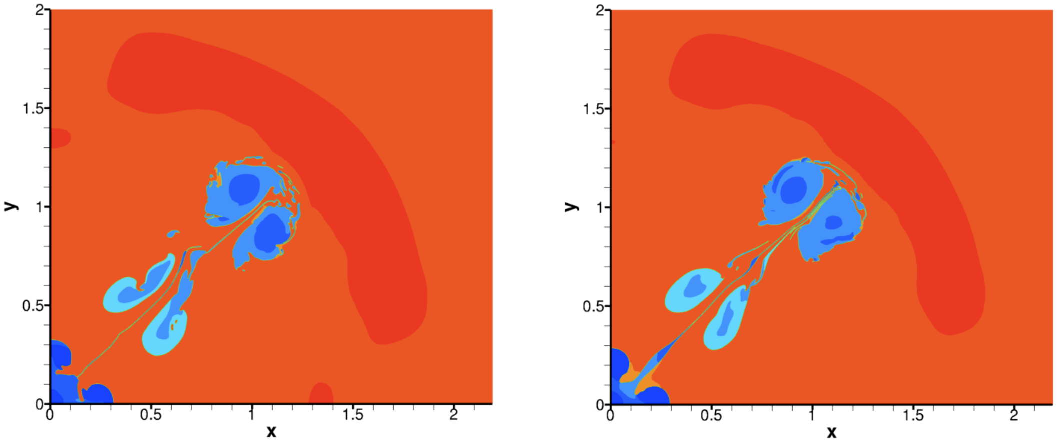

(a) $\sigma_Y = 0\,\mathrm{GPa}$

(b) $\sigma_Y = 0.12\,\mathrm{GPa}$

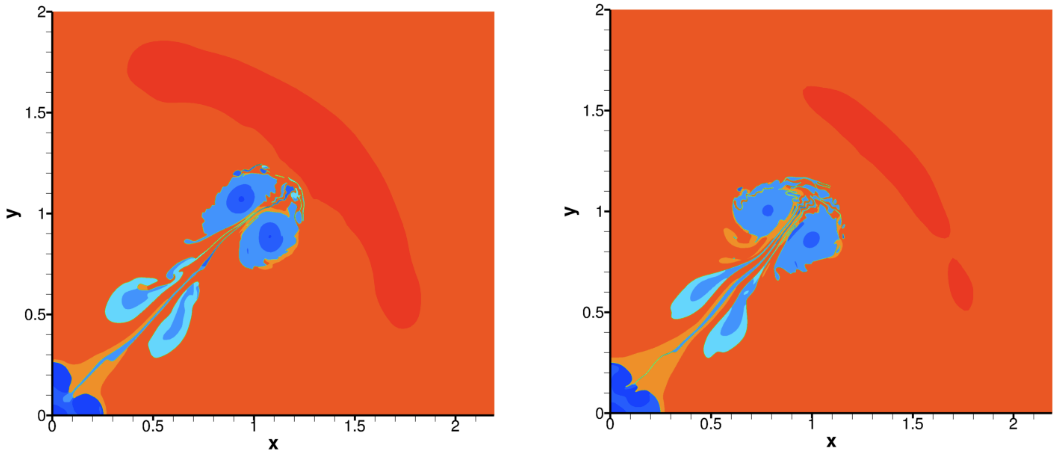

(c) $\sigma_Y = 0.5\,\mathrm{GPa}$

(d) $\sigma_Y = 1.0\,\mathrm{GPa}$

Figure 6.25: Density contour plots close to the axis at $t = 1.5$ for $\sigma_Y = \{0,\, 0.12,\, 0.5,\, 1\}\,\mathrm{GPa}$ and $n = 4$

indicating a less "turbulent" mixing zone. In particular, for the highest yield stress case, the central pocket of fluid surrounding the origin is also almost circular and the initial wave number is conserved, as four exterior pockets of fluid are visible in a quadrant.

6.4.4.5 Summary of parametric analysis

Parametric studies revealed interesting features of the converging Richtmyer–Meshkov problem in solid–gas interfaces that are summarized in this paragraph. From the analysis of the geometrical parameters of the interface:

- ◇ Interface parameters show good collapse when scaled with the initial amplitude.
- ◇ A second phase reversal is produced before the first re-shock when the wave number and the Atwood ratio are sufficiently large.

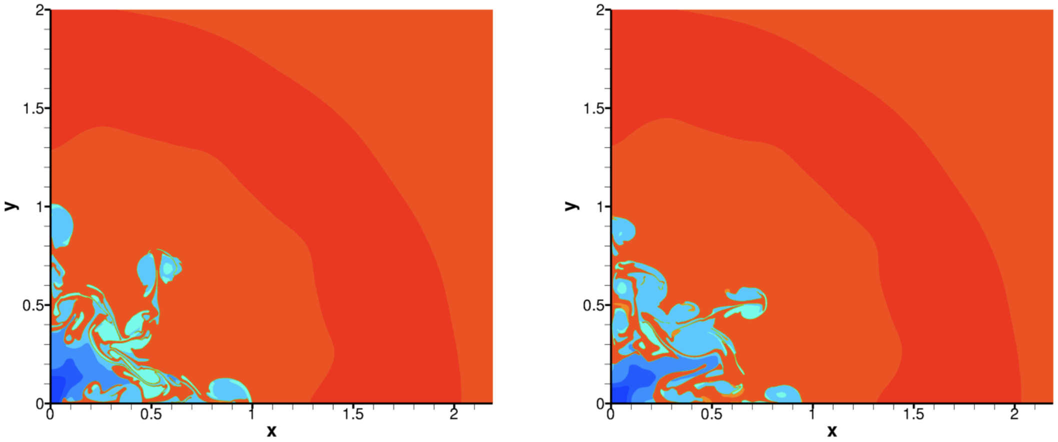

(a) $\sigma_Y = 0\,\mathrm{GPa}$ (b) $\sigma_Y = 0.12\,\mathrm{GPa}$

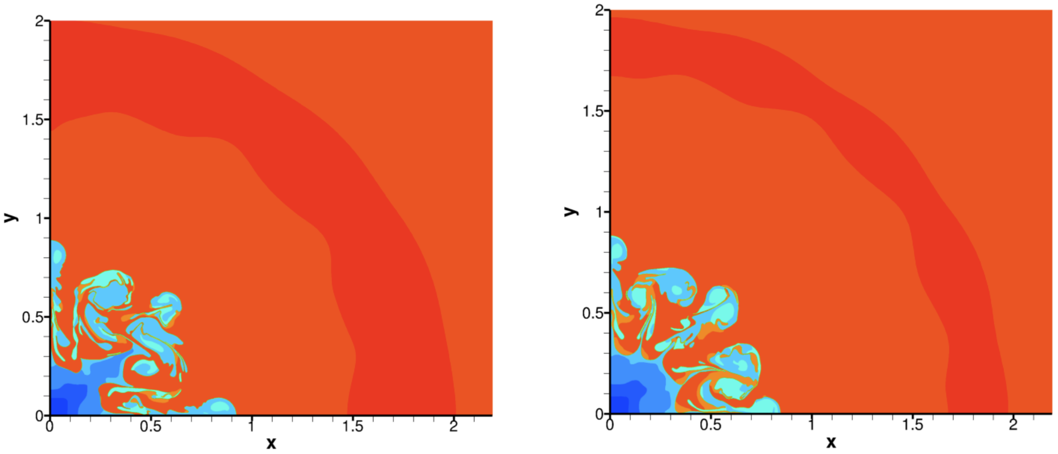

(c) $\sigma_Y = 0.5\,\mathrm{GPa}$ (d) $\sigma_Y = 1.0\,\mathrm{GPa}$

Figure 6.26: Density contour plots close to the axis at $t = 1.5$ for $\sigma_Y = \{0,\ 0.12,\ 0.5,\ 1\}\,\mathrm{GPa}$ and $n = 16$

- ◇ As the linear perturbations break down in smaller structures, a “mixing zone” is created, which resembles a fluid–fluid problem, especially for large wave numbers.

Variation of the initial solid–gas density ratio shows that:

- ◇ As the density ratio increases, results approach the solid–vacuum limit. A variation from $r_i = 100$ to $r_i = 500$ does not produce significant differences in the behavior of the interface.
- ◇ The mixing zone when the fluid is less dense can be wider, but the mass and volume fraction of fluid in the mixing zone is lower.
- ◇ A lower density ratio makes the fluid become more dense than the solid. This changes the characteristics of the interface, a second phase reversal does not occur before the first re-shock, but happens after it since the re-shock is in a heavy–light configuration.

The following conclusions can be extracted from the parametric study of different initial shock Mach numbers:

- ◇ A higher shock Mach number leads to a more fluid-like mixing zone.
- ◇ When results are scaled with the initial interface velocity, converging effects accelerate and compress the interface more when a low Mach number is used, thus leading to a faster growth rate with respect to the initial velocity of the interface.

Finally, modifying the yield stress of the material has the following effects:

- ◇ A higher yield stress produces a slower growth rate and less perturbation amplitude, especially after re-shocks.
- ◇ The mixing zone becomes more fluid–like as the yield stress decreases. A higher yield stress reduces the instability of the interface, as expected by analyzing the elastic regime (which is the limit of the plastic model as $\sigma_Y \to \infty$).

6.5 Summary

This final chapter focused on numerical simulations of the Richtmyer–Meshkov instability in interfaces separating solids to other media and different geometrical configurations. The results for the planar solid–vacuum case were compared to previous results found in the literature with acceptable agreement, contributing to the validation of the AMROC multi-material code. It was shown that the initial conditions of the interface and the yield stress of the material determine the formation of ejecta. For lower initial amplitudes or shock strengths the stresses at the interface are eventually relaxed by plastic dissipation and the interface amplitude saturates to a constant mean value in the long term. Ejecta, defined as unbounded growth of the perturbations, are formed whenever the initial parameters exceed some threshold values.

With respect to converging simulations of solid–gas interfaces, two goals were achieved. The first one was to determine the capabilities of the code. Problems in being able to run the simulations after the first re-shock led to development and implementation of the stretch formulation described in Chapter 3. Mass conservation in this demanding problem was deemed acceptable with errors of the order of 2% for a high solid–gas density ratio and when using the maximum resolution made available by computational constraints. Simulations of higher density ratios with acceptable mass conservation may be possible by increasing computational power. The second purpose of this study was to characterize the interface behavior under the influence of different geometrical and material parameters. In general, results exhibit dependency on the initial wave number, density ratio, shock Mach number, and yield stress. Conclusions for the effect of each of these parameters were summarized in paragraph 6.4.4.5.

Chapter 7

Conclusion

7.1 Summary

The general theme of this dissertation was the study of the Richtmyer–Meshkov flow in elastic and elastic–plastic materials for both planar and cylindrically converging geometries. This led to the investigations of two problems of interest in the field of large deformation solid mechanics, namely converging shocks and Richtmyer–Meshkov flow in elastic–plastic solids, by means of analytical and computational techniques. In the process, several improvements were implemented in the AMROC multi-material code originally developed by Barton et al. [8], resulting in a more robust algorithm for the type of problems examined here.

The equations that govern the motion of solid media were introduced in Chapter 2 where special emphasis was given to the analysis of the polar decomposition of the deformation and inverse deformation gradients, the use of hyper-elastic equations of state in order to preserve the hyperbolic characteristics of the system of equations, and the plasticity update, which was formulated in consistency with the basic postulates of metal plasticity.

Chapter 3 focused on the numerical implementation of the equations of motion. A new formulation based on the elastic part of the inverse deformation tensor was developed, with the advantage of a reduced number of equations with respect to the system originally used by Miller and Colella [78] but that accepts a density penalty term for adjusting the evolution of the determinant of the inverse deformation tensor to the mass conservation equation. This fix cannot be included in the set of equations developed by Godunov and Romenski [42]. In addition, it was shown that the equations of motion for each of the components of the deformation or inverse deformation tensor can be applied to the symmetric stretch tensor when a corrector is introduced at the end of each computational time-step. The properties of the symmetric stretch tensor make possible the computational solution of Riemann problems between parts of the same material that have been rigidly rotated with respect to each other. In the last part of the chapter, the description of the level-set multi-material implementation included a new Riemann solver adapted from the HLLD scheme originally used in magnetohydrodynamics [80]. The new solver was compared to the previous version, which was based on a method of linearized characteristics, for the case of a solid–gas interface with a difference in pressure that replicated a Richtmyer–Meshkov shock–interface interaction, showing that results were closer to the exact solution when employing HLLD. The study of the multi-material capabilities was complemented with tests showing the influence of the AMR algorithm and the level set in mass conservation. This tests revealed extremely small errors due to the restriction–prolongation algorithm of AMR and at most first-order convergence rate in mass errors as the base grid is refined.

Chapter 4 explored the problem of cylindrically and spherically symmetric converging shocks in elastic–plastic solids. This interesting problem was judged to be a useful precursor to the study of the cylindrically convergent Richtmyer–Meshkov instability. Whitham's shock dynamics equations for compressible neo-Hookean elastic–plastic solids were derived obtaining closed expressions for the shock evolution in terms of definite integrals. Comparison with numerical simulations revealed that this approximate theory is extremely accurate, even when shear deformations and plasticity are considered. Strong-shock limits were identified for purely elastic and elastic–perfectly plastic solids, exhibiting a large dependence on the constitutive law used to model the material. This study was closed with the numerical analysis of the transition of a shock from the elastic to the plastic regime due to the effects of a converging geometry. Contrary to the elastic precursor–plastic shock structure observed in planar shocks, the plastic shock travels faster in this case and eventually catches up with the elastic precursor, producing a single imploding plastic shock.

Chapter 5 described an analytical model for the impulsive driven Richtmyer–Meshkov instability in incompressible elastic solids. No-slip and free-slip conditions at the interface were examined. Laplace transform and modal decomposition techniques were used to determine the stability of the interface, which exhibits ringing or decaying oscillatory depending on material parameters and the interface conditions considered. Stability of the interface was identified to be related to propagation of shear waves, which carry the baroclinic vorticity originally deposited at the interface into the materials. To conclude the chapter, numerical simulations were performed and compared to analytical results, with results exhibiting excellent agreement for no-slip boundary conditions. In the case of free-slip, the period and amplitude of the oscillations are similar but a phase-lag appears as a result of the differences between the impulsive and the shock-driven models.

In Chapter 6, Richtmyer–Meshkov instability in solid–vacuum and solid–gas interfaces was examined by means of numerical simulations. The first example, motivated by previous results by Dimonte et al. [27] and Piriz et al. [91], attempted to validate the accuracy of the numerical code by finding a postulated linear relation between the yield stress of a plastic material and the maximum amplitude of the perturbations achieved in a Richtmyer–Meshkov experiment in which a perturbed free surface is excited by a planar shock wave. Comparison with results in the literature was successful. In the last part of the chapter, the more demanding case of a solid–gas configuration in a cylindrical geometry was employed to first describe the mass conservation accuracy of the numerical implementation in well- and ill-posed problems and, finally, to perform a parametric study of the characteristics of the interface under the variation of initial geometrical and physical conditions and material parameters. Evolution of the interface was modified by the wave number of the initial perturbation with a second phase inversion occurring in some cases. The solid–gas interface, upon re-shock, exhibited progressively more turbulent mixing-zone features as the yield stress of the solid was decreased and/or the Mach number of the driving shock increased. The initial solid–gas density ratio was identified as another important parameter in the evolution of the interface, with high values tending to the vacuum–solid limit behavior and low values making the fluid more dense than the solid due to the difference in compressibility between the two materials.

7.2 Future work

Multiple directions have been identified for continuing the work presented in this dissertation, both in the designing of algorithms and in the analysis of shock-driven problems in solid mechanics.

Improvements in the multi-material solid mechanics solver. Important additions to the algorithm are being considered in the short term. A considerable effort must be placed in improving the physics of the model. In this respect, two goals are clearly identified: the inclusion of a damage model that could predict realistic rupture of materials (at this point this occurs by regularization of the level set, being therefore dependent on the mesh resolution) and the development of accurate phase-change models for different metallic materials. Another possibility for improvement lies in decreasing errors due to mass conservation although the implementation of a conservative level-set method seems complicated at the moment.

Converging shocks in solids More complex constitutive laws can be included in Whitham's shock dynamics equations. As an application of the future implementation of more realistic phase-change models in the numerical algorithm, shock-induced melting can be investigated. During shock compression, temperatures can rise dramatically, but due to the corresponding increase in pressure, the solid does not necessarily melt. However, melting can occur during the post-shock release phase. To be more precise, continuously driven shock waves are usually experimentally difficult to maintain. For example, high-velocity flyer-plate impactors have finite momentum, and high-intensity lasers have finite pulse times. The shock driving force ultimately vanishes and a release wave starts propagating behind the compressed material, usually at a faster speed than the shock front. The release is isentropic and reduces the density and pressure while maintaining the temperature, making possible the melting of the material. In addition, the work can be extended to the study of outward-moving shocks.

Richtmyer–Meshkov flow in elastic–plastic solids An interest exists in developing an analytical model for converging geometries in line with the planar model described in this dissertation. Preliminary work on the subject shows that the equations in cylindrical or spherical coordinates become extremely hard to solve unless only first-order effects of the converging geometry are considered (i.e., velocity of the interface remains constant and radial position of the interface stays extremely close to its initial value). With these assumptions, the planar behavior is practically replicated in converging geometries, even for low wave numbers. Options for carrying out this study certainly involve the application of a semi-numerical approach. With respect to elastic–plastic solids, a detailed study of the "mixing zone" and its similarities and differences with the fluid case will be of interest for both the fluid and solid mechanics community. Other options for expanding the presented work include Richtmyer–Meshkov numerical experiments using more complex models of plasticity (hardening, thermal softening) or a phase-change model at the time it becomes available.

Appendix A

Method of characteristics and Whitham's shock dynamics

The equations of motion for a radially symmetric flow (4.1) and (4.3) can be written in the following matrix form,

$$\frac{\partial \mathbf{W}}{\partial t} + \mathbf{A}(\mathbf{W})\frac{\partial \mathbf{W}}{\partial r} = \mathbf{S}, \tag{A.1}$$

where

$$\mathbf{W} = \begin{pmatrix} \rho \\ u \\ e \\ g_{Rr} \end{pmatrix}, \tag{A.2a}$$

$$\mathbf{A} = \begin{pmatrix} u & \rho & 0 & 0 \\ -\dfrac{1}{\rho}\dfrac{\partial \sigma_{rr}}{\partial \rho} & u & -\dfrac{1}{\rho}\dfrac{\partial \sigma_{rr}}{\partial e} & -\dfrac{1}{\rho}\dfrac{\partial \sigma_{rr}}{\partial g_{Rr}} \\ 0 & -\dfrac{\sigma_{rr}}{\rho} & u & 0 \\ 0 & g_{Rr} & 0 & u \end{pmatrix}, \tag{A.2b}$$

$$\mathbf{S} = \frac{s-1}{r}\begin{pmatrix} -\rho u \\ \frac{(\sigma_{rr}-\sigma_{\theta\theta})}{\rho} \\ \frac{u\sigma_{\theta\theta}}{\rho} \\ 0 \end{pmatrix}. \tag{A.2c}$$

$\mathbf{W}$ is called the vector of primitive variables, $\mathbf{S}$ contains the geometric terms in the right-hand side of Eq. (4.1) and (4.3), and $\mathbf{A}$ is a matrix whose eigenvalues and eigenvectors define the characteristic equations. There exist two repeated eigenvalues u associated to two convective modes (along which ς and g_{Rr} are conserved), and two distinct eigenvalues $u \pm a$ associated to compression modes. The system (A.1) decouples as

$$\mathbf{L}\frac{\partial \mathbf{W}}{\partial \mathbf{t}} + \mathbf{LARL}\frac{\partial \mathbf{W}}{\partial \mathbf{r}} = \mathbf{LS}, \tag{A.3}$$

where $\mathbf{L}$ and $\mathbf{R}$ are the matrices whose rows and columns, respectively, contain the left and right eigenvectors of $\mathbf{A}$.

In the WSD approximation, the family of characteristic curves whose slope in the $r-t$ plane is closer to that of the shock wave is chosen. If the shock advances with positive radial velocity, the correct family of characteristics to approximate the shock path is the one whose eigenvalue is given by $u+a$. Provided that a constitutive law is prescribed, an ODE that relates the changes in the primitive variables dW_i for an infinitesimal change $\mathrm{d}r$ along this characteristic curve can be written. The dW_i can ultimately be related to the change in one variable, the shock Mach number, using the RH conditions (4.7). For convenience, it is easier to use $J = \rho_0/\rho$ instead of M as the natural variable in the problem, and differentiation of J and of the RH conditions (4.7a,b,d) gives:

$$\mathrm{d}\mathbf{W} = \begin{pmatrix} \mathrm{d}\rho \\ \mathrm{d}u \\ \mathrm{d}e \\ \mathrm{d}g_{Rr} \end{pmatrix} = \begin{pmatrix} -\rho_0/J^2 \\ a_0\left[(1-J)M'(J) - M\right] \\ \sigma_{rr0}/\rho_0 + a_0^2(1-J)M\left[(1-J)M'(J)-M\right] \\ -1/J^2 \end{pmatrix} \mathrm{d}J. \tag{A.4}$$

This method is now applied to different constitutive laws.

A.1 Isothermal constitutive law

A.1.1 Elastic motion

As mentioned in Section 4.2.4, the energy equation is redundant for the isothermal elastic case. This reduces the system of PDEs to Eq. (4.1a), (4.1b) and (4.3). As a consequence, three simple eigenvalues are found (there is no entropy mode traveling with the material velocity): $(\lambda_1, \lambda_2, \lambda_3) = (u-a\,, u\,, u+a)$, where a is the sound speed. For the constitutive law (4.8), the matrices $\mathbf{A}$, $\mathbf{L}$ and $\mathbf{R}$ reduce to:

$$\mathbf{A} = \begin{pmatrix} u & \rho & 0 \\ -\dfrac{1}{\rho}\dfrac{\partial \sigma_{rr}}{\partial \rho} & u & -\dfrac{1}{\rho}\dfrac{\partial \sigma_{rr}}{\partial g_{Rr}} \\ 0 & g_{Rr} & u \end{pmatrix}, \tag{A.5a}$$

$$\mathbf{L} = \begin{pmatrix} \dfrac{a^2 - 2a_\mu^2/g_{Rr}^2}{\rho a^2} & -\dfrac{1}{a} & \dfrac{2a_\mu^2}{g_{Rr}^2 a^2} \\ \dfrac{g_{Rr}}{\rho a^2} & 0 & -\dfrac{1}{a^2} \\ \dfrac{a^2 - 2a_\mu^2/g_{Rr}^2}{\rho a^2} & \dfrac{1}{a} & \dfrac{2a_\mu^2}{g_{Rr}^2 a^2} \end{pmatrix}, \tag{A.5b}$$

$$\mathbf{R} = \begin{pmatrix} \rho & \dfrac{2a_\mu^2\rho}{g_{Rr}^3} & \rho \\ -a & 0 & a \\ g_{Rr} & \dfrac{2a_\mu^2}{g_{Rr}^2} - a^2 & g_{Rr} \end{pmatrix}, \tag{A.5c}$$

where the partial derivatives of σ_{rr} are given by:

$$\frac{1}{\rho}\frac{\partial\sigma_{rr}}{\partial\rho} = \frac{1}{\rho}\left\{ a_\mu^2 \left[\frac{1}{g_{Rr}^2} - \frac{1}{3}\left(\frac{\rho_0}{\rho}\right)^{2/3} \right] - \frac{\mathrm{d}p}{\mathrm{d}\rho} \right\}, \tag{A.6a}$$

$$\frac{1}{\rho}\frac{\partial\sigma_{rr}}{\partial g_{Rr}} = -\frac{2a_\mu^2}{g_{Rr}^3}. \tag{A.6b}$$

In the above expressions, the sound speed a is expressed as

$$a = \sqrt{a_\mu^2 \left[\frac{1}{{g_{Rr}}^2} + \frac{1}{3}\left(\frac{\rho_0}{\rho}\right)^{2/3} \right] + \frac{\mathrm{d}p}{\mathrm{d}\rho}}. \tag{A.7}$$

The characteristic equation corresponding to $\lambda_3 = u + a$ reads:

$$\frac{a^2 - a_\mu^2/g_{Rr}^2}{a^2\rho}\frac{\mathrm{d}\rho}{\mathrm{d}r} + \frac{1}{a}\frac{\mathrm{d}u}{\mathrm{d}r} + \frac{2a_\mu^2}{g_{Rr}^2 a^2}\frac{\mathrm{d}g_{Rr}}{\mathrm{d}r} = \frac{s-1}{\rho a(u+a)r}\left[-\left(a^2 - \frac{2a_\mu^2}{g_{Rr}^2} \right)\frac{\rho u}{a} + \sigma_{rr} - \sigma_{\theta\theta} \right], \tag{A.8}$$

and using Eq. (4.9) and (A.4), and the fact that $r = R(t)$ at the shock location, leads to the ODE

$$\frac{\mathrm{d}R}{R} = -\frac{1}{s-1}\frac{a\left[a + a_0(1-J)M\right]\left[-a/J + a_0(1-J)M'(J) - a_0 M\right]}{(1-J)\left[a_0\left(a^2 - 2a_\mu^2 J^2\right)M + a_\mu^2 a(1+J)\right]}\mathrm{d}J, \tag{A.9a}$$

$$M(J) = \frac{1}{a_0}\sqrt{\frac{1}{1-J}\left[\frac{p(\rho_0/J)}{\rho_0} - a_\mu^2\left(J - J^{-1/3}\right)\right]}, \tag{A.9b}$$

for any isothermal pressure form $p(\rho)$.

A.1.2 Perfectly plastic motion

The existence of a finite yield stress makes it impossible to have an explicit dependency of the radial stress with respect to g_{Rr}. In contrast, σ_{rr} depends on the density both explicitly through J and through g_{Rr}^e by Eq. (4.30). Three distinct eigenvalues are obtained: $(\lambda_1, \lambda_2, \lambda_3) = (u - a\,, u\,, u + a)$, with the sound speed being

$$a = \sqrt{-\frac{\mathrm{d}\sigma_{rr}}{\mathrm{d}\rho}} = \sqrt{-a_\mu^2\left(\frac{1}{{g_{Rr}^e}^2} + \frac{2}{{g_{Rr}^e}^3}\frac{\mathrm{d}g_{Rr}^e}{\mathrm{d}J}J - \frac{1}{3}J^{2/3}\right) + \frac{\mathrm{d}p}{\mathrm{d}\rho}}, \tag{A.10}$$

with $J = (\rho_0/\rho)$, where the derivative of the elastic deformation with respect to the density ratio can be obtained by differentiating Eq. (4.30):

$$\frac{\mathrm{d}g^e_{Rr}}{\mathrm{d}J} = \frac{{g^e_{Rr}}^3}{2g^e_{Rr}\sigma_Y/\mu - 3J{g^e_{Rr}}^2}. \tag{A.11}$$

Then, the matrices $\mathbf{A}$,$\mathbf{L}$ and $\mathbf{R}$ read:

$$\begin{aligned}
\mathbf{A} &= \begin{pmatrix} u & \rho & 0 \\ -\dfrac{1}{\rho}\dfrac{\partial\sigma_{rr}}{\partial\rho} & u & 0 \\ 0 & g_{Rr} & u \end{pmatrix}, \\
\mathbf{L} &= \begin{pmatrix} \dfrac{g_{Rr}}{2\rho} & -\dfrac{g_{Rr}}{2a} & 0 \\ -\dfrac{g_{Rr}}{\rho} & 0 & 1 \\ \dfrac{g_{Rr}}{2\rho} & \dfrac{g_{Rr}}{2a} & 0 \end{pmatrix}, \qquad \text{(A.12a)} \\
\mathbf{R} &= \begin{pmatrix} \dfrac{\rho}{g_{Rr}} & 0 & \dfrac{\rho}{g_{Rr}} \\ -\dfrac{a}{g_{Rr}} & 0 & \dfrac{a}{g_{Rr}} \\ 1 & 1 & 1 \end{pmatrix}.
\end{aligned}$$

After finding the left and right eigenvectors, the following ODE holds along the characteristic $\lambda_3 = u + a$:

$$\frac{1}{\rho}\frac{\mathrm{d}\rho}{\mathrm{d}r} + \frac{1}{a}\frac{\mathrm{d}u}{\mathrm{d}r} = \frac{2}{(u+a)r}\left(-\frac{\sigma_Y}{\rho_0 a} - u\right). \tag{A.13}$$

Using the RH conditions finally leads to:

$$\begin{aligned}
\frac{\mathrm{d}R}{R} &= -\frac{1}{2}\frac{[a + a_0(1-J)M]\,[-a/J + a_0(1-J)M'(J) - a_0M]}{[a_0a(1-J)M + \sigma_Y/\rho_0]}\mathrm{d}J, && \text{(A.14a)} \\
M(J) &= \frac{1}{a_0}\sqrt{\frac{1}{1-J}\left[\frac{p(\rho_0/J)}{\rho_0} - a_\mu^2\left(\frac{1}{J{g^e_{Rr}}^2} - J^{-1/3}\right)\right]}, && \text{(A.14b)}
\end{aligned}$$

where g^e_{Rr} is implicitly given by (4.30).

A.2 Non-isothermal constitutive law for elastic motion

In this case, the complete system of equations given by Eq. (4.1) and (4.3) is considered. Two simple eigenvalues and one eigenvalue of multiplicity two are found: $(\lambda_1, \lambda_2^{(2)}, \lambda_3) = (u - a\,, u\,, u + a)$, with the speed of sound being:

$$a = \sqrt{-\frac{\gamma\sigma_{rr}}{\rho} + \frac{a_\mu^2}{{g_{Rr}}^2}(1+\gamma)}, \tag{A.15}$$

where σ_{rr} is given by Eq. (4.20a). The matrices $\mathbf{A}$, $\mathbf{L}$ and $\mathbf{R}$ are:

$$\mathbf{A} = \begin{pmatrix} u & \rho & 0 & 0 \\ -\dfrac{1}{\rho}\dfrac{\partial\sigma_{rr}}{\partial\rho} & u & -\dfrac{1}{\rho}\dfrac{\partial\sigma_{rr}}{\partial e} & -\dfrac{1}{\rho}\dfrac{\partial\sigma_{rr}}{\partial g_{Rr}} \\ 0 & -\dfrac{\sigma_{rr}}{\rho} & u & 0 \\ 0 & g_{Rr} & 0 & u \end{pmatrix}, \tag{A.16a}$$

$$\mathbf{L} = \begin{pmatrix} -\dfrac{g_{Rr}}{2\rho a^2}\dfrac{\partial\sigma_{rr}}{\partial\rho} & -\dfrac{g_{Rr}}{2a} & -\dfrac{g_{Rr}}{2\rho a^2}\dfrac{\partial\sigma_{rr}}{\partial e} & -\dfrac{g_{Rr}}{2\rho a^2}\dfrac{\partial\sigma_{rr}}{\partial g_{Rr}} \\ \dfrac{g_{Rr}}{\rho a^2}\dfrac{\partial\sigma_{rr}}{\partial\rho} & 0 & \dfrac{g_{Rr}}{\rho a^2}\dfrac{\partial\sigma_{rr}}{\partial e} & \dfrac{1}{\rho^2 a^2}\left(\sigma_{rr}\dfrac{\partial\sigma_{rr}}{\partial e} - \rho^2\dfrac{\partial\sigma_{rr}}{\partial\rho}\right) \\ -\dfrac{\sigma_{rr}}{\rho^2 a^2}\dfrac{\partial\sigma_{rr}}{\partial\rho} & 0 & -\dfrac{1}{\rho a^2}\left(g_{Rr}\dfrac{\partial\sigma_{rr}}{\partial g_{Rr}} + \rho\dfrac{\partial\sigma_{rr}}{\partial\rho}\right) & -\dfrac{\sigma_{rr}}{\rho^2 a^2}\dfrac{\partial\sigma_{rr}}{\partial g_{Rr}} \\ -\dfrac{g_{Rr}}{2\rho a^2}\dfrac{\partial\sigma_{rr}}{\partial\rho} & \dfrac{g_{Rr}}{2a} & -\dfrac{g_{Rr}}{2\rho a^2}\dfrac{\partial\sigma_{rr}}{\partial e} & -\dfrac{g_{Rr}}{2\rho a^2}\dfrac{\partial\sigma_{rr}}{\partial g_{Rr}} \end{pmatrix}, \tag{A.16b}$$

$$\mathbf{R} = \begin{pmatrix} \dfrac{\rho}{g_{Rr}} & -\dfrac{\partial\sigma_{rr}}{\partial g_{Rr}}\Big/\dfrac{\partial\sigma_{rr}}{\partial\rho} & -\dfrac{\partial\sigma_{rr}}{\partial e}\Big/\dfrac{\partial\sigma_{rr}}{\partial\rho} & \dfrac{\rho}{g_{Rr}} \\ -\dfrac{a}{g_{Rr}} & 0 & 0 & \dfrac{a}{g_{Rr}} \\ -\dfrac{\sigma_{rr}}{g_{Rr}\rho} & 0 & 1 & -\dfrac{\sigma_{rr}}{g_{Rr}\rho} \\ 1 & 1 & 0 & 1 \end{pmatrix}, \tag{A.16c}$$

where the partial derivatives of the radial stress are computed as follows:

$$\frac{\partial\sigma_{rr}}{\partial\rho} = \frac{2J\sigma_{rr} - \mu(\gamma-1)(s-1)(4-s)J^{4-s}{g_{Rr}}^{4-s}}{2\rho_0}, \tag{A.17a}$$

$$\frac{\partial\sigma_{rr}}{\partial e} = -\frac{(\gamma-1)\rho_0}{J}, \tag{A.17b}$$

$$\frac{\partial\sigma_{rr}}{\partial g_{Rr}} = \frac{\mu}{J}\left[-\frac{\gamma+1}{{g_{Rr}}^3} + \frac{(\gamma-1)(s-1)(4-s)J^{4-s}{g_{Rr}}^{3-s}}{2}\right]. \tag{A.17c}$$

The characteristic equation corresponding to $\lambda_4 = u + a$ can be written as

$$\mathbf{L}_{4,:}\frac{\mathrm{d}\mathbf{W}}{\mathrm{d}r} = \frac{1}{u+a}\mathbf{L}_{4,:}\mathbf{S}, \tag{A.18}$$

where $\mathbf{L}_{4,:}$ is the fourth row of matrix (A.16b). Writing the source term (A.2c) as $\mathbf{S} = (s-1)\mathbf{S}'/r$ and using Eq. (4.7), (4.20) and (A.4), a closed ODE is obtained:

$$\frac{\mathrm{d}R}{R} = \frac{1}{s-1}\frac{\left[a + a_0(1-J)M\right]\mathbf{L}_{4,:}(J)\mathrm{d}\mathbf{W}/\mathrm{d}J}{\mathbf{L}_{4,:}(J)\mathbf{S}'(J)}\mathrm{d}J, \tag{A.19a}$$

$$M(J) = \frac{1}{a_0}\sqrt{\frac{a_\mu^2\left[2 - J^2 - \gamma(J+2)^2\right] + 2e_0(\gamma-1) + 2\sigma_{rr_0}\left[1 - \gamma(1-J)\right]/\rho_0}{(1-J)\left[1 + J - \gamma(1-J)\right]}}. \tag{A.19b}$$

Appendix B

Approximation for the growth rate using linearization around branch cuts

The symmetry of the problem allows us to only consider the integrals around the branch cuts located in $Im(s) > 0$, multiply the result by 2 and take the real part of the expression:

$$\frac{\partial \hat{\eta}}{\partial t} = \hat{u_1}(t, x_1 = 0) = u_{poles}(t, 0) + \sum_{j=1}^{4} u_{bj}(t, 0) \tag{B.1}$$

where u_{poles} is the contribution of the residues of the poles to the normal velocity and leading-order branch cut contributions u_{bj} are:

$$u_{b1}(t, 0) = -\frac{\sqrt{c_- k}\sqrt{2}e^{ic_- kt - i\pi/4}}{\sqrt{\pi}t^{3/2}} K_1, \tag{B.2}$$

$$u_{b2}(t, 0) = -\frac{\sqrt{c_+ k}\sqrt{2}e^{ic_+ kt - i\pi/4}}{\sqrt{\pi}t^{3/2}} K_2. \tag{B.3}$$

For $c_- > c_+$:

$$u_{b3}(t, 0) = -A_t V \eta_0 k \frac{i\sqrt{c_-(c_-^2 - c_+^2)k^3}\sqrt{2}e^{ic_- kt - i\pi/4}}{\sqrt{\pi}t^{3/2}} K_3, \tag{B.4}$$

$$u_{b4}(t, 0) = -A_t V \eta_0 k \frac{\sqrt{c_+(c_-^2 - c_+^2)k^3}\sqrt{2}e^{ic_+ kt - i\pi/4}}{\sqrt{\pi}t^{3/2}} K_4. \tag{B.5}$$

For $c_- < c_+$:

$$u_{b3}(t, 0) = -A_t V \eta_0 k \frac{\sqrt{c_-(c_+^2 - c_-^2)k^3}\sqrt{2}e^{ic_- kt - i\pi/4}}{\sqrt{\pi}t^{3/2}} K_3, \tag{B.6}$$

$$u_{b4}(t, 0) = -A_t V \eta_0 k \frac{i\sqrt{c_+(c_+^2 - c_-^2)k^3}\sqrt{2}e^{ic_+ kt - i\pi/4}}{\sqrt{\pi}t^{3/2}} K_4. \tag{B.7}$$

In particular, for free-slip boundary conditions the coefficients K_i are:

$$K_1 = \frac{4c_-^2(1+r)[-48c_-^2c_+^6r^2 + 32c_+^8r^2 - 8c_-^6c_+^2r(1+r) + c_-^8(1+r)^2 + 8c_-^4c_+^4r(1+3r)]}{k^2[-16c_+^6r^2 - 8c_-^4c_+^2r(1+r) + c_-^6(1+r)^2 + 8c_-^2c_+^4r(1+3r)]^2}, \tag{B.8}$$

$$K_2 = \frac{4c_+^2r(1+r)[32c_-^8 - 48c_-^6c_+^2 - 8c_-^2c_+^6(1+r) + c_+^8(1+r)^2 + 8c_-^4c_+^4(3+r)]}{k^2[-16c_-^6 - 8c_-^2c_+^4(1+r) + c_+^6(1+r)^2 + 8c_-^4c_+^2(3+r)]^2}, \tag{B.9}$$

$$K_3 = \frac{32c_-^2c_+^3r(1+r)[-4c_-^2c_+^2r + 4c_+^4r + c_-^4(1+r)]}{k^3[-16c_+^6r^2 - 8c_-^4c_+^2r(1+r) + c_-^6(1+r)^2 + 8c_-^2c_+^4r(1+3r)]^2}, \tag{B.10}$$

$$K_4 = \frac{32c_-^3c_+^2r(1+r)[4c_-^4 - 4c_-^2c_+^2 + c_+^4(1+r)]}{k^3[-16c_-^6 - 8c_-^2c_+^4(1+r) + c_+^6(1+r)^2 + 8c_-^4c_+^2(3+r)]^2}. \tag{B.11}$$

When no-slip boundary conditions are imposed, the coefficients K_i become:

$$\begin{aligned}
K_1 &= 4c_-^2(1+r)(16c_+^{12}r^6 + c_-^{12}(1+r)^2 - 8c_-^2c_+^{10}r^5(1+5r) + ... \\
&+ 2c_-^4c_+^8r^4(-11+14r+17r^2) + c_-^6c_+^6r^3(14+33r-24r^2-11r^3) + \\
&+ 2c_-^{10}c_+^2r(-3-r+3r^2+r^3) + c_-^8c_+^4r^2(7-24r-12r^2+4r^3+r^4))/... \\
&/ k^2(-16c_+^8r^4 + c_-^8(1+r)^2 + 8c_-^2c_+^6r^3(1+3r) - ... \\
&- 8c_-^4c_+^4r^2(-1+2r+r^2) + c_-^6c_+^2r(-6-3r+4r^2+r^3))^2.
\end{aligned} \tag{B.12}$$

$$\begin{aligned}
K_2 &= 4c_+^2(1+r)r(16c_-^{12} + c_+^{12}r^4(1+r)^2 - 8c_-^{10}c_+^2(5+r) + ... \\
&+ 2c_-^8c_+^4(17+14r-11r^2) - 2c_-^2c_+^{10}r^2(-1-3r+r^2+3r^3) + ... \\
&+ c_-^6c_+^6(-11-24r+33r^2+14r^3) + c_-^4c_+^8(1+4r-12r^2-24r^3+7r^4))/... \\
&/ k^2(-16c_-^8 + c_+^8r^2(1+r)^2 + 8c_-^6c_+^2(3+r) + ... \\
&+ 8c_-^4c_+^4(-1-2r+r^2) + c_-^2c_+^6(1+4r-3r^2-6r^3))^2.
\end{aligned} \tag{B.13}$$

$$\begin{aligned}
K_3 &= 8c_-^4c_+^3r^2(1+r)^2(4c_+^6r^3 + c_-^6(1+r) - c_-^2c_+^4r^2(1+5r) + c_-^4c_+^2r(-3+2r+r^2))/... \\
&/ k^3(-16c_+^8r^4 + c_-^8(1+r)^2 + 8c_-^2c_+^6r^3(1+3r) - ... \\
&- 8c_-^4c_+^4r^2(-1+2r+r^2) + c_-^6c_+^2r(-6-3r+4r^2+r^3))^2.
\end{aligned} \tag{B.14}$$

$$\begin{aligned}
K_4 &= 8c_-^3 c_+^4 r(1+r)^2(4c_-^6 + c_+^6 r^2(1+r) - c_-^4 c_+^2(5+r) + c_-^2 c_+^4(1+2r-3r^2))/ \\
/ &\ k^3(-16c_-^8 + c_+^8 r^2(1+r)^2 + 8c_-^6 c_+^2(3+r) + \ldots \\
+ &\ 8c_-^4 c_+^4(-1-2r+r^2) + c_-^2 c_+^6(1+4r-3r^2-6r^3))^2. \qquad \text{(B.15)}
\end{aligned}$$

The results shown in Figure B.1 for free-slip boundary conditions are quite accurate even using only the first term (the term in $1/t^{3/2}$) of the approximation. Normally this approximation matches the complete integration result earlier when the two shear wave velocities are very different from each other. Figs. $B.1(a)$ and $B.1(b)$ show a comparison of both results (actual and approximate) for $c_-/c_+ = 2$ and $r = 2$, and $c_-/c_+ = 1$ and $r = 2$, respectively.

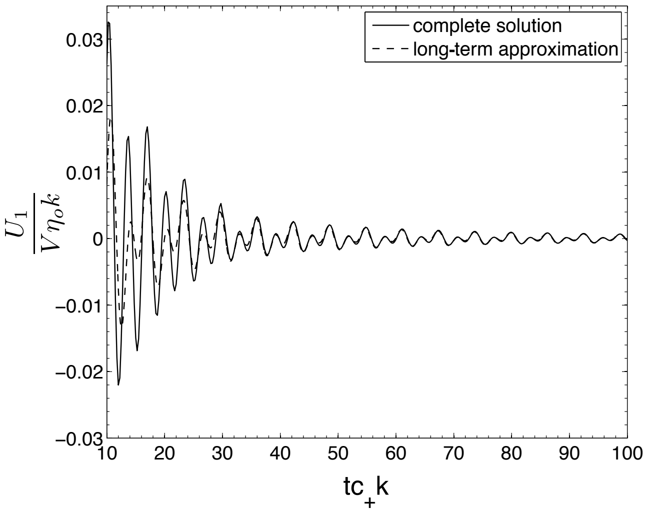

(a) $c_-/c_+ = 2, r = 2$.

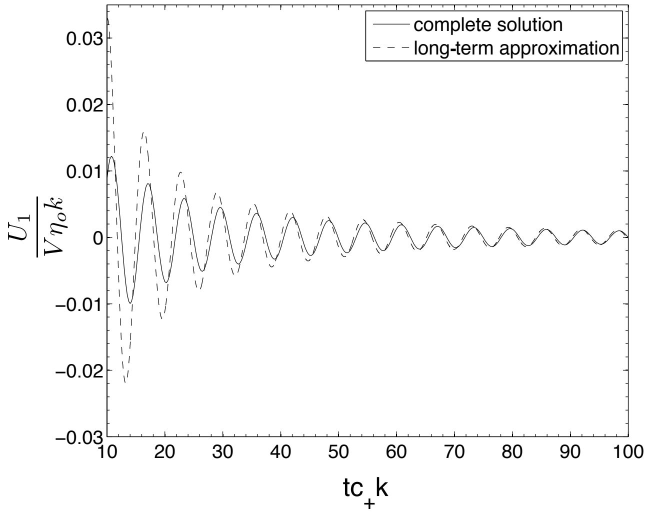

(b) $c_-/c_+ = 1, r = 2$.

Figure B.1: Contribution of the integral over the branch cuts to the growth rate using a numerical quadrature method to integrate the growth rate function and using the first term of the approximation around the branch points

Appendix C

Additional mass conservation examples

The quality of mass conservation must be considered in all the applications in which a non-conservative level-set method is used. Two additional mass conservation studies are exposed in this Appendix, with the purpose of complementing the results in sections 3.3.5 and 6.4.3.1.

C.1 Planar solid–gas with no perturbation in a two-dimensional grid

This analysis constitutes a largely simplified version of the converging solid–gas Richtmyer–Meshkov problem. A rectangular computational domain $\{0, 8\} \times \{0, 1\}$ composed of rectangular cells with aspect ratio 2 in which the fluid lies on the left and the solid (copper, with equation of state (6.1) on the right is considered. The initial solid–gas density ratio is 100. Boundary conditions are reflective and zero-gradient at the left and right boundary, respectively, and periodic for the top and bottom. A left-moving shock is generated in the solid in the way explained in Section 6.4.2 and propagates towards the interface, which lies parallel to the shock, constituting a strictly one-dimensional problem simulated in a two-dimensional grid. Due to the reflective boundary conditions on the left, the fluid is confined to a small region close to the boundary in a way similar to how the fluid is confined to a small region close to the axis in the converging case. Figure C.1 shows the initial configuration with gas (blue), solid (green) and driving solid (red).

Figure C.2 shows the time evolution of the fluid mass when compared with its initial value for

Figure C.1: Initial configuration for solid–gas one-dimensional shock–interface problem

Table C.1: L_2-errors and convergence rate for different levels of refinement

	1 level		2 levels no fix		2 levels fix	
effective resolution	L_2-error	**C.R.**	L_2-error	**C.R.**	L_2-error	**C.R.**
64x16	1.801e-2					
128x32	1.575e-2	**0.193**	1.519e-2		1.533e-2	
256x64	0.727e-2	**1.117**	0.724e-2	**1.070**	0.737e-2	**1.057**
512x128	0.234e-2	**1.634**	0.430e-2	**0.751**	0.153e-2	**2.268**
1024x128	0.159e-2	**0.561**	0.288e-2	**0.576**	0.159e-2	**-0.058**
2048x256	0.078e-2	**1.018**	0.191e-2	**0.591**	0.070e-2	**1.173**
4096x512			0.095e-2	**1.014**	0.050e-2	**0.493**

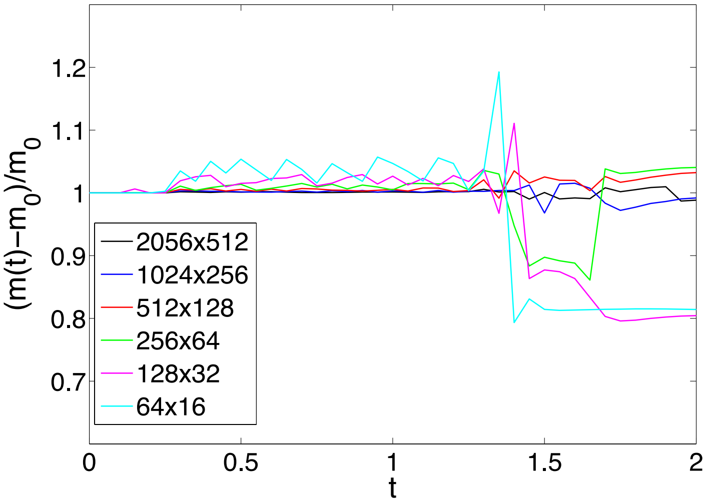

Figure C.2: Fluid mass conservation time evolution with respect to the initial value

uni-grid simulations. Errors and oscillations of the mass value are reduced as resolution increases. Mass conservation is degraded, similarly to the behavior observed in the converging case, after the re-shocks occur (after $t \approx 1.2$). At that point the fluid is restricted to a very small layer. The total errors in mass of fluid are evaluated by means of the same equation employed for the converging case:

$$\varepsilon_{mass}(t_f) = \frac{1}{n_f}\sqrt{\sum_{n=1}^{n_f}\left(\frac{|m_n - m_{n-1}|}{m_{n-1}}\right)^2}, \tag{C.1}$$

where t_f is the final simulation time and n_f the total number of time points for which the mass has been evaluated. Results are shown in Table C.1 and Fig. C.2. The convergence rate is not monotonic for any of the cases studied (uni-grid and two-level simulations with and without conservative fix-up). This is due to the small area occupied by the fluid, which has a length of only a few cells in the higher resolution tested, as shown in Fig. C.4, where the left wall corresponds to the left reflective boundary condition. Similarly to the cases tested in Section 3.3.5, enabling the fix-up algorithm clearly improves fluid mass conservation.

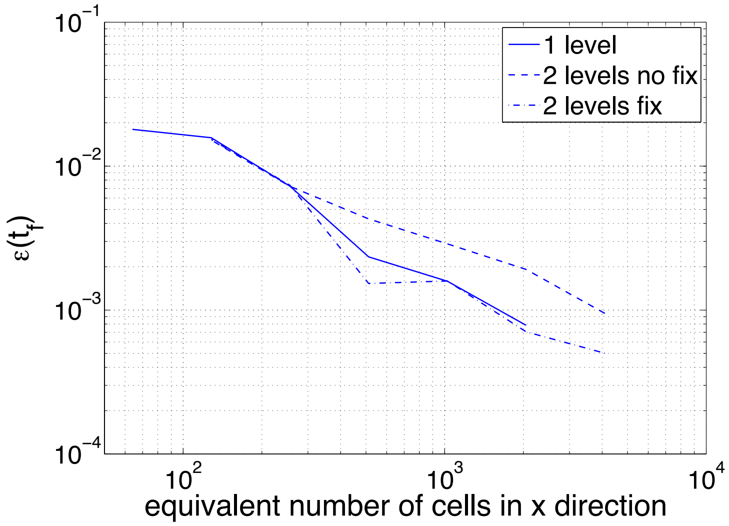

Figure C.3: Fluid mass conservation errors computed using Eq. (C.1) with $t_f = 2$ (final simulation time)

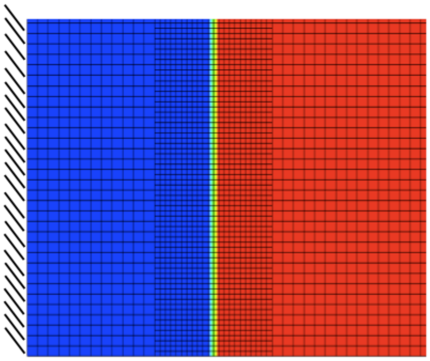

Figure C.4: Close up near the left boundary for the final simulation time ($t_f = 2$) in a simulation with effective resolution 4096 × 512 (base grid 2048 × 256 and one level of refinement). The fluid region spans over a very small number of computational cells.

C.2 Planar solid–solid Richtmyer–Meshkov

In this case, a rectangular domain $\{0, 12\} \times \{0, 4\}$ composed of square cells in considered with aluminum and copper on the left and right side, respectively. The aim of this study is to examine the effects of ill-posedness on mass conservation in a more simple configuration than the solid–gas converging case. Some typical phenomena observed in the solid–gas converging simulations are present, such as the development of the Richtmyer–Meshkov instability and the re-shocks. However, the characteristic Atwood ratio is smaller and there are no converging geometry effects. Aluminum follows the same form of constitutive law as copper (Eq. 6.1) with parameters $\rho_0 = 2.712\,\mathrm{g/cm^3}$, $K = 25.39e6\,\mathrm{m^2/s^2}$, $c_v = 9.0e5\,\mathrm{m^2/Ks^2}$, $T_0 = 300\,\mathrm{K}$, $\mu_0 = 27.09\,\mathrm{GPa}$, $\alpha = 1$, $\beta = 3.577$, $\gamma_s = 2.088$, and $\sigma_Y = 0.297\,\mathrm{GPa}$. Boundary conditions are reflective and zero-gradient, respectively, on the left and right boundaries and periodic for the top and bottom. A shock, driven as explained in Section 6.3, propagates from the copper into the aluminum. The interface is initially sinusoidal with $\eta_0 k = 0.4$. Two different material boundary conditions are considered: free-slip and no-slip.

Figure C.5 shows the time evolution of the density for the case of free-slip boundary conditions, starting with the initial configuration and the state before the shock passage (Figs. C.5(a,b)). Interface phase reversal and re-shock are depicted in Figs. C.5(c,d), with the final evolution of the vortices in the last two frames (Figs. C.5(e,f)). Figure C.6 shows the mass evolution in time with respect to its initial value for the free-slip and no-slip cases and multiple grid resolutions. Results suggest that, as expected, increased resolution reduces mass errors.

Table C.2 and Fig. C.7 show mass errors as function of the grid resolution. Values are computed using Eq. (C.1). The analysis of these results reveals that mass conservation in the no-slip case converges monotonically (even with a converging rate greater than 1). However, this trend is not repeated when considering free-slip boundary conditions, which exhibits an irregular behavior in terms of convergence rate (although always decreasing) similar to what is found for the converging solid-gas case. The examination of the final density contour plots for different resolutions for both interface boundary conditions (Figs. C.8 and C.9) shows that, in the free-slip case, new scales, such as thinner copper ligaments, appear as the resolution increases. This phenomenon is caused by the Kelvin–Helmholtz instability developed due to the discontinuity in tangential velocities across the material interface. The appearance of new features as the resolution is augmented effectively increases the length of the interface between the two solids and thus the possibility of mass conservation errors. On the other hand, for the case of no-slip, the final vortices exhibit a similar structure in the higher resolution cases, leading to the previously described monotonic behavior.

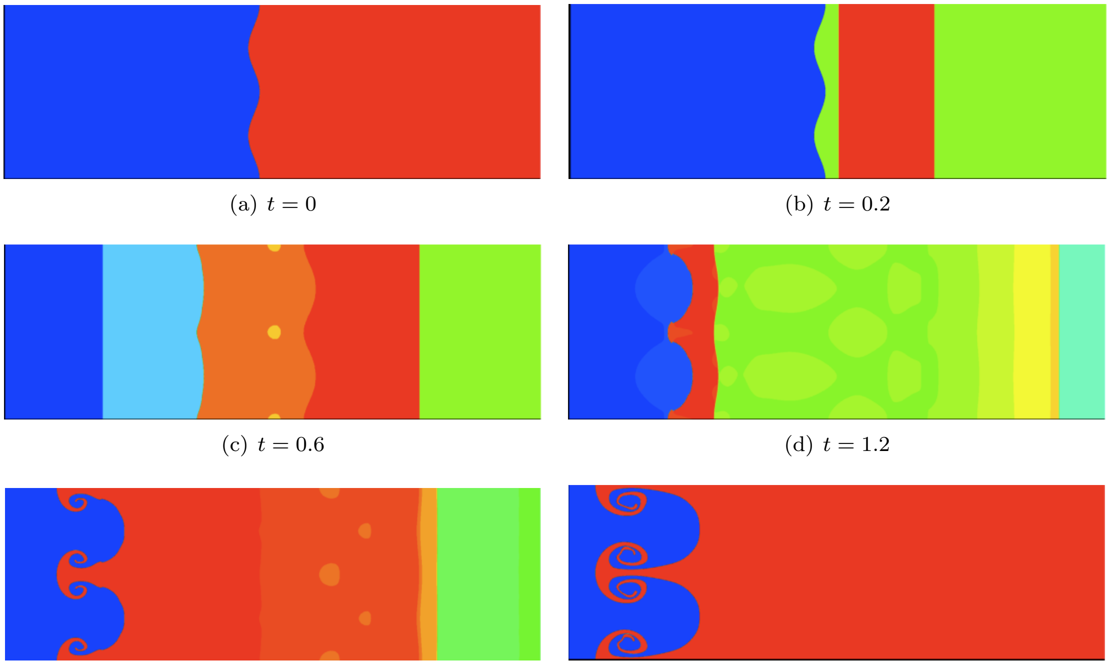

(a) $t = 0$ (b) $t = 0.2$

(c) $t = 0.6$ (d) $t = 1.2$

(e) $t = 2.2$ (f) $t = 4.0$

Figure C.5: Time evolution of density contour plots for the free-slip case. (a) Initial configuration, (b) shock directed towards interface, (c) interface reversal typical of heavy–light configurations, (d) re-shock, (e,f) vortex development

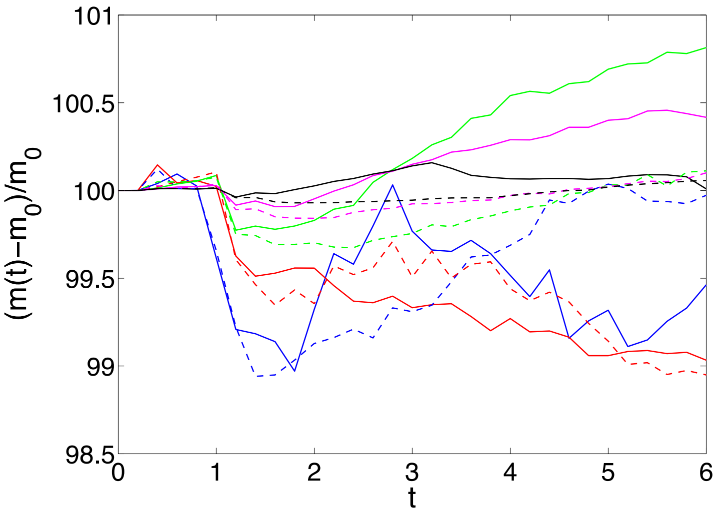

Figure C.6: Mass conservation evolution with respect to the initial value with time. Continuous and dashed lines represent free-slip and no-slip simulations respectively. All simulations are run with four total levels (3 levels of refinement) with base-grid resolutions: 48 × 16 (blue), 96 × 32 (red), 192 × 64 (green), 384 × 128 (magenta), and 768 × 256 (black).

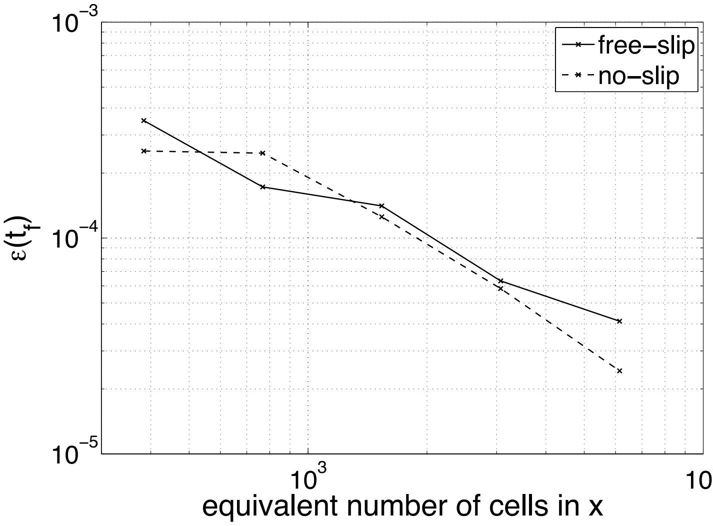

Figure C.7: Mass conservation errors computed using Eq. (C.1) with $t_f = 6$ (final simulation time)

Table C.2: L_2-errors and convergence rate for free-slip and no-slip boundary conditions

4 levels	no-slip		free-slip	
base grid	L_2-error	**C.R.**	L_2-error	**C.R.**
48x16	2.530e-4		3.501e-4	
96x32	2.472e-4	**0.033**	1.725e-4	**1.021**
192x64	1.254e-4	**0.980**	1.409e-4	**0.292**
384x128	0.583e-4	**1.104**	0.633e-4	**1.154**
768x256	0.243e-4	**1.266**	0.412e-4	**0.621**

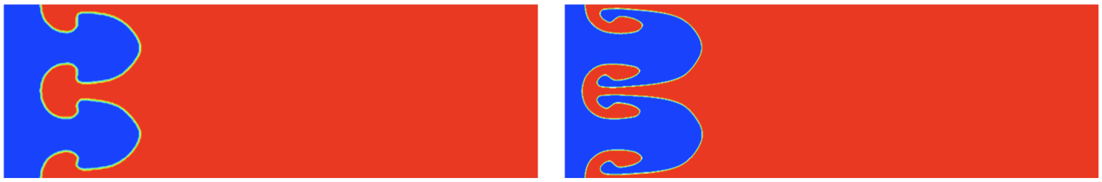

(a) 48 × 16, 4 levels

(b) 96 × 32, 4 levels

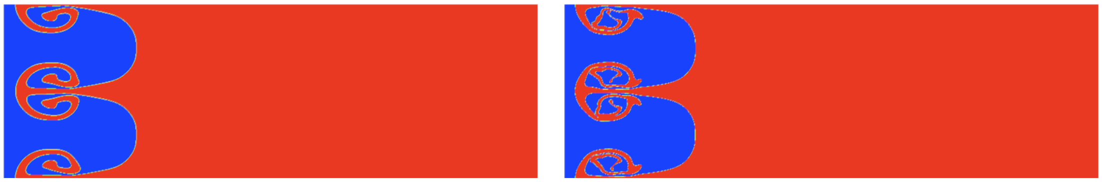

(c) 192 × 64, 4 levels

(d) 384 × 128, 4 levels

(e) 768 × 256, 4 levels

Figure C.8: Density color-contour plots for final simulation time and different resolutions in the free-slip case

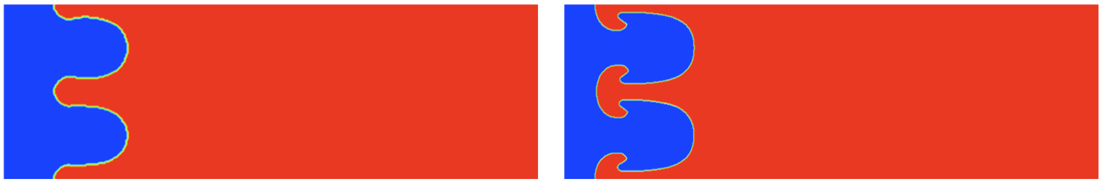

(a) 48 × 16, 4 levels

(b) 96 × 32, 4 levels

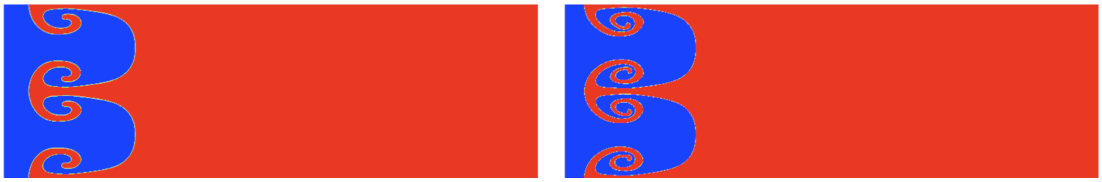

(c) 192 × 64, 4 levels

(d) 384 × 128, 4 levels

(e) 768 × 256, 4 levels

Figure C.9: Density color-contour plots for final simulation time and different resolutions in the no-slip case

Appendix D

Density contour plots from parametric studies

Selected density contour plots of the evolution of the solid–gas interface close to the origin for all the cases considered in the parametric study performed in Chapter 6 are shown in this Appendix. As regards to the initial conditions and material properties being modified, each section contains the following examples:

Variation of the initial parameters:

$C \equiv \frac{\eta_0 n}{R_0} = \{0.05, 0.1\}$, $n = \{4, 8, 12, 16\}$, $r_i = 100$, $M_s = 1.65$, $\sigma_Y = 0.12\,\mathrm{GPa}$.

Variation of the initial solid–gas density ratio:

$C \equiv \frac{\eta_0 n}{R_0} = \{0.05, 0.1\}$, $n = \{4, 16\}$, $r_i = \{10, 500\}$, $M_s = 1.65$, $\sigma_Y = 0.12\,\mathrm{GPa}$.

Variation of the initial shock Mach number:

$C \equiv \frac{\eta_0 n}{R_0} = 0.05$, $n = \{4, 16\}$, $r_i = 100$, $M_s = \{1.61, 1.31, 1.48, 1.65, 1.83\}$, $\sigma_Y = 0.12\,\mathrm{GPa}$.

Variation of the yield stress:

$C \equiv \frac{\eta_0 n}{R_0} = 0.05$, $n = \{4, 16\}$, $r_i = 100$, $M_s = 1.65$, $\sigma_Y = \{0, 0.5, 1\}\,\mathrm{GPa}$.

D.1 Influence of the initial interface parameters

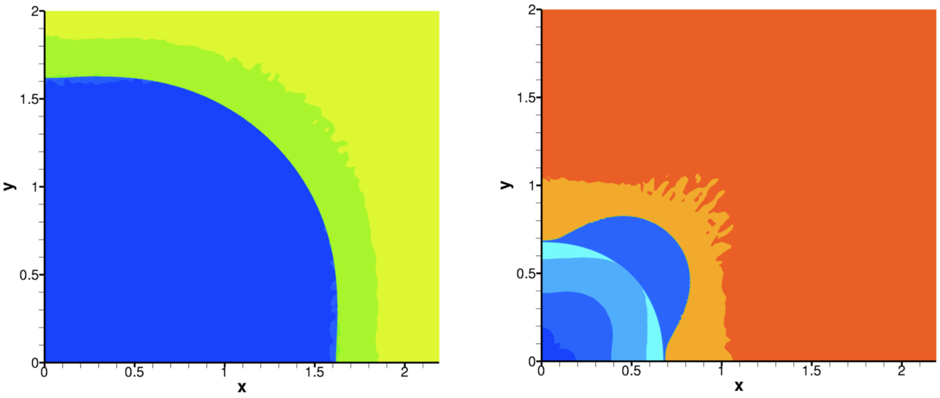

(a) $t = 0.8$ (b) $t = 0.9$

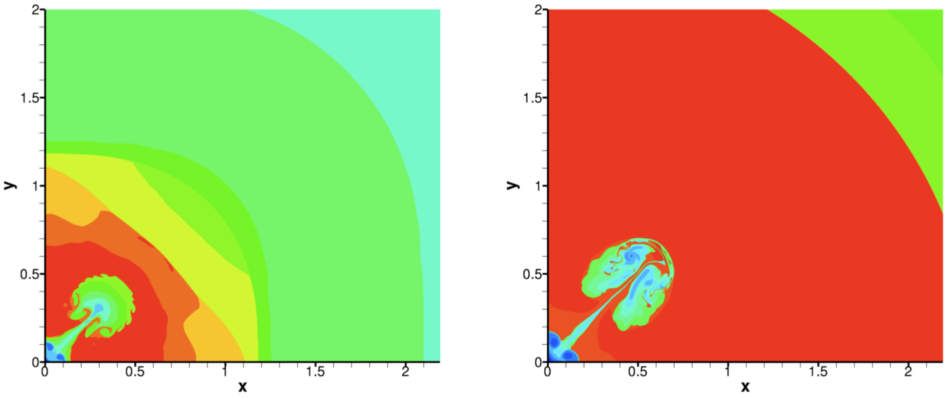

(c) $t = 1.0$ (d) $t = 1.1$

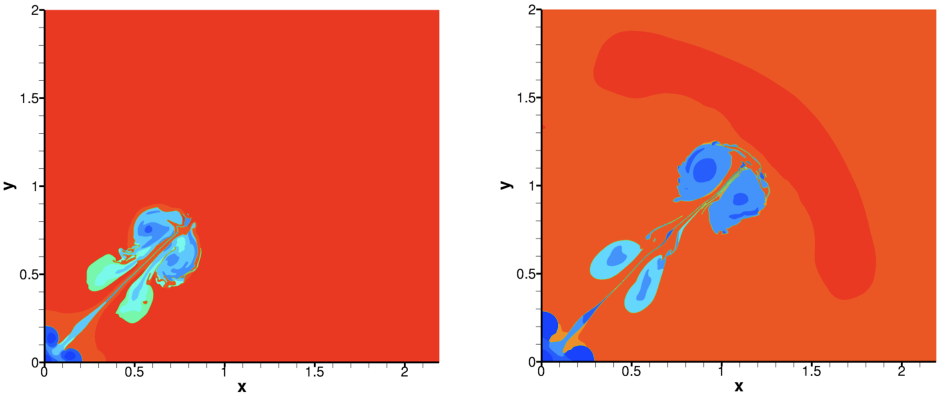

(e) $t = 1.2$ (f) $t = 1.5$

Figure D.1: $C \equiv \frac{\eta_0 n}{R_0} = 0.05$, $n = 4$, $r_i = 100$, $M_s = 1.65$, $\sigma_Y = 0.12\,\text{GPa}$.

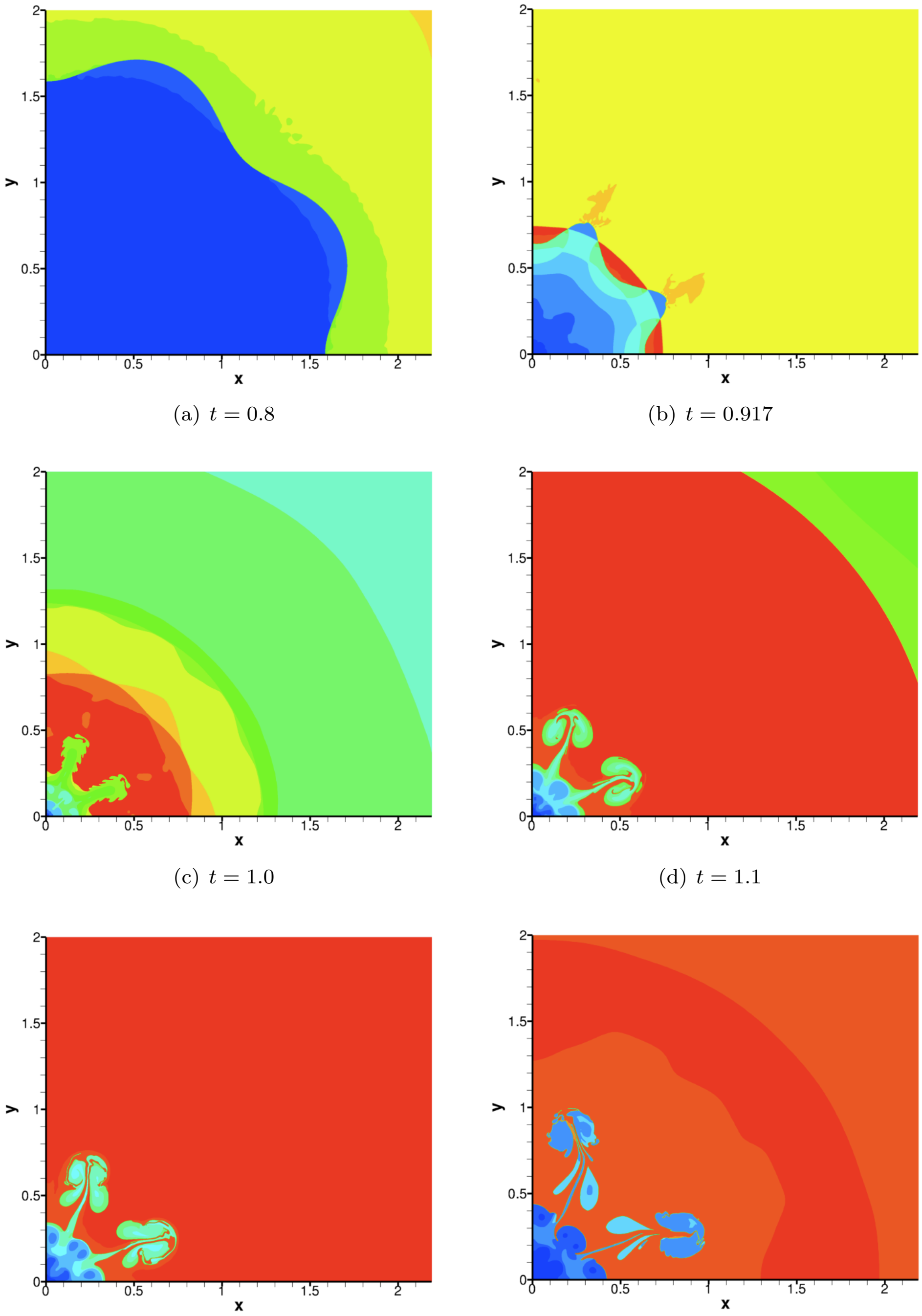

(a) $t = 0.8$

(b) $t = 0.917$

(c) $t = 1.0$

(d) $t = 1.1$

(e) $t = 1.2$

(f) $t = 1.5$

Figure D.2: $C \equiv \frac{\eta_0 n}{R_0} = 0.05$, $n = 8$, $r_i = 100$, $M_s = 1.65$, $\sigma_Y = 0.12\,\mathrm{GPa}$.

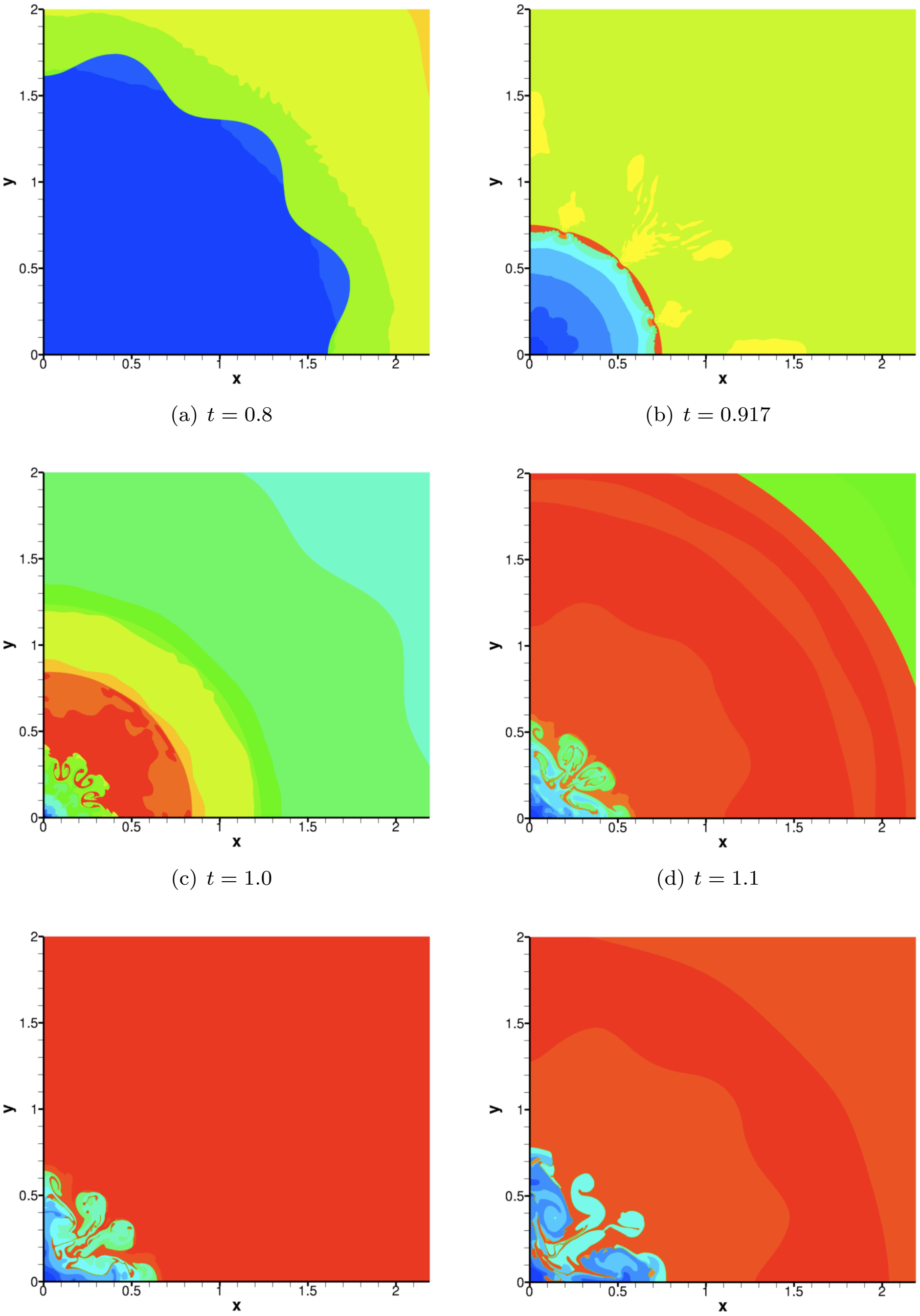

(a) $t = 0.8$

(b) $t = 0.917$

(c) $t = 1.0$

(d) $t = 1.1$

(e) $t = 1.2$

(f) $t = 1.5$

Figure D.3: $C \equiv \frac{\eta_0 n}{R_0} = 0.05$, $n = 12$, $r_i = 100$, $M_s = 1.65$, $\sigma_Y = 0.12\,\mathrm{GPa}$.

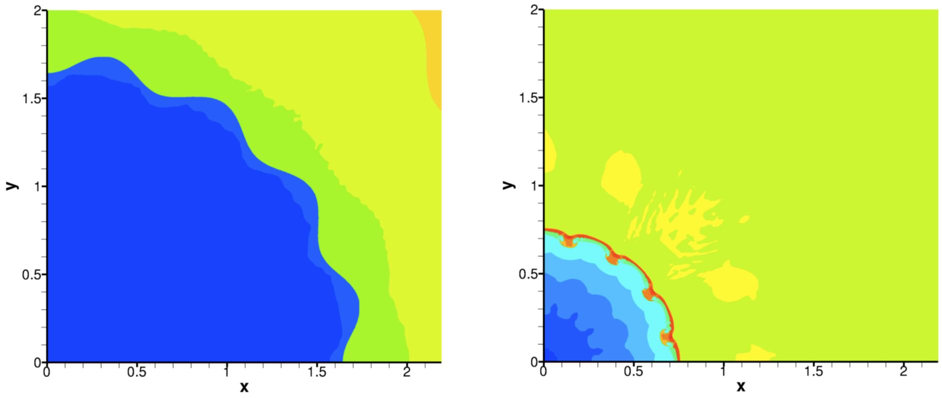

(a) $t = 0.8$ (b) $t = 0.917$

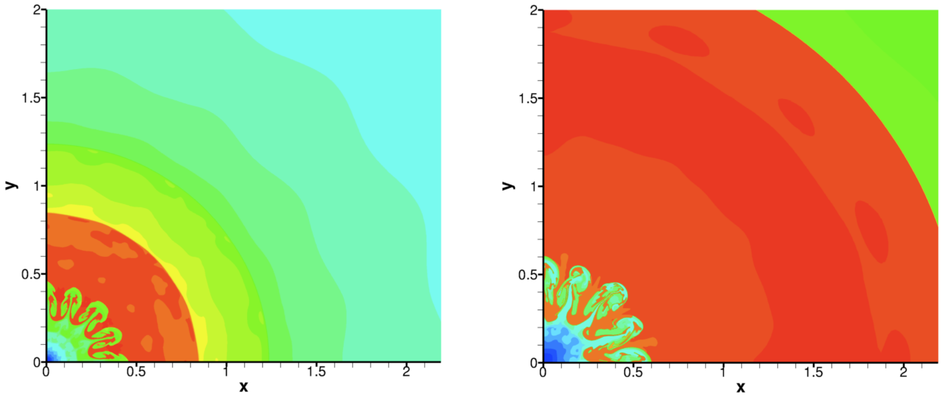

(c) $t = 1.0$ (d) $t = 1.1$

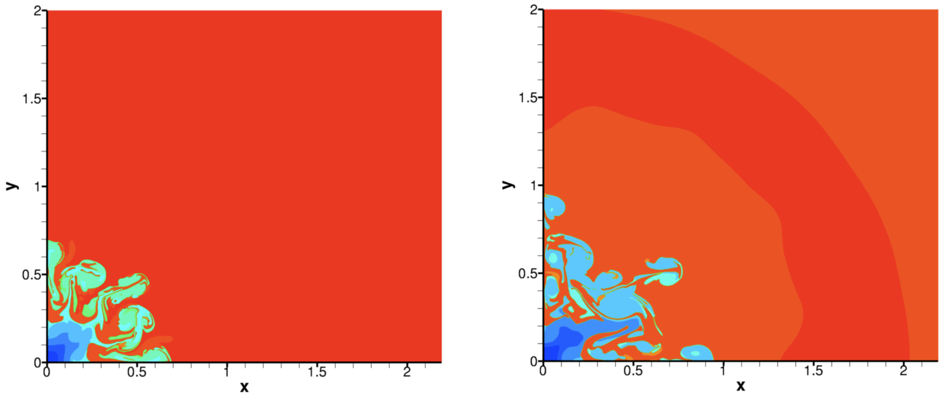

(e) $t = 1.2$ (f) $t = 1.5$

Figure D.4: $C \equiv \frac{\eta_0 n}{R_0} = 0.05$, $n = 16$, $r_i = 100$, $M_s = 1.65$, $\sigma_Y = 0.12\,\mathrm{GPa}$.

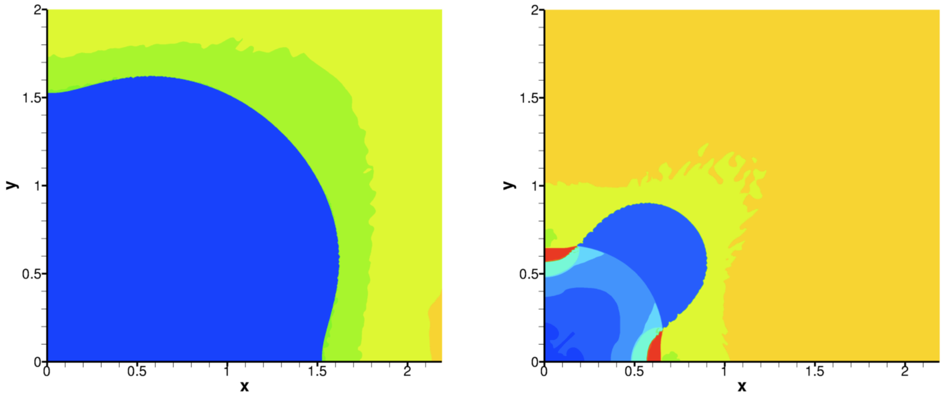

(a) $t = 0.8$

(b) $t = 0.9$

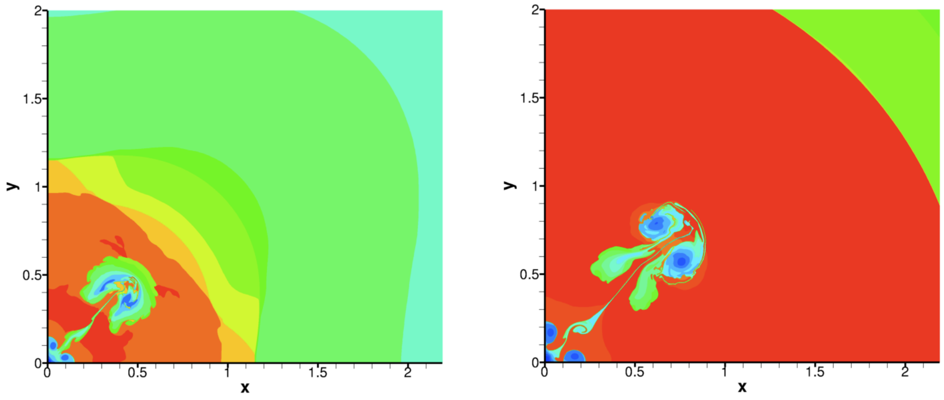

(c) $t = 1.0$

(d) $t = 1.1$

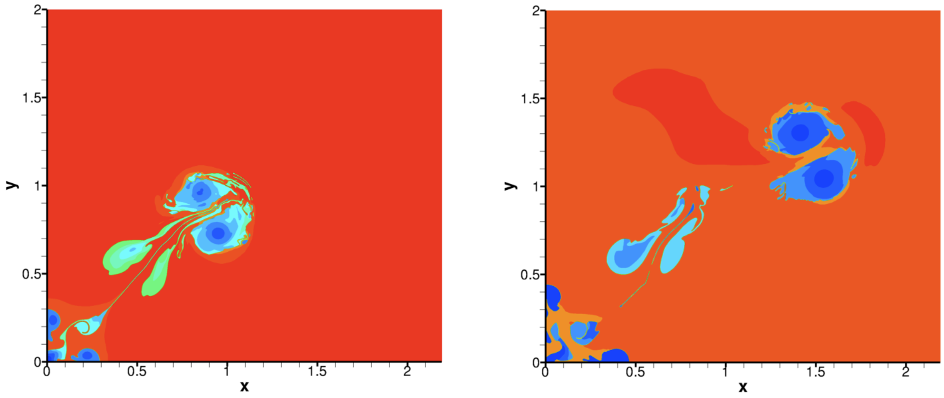

(e) $t = 1.2$

(f) $t = 1.5$

Figure D.5: $C \equiv \frac{\eta_0 n}{R_0} = 0.1$, $n = 4$, $r_i = 100$, $M_s = 1.65$, $\sigma_Y = 0.12\,\text{GPa}$.

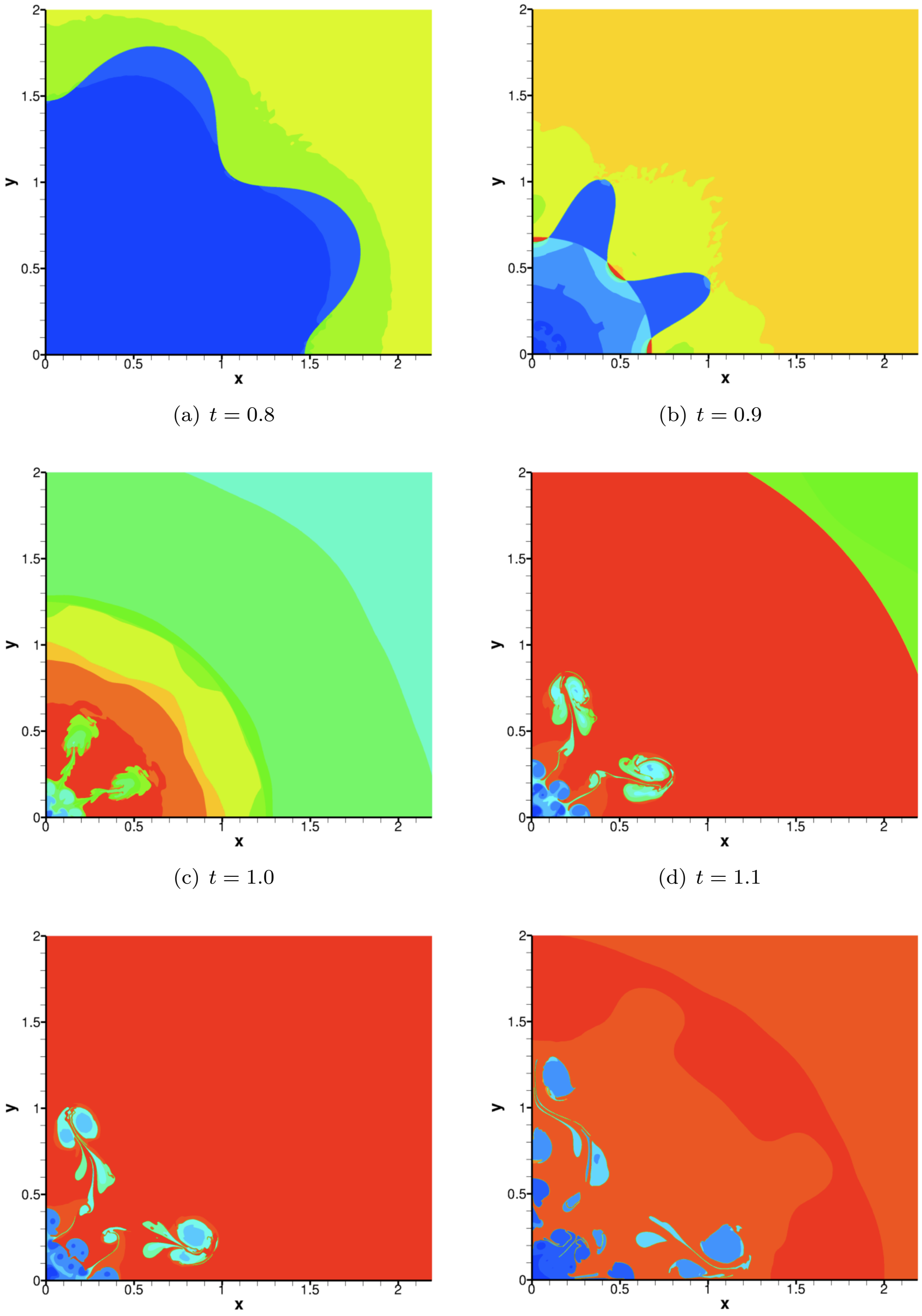

(a) $t = 0.8$

(b) $t = 0.9$

(c) $t = 1.0$

(d) $t = 1.1$

(e) $t = 1.2$

(f) $t = 1.5$

Figure D.6: $C \equiv \frac{\eta_0 n}{R_0} = 0.1$, $n = 8$, $r_i = 100$, $M_s = 1.65$, $\sigma_Y = 0.12\,\text{GPa}$.

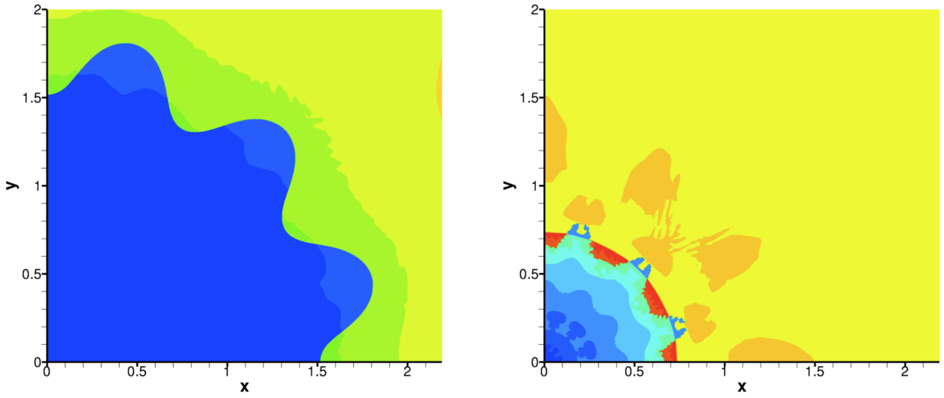

(a) $t = 0.8$ (b) $t = 0.917$

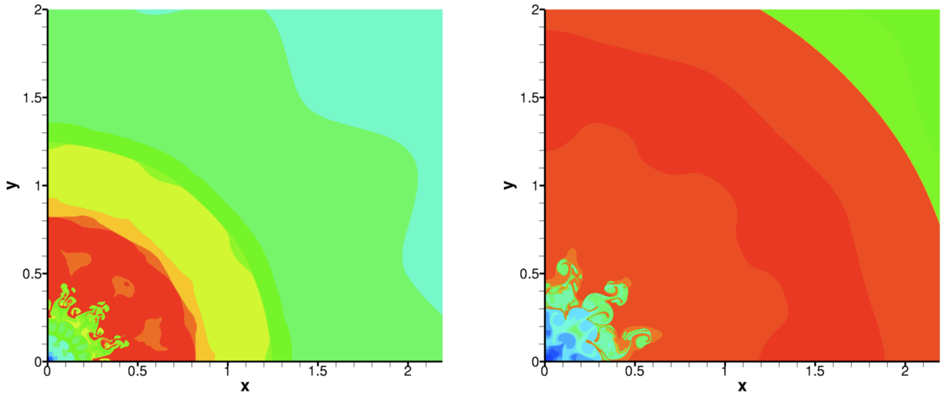

(c) $t = 1.0$ (d) $t = 1.1$

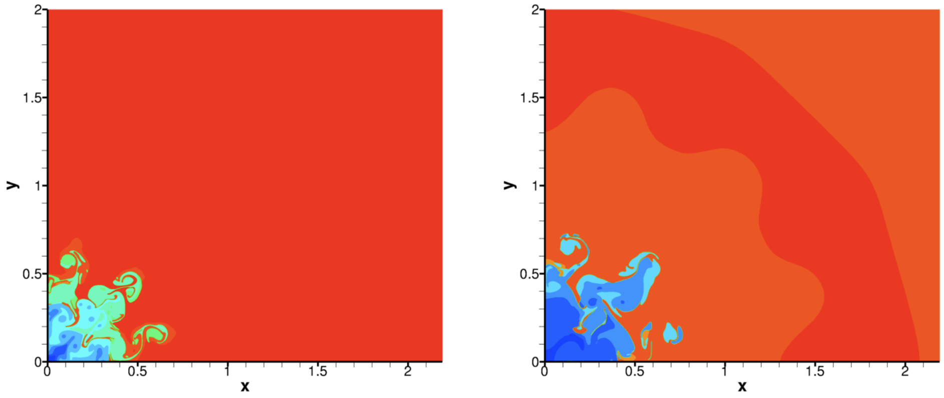

(e) $t = 1.2$ (f) $t = 1.5$

Figure D.7: $C \equiv \frac{\eta_0 n}{R_0} = 0.1$, $n = 12$, $r_i = 100$, $M_s = 1.65$, $\sigma_Y = 0.12\,\text{GPa}$.

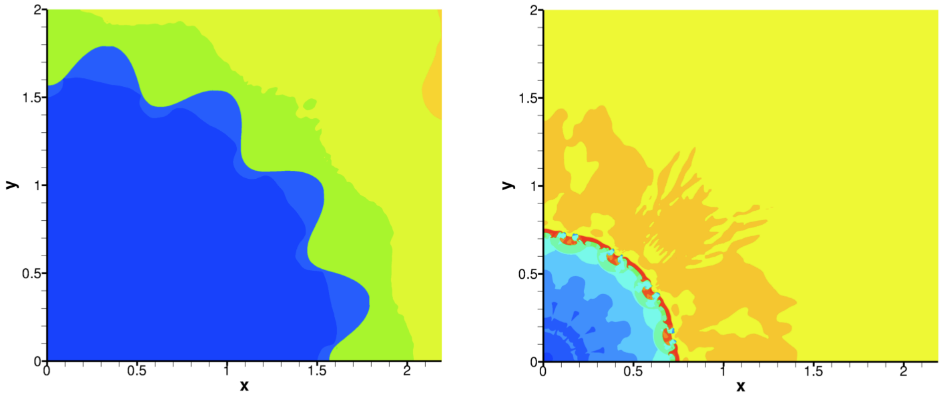

(a) $t = 0.8$ (b) $t = 0.917$

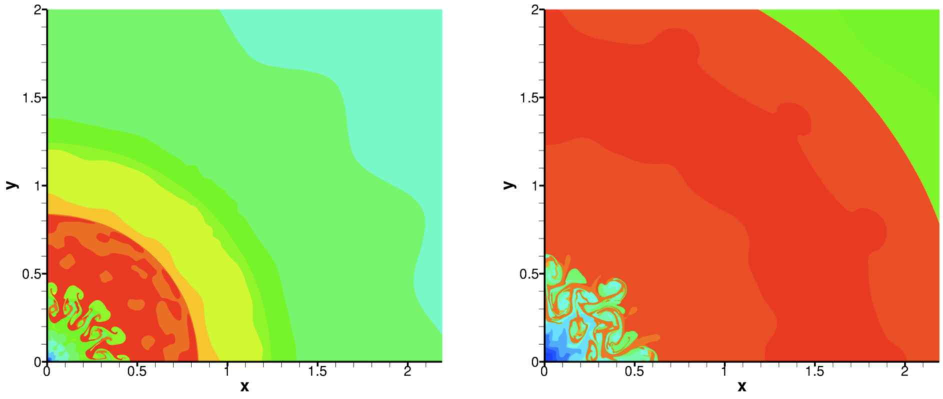

(c) $t = 1.0$ (d) $t = 1.1$

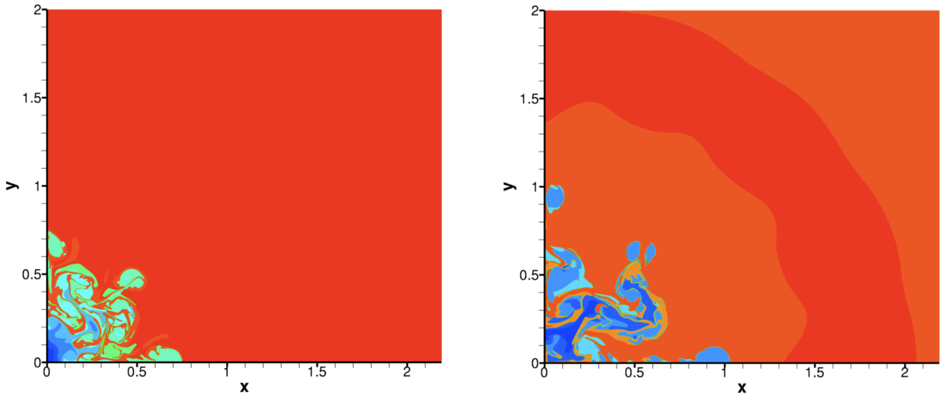

(e) $t = 1.2$ (f) $t = 1.5$

Figure D.8: $C \equiv \frac{\eta_0 n}{R_0} = 0.1$, $n = 16$, $r_i = 100$, $M_s = 1.65$, $\sigma_Y = 0.12\,\mathrm{GPa}$.

D.2 Influence of the density ratio

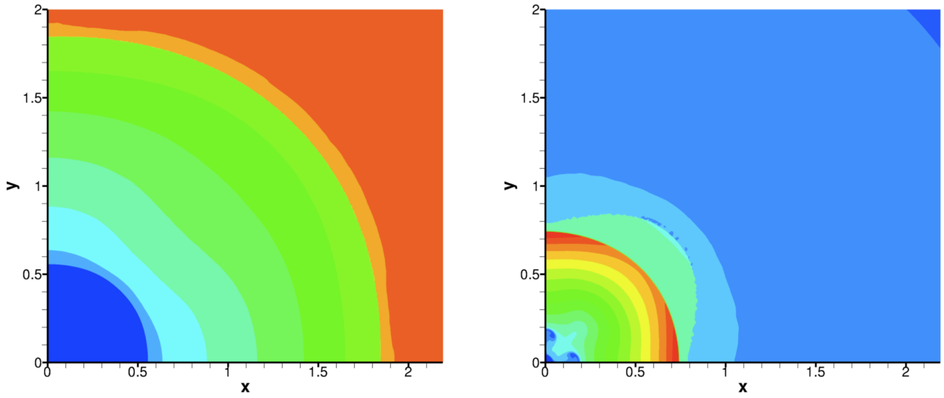

(a) $t = 0.85$ (b) $t = 1.0$

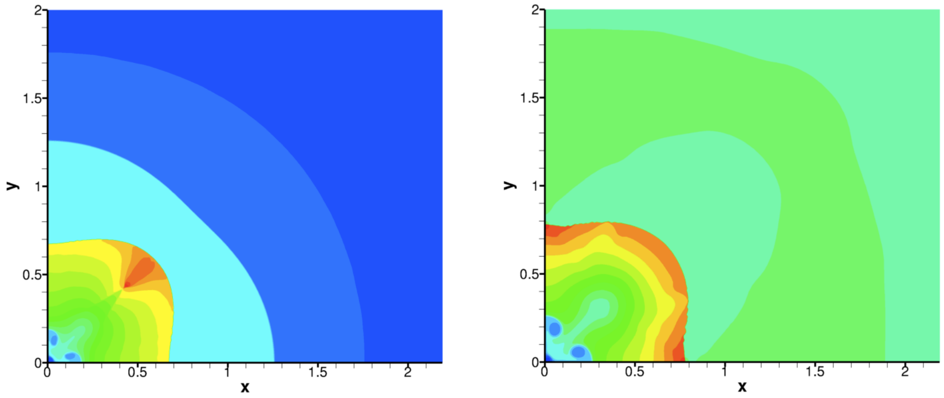

(c) $t = 1.05$ (d) $t = 1.2$

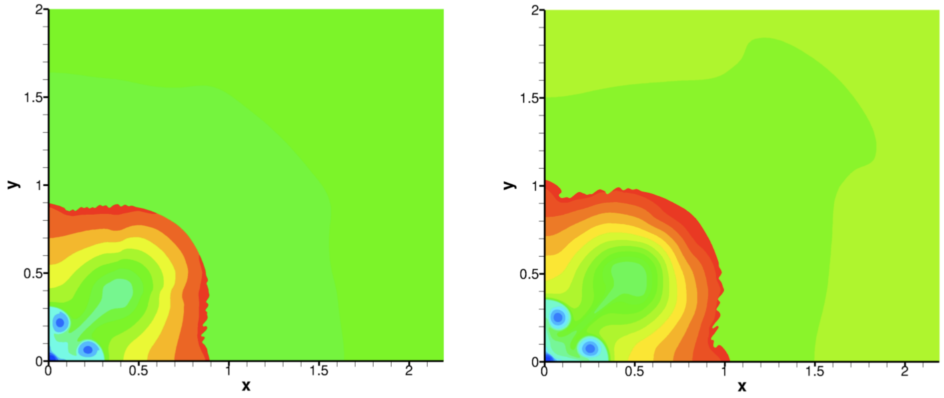

(e) $t = 1.3$ (f) $t = 1.5$

Figure D.9: $C \equiv \frac{\eta_0 n}{R_0} = 0.05$, $n = 4$, $r_i = 10$, $M_s = 1.65$, $\sigma_Y = 0.12\,\mathrm{GPa}$.

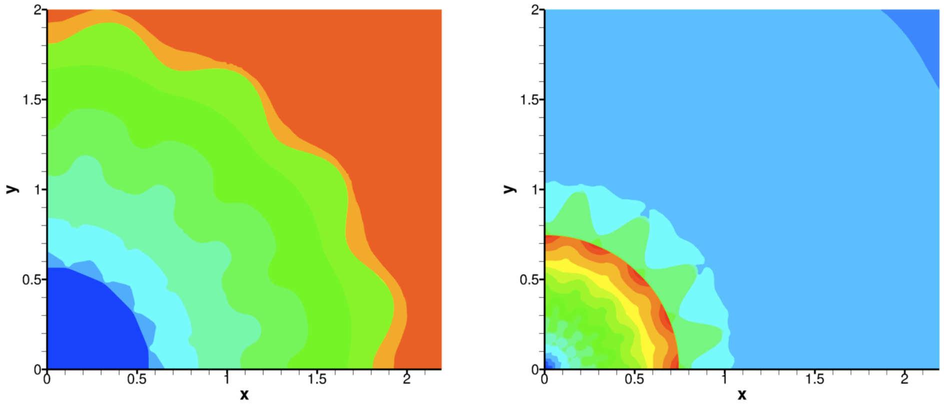

(a) $t = 0.85$ (b) $t = 1.0$

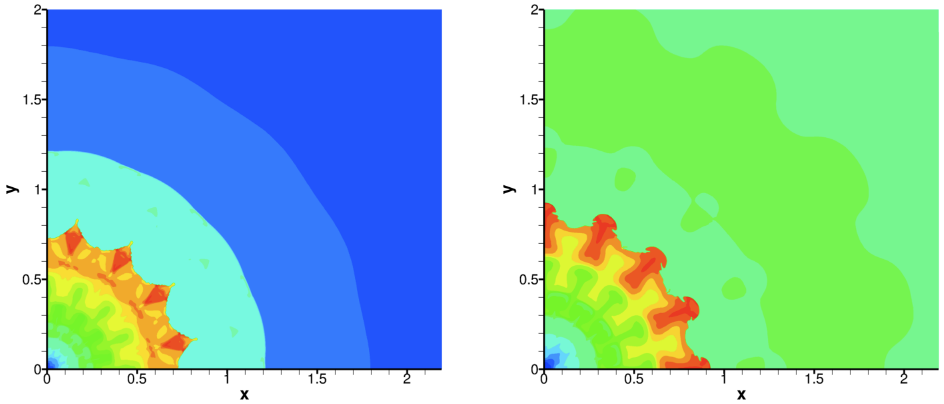

(c) $t = 1.05$ (d) $t = 1.2$

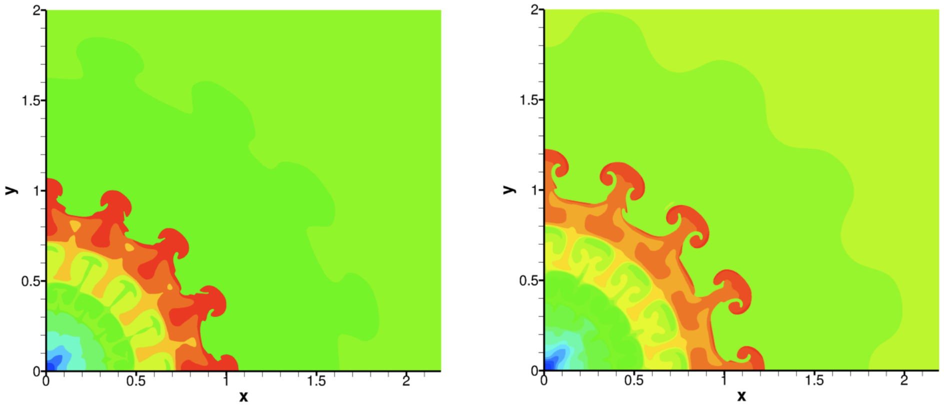

(e) $t = 1.3$ (f) $t = 1.5$

Figure D.10: $C \equiv \frac{\eta_0 n}{R_0} = 0.05$, $n = 16$, $r_i = 10$, $M_s = 1.65$, $\sigma_Y = 0.12\,\text{GPa}$.

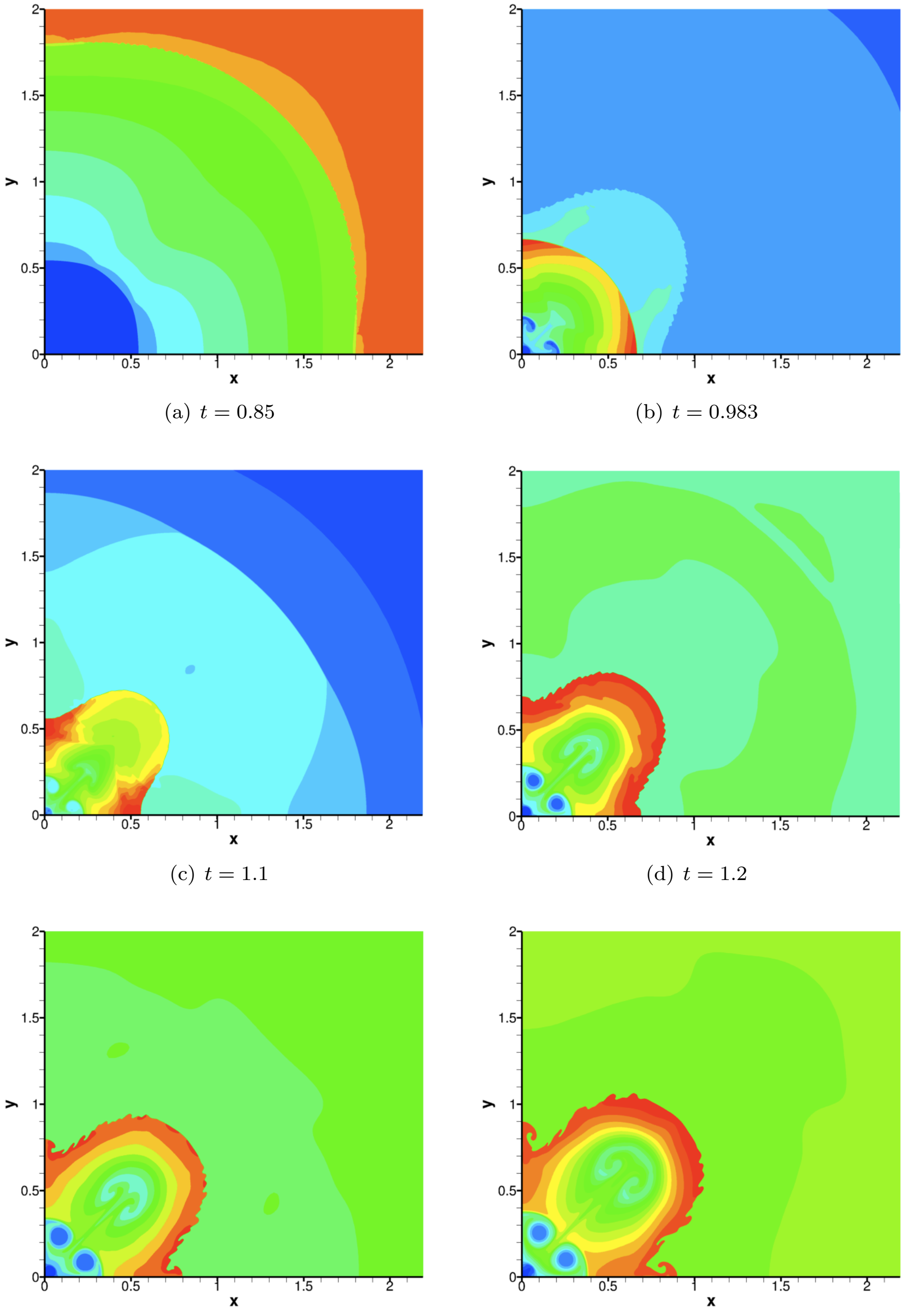

(a) $t = 0.85$

(b) $t = 0.983$

(c) $t = 1.1$

(d) $t = 1.2$

(e) $t = 1.3$

(f) $t = 1.5$

Figure D.11: $C \equiv \frac{\eta_0 n}{R_0} = 0.1$, $n = 4$, $r_i = 10$, $M_s = 1.65$, $\sigma_Y = 0.12\,\mathrm{GPa}$.

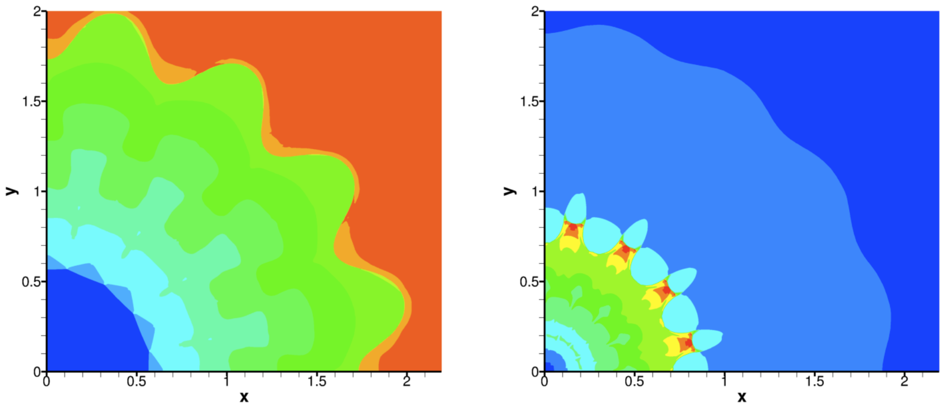

(a) $t = 0.85$ (b) $t = 1.017$

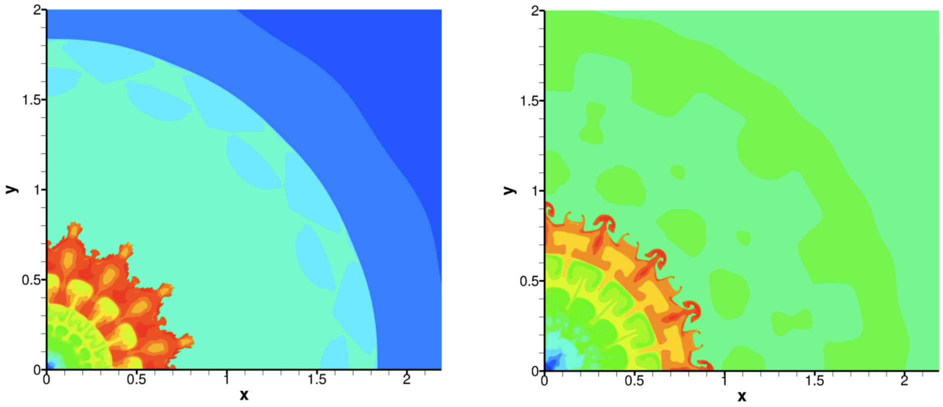

(c) $t = 1.1$ (d) $t = 1.2$

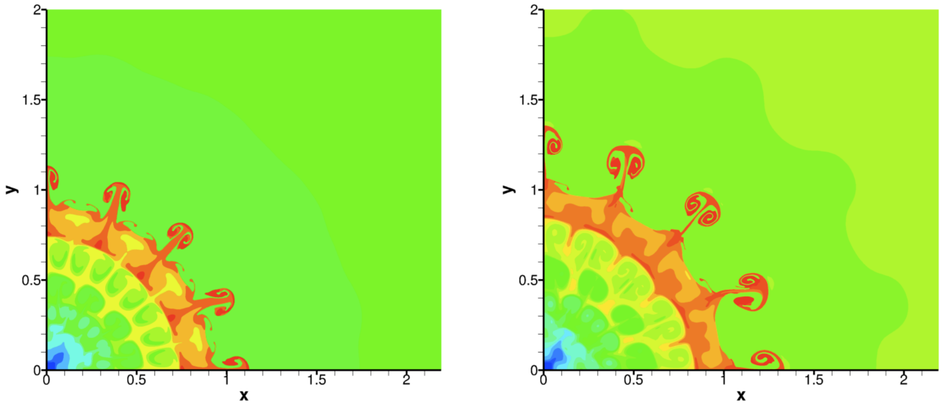

(e) $t = 1.3$ (f) $t = 1.5$

Figure D.12: $C \equiv \frac{\eta_0 n}{R_0} = 0.1$, $n = 16$, $r_i = 10$, $M_s = 1.65$, $\sigma_Y = 0.12\,\text{GPa}$.

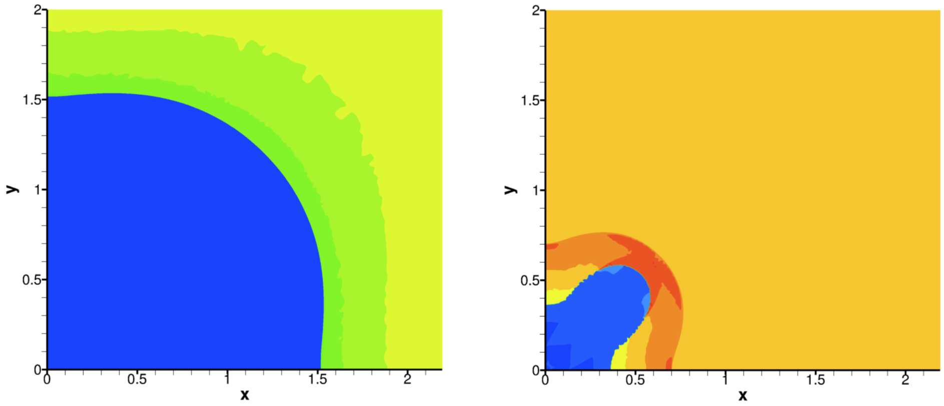

(a) $t = 0.8$ (b) $t = 0.917$

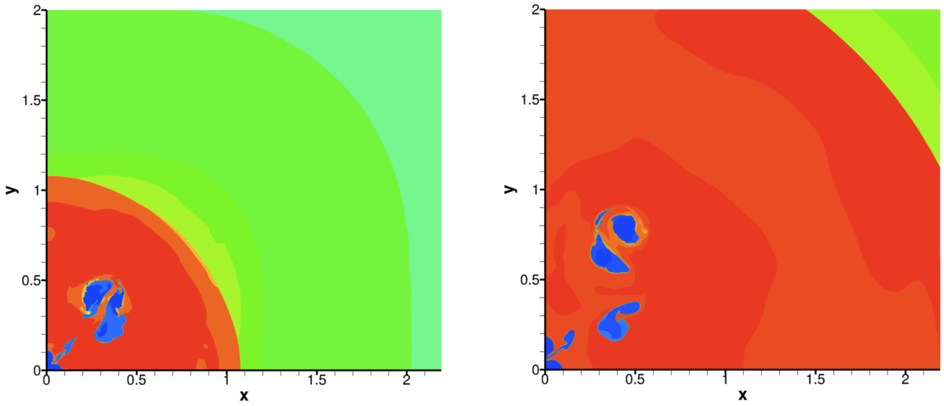

(c) $t = 1.0$ (d) $t = 1.1$

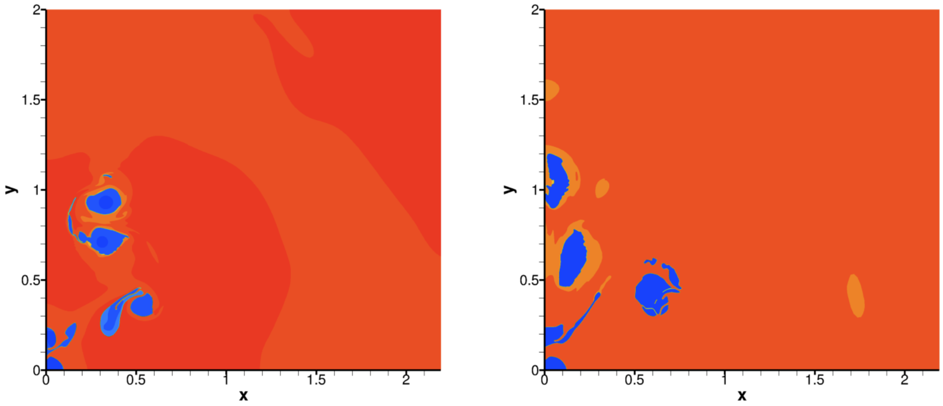

(e) $t = 1.2$ (f) $t = 1.5$

Figure D.13: $C \equiv \frac{\eta_0 n}{R_0} = 0.05$, $n = 4$, $r_i = 500$, $M_s = 1.65$, $\sigma_Y = 0.12\,\text{GPa}$.

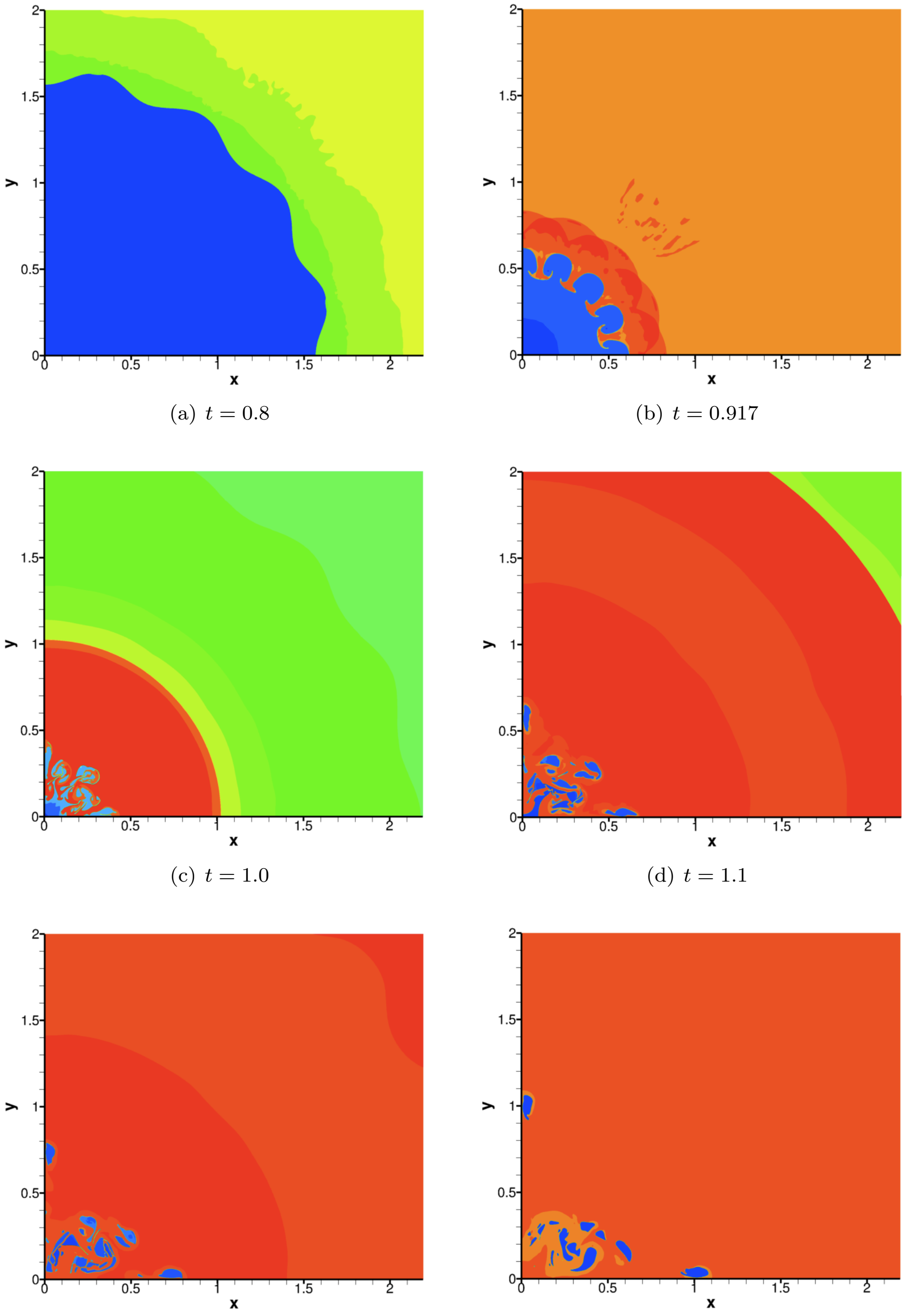

(a) $t = 0.8$

(b) $t = 0.917$

(c) $t = 1.0$

(d) $t = 1.1$

(e) $t = 1.2$

(f) $t = 1.5$

Figure D.14: $C \equiv \frac{\eta_0 n}{R_0} = 0.05$, $n = 16$, $r_i = 500$, $M_s = 1.65$, $\sigma_Y = 0.12\,\text{GPa}$.

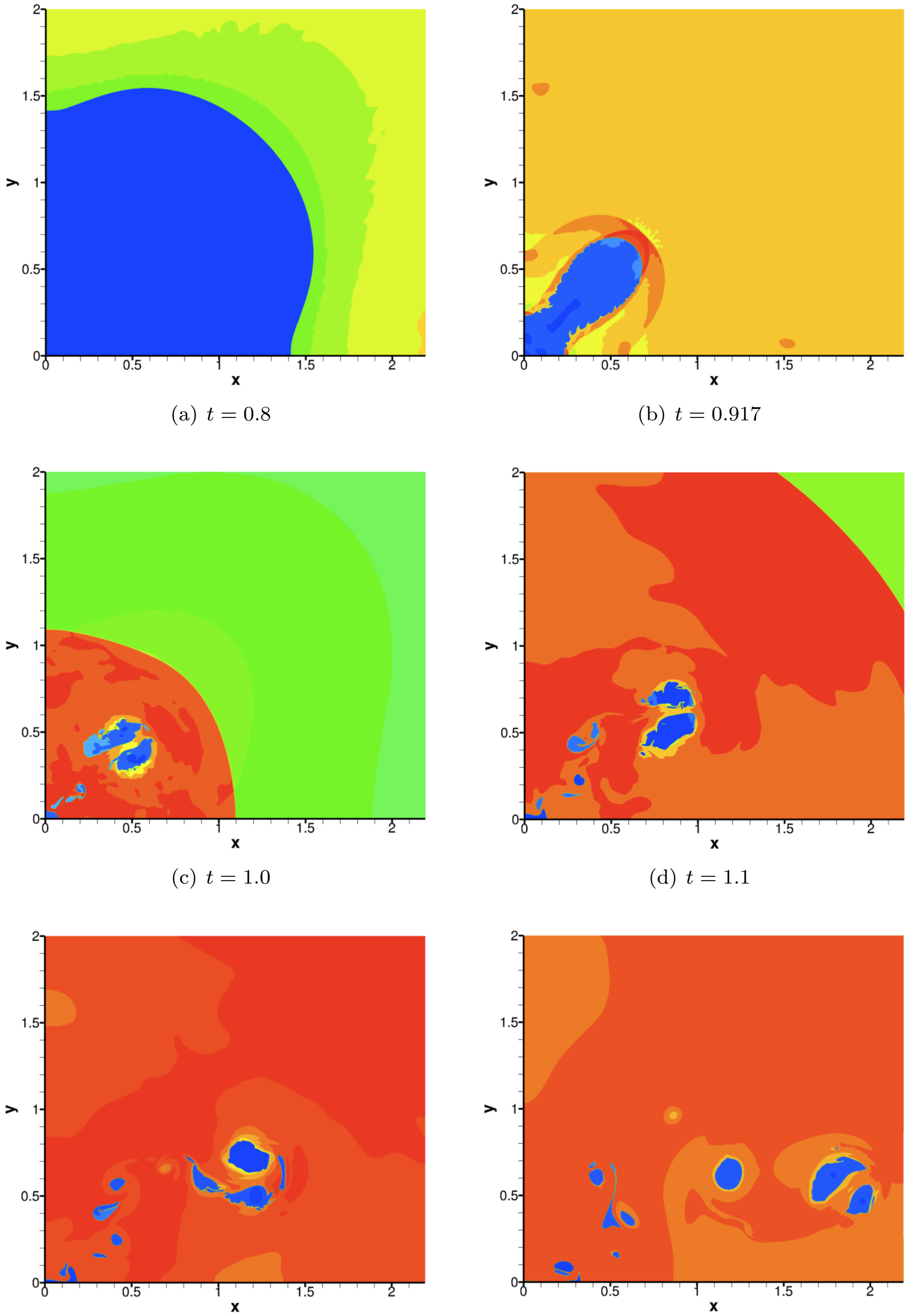

(a) $t = 0.8$

(b) $t = 0.917$

(c) $t = 1.0$

(d) $t = 1.1$

(e) $t = 1.2$

(f) $t = 1.5$

Figure D.15: $C \equiv \frac{\eta_0 n}{R_0} = 0.1$, $n = 4$, $r_i = 500$, $M_s = 1.65$, $\sigma_Y = 0.12\,\mathrm{GPa}$.

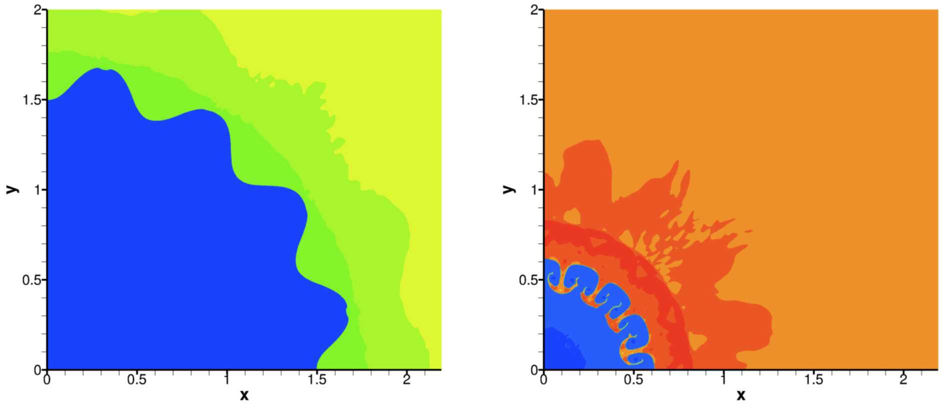

(a) $t = 0.8$ (b) $t = 0.917$

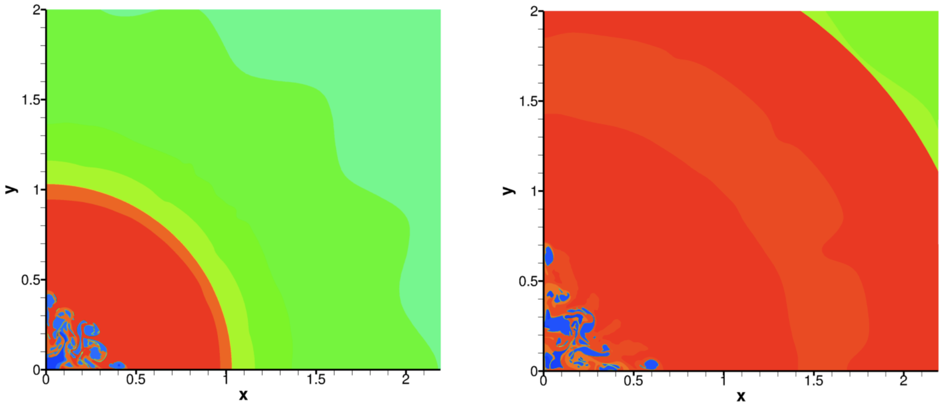

(c) $t = 1.0$ (d) $t = 1.1$

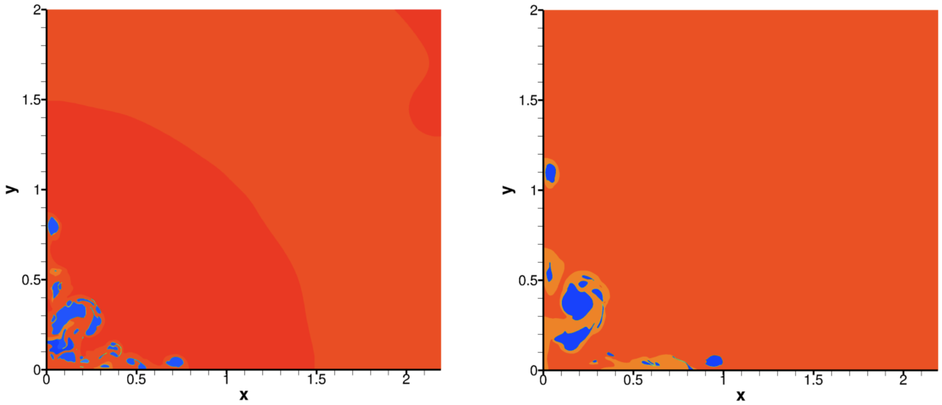

(e) $t = 1.2$ (f) $t = 1.5$

Figure D.16: $C \equiv \frac{\eta_0 n}{R_0} = 0.1$, $n = 16$, $r_i = 500$, $M_s = 1.65$, $\sigma_Y = 0.12\,\mathrm{GPa}$.

D.3 Influence of the initial shock Mach number

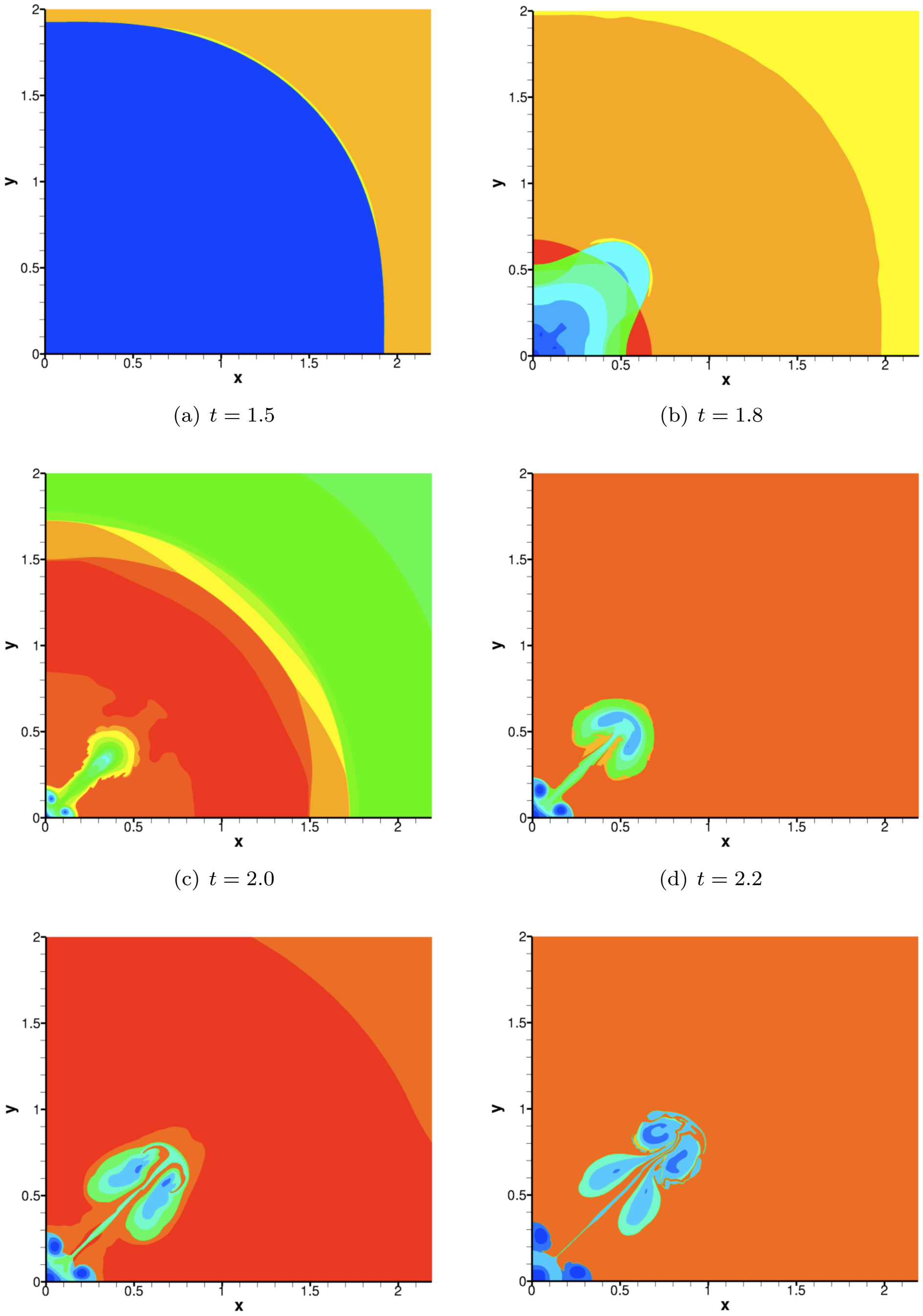

(a) $t = 1.5$

(b) $t = 1.8$

(c) $t = 2.0$

(d) $t = 2.2$

(e) $t = 2.5$

(f) $t = 3.0$

Figure D.17: $C \equiv \frac{\eta_0 n}{R_0} = 0.05$, $n = 4$, $r_i = 100$, $M_s = 1.16$, $\sigma_Y = 0.12\,\text{GPa}$.

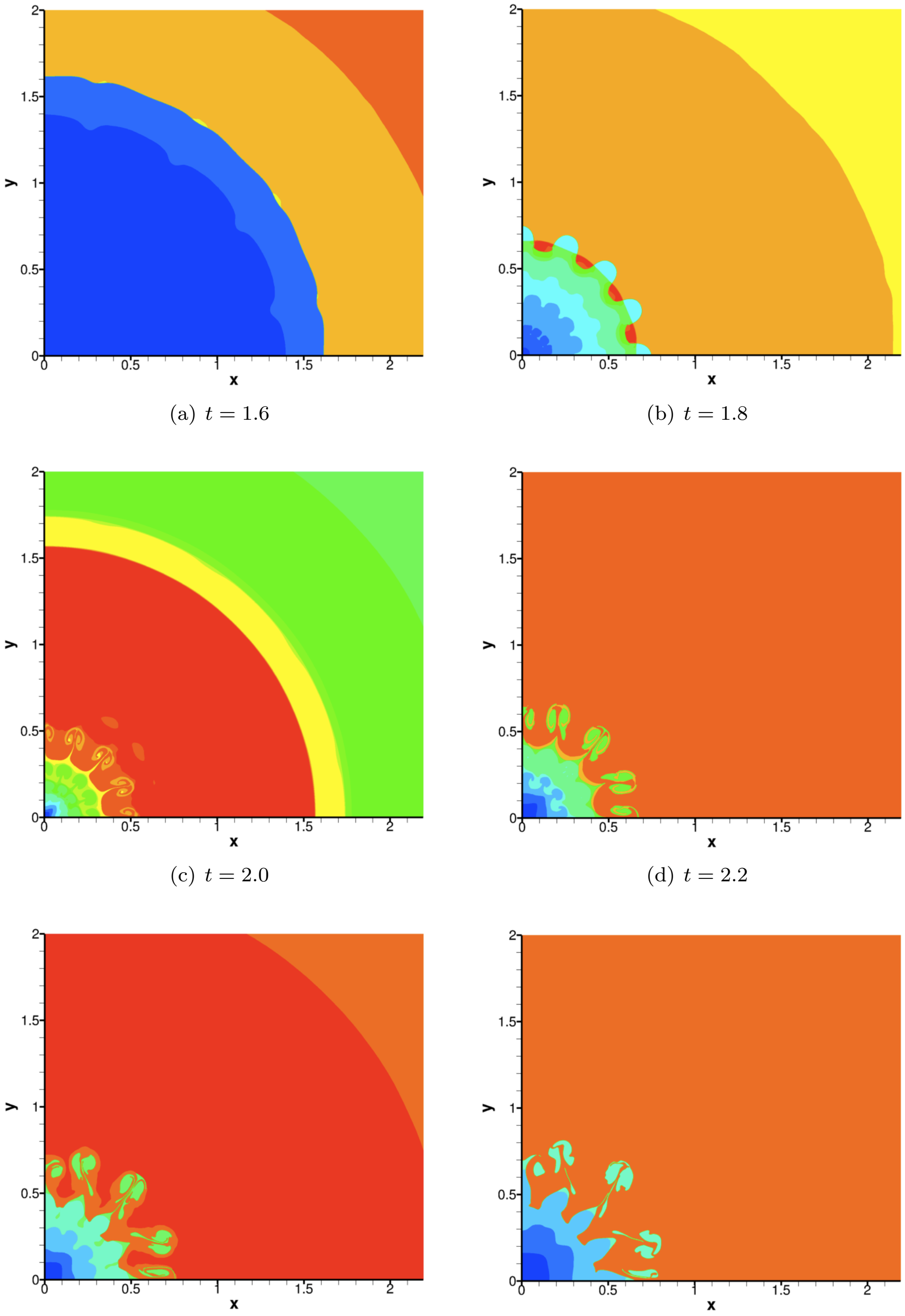

(a) $t = 1.6$

(b) $t = 1.8$

(c) $t = 2.0$

(d) $t = 2.2$

(e) $t = 2.5$

(f) $t = 3.0$

Figure D.18: $C \equiv \frac{\eta_0 n}{R_0} = 0.05$, $n = 16$, $r_i = 100$, $M_s = 1.16$, $\sigma_Y = 0.12\,\text{GPa}$.

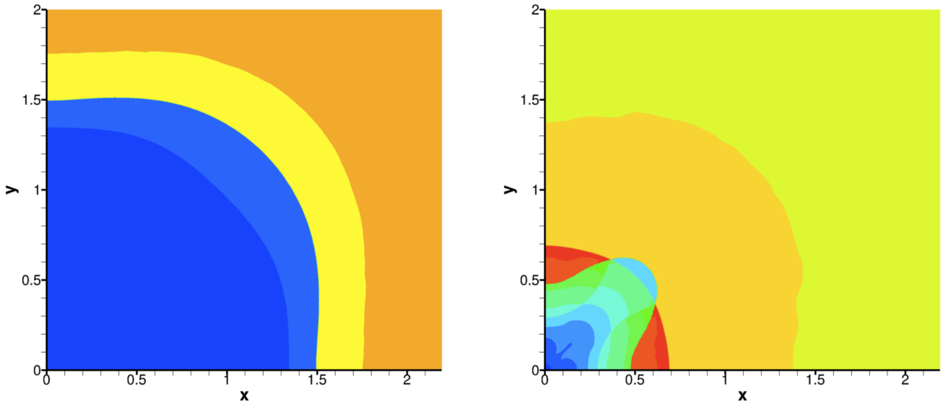

(a) $t = 1.2$ (b) $t = 1.36$

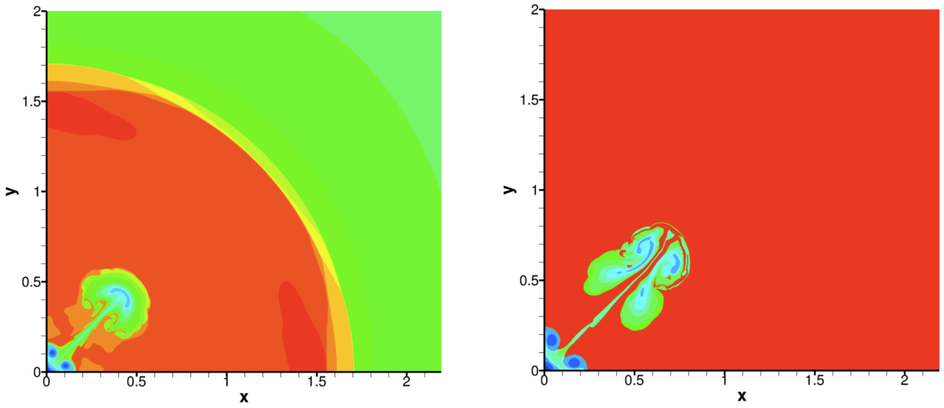

(c) $t = 1.52$ (d) $t = 1.76$

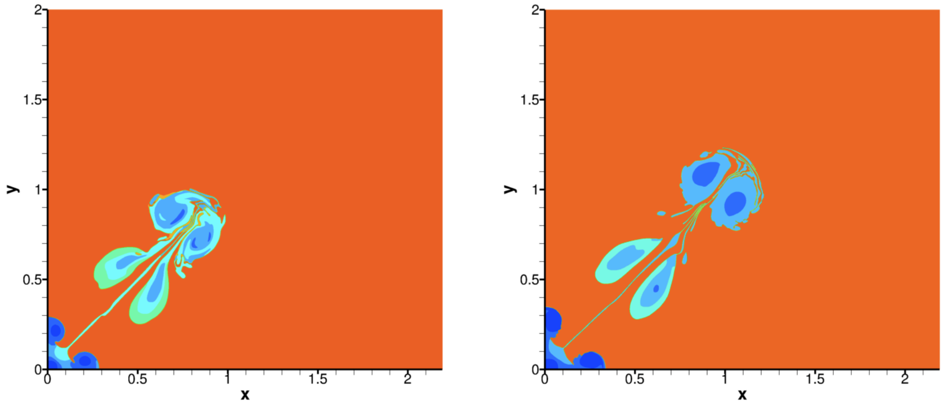

(e) $t = 2.0$ (f) $t = 2.4$

Figure D.19: $C \equiv \frac{\eta_0 n}{R_0} = 0.05$, $n = 4$, $r_i = 100$, $M_s = 1.31$, $\sigma_Y = 0.12\,\text{GPa}$.

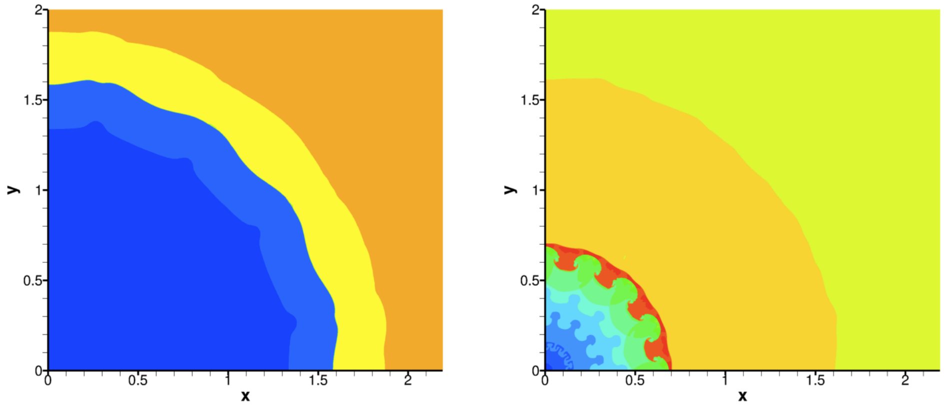

(a) $t = 1.2$ (b) $t = 1.36$

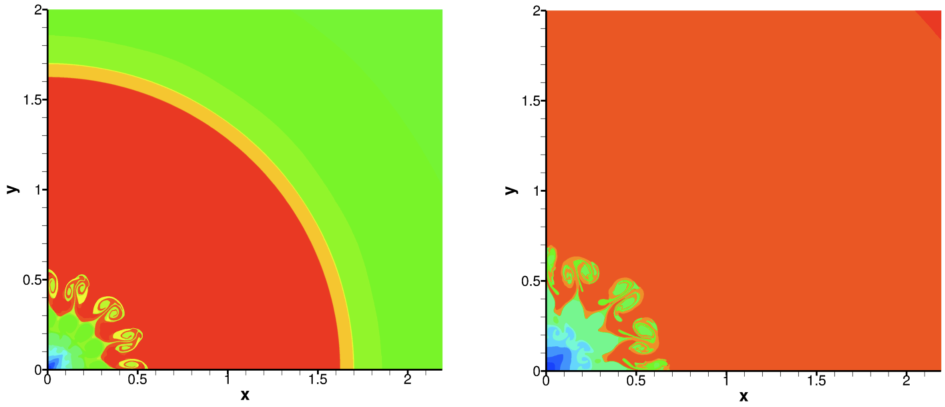

(c) $t = 1.52$ (d) $t = 1.68$

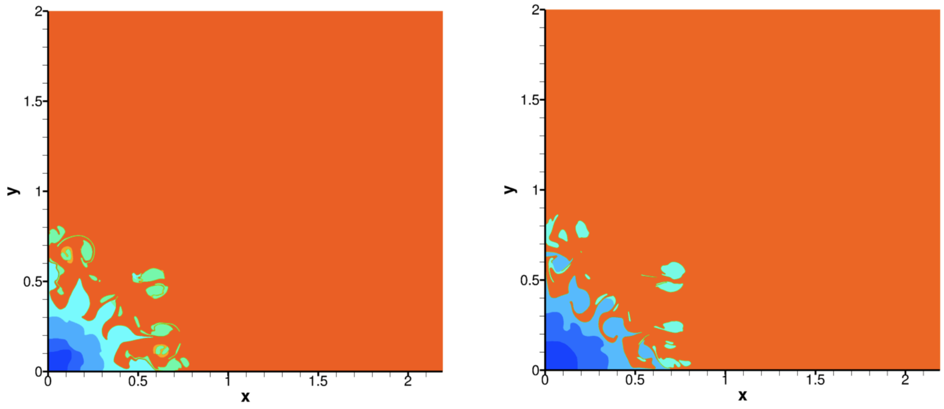

(e) $t = 2.0$ (f) $t = 2.4$

Figure D.20: $C \equiv \frac{\eta_0 n}{R_0} = 0.05$, $n = 16$, $r_i = 100$, $M_s = 1.31$, $\sigma_Y = 0.12\,\text{GPa}$.

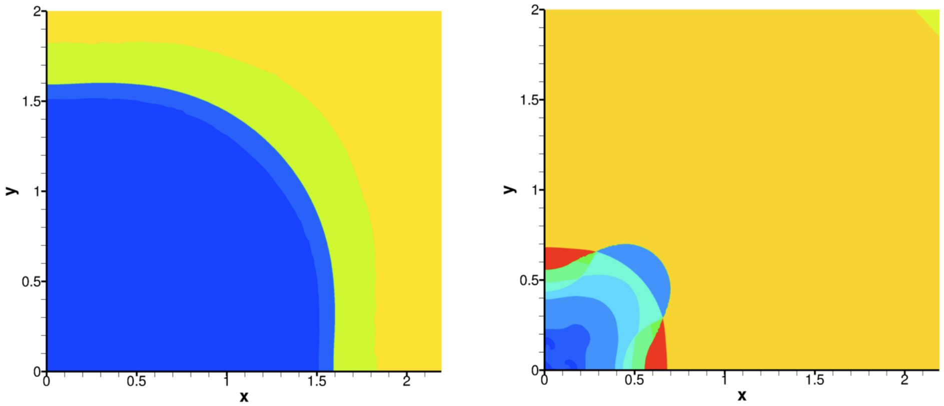

(a) $t = 0.956$ (b) $t = 1.089$

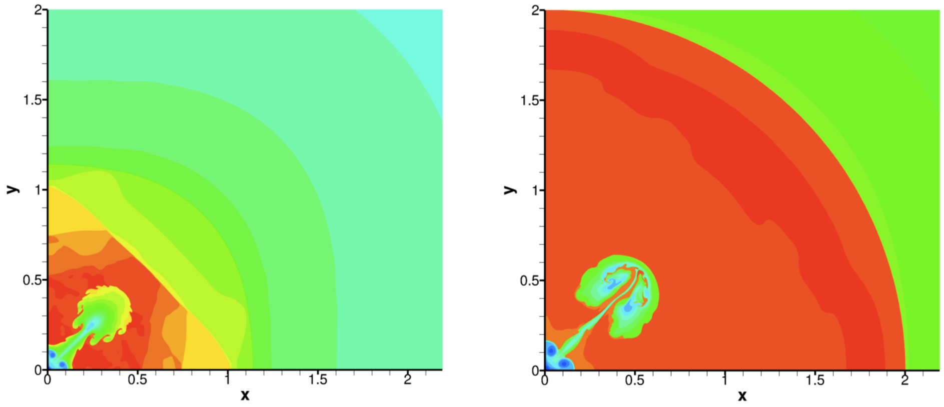

(c) $t = 1.178$ (d) $t = 1.267$

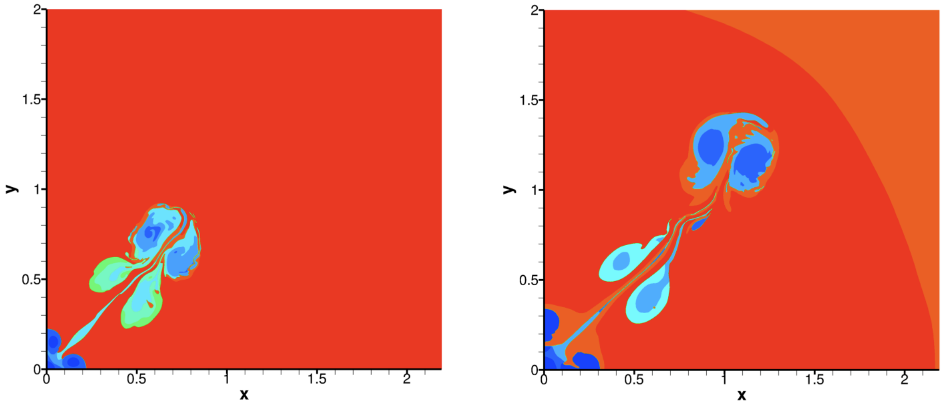

(e) $t = 1.444$ (f) $t = 2.0$

Figure D.21: $C \equiv \frac{\eta_0 n}{R_0} = 0.05$, $n = 4$, $r_i = 100$, $M_s = 1.48$, $\sigma_Y = 0.12\,\mathrm{GPa}$.

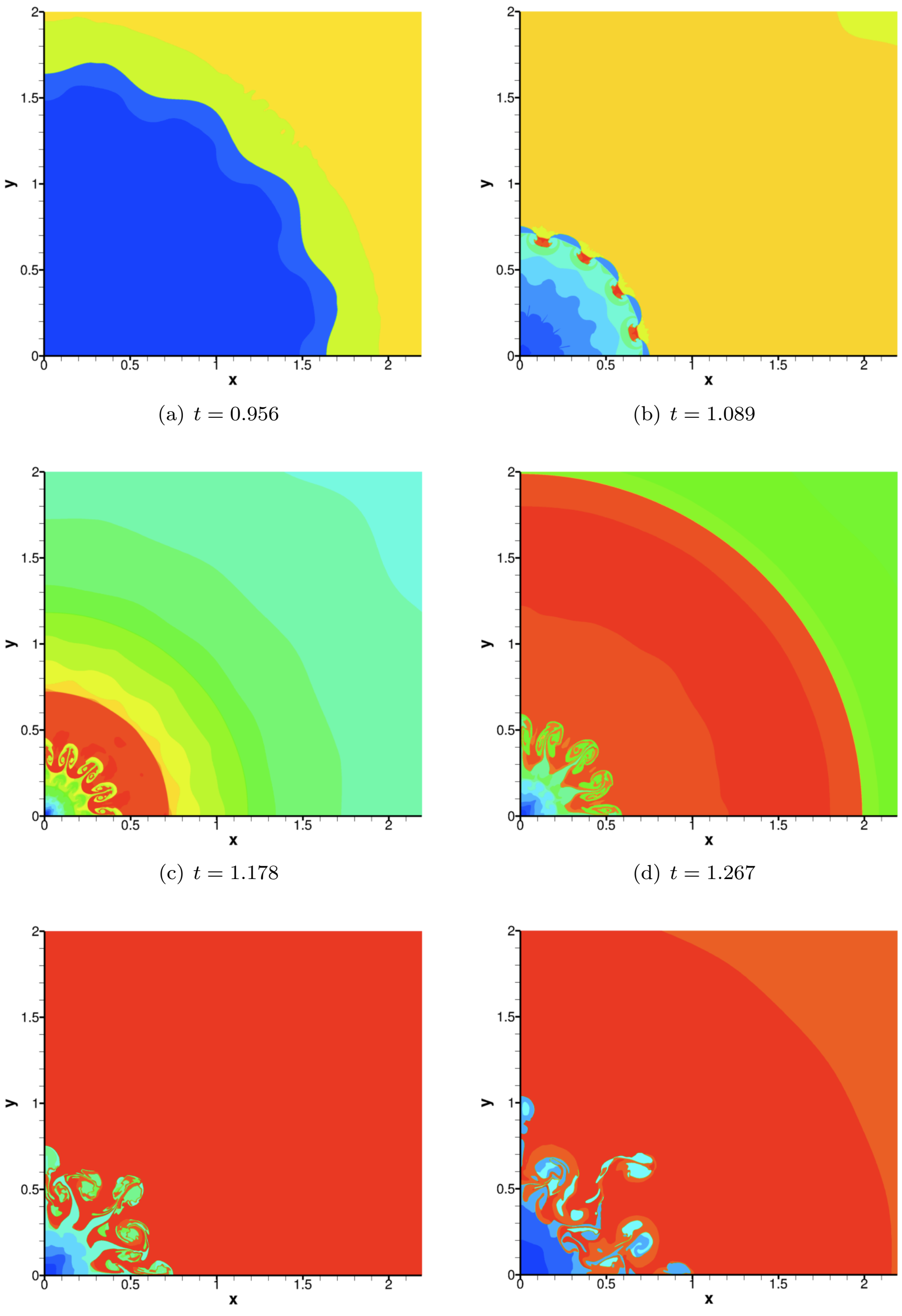

(a) $t = 0.956$

(b) $t = 1.089$

(c) $t = 1.178$

(d) $t = 1.267$

(e) $t = 1.444$

(f) $t = 2.0$

Figure D.22: $C \equiv \frac{\eta_0 n}{R_0} = 0.05$, $n = 16$, $r_i = 100$, $M_s = 1.48$, $\sigma_Y = 0.12\,\mathrm{GPa}$.

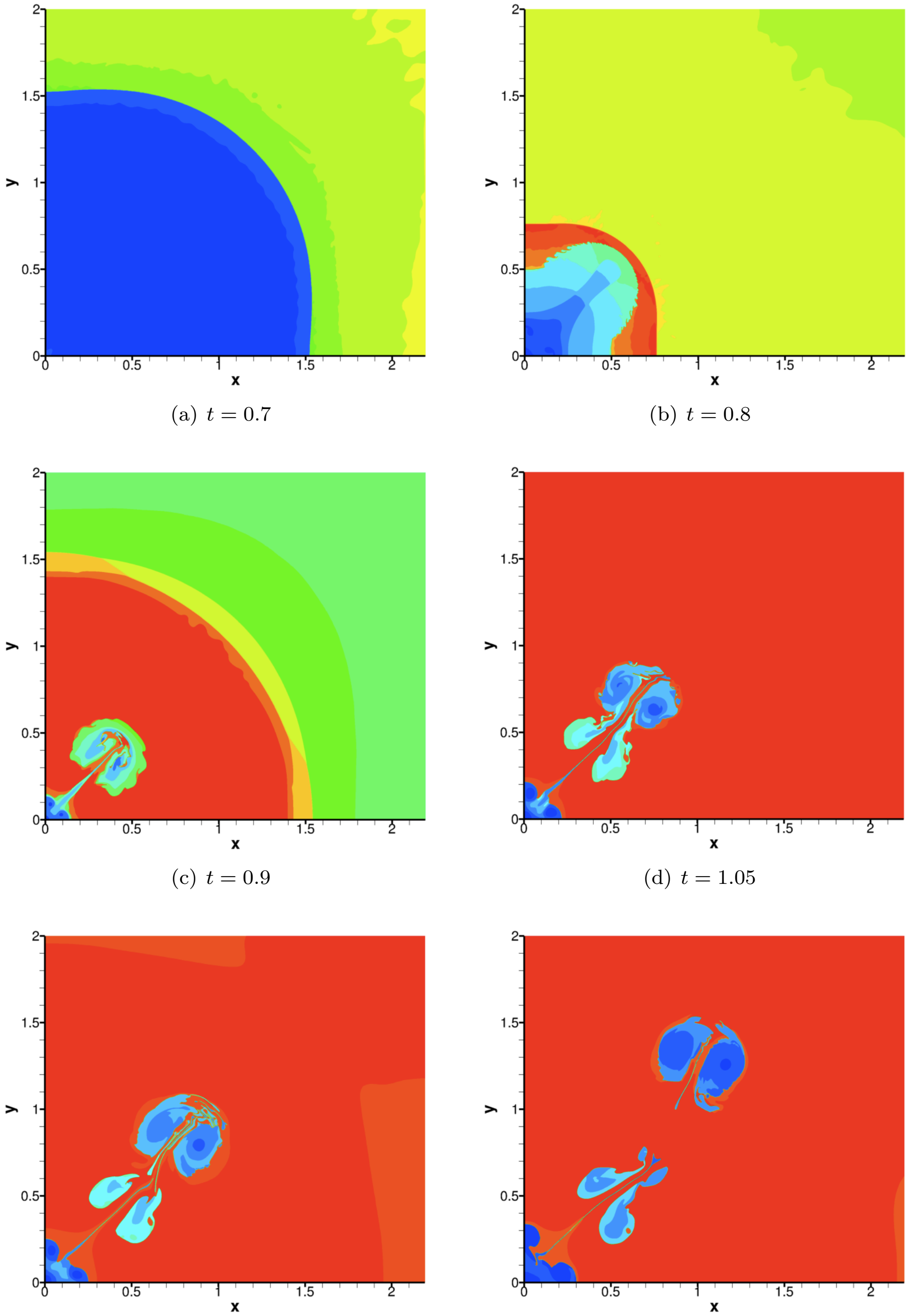

(a) $t = 0.7$

(b) $t = 0.8$

(c) $t = 0.9$

(d) $t = 1.05$

(e) $t = 1.15$

(f) $t = 1.5$

Figure D.23: $C \equiv \frac{\eta_0 n}{R_0} = 0.05$, $n = 4$, $r_i = 100$, $M_s = 1.83$, $\sigma_Y = 0.12\,\mathrm{GPa}$.

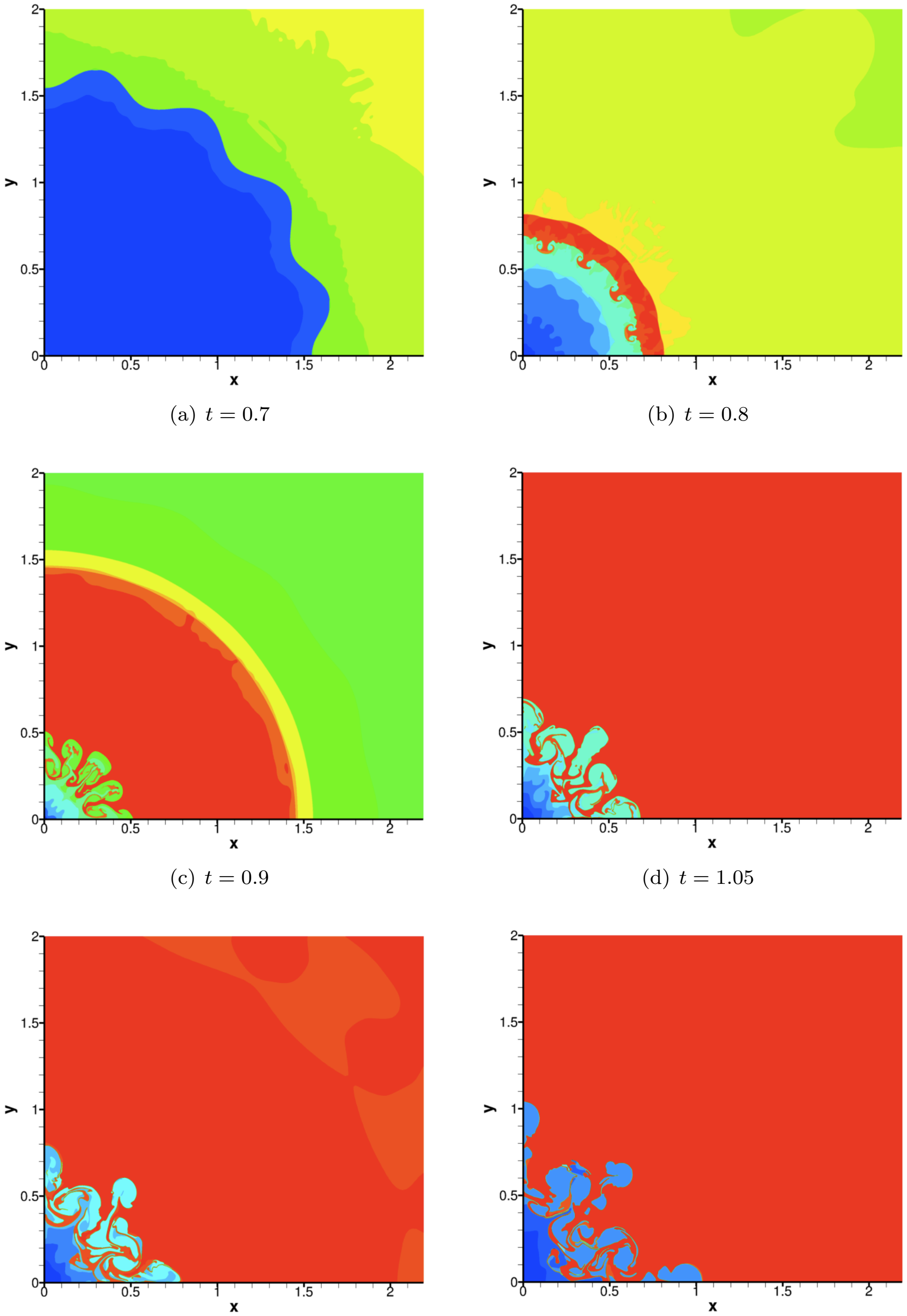

(a) $t = 0.7$

(b) $t = 0.8$

(c) $t = 0.9$

(d) $t = 1.05$

(e) $t = 1.15$

(f) $t = 1.5$

Figure D.24: $C \equiv \frac{\eta_0 n}{R_0} = 0.05$, $n = 16$, $r_i = 100$, $M_s = 1.83$, $\sigma_Y = 0.12\,\text{GPa}$.

D.4 Influence of the yield stress

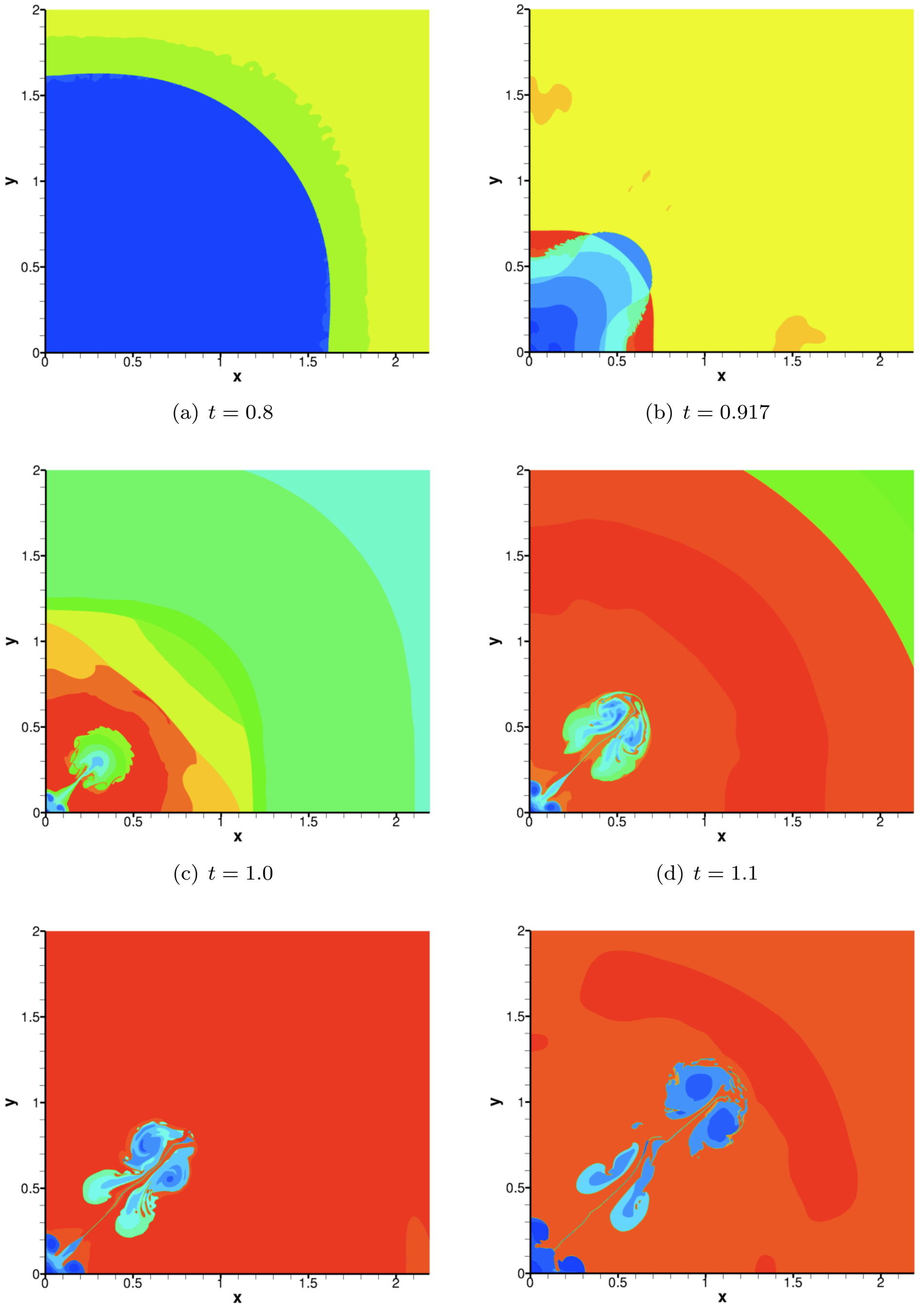

(a) $t = 0.8$

(b) $t = 0.917$

(c) $t = 1.0$

(d) $t = 1.1$

(e) $t = 1.2$

(f) $t = 1.5$

Figure D.25: $C \equiv \frac{\eta_0 n}{R_0} = 0.05$, $n = 4$, $r_i = 100$, $M_s = 1.65$, $\sigma_Y = 0\,\mathrm{GPa}$.

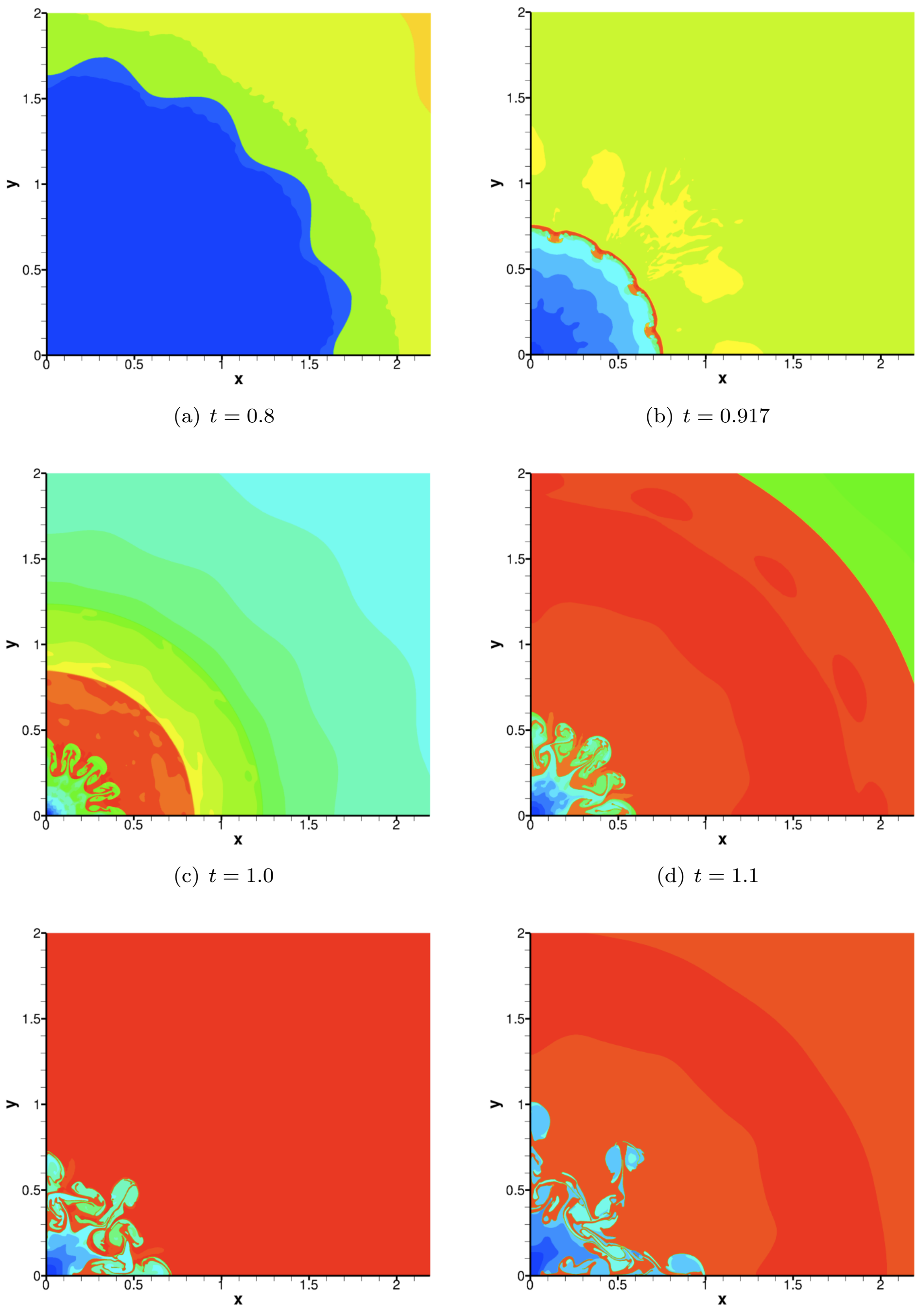

(a) $t = 0.8$

(b) $t = 0.917$

(c) $t = 1.0$

(d) $t = 1.1$

(e) $t = 1.2$

(f) $t = 1.5$

Figure D.26: $C \equiv \frac{\eta_0 n}{R_0} = 0.05$, $n = 16$, $r_i = 100$, $M_s = 1.65$, $\sigma_Y = 0\,\text{GPa}$.

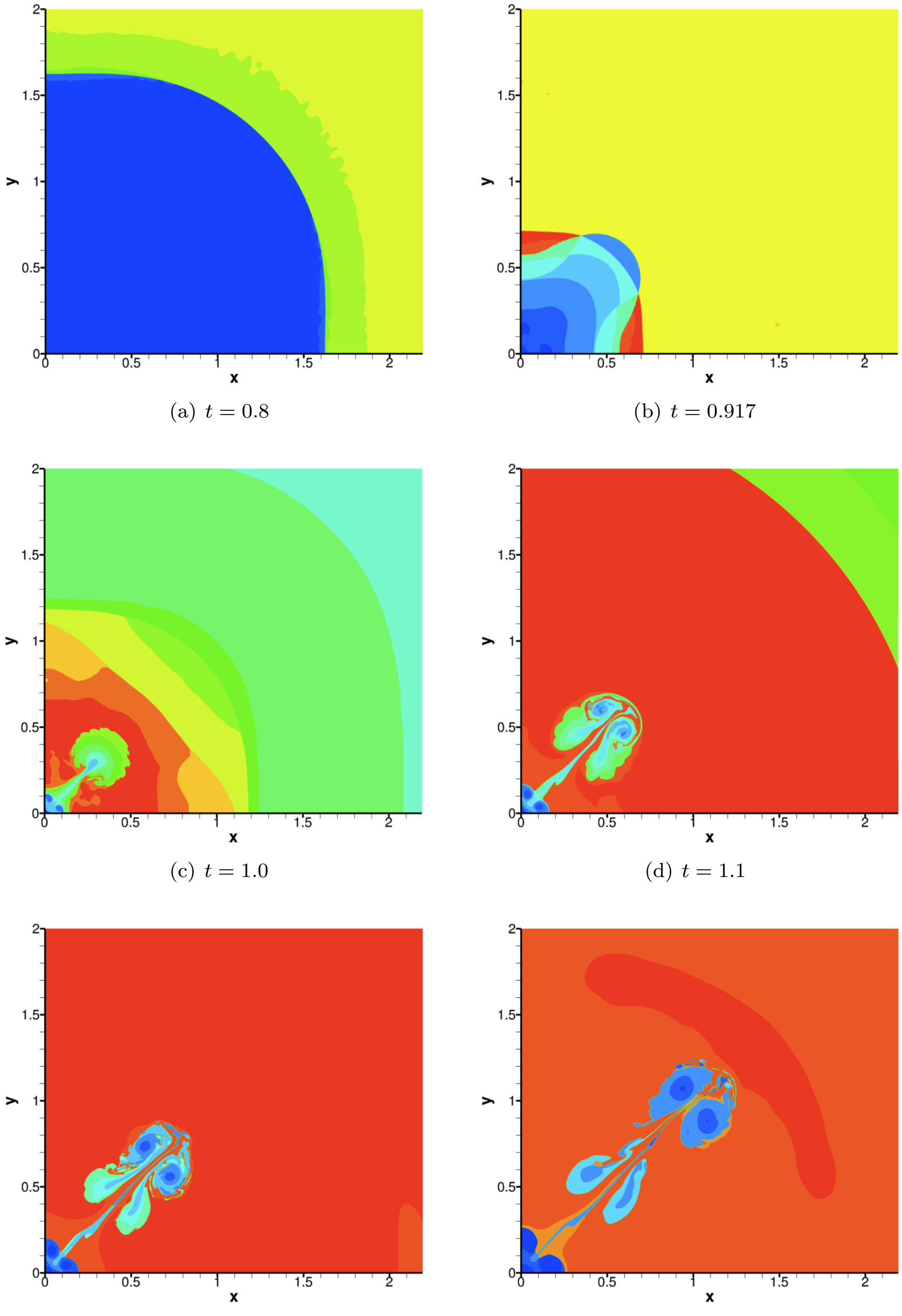

(a) $t = 0.8$

(b) $t = 0.917$

(c) $t = 1.0$

(d) $t = 1.1$

(e) $t = 1.2$

(f) $t = 1.5$

Figure D.27: $C \equiv \frac{\eta_0 n}{R_0} = 0.05$, $n = 4$, $r_i = 100$, $M_s = 1.65$, $\sigma_Y = 0.5\,\text{GPa}$.

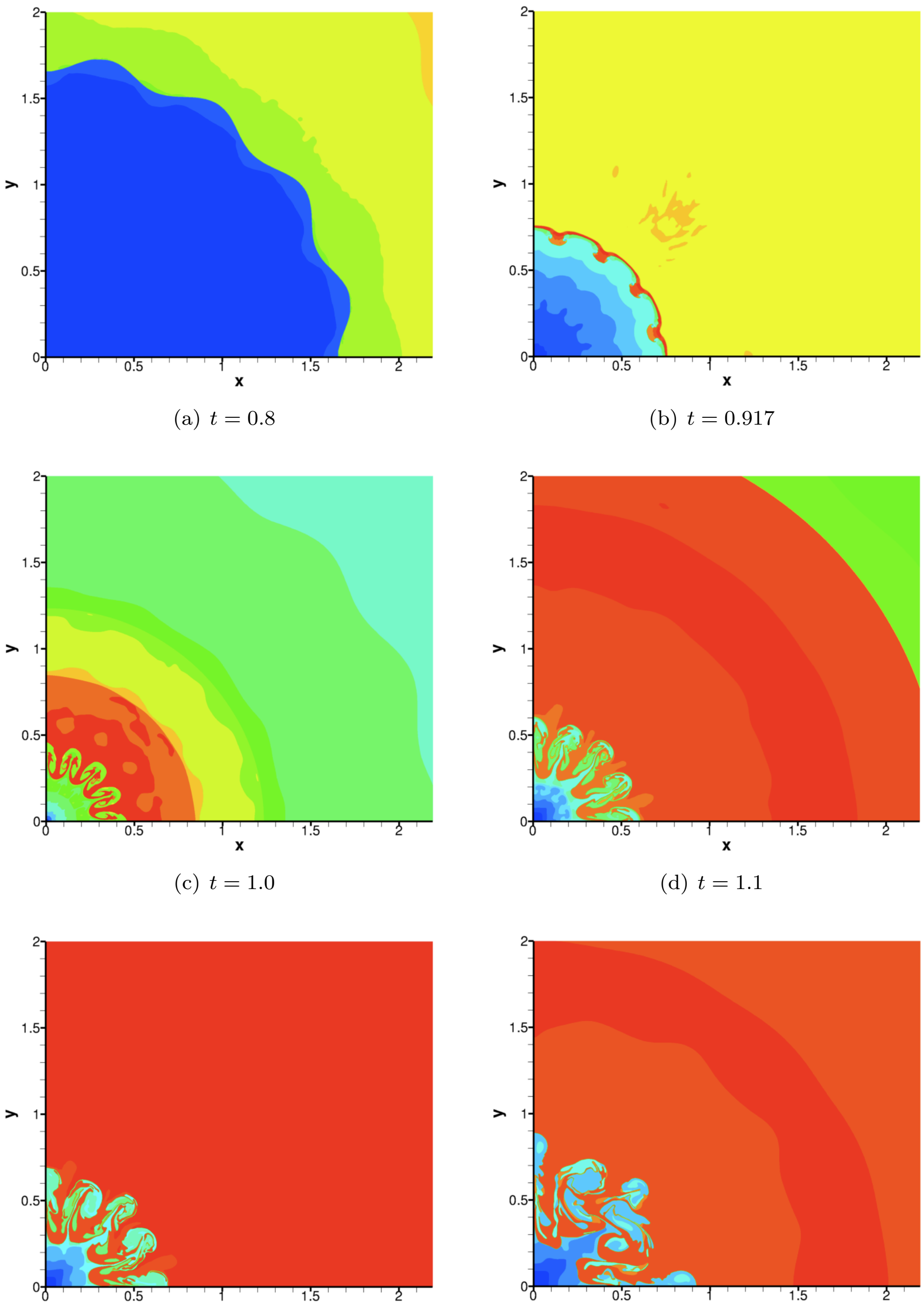

(a) $t = 0.8$

(b) $t = 0.917$

(c) $t = 1.0$

(d) $t = 1.1$

(e) $t = 1.2$

(f) $t = 1.5$

Figure D.28: $C \equiv \frac{\eta_0 n}{R_0} = 0.05$, $n = 16$, $r_i = 100$, $M_s = 1.65$, $\sigma_Y = 0.5\,\mathrm{GPa}$.

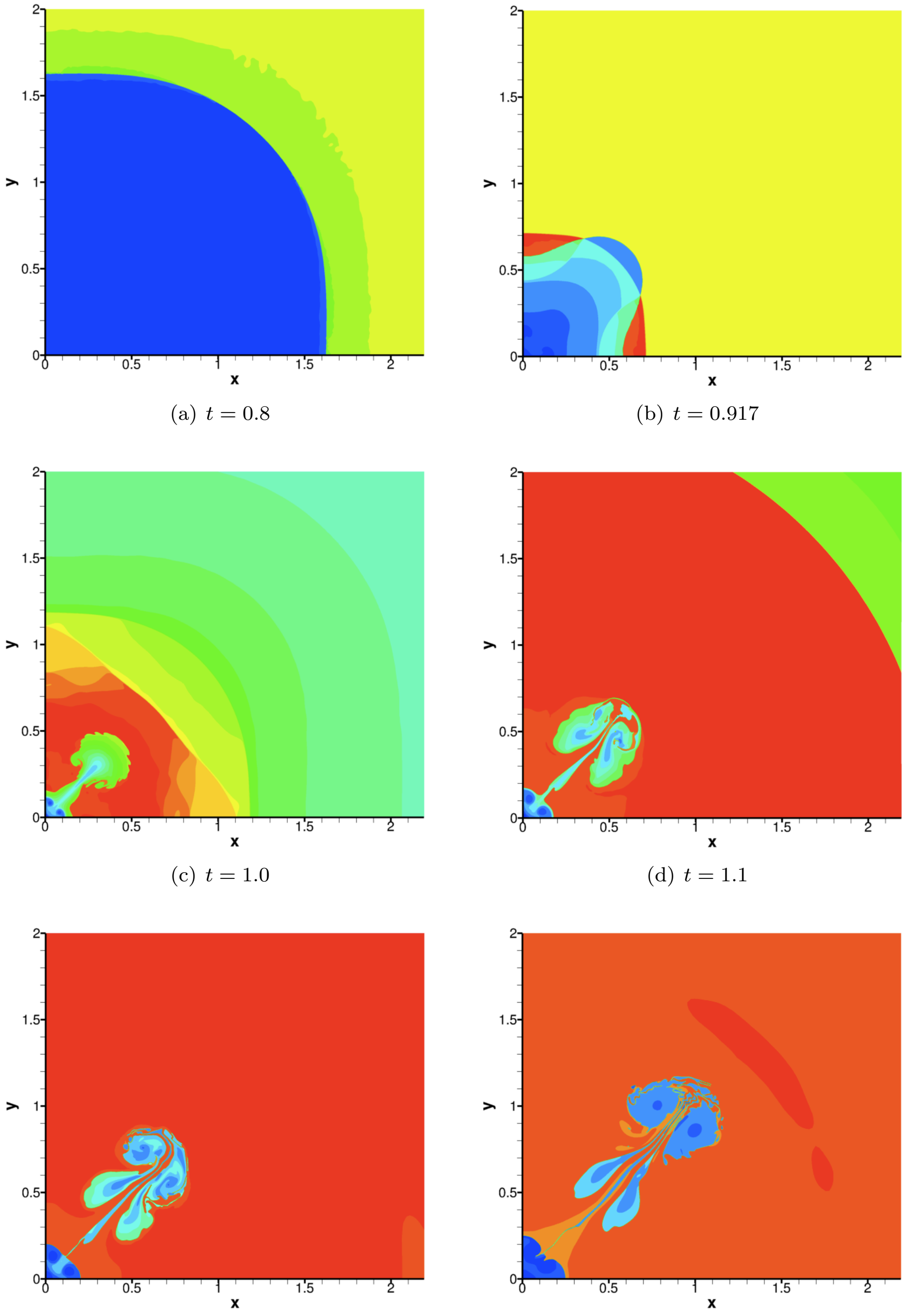

(a) $t = 0.8$

(b) $t = 0.917$

(c) $t = 1.0$

(d) $t = 1.1$

(e) $t = 1.2$

(f) $t = 1.5$

Figure D.29: $C \equiv \frac{\eta_0 n}{R_0} = 0.05$, $n = 4$, $r_i = 100$, $M_s = 1.65$, $\sigma_Y = 1\,\mathrm{GPa}$.

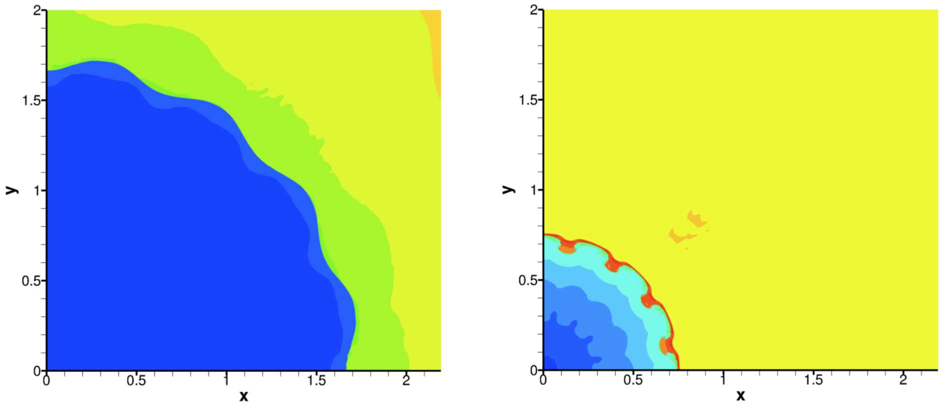

(a) $t = 0.8$ (b) $t = 0.917$

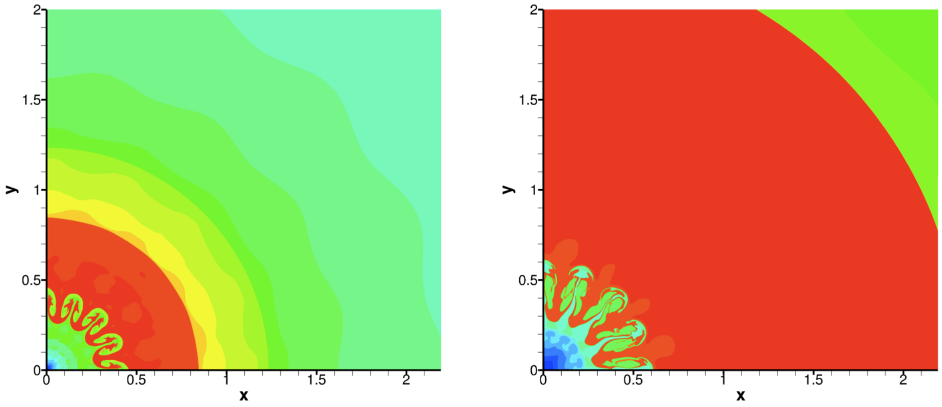

(c) $t = 1.0$ (d) $t = 1.1$

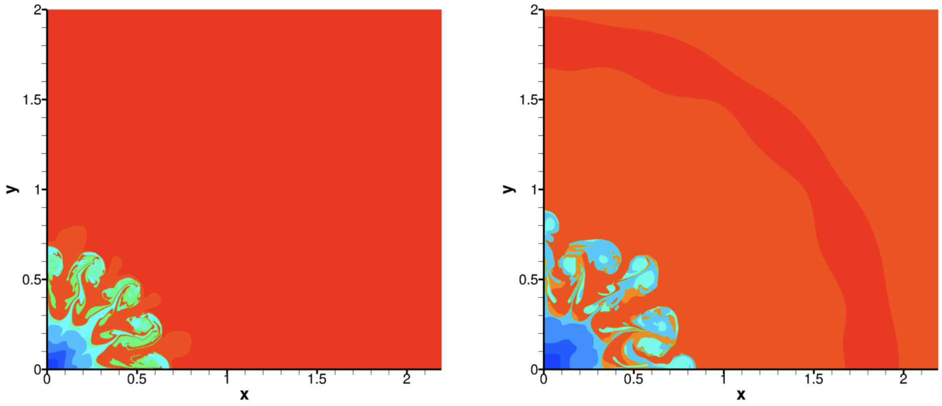

(e) $t = 1.2$ (f) $t = 1.5$

Figure D.30: $C \equiv \frac{\eta_0 n}{R_0} = 0.05$, $n = 16$, $r_i = 100$, $M_s = 1.65$, $\sigma_Y = 1\,\mathrm{GPa}$.

Bibliography

[1] Abgrall, R., and Karni, S. Computations of compressible multifluids. *Journal of Computational Physics 169*, 2 (2001), 594–623. Cited on page 25.

[2] Ahrens, T. Equations of state. In *High-Pressure Shock Compression of Solids* (1993), M. S. J. R. Asay, Ed., vol. 1, Springer, pp. 75–114. Cited on page 61.

[3] Anderson, J. C., Garth, C., Duchaineau, M. A., and Joy, K. I. Discrete multimaterial interface reconstruction for volume fraction data. *Computer Graphics Forum 27*, 3 (2008), 1015–1022. Cited on pages 6 and 26.

[4] Anderson, J. D. *Modern compressible flow with historical perspective.* McGraw-Hill, 2004. Cited on page 25.

[5] Andersson, P. U., and Holmlid, L. Ultra-dense deuterium: a possible nuclear fuel for inertial confinement fusion (ICF). *Physics Letters A 373*, 34 (2009), 3067–3070. Cited on pages 2 and 60.

[6] Arnett, D. The role of mixing in astrophysics. *Astrophysical Journal 127* (2000), 213–217. Cited on pages 3 and 82.

[7] Barton, P. *A novel multi-dimensional Eulerian approach to computational solid dynamics.* PhD thesis, Cranfield University, 2010. Cited on pages 10, 17, 23, and 27.

[8] Barton, P., Deiterding, R., Meiron, D., and Pullin, D. Eulerian adaptive finite-difference method for high-velocity impact and penetration problems. *Journal of Computational Physics* (2012). Cited on pages 3, 5, 10, 26, 27, 33, 36, 39, 40, 46, 49, 57, 63, 117, and 151.

[9] Barton, P., and Romenski, E. On computational modelling of strain-hardening material dynamics. *Communications on Computational Physics 11* (2012), 1525. Cited on pages xiii, 21, 22, and 38.

[10] Barton, P. T., Drikakis, D., and Romenski, E. I. An Eulerian finite-volume scheme for large elastoplastic deformations in solids. *International Journal for Numerical Methods in Engineering 81*, 4 (2010), 453–484. Cited on pages 4, 5, 10, 20, 23, and 27.

[11] Belov, S., Boriskov, G., Bykov, A., Ilkaev, R., Lukyanov, N., Matveev, A., Mikhailova, O., Selemir, V., Simakov, G., Trunin, R., Trusov, I., Urlin, V., Fortov, V., and Shuikin, A. Shock compression of solid deuterium. *JETP Letters 76* (2002), 433–435. Cited on pages 2, 7, and 60.

[12] Belytschko, T. Fluid-structure interaction. *Computers & Structures 12*, 4 (1980), 459–469. Cited on page 5.

[13] Belytschko, T., Liu, W. K., and Moran, B. *Nonlinear finite elements for continua and structures.* Wiley, 2000. Cited on page 25.

[14] Ben-Dor, G. Two dimensional interactions. In *Handbook of shock waves* (2001), G. Ben-Dor, O. Igra, and T. Elperin, Eds., vol. 2, Academic Press, pp. 68–265. Cited on pages 6 and 60.

[15] Bender, C. M., and Orszag, S. A. *Advanced mathematical methods for scientists and engineers.* McGraw-Hill, 1978. Cited on page 93.

[16] Benson, D. J. Computational methods in Lagrangian and Eulerian hydrocodes. *Computer Methods in Applied Mechanics and Engineering 99*, 23 (1992), 235–394. Cited on page 1.

[17] Benson, D. J. Momentum advection on unstructured staggered quadrilateral meshes. *International Journal for Numerical Methods in Engineering 75*, 13 (2008), 1549–1580. Cited on page 25.

[18] Berger, M., and Colella, P. Local adaptive mesh refinement for shock hydrodynamics. *Journal of Computational Physics 82*, 1 (1989), 64–84. Cited on page 26.

[19] Blatz, P. J., and Ko, W. L. Application of finite elastic theory to the deformation of rubbery materials. *Trans. Soc. Rheology 6* (1962), 223–252. Cited on page 64.

[20] Brouillette, M. The Richtmyer–Meshkov instability. *Annual Review of Fluid Mechanics 34* (2002), 445–468. Cited on pages 3 and 82.

[21] Brown, J. L., Ravichandran, G., Reinhart, W. D., and Trott, W. M. High pressure Hugoniot measurements using converging shocks. *Journal of Applied Physics 109*, 9 (2011), 093520. Cited on page 7.

[22] Burakovsky, L., and Preston, D. L. Analytic model of the Gruneisen parameter all densities. *Journal of Physics and Chemistry of Solids 65*, 8–9 (2004), 1581 – 1587. Cited on page 50.

[23] Cleja-Tigoiu, S., and Maugin, G. Eshelby's stress tensors in finite elastoplasticity. *Acta Mechanica 139* (2000), 231–249. Cited on page 74.

[24] Coleburn, N. L., and Forbes, J. W. Irreversible transformation of hexagonal boron nitride by shock compression. *The Journal of Chemical Physics 48*, 2 (1968), 555–559. Cited on page 7.

[25] Deiterding, R. Construction and application of an AMR algorithm for distributed memory computers. In *Adaptive Mesh Refinement–Theory and Applications*, T. Plewa, T. Linde, and V. G. Weirs, Eds., vol. 41 of *Lectures Notes in Computational Science and Engineering.* Springer, 2005, pp. 361–372. Cited on pages 3 and 26.

[26] Deiterding, R., Radovitzky, R., Mauch, S., Noels, L., Cummings, J., and Meiron, D. A virtual test facility for the efficient simulation of solid material response under strong shock and detonation wave loading. *Engineering with Computers 22* (2006), 325–347. Cited on page 3.

[27] Dimonte, G., Terrones, G., Cherne, F. J., Germann, T. C., Dupont, V., Kadau, K., Buttler, W. T., Oro, D. M., Morris, C., and Preston, D. L. Use of the Richtmyer–Meshkov instability to infer yield stress at high-energy densities. *Physical Review Letters 107* (2011), 264502. Cited on pages xvi, xvii, 8, 109, 111, 112, 113, 114, 115, 116, and 152.

[28] Dimotakis, P. E., and Samtaney, R. Planar shock cylindrical focusing by a perfect-gas lens. *Physics of Fluids 18*, 3 (2006), 031705. Cited on page 7.

[29] Donea, J., Giuliani, S., and Halleux, J. An Arbitrary Lagrangian-Eulerian finite element method for transient dynamic fluid-structure interactions. *Computer Methods in Applied Mechanics and Engineering 33*, 13 (1982), 689–723. Cited on page 2.

[30] Dorovskii, V. N., Iskol'dskii, A. M., and Romenskii, E. I. Dynamics of impulsive metal heating by a current and electrical explosion of conductors. *Journal of Applied Mechanics and Technical Physics 24* (1983), 454–467. Cited on pages 46 and 110.

[31] Dyadechko, V., and Shashkov, M. Moment-of-fluid interface reconstruction. *Tech. Rep. 05-7571 Los Alamos National Laboratory* (2005). Cited on pages 6 and 26.

[32] Fedkiw, R. P., Aslam, T., Merriman, B., and Osher, S. A non-oscillatory Eulerian approach to interfaces in multimaterial flows (the ghost fluid method). *Journal of Computational Physics 152*, 2 (1999), 457–492. Cited on page 40.

[33] Fix, G. J. Phase field methods for free boundary problems. In *Free boundary problems: theory and applications*, A. Fasano and M. Primicerio, Eds. Pitman, 1983, p. 580. Cited on page 6.

[34] Floch, P. L., and Olsson, F. A second-order Godunov method for the conservation laws of nonlinear elastodynamics. *IMPACT of Computing in Science and Engineering 2*, 4 (1990), 318–354. Cited on page 5.

[35] Fressmann, D., and Wriggers, P. Advection approaches for single- and multi-material arbitrary Lagrangian–Eulerian finite element procedures. *Computational Mechanics 39* (2007), 153–190. Cited on page 25.

[36] Fryxell, B., Arnett, D., and Mueller, E. Instabilities and clumping in SN 1987A. I-early evolution in two dimensions. *Astrophysical Journal* (1991), 619–634. Cited on pages 3 and 110.

[37] Gavrilyuk, S., Favrie, N., and Saurel, R. Modelling wave dynamics of compressible elastic materials. *Journal of Computational Physics 227*, 5 (2008), 2941–2969. Cited on pages 5 and 61.

[38] Gillis, P. P., and Gilman, J. J. Dynamical dislocation theory of crystal plasticity. Part I: The yield stress. *Journal of Applied Physics 36*, 11 (1965), 3370–3380. Cited on page 18.

[39] Gillis, P. P., and Gilman, J. J. Dynamical dislocation theory of crystal plasticity. Part II: Easy glide and strain hardening. *Journal of Applied Physics 36*, 11 (1965), 3380–3386. Cited on page 18.

[40] Gilman, J. J. Dislocation mobility in crystals. *Journal of Applied Physics 36*, 10 (1965), 3195–3206. Cited on page 17.

[41] Gilman, J. J. Microdynamics of plastic flow at constant stress. *Journal of Applied Physics 36*, 9 (1965), 2772–2777. Cited on page 17.

[42] Godunov, S., and Romenski, E. *Elements of Continuum Mechanics and Conservation Laws*. Kluwer Academic/Plenum Publishers, 2003. Cited on pages 4, 8, 10, 19, 21, 23, 27, and 151.

[43] Godunov, S., and Romenskii, E. Nonstationary equations of nonlinear elasticity theory in Eulerian coordinates. *Journal of Applied Mechanics and Technical Physics 13* (1972), 868–884. Cited on pages 4 and 10.

[44] Godunov, S. K. A difference method for numerical calculation of discontinuous solutions of the equations of hydrodynamics. *Matematicheskii Sbornik 47(89)* (1959), 271–306. Cited on page 25.

[45] Griffond, J. Linear interaction analysis for Richtmyer–Meshkov instability at low Atwood numbers. *Physics of Fluids 18*, 5 (2006), 054106. Cited on page 8.

[46] Guderley, G. Starke Kugelige und zylindrische Verdichtungsstösse in der Nähe des Kugelmittelpunktes bzw der Zylinderachse. *Luftfahrtforschung 19* (1942), 302–312. Cited on pages 6 and 60.

[47] Guo, W. G. Flow stress and constitutive model of OFHC Cu for large deformation, different temperatures and different strain rates. *Baozha Yu Chongji/Explosion and Shock Waves (in Chinese) 25* (2005), 244. Cited on pages xiii, 21, and 22.

[48] Harten, A., Lax, P., and Leer, B. On upstream differencing and Godunov-type schemes for hyperbolic conservation laws. *SIAM Review 25*, 1 (1983), 35–61. Cited on page 42.

[49] Hill, D. J., Pullin, D. I., Ortiz, M., and Meiron, D. I. An Eulerian hybrid WENO centered-difference solver for elastic-plastic solids. *Journal of Computational Physics 229* (2010), 9053–9072. Cited on pages 5, 10, 17, 19, 25, 28, 57, 63, and 75.

[50] Hiroe, T., Matsuo, H., and Fujiwara, K. Numerical simulation of cylindrical converging shocks in solids. *Journal of Applied Physics 72* (1992), 2605–2611. Cited on pages 6, 61, and 79.

[51] Hirt, C., Amsden, A., and Cook, J. An arbitrary Lagrangian-Eulerian computing method for all flow speeds. *Journal of Computational Physics 14*, 3 (1974), 227–253. Cited on page 2.

[52] Hirt, C., and Nichols, B. Volume of fluid (VOF) method for the dynamics of free boundaries. *Journal of Computational Physics 39*, 1 (1981), 201–225. Cited on page 6.

[53] Holmes, R. L., Dimonte, G., Fryxell, B., Gittings, M. L., Grove, J. W., Schneider, M., Sharp, D. H., Velikovich, A. L., Weaver, R. P., and Zhang, Q. Richtmyer–Meshkov instability growth: experiments, simulation and theory. *Journal of Fluid Mechanics 389* (5 1999), 55–79. Cited on page 8.

[54] Hornung, H. G., Pullin, D. I., and Ponchaut, N. F. On the question of universality of imploding shock waves. *Acta Mechanica 201* (2008), 31–35. Cited on pages 6 and 60.

[55] Hosseini, S. H. R., and Takayama, K. Experimental study of Richtmyer–Meshkov instability induced by cylindrical shock waves. *Physics of Fluids 17*, 8 (2005), 084101. Cited on page 7.

[56] Howell, B., and Ball, G. A free-Lagrange augmented Godunov method for the simulation of elastic-plastic solids. *Journal of Computational Physics 175*, 1 (2002), 128–167. Cited on pages xiii, 2, 50, and 52.

[57] Jiang, G.-S., and Shu, C.-W. Efficient implementation of weighted ENO schemes. *Journal of Computational Physics 126*, 1 (1996), 202–228. Cited on pages 5, 35, and 36.

[58] Jones, M. A., and Jacobs, J. W. A membraneless experiment for the study of Richtmyer–Meshkov instability of a shock-accelerated gas interface. *Physics of Fluids 9*, 10 (1997), 3078–3085. Cited on page 8.

[59] Khokhlov, A., Oran, E., and Thomas, G. Numerical simulation of deflagration-to-detonation transition: the role of shock–flame interactions in turbulent flames. *Combustion and Flame 117*, 12 (1999), 323–339. Cited on page 3.

[60] Lanier, N., Barnes, C., Batha, S., Day, R., Magelssen, G., Scott, J., Dunne, A., Parker, K., and Rothman, S. Multimode seeded Richtmyer–Meshkov mixing in a convergent, compressible, miscible plasma system. *Physics of Plasmas 10* (2003), 1816. Cited on page 109.

[61] Levinson, M., and Burgess, I. A comparison of some simple constitutive relations for slightly compressible rubber-like materials. *International Journal of Mechanical Sciences 13*, 6 (1971), 563–572. Cited on pages 61, 85, and 105.

[62] Lindl, J. D. *Inertial confinement fusion: The quest for ignition and energy gain using indirect drive.* Springer, 1998. Cited on pages 2, 60, and 109.

[63] Lindl, J. D., McCrory, R. L., and Campbell, E. M. Progress toward ignition and burn propagation in inertial confinement fusion. *Physics Today 45*, 9 (1992), 32–40. Cited on pages 3 and 82.

[64] Liu, G. *Meshfree methods. Moving beyond the finite element method.* CRC Press, 2010. Cited on page 2.

[65] Liu, T., Khoo, B., and Yeo, K. Ghost fluid method for strong shock impacting on material interface. *Journal of Computational Physics 190*, 2 (2003), 651–681. Cited on pages 26 and 40.

[66] Lombardini, M. *Richtmyer–Meshkov instability in converging geometries.* PhD thesis, California Institute of Technology, 2008. Cited on pages 3 and 110.

[67] Lombardini, M., and Pullin, D. Small-amplitude perturbations in the three-dimensional cylindrical Richtmyer–Meshkov instability. *Physics of Fluids 21* (2009), 114103. Cited on pages 8 and 110.

[68] Lombardini, M., and Pullin, D. I. Startup process in the Richtmyer–Meshkov instability. *Physics of Fluids 21*, 4 (2009), 044104. Cited on pages 8 and 106.

[69] López Ortega, A., and Scovazzi, G. A geometrically-conservative, synchronized, flux-corrected remap for arbitrary Lagrangian–Eulerian computations with nodal finite elements. *Journal of Computational Physics 230*, 17 (2011), 6709–6741. Cited on page 2.

[70] Maran, S. P., Sonneborn, G., Pun, C. S. J., Lundqvist, P., Iping, R. C., and Gull, T. R. Physical conditions in circumstellar gas surrounding SN 1987A 12 years after outburst. *The Astrophysical Journal 545*, 1 (2000), 390. Cited on page 3.

[71] Marsden, J., and Hughes, T. *Mathematical foundations of elasticity.* Dover Publications, 1993. Cited on pages 1, 15, and 23.

[72] Masri, R., and Durban, D. Dynamic spherical cavity expansion in an elastoplastic compressible Mises solid. *Journal of Applied Mechanics 72* (2005), 887–898. Cited on page 60.

[73] Menikoff, R. Elastic–plastic shock waves. In *Shock Wave Science and Technology Reference Library* (2007), Y. Horie, Ed., vol. 2, Solids I, Springer, pp. 189–224. Cited on page 78.

[74] Meshkov, E. E. Instability of a shock wave accelerated interface between two gases. *NASA Technical Transcriptions F-13*, 2 (1970), 074. Cited on pages 3 and 82.

[75] Mikaelian, K. O. Turbulent mixing generated by Rayleigh–Taylor and Richtmyer–Meshkov instabilities. *Physica D: Nonlinear Phenomena 36*, 3 (1989), 343–357. Cited on page 3.

[76] Mikaelian, K. O. Rayleigh–Taylor and Richtmyer–Meshkov instabilities and mixing in stratified cylindrical shells. *Physics of Fluids 17* (2004), 094105. Cited on pages 8 and 110.

[77] Miller, G., and Colella, P. A conservative three-dimensional Eulerian method for coupled solid–fluid shock capturing. *Journal of Computational Physics 183*, 1 (2002), 26–82. Cited on pages 5, 6, and 61.

[78] Miller, G. H., and Colella, P. A high-order Eulerian Godunov method for elastic–plastic flow in solids. *Journal of Computational Physics 167* (2001), 131–176. Cited on pages 4, 5, 10, 19, 25, 28, 29, 57, 66, and 151.

[79] Min, C. On reinitializing level set functions. *Journal of Computational Physics 229*, 8 (2010), 2764 – 2772. Cited on page 40.

[80] Miyoshi, T., and Kusano, K. A multi-state HLL approximate Riemann solver for ideal magnetohydrodynamics. *Journal of Computational Physics 208*, 1 (2005), 315–344. Cited on pages 26, 42, 45, and 152.

[81] Nagayama, K., and Murakami, T. Numerical analysis of converging shock waves in concentric solid layer. *Journal of the Physical Society of Japan 40* (1976), 1479–1486. Cited on page 7.

[82] Ogden, R. W. Large deformation isotropic elasticity—on the correlation of theory and experiment for incompressible rubberlike solids. *Proceedings of the Royal Society of London. Series A. Mathematical and Physical Sciences 326*, 1567 (1972), 565–584. Cited on page 5.

[83] Olsson, E., and Kreiss, G. A conservative level set method for two phase flow. *Journal of Computational Physics 210*, 1 (2005), 225–246. Cited on pages 6 and 39.

[84] Orowan, E. Problems of plastic gliding. *Proceedings of the Physical Society 52*, 1 (1940), 8. Cited on page 17.

[85] Osher, S. Level set methods. In *Geometric Level Set Methods in Imaging, Vision, and Graphics*. Springer New York, 2003, pp. 3–20. Cited on page 6.

[86] Osher, S., and Sethian, J. A. Fronts propagating with curvature-dependent speed: Algorithms based on Hamilton–Jacobi formulations. *Journal of Computational Physics 79*, 1 (1988), 12–49. Cited on page 6.

[87] Payne, R. B. A numerical method for a converging cylindrical shock. *Journal of Fluid Mechanics 2* (1957), 185–200. Cited on page 6.

[88] Peery, J. S., and Carroll, D. E. Multi-material ALE methods in unstructured grids. *Computer Methods in Applied Mechanics and Engineering 187*, 3–4 (2000), 591–619. Cited on page 25.

[89] Piriz, A. R., Cela, J. J. L., Cortázar, O. D., Tahir, N. A., and Hoffmann, D. H. H. Rayleigh-Taylor instability in elastic solids. *Physical Review E 72*, 5 (Nov 2005), 056313. Cited on page 83.

[90] Piriz, A. R., López Cela, J. J., Tahir, N. A., and Hoffmann, D. H. H. Richtmyer–Meshkov flow in elastic solids. *Physical Review E 74*, 3 (Sep 2006), 037301. Cited on pages 3, 8, 82, 97, 98, 101, and 108.

[91] Piriz, A. R., López Cela, J. J., Tahir, N. A., and Hoffmann, D. H. H. Richtmyer–Meshkov instability in elastic-plastic media. *Physical Review E 78* (Nov 2008), 056401. Cited on pages 8, 109, 111, 114, and 152.

[92] Plohr, B. J., and Sharp, D. H. A conservative Eulerian formulation of the equations for elastic flow. *Advances in Applied Mathematics 9*, 4 (1988), 481–499. Cited on pages 4, 8, and 10.

[93] Plohr, B. J., and Sharp, D. H. A conservative formulation for plasticity. *Advances in Applied Mathematics 13* (1992), 462–493. Cited on page 4.

[94] Plohr, B. J., and Sharp, D. H. Instability of accelerated elastic metal plates. *Zeitschrift fur angewandte Mathematik und Physik 49* (1998), 786–804. Cited on page 82.

[95] Plohr, J. N., and Plohr, B. J. Linearized analysis of Richtmyer-Meshkov flow for elastic materials. *Journal of Fluid Mechanics 537* (2005), 55–89. Cited on pages 3, 8, and 82.

[96] Richtmyer, R. D. Taylor instability in shock acceleration of compressible fluids. *Communications on Pure and Applied Mathematics 13*, 2 (1960), 297–319. Cited on pages 3, 82, and 129.

[97] Samtaney, R., and Zabusky, N. J. Circulation deposition on shock-accelerated planar and curved density-stratified interfaces: models and scaling laws. *Journal of Fluid Mechanics 269* (1993), 45–78. Cited on page 8.

[98] Schwendeman, D. W., and Whitham, G. B. On converging shock waves. *Proceedings of the Royal Society of London. Series A. Mathematical and Physical Sciences 413*, 1845 (1987), 297–311. Cited on page 7.

[99] Shu, C.-W. Essentially non-oscillatory and weighted essentially non-oscillatory schemes for hyperbolic conservation laws. *ICASE Report*, 97-65 (1997), 202–228. NASA/CR-97-206253. Cited on pages 4, 35, and 39.

[100] Simo, J. C., and Hughes, T. J. R. *Computational Inelasticity.* Springer, 1998. Cited on page 17.

[101] Simo, J. C., and Taylor, R. L. A return mapping algorithm for plane stress elastoplasticity. *International Journal for Numerical Methods in Engineering 22*, 3 (1986), 649–670. Cited on page 5.

[102] Stone, J. M., Xu, J., and Mundy, L. G. Formation of 'bullets' by hydrodynamical instabilities in stellar outflows. *Nature 377* (1995), 315–317. Cited on page 3.

[103] Taylor, G. The instability of liquid surfaces when accelerated in a direction perpendicular to their planes I. *Proceedings of the Royal Society of London. Series A. Mathematical and Physical Sciences 201*, 1065 (1950), 192–196. Cited on page 3.

[104] Taylor, G. I. The mechanism of plastic deformation of crystals. Part I: Theoretical. *Proceedings of the Royal Society of London. Series A 145*, 855 (1934), 362–387. Cited on page 17.

[105] Terrones, G. Fastest growing linear Rayleigh–Taylor modes at solid–fluid and solid–solid interfaces. *Physical Review E 71*, 3 (Mar 2005), 036306. Cited on page 83.

[106] Timothy, S. The structure of adiabatic shear bands in metals: A critical review. *Acta Metallurgica 35*, 2 (1987), 301–306. Cited on page 7.

[107] Titarev, V. A., Romenski, E., and Toro, E. F. Musta-type upwind fluxes for non-linear elasticity. *International Journal for Numerical Methods in Engineering 73*, 7 (2008), 897–926. Cited on pages 5, 46, and 110.

[108] Toro, E. F. *Riemann Solvers and Numerical Methods for Fluid Dynamics.* Springer, 1999. Cited on pages 24 and 45.

[109] Toro, E. F., Spruce, M., and Speares, W. Restoration of the contact surface in the HLL-Riemann solver. *Shock Waves 4* (1994), 25–34. Cited on page 42.

[110] Trangenstein, J. A., and Colella, P. A higher-order Godunov method for modeling finite deformation in elastic-plastic solids. *Communications on Pure and Applied Mathematics 44*, 1 (1991), 41–100. Cited on pages 4 and 10.

[111] Truesdell, C. Hypo-elasticity. *Journal of Rational Mechanics and Analysis 4* (1955), 83–133. Cited on page 16.

[112] van der Pijl, S. P., Segal, A., Vuik, C., and Wesseling, P. A mass-conserving level-set method for modelling of multi-phase flows. *International Journal for Numerical Methods in Fluids 47*, 4 (2005), 339–361. Cited on page 5.

[113] Vandenboomgaerde, M., Mügler, C., and Gauthier, S. Impulsive model for the Richtmyer–Meshkov instability. *Physical Review E 58* (Aug 1998), 1874–1882. Cited on page 8.

[114] Vetter, M., and Sturtevant, B. Experiments on the Richtmyer–Meshkov instability of an air/SF6 interface. *Shock Waves 4* (1995), 247–252. Cited on page 3.

[115] Walter, J., Glimm, J., Grove, J., Hwang, H.-C., Lin, X., Plohr, B. J., and Sharp, D. H. Eulerian front tracking for solid dynamics. In *U.S. Army Symposium on Solid Mechanics* (1999), K. Iyer and S. Chou, Eds., Batelle Press, pp. 343–366. Cited on page 5.

[116] Walter, J., Yu, D., Plohr, B. J., Grove, J., and Glimm, J. An algorithm for Eulerian front tracking for solid deformation. Tech. Rep. SUNY SB-AMS-00-24, State University of New York, 2000. Cited on page 5.

[117] Ward, G. *The simulation of shock- and impact-driven flows with Mie-Gruneisen equations of state.* PhD thesis, California Institute of Technology, 2011. Cited on page 41.

[118] Watanabe, M., and Takayama, K. Stability of converging cylindrical shock waves. *Shock Waves 1* (1991), 149–160. Cited on pages 2 and 7.

[119] Weseloh, W. N., Clancy, S. P., and Painter, J. *PAGOSA manual.* Tech. Rep. LAUR-14425-M, Los Alamos National Laboratory, 2010. Cited on page 111.

[120] Wheatley, V., Pullin, D. I., and Samtaney, R. Stability of an impulsively accelerated density interface in magnetohydrodynamics. *Physical Review Letters 95*, 12 (Sep 2005), 125002. Cited on pages 3 and 82.

[121] Whitham, G. B. A new approach to problems of shock dynamics Part I: Two-dimensional problems. *Journal of Fluid Mechanics 2* (1957), 145–171. Cited on page 60.

[122] Whitham, G. B. *Linear and Nonlinear Waves.* John Wiley and Sons, 1974. Cited on pages 6, 60, and 71.

[123] Wouchuk, J. G., and Nishihara, K. Linear perturbation growth at a shocked interface. *Physics of Plasmas 3*, 10 (1996), 3761–3776. Cited on page 8.

[124] Xue, Q., Meyers, M., and Nesterenko, V. Self-organization of shear bands in titanium and Ti–6Al–4V alloy. *Acta Materialia 50*, 3 (2002), 575–596. Cited on page 7.

[125] Yadav, H. S., and Singh, V. P. Converging shock waves in metals. *Pramana 18* (1982), 331–338. Cited on pages 6, 60, and 79.

[126] Youngs, D. Numerical simulation of mixing by Rayleigh–Taylor and Richtmyer–Meshkov instabilities. *Laser and Particle Beams 12* (11 1994), 725–750. Cited on page 3.

[127] Yu, H., and Livescu, D. Rayleigh–Taylor instability in cylindrical geometry with compressible fluids. *Physics of Fluids 20* (2008), 104103. Cited on page 110.

[128] Zabusky, N. J. Vortex paradigm for accelerated inhomogeneous flows: visiometrics for the Rayleigh–Taylor and Richtmyer–Meshkov environments. *Annual Review of Fluid Mechanics 31* (1999), 495–536. Cited on page 3.

[129] Zhang, Q., and Graham, M. J. A numerical study of Richtmyer–Meshkov instability driven by cylindrical shocks. *Physics of Fluids 10* (1998), 974. Cited on pages 8 and 110.

[130] Zhou, Y., Remington, B. A., Robey, H. F., Cook, A. W., Glendinning, S. G., Dimits, A., Buckingham, A. C., Zimmerman, G. B., Burke, E. W., Peyser, T. A., Cabot, W., and Eliason, D. Progress in understanding turbulent mixing induced by Rayleigh–Taylor and Richtmyer–Meshkov instabilities. *Physics of Plasmas 10*, 5 (2003), 1883–1896. Cited on page 3.